The theory and applications
of
writhing

Submitted by : Christopher Brooke Prior
UCL
University of London

I, Christopher Brooke Prior, confirm that the work presented in this thesis is my own. Where information has been derived from other sources, I confirm that this has been indicated in the thesis

....

Acknowledgements

Firstly I must thank my supervisor Mitchell Berger, for his considerable knowledge, insight and most importantly his encouragement. I greatly enjoyed our discussions and always left his office with a renewed enthusiasm and desire to advance my research. To my parents my thanks and love; I have always felt their unswerving support and could not have got to this point in my life without it. I must also thank the EPSRC research board, without whom non of this would be possible. For those I have encountered through my time in the UCL maths department I must thank you for your support and knowledge. Finally, I thank my examiners for taking the time to provide their insight and help improve my work.

Finally to my Bee, I take this opportunity to give congratulations. You won, and somehow managed to drag me over the finish line with you xxxx.

Abstract

Writhe measures the extent to which a curve is kinked and coiled about itself in space. It has generally been expressed as a double integral. This measure can be interpreted as the average number of signed crossings seen by each viewer, over all possible viewpoints of the curve. This simple geometrical interpretation is used to describe the established properties of the writhe, as applied to closed spacecurves. These descriptions differ from previous work as they do not require the construction of an artificial ribbon structure.

A major feature of this thesis concerns the evaluation of the writhe along a preferred direction. A directional measure termed the polar writhe will be developed which can be applied to generic curves (open or closed) . This single integral expression is shown to be equivalent to the double integral writhe measure for closed curves. However for open curves the two measures are shown to differ. Further, it is shown that the polar writhe has distinct advantages when analysing curves with a strong directional bias.

The thesis then discusses in detail the properties of both the writhe and the polar writhe measures for open curves. The use of artificial closures for both measures is examined. In the case of the writhe a new closure is defined that allows the evaluation of the writhe using single integral expression via the theorems of Fuller. This closure is unique in that it can be applied to open curves whose end points are in general position. A simple expression for calculating the non-local polar writhe is derived which generalises a closed curve expression defined in (Berger Prior J. Phys. A: Math. Gen. 39, 8321-8348, (2006)). A quantitative study on the effect of the choice of evaluation direction of the polar writhe is conducted.

The polar writhe formulation is applied to a simple linear force-free magnetic field model where the field lines form loops above a boundary plane. Loops with a sufficient amount of kinking are generally seen to form S or inverse S (Z) shaped structures. Such field lines structures are commonly observed in the Sun's corona. A popular measure of the field line morphology is the magnetic helicity. We use the polar writhe, the correct form for the writhe helicity in the coronal region, to challenge some popular assumptions of the field. Firstly, the writhe of field lines of significant aspect ratio (the apex height divided by the foot point width) can often have the opposite sign to that assumed in a recent review paper by Green et al (Solar Phys., 365-391, (2007)). Secondly, we demonstrate the possibility of field lines forming apparent Z shaped structures which are in fact constructed from a pair of S shapes and have a writhe sign expected of an S shaped structure. Such field lines could be misinterpreted without full knowledge of the line's three dimensional structure. Thirdly, we show that much of the interesting morphological behaviour occurs for field lines located next to separatrices.

Contents

4 A comparison of writhing expressions for open spacecurves 103

5 The writhing of open spacecurves 122

6 Coronal loop morphology 151

List of Figures

Chapter 1

Introduction

Topology is the branch of mathematics which studies the properties of objects preserved under continuous deformations. Its meaning derives from the Greek terms topos meaning “place”, and logos “study”. The field appears to have been given its name by Johann Benedict Listing, a student of Gauss (as related by Epple [39]). Previous to this, the field was known as *Geometria Situs*, that is the geometrical study of position. In contrast to the more popular *Geometria magnitudis*, the study of analytical geometry with regards to size, *Geometria situs* had received little attention up until this point. As Gauss himself states in his mathematical notes [47];

> *“Of the geometria situs, which Leibniz forsaw and which only a pair of geometers (Euler and Vandermonde) were granted the privilege of taking a faint glance, we know and have, after a century and a half, little more than nothing”*

Gauss states that a central problem in the area of Geometria Situs will be to count the intertwining of two closed or infinite curves and introduces an expression for the linking of two such curves (Figure 1.1 depicts two interlinked closed curves). This expression is known today as the linking number. Gauss’s work found a conduit in James Clerk Maxwell, who reported this work to the London Mathematical Society in 1869. Maxwell applied these ideas, to the study of electromagnetism, in his major work *Treatise on Electricity and Magnetism* 1873 [70].

The latter half of the twentieth century witnessed a rapid expansion in the interest of the possible physical applications of topological quantities, such as the linking number and the writhing number. The writhing, first considered by Călugăreanu [24],

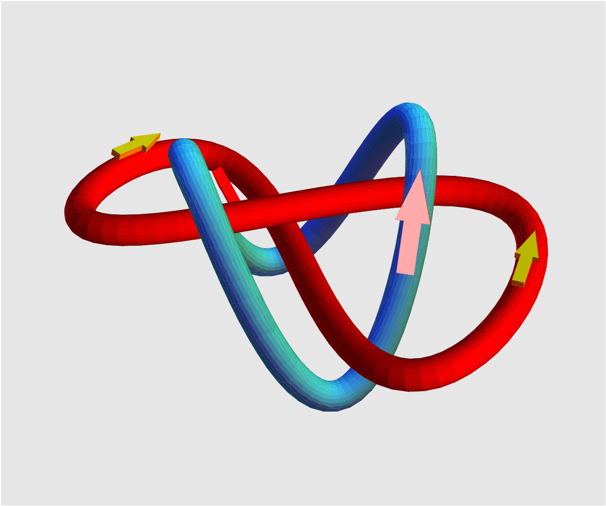

Figure 1.1: An example of two inter-linked curves, this particular link is known as the Whitehead link. Despite the obvious inter-linking of the two curves, the actual linking number, as measured by Gauss's expression (1.16), is zero.

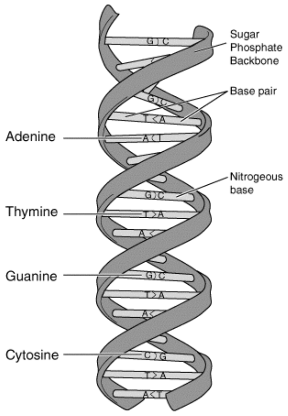

Figure 1.2: A representation of the helical structure inherent to the DNA molecule. This figure represents a section of a DNA molecule. Shown are the molecules twin phosphate backbones, which wind around each other. These backbones are joined by four base molecules which link to form base pairs. The four protein types are marked in the figure. This figure is reprinted from the National Human Genome Research Institute website (www.genome.gov)

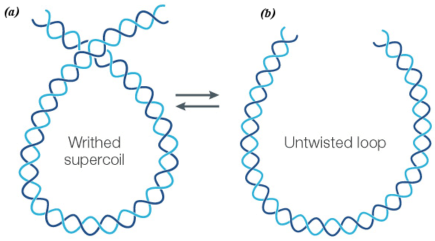

Figure 1.3: An example of supercoiling of a section of DNA. The two figures are representations of a section of DNA molecule. In (a) the DNA's axis coils around itself to form a loop type structure. This loop is said to have writhing. This writhing is not present in (b). The two figures are interchangeable by an appropriate set of deformations applied to the axis (Section 1.3.1). This figure is reprinted from Travers and Muskhelishvili [111].

is a geometrical measurement of the extent to which a curve is kinked and coiled about itself in space; essentially it represents the self-linking of a single curve. It is to be noted that the writhing of a curve is not itself a topological entity, as it is **not** invariant to continuous deformations. It is however a geometrical measure of position, without scale. Writhing and linking have proven useful tools in applications such as magnetic field theory, polymer physics and molecular biology. For example, in magnetic field theory, Moffatt 1969 [74] and Arnold 1979 [6] demonstrated that the magnetic helicity of a pair of linked magnetic flux tubes is simply the multiple of the linking number of the two tubes and the magnetic flux flowing through each tube. Here a topological quantity, represented by the spatial relationship of the tube pair, is mixed with a magnitude, i.e. the amount of flux. The use of the linking and writhing numbers is commonplace in the field of molecular biology, following the work of Crick 1976 [31], where the complexity of coiled DNA molecules can be measured by the linking number of the two polymer structures comprising the molecules double helical structure (see Figure 1.2). The molecules can additionally coil about their own axis, a process known as *supercoiling* (see Figure 1.3); this self-linking can be represented by the writhing number. A key role of DNA supercoiling is its role in compacting the lengthy DNA molecules (see Bates and Maxwell [9] for an overview of the role played by topology in the analysis of DNA).

The concepts of writhing and linking are well understood for curves which close upon themselves. This is fine for closed DNA molecules such as some plasmids, bacterial DNA and mitochondrial DNA. However, many applications involve curves

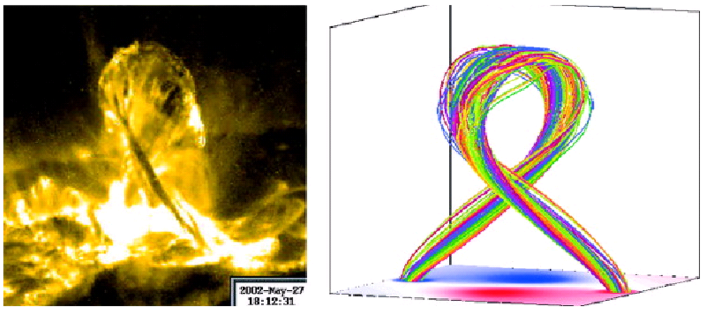

Figure 1.4: A kinked magnetic filament in the solar corona on 27 May 2002. On the left is an image from the TRACE 195 Å line. The right picture is from a numerical simulation by Török and Kliem 2005 [110].

with endpoints. For example recent experiments have examined the properties of open sections of DNA using magnetic micro-manipulation techniques (Smith *et al* [105], Bustamante *et al* [20]). The coronal magnetic field is a second example of an open field structure; as can be seen in Figure 1.4 it tends to form open helical structures. Various methods for evaluating the linking and writhing of open curves have been proposed. One approach involves extending an open helical structure with a planar section of curve, which allows the use of well established, linking and writhe expressions for closed curves (Fuller [45], Vologodskii and Marko [115], Rosetto and Maggs [92] and van der Heijden *et al* [114]). A second approach has been to define expressions which measure the open linking and writhing (Fain *et al* [40], Bouchiat and Mézard [17]). As shall be discussed in section 1.6.6, both methods, as currently applied, present certain difficulties and inconsistencies in the evaluating of open linking and writhing. A major theme of this thesis will be the development of a new measure of open writhing and linking which is consistent for open spacecurves.

The concepts of writhing and linking can be introduced, in simple terms, by way of knot theory.

1.1 Writhe, Link and Knot theory

We will define a knot as a circle $\mathbb{S}^1$ embedded in $\mathbb{R}^3$ without any double points. Figure 1.5 is an example of a knot. A link represents the disjoint union of a set of such

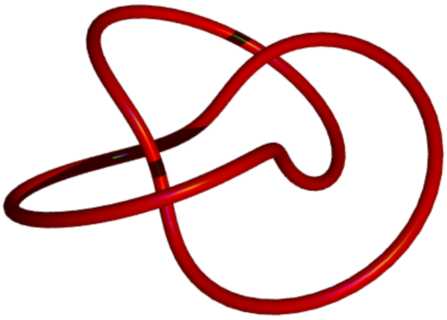

Figure 1.5: A 2-3 torus (trefoil) knot.

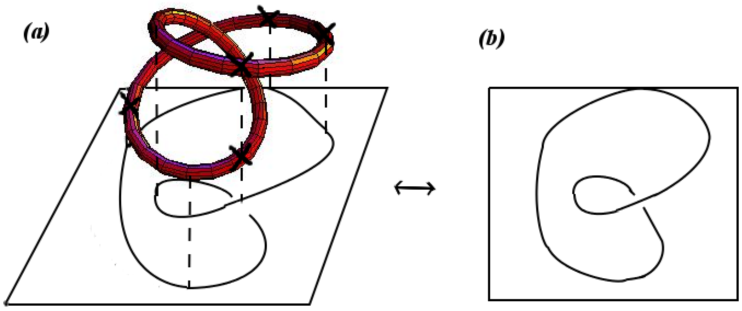

Figure 1.6: (a) depicts a knot being projected onto the x-y plane. The resulting knot diagram is drawn. There exists a point where the projection has a crossing point at which the two curves share mutual $\{x, y\}$ coordinates. In figure (b) this is characterised with one strand of the projected curve crossing over the other.

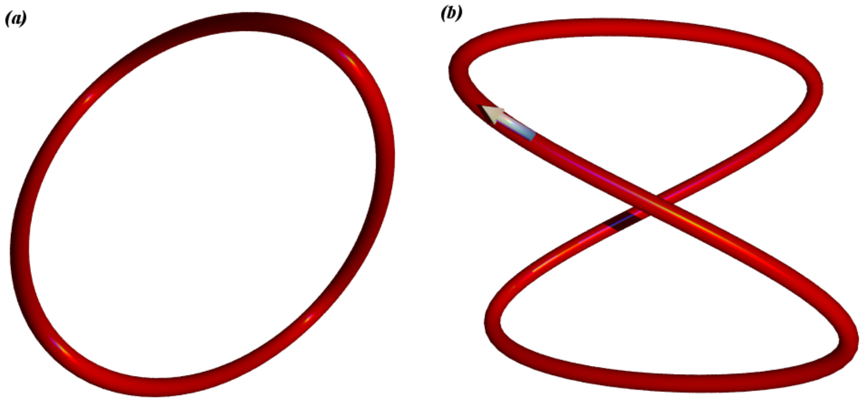

Figure 1.7: The curve $\mathbf{x} = (\sin 2\pi t, \sin 4\pi t, -\cos 2\pi t)$, $t \in [0, 1]$ as viewed along the x and y axes, in figures (a) and (b) respectively. Clearly the knot projections produced would differ as the y-axis projection would have a crossing absent form the x-axis viewpoint.

embeddings; here 'disjoint' means no double points, i.e. there are no points which are in the image of two curves. The foundation of modern knot theory is considered (as related by Sossinsky [102] p1-3) to have been inspired by Lord Kelvin's attempt to explain the atomic table in terms of increasingly complex knotted shapes [57]. P G Tait studied the properties of knots as a result of Lord Kelvin's conjecture [57]. Modern knot theory is a highly technical branch of topology, the majority of which is beyond the scope of this thesis. The interested reader is directed to introductory works such as Cromwell [33] for a graduate level introduction to knot theory, Kauffman [56] for an insight into its applications, and [102] for a historical view of the development of the subject. A particular planar representation of knots is used here (a common procedure in knot theory literature), as a simple introductory tool for concepts inherent to the more complex three-dimensional knot representation. The reader will be directed to suitable references for more detailed coverage if and when appropriate.

The projection of a knot onto a plane is referred to in knot theory literature as a *knot* or *link diagram* (Cromwell pg 51); Figure (1.6) is a representation of this process. A particular knot does **not**, in general, have a unique knot diagram, as the choice of projection will alter representation produced (See Figure 1.7). Further, if we deform the knot, without letting the curve pass through itself, it will in general

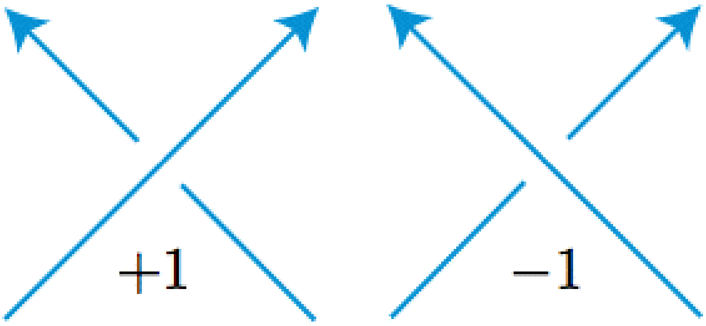

Figure 1.8: Rules for assigning a numerical value to oriented crossings for a planar knot or link diagram.

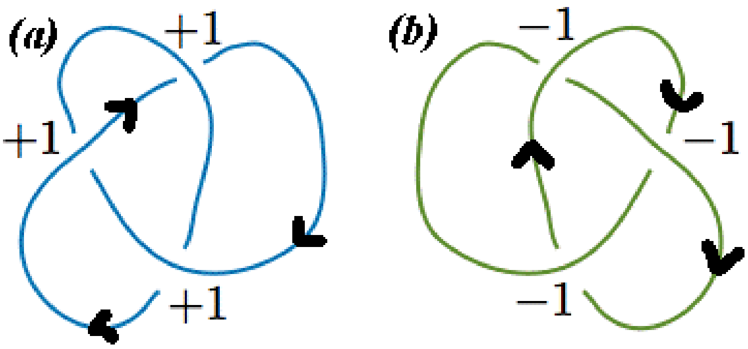

Figure 1.9: Figures (a) and (b) represent right-handed and left-handed trefoil knot diagrams respectively. By following the orientation of each curve, numerical values can be assigned to the crossings using Figure 1.8. Figure (b) has planar writhe value of $w = -3$ and (a) has $w = 3$.

also deform the knot diagram. Consider the projection of a knot onto the x-y plane, points with the same x-y coordinates, but differing z coordinates, are drawn as crossing over or under each other. The higher z point is depicted as crossing over the lower one (Figure 1.6). A link diagram is a union of such knot diagrams, with the same crossing rules applied to the intersections of two knots.

1.1.1 Planar writhing number w

Applying an orientation to the original spacecurve will induce an orientation on the planar curve projection. The two types of the projection crossings which occur are assigned a value of 1 or -1 as demonstrated in Figure 1.8.

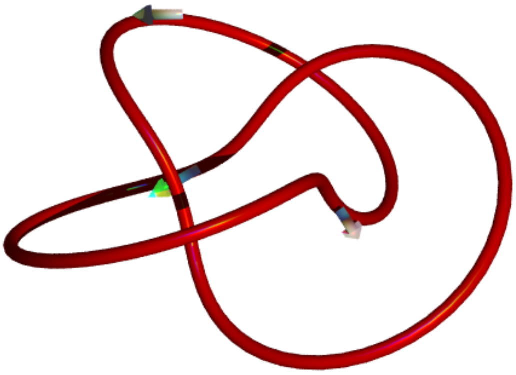

Figure 1.10: The 2-3 torus (trefoil) knot with orientation marked by arrows. The projection of this curve produces the knot diagram marked (b) in Figure 1.9.

Definition *Planar Writhing number w*

Consider a knot diagram $\mathcal{K}$ which has n self-crossings labelled $\mathcal{C}_i$. If we induce an orientation on $\mathcal{K}$ we can label the crossings with a sign $\mathcal{S}(\mathcal{C}_i)$ as shown in Figure 1.8. The planar writhing number of $\mathcal{K}$ represents the sum of the signed self crossings

$$w(\mathcal{K}) = \sum_{i=1}^{n} \mathcal{S}(\mathcal{C}_i). \tag{1.1}$$

Example w calculations are detailed in Figure 1.9. In knot theory literature this quantity is often referred to as the writhe, without the planar prefix (see Cromwell [33] or Kauffmann [56] for example). In this thesis the distinction is critical. The bulk of its content will concern the three-dimensional analogue, which is **not** equivalent to the above definition. For example, the knot depicted in Figure 1.10 has a writhe value of -3.52 (as defined by equation (1.19), discussed in Section 1.5.1), but a projection produces diagram (b) depicted in Figure 1.9, whose w value is -3. It is clear from this example that a finite amount of geometrical information is lost as a result of the projection. We will see (in section 1.5.1) that the three dimensional writhe averages w over all projection angles.

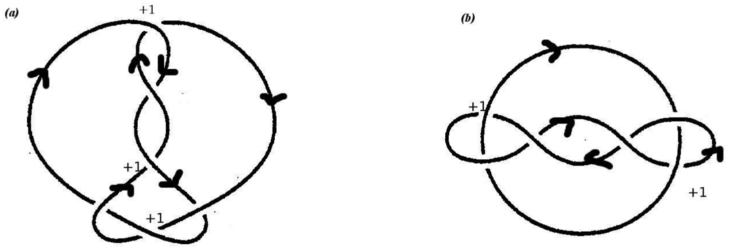

Figure 1.11: Two planar linking number calculations. Figure (a) has $\mathcal{L} = 3$. Figure (b) has $\mathcal{L} = 2$ (note; there are technically 6 crossings of positive sign, but we only need count half of them). In (b) two of the crossings are ignored as they are generated by one curve crossing itself. In other words one of the curves on the right has a writhe value of -2.

1.1.2 Planar linking number $\mathcal{L}$

An orientation can be assigned to a link diagram by assigning orientations to all its constituent knots. A sign is applied to all mutual crossings using the method depicted in Figure 1.8. Half the total sum of signs of crossings yields the planar linking number.

Definition *Planar Linking number $\mathcal{L}$*

Consider a link diagram L which contains m constituent knots $\mathcal{K}_1, \mathcal{K}_2, \ldots \mathcal{K}_m$ (all oriented). If knots $\mathcal{K}_i$ and $\mathcal{K}_j$ themselves generate n_{ij} mutual crossings, these crossings are labelled $\mathcal{C}_k^{ij}$ for $k = 1, ..., n_{ij}$. For each knot pairing we denote the total $\mathcal{L}_{ij}$ between $\mathcal{K}_i$ and $\mathcal{K}_j$ as the sum of all signed crossings.

$$\mathcal{L}_{ij}(\mathcal{K}_i, \mathcal{K}_j) = \frac{1}{2}\sum_{k=1}^{n_{ij}} \mathcal{S}(\mathcal{C}_k^{ij}). \tag{1.2}$$

$\mathcal{L}(L)$ represents the sum of all $\mathcal{L}_{ij}$ between all knot combinations. There exists no redundancy in this calculation, so crossings are only counted once.

$$\mathcal{L}(L) = \sum_{i=1}^{m-1}\sum_{j=i+1}^{m} \mathcal{L}_{ij}. \tag{1.3}$$

Figure 1.11 details example $\mathcal{L}$ calculations. As shall be discussed in section 1.4 the measure $\mathcal{L}$ is independent of the choice of projection direction.

The above definitions present a simple understanding of the writhing and linking numbers, as the self-crossing of an individual projection, and the inter-crossing of a pair of projections respectively. As discussed, in the case of w much of the torsional nature of the knot is lost as a result of projection. It is necessary to build up a definition for the self-linking and inter-linking, as defined in three dimensions, to gauge this effect.

1.2 Preliminaries

1.2.1 Notations

We denote a point in $\mathbb{R}^3$ as (x, y, z) in Cartesian coordinates and (r, θ, ϕ) for spherical representation (where ϕ is the *azimuthal* angle and θ the *polar angle*). Derivatives are denoted with a prime (i.e $x'(t) = \mathrm{d}x/\mathrm{d}t$).

1.2.2 Spacecurves and smoothness

In this thesis a spacecurve $\mathbf{x}(t)$ shall represent a three-dimensional vector $(\mathbf{x}_x, \mathbf{x}_y, \mathbf{x}_z)$, depending continuously on an arbitrary parameter t, for $t \in [a, b]$. All such curves will be considered *smooth*, where smoothness implies $\mathbf{x}$ is at least $\mathcal{C}^3$ differentiable for all t, unless stated otherwise (in some cases this can be relaxed to $\mathcal{C}^2$), that is to say we are assuming $|\mathbf{x}'| > 0$.

There will be two major classes of curve discussed in this thesis. Closed spacecurves represent the set of curves whose endpoints are equal ($\mathbf{x}(a) = \mathbf{x}(b)$), and for which all derivatives agree at a and b. Open curves will be those for which $\mathbf{x}(a) \neq \mathbf{x}(b)$. A commonly used subset of open curves are those for which $\mathbf{x}'(t = a) = \mathbf{x}'(t = b)$.

Spacecurve concatenation

An important aspect of this thesis will be the joining of sections of spacecurve. Consider two sections of spacecurve $\mathbf{x}_1$ and $\mathbf{x}_2$, the smooth attachment of $\mathbf{x}_1$ and $\mathbf{x}_2$ is denoted as $\mathbf{x}_1 + \mathbf{x}_2$. This indicates that there is at least one point p, at which the curves are joined, such that $\mathbf{x}_1'(t) = \mathbf{x}_2'(\mathrm{t})$ for the value of t at which they meet.

1.2.3 Tantrix curves and arclength

Tantrix curves

The tantrix curve $\widehat{\mathbf{T}}_{\mathbf{x}}(t)$, is the curve mapped out by the unit tangent of a spacecurve $\mathbf{x}$, it is defined as

$$\widehat{\mathbf{T}}_{\mathbf{x}}(t) = \frac{\mathbf{x}'(t)}{|\mathbf{x}'(t)|}. \tag{1.4}$$

The term tantrix is an abbreviation of the more formal *Tangent indicatrix*. It appears to have been introduced by Solomon [101] and has been applied as a shorthand term in recent notes concerning the writhing of open spacecurves (Berger and Prior [15], van der Hejden et al [114]).

Arclength

A natural method for parameterising spacecurves is by *arclength*, here denoted s. The arclength can be related to an arbitrary parametrisation t as

$$s(t) = \int_0^t \sqrt{x'^2(t) + y'^2(t) + z'^2(t)}\ \mathrm{d}t, \tag{1.5}$$

where s represents the total distance travelled along the curve. The derivative of a curve $\mathbf{x}$ parameterised by s is always of unitary value ($|\mathbf{x}'(s)| = 1$), thus $\widehat{\mathbf{T}}_{\mathbf{x}}(s) = \mathbf{x}'(s)$. In this thesis it is required that all spacecurves $\mathbf{x}(s)$ are smooth over the period $[0, L]$, where $\mathbf{x}(t = a) \equiv \mathbf{x}(s = 0)$ and $\mathbf{x}(t = b) \equiv \mathbf{x}(s = L)$ and L represents the total arclength of $\mathbf{x}$.

1.2.4 Tantrix curves and the unit sphere

One can view the tantrix curve as lying on the surface of the unit sphere. This interpretation is shown in Figure 1.12. Each value of the tantrix curve $\widehat{\mathbf{T}}_{\mathbf{x}}(s)$ can be represented as a point on the sphere's surface, indicated by an arrow drawn from the centre of the sphere to its surface. The tantrix curve will thus represent a curve lying on the surface of the unit sphere for $s \in [0, L]$. Any continuous (isotopic) transformations applied to curves in this thesis will cause $\widehat{\mathbf{T}}_{\mathbf{x}}$ to deform continously also.

The concept of the sphere of directions can be applied further. All directional unit vectors (circular chords or secants) can be represented by a point on the unit

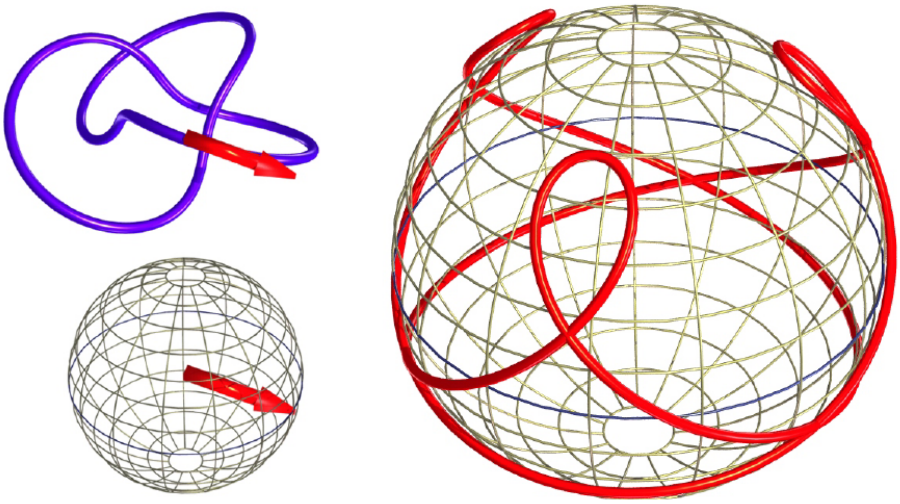

Figure 1.12: A 2-3 torus (trefoil) knot and its associated tantrix. The upper left figure shows the knot with a tangent vector drawn at one point along the curve. Below, the vector has been drawn so that its tip lies on the unit sphere. The figure to the right displays the full tantrix for the knot (for this curve $\mathcal{W} = 3.52$).

sphere. One can imagine all points on the sphere's surface as the set of all possible directions a unit vector can take. If we imagine a knot being evaluated as lying inside the sphere's surface, each point on the sphere's surface could be regarded as a viewpoint of the knot. As shall be discussed in section 1.4, $\mathcal{L}$ is independent of projection (for closed curves), which is akin to stating that it is the same for all view points.

Unit sphere area

Many of the topological and geometrical quantities discussed in this thesis can be attributed an interpretation, as an area on the surface of the unit sphere. For example projecting a knot along a specific direction will lead to a number of points at which the curve crosses over itself (in terms of its knot projection). The crossing attributed to this direction could be marked with a point on the unit sphere. These points are given a sign in the manner defined in Figure 1.8 (the sum of these crossings is of course w). Several of the expressions under consideration involve an average, over all viewpoints, of the signed crossings which occur on projecting the knot or link. This will lead to an area covered on the surface of the unit sphere by the points marked for each direction (assuming there are crossings). This construction

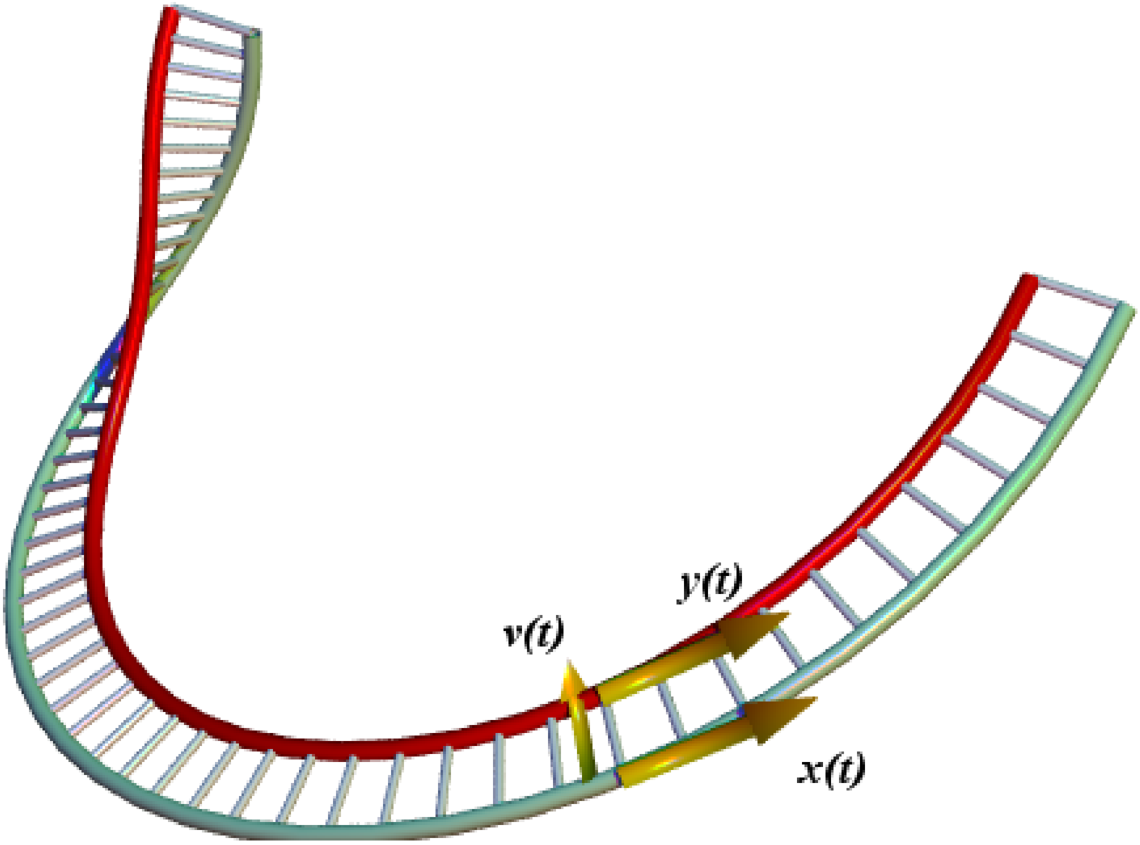

Figure 1.13: A typical ribbon construct with $\mathbf{x}(t)$ representing the ribbon's axis. The vector $\mathbf{v}(t)$ generates the curve $\mathbf{y}(t)$ as defined by the equation $\mathbf{y}(t) = \mathbf{x}(t) + \epsilon\mathbf{v}(t)$.

will form a major theme of this thesis.

1.2.5 Ribbons and tubes

Ribbons

The ribbon is a mathematical construction used to represent physical systems such as the two strands of a DNA molecule (Fuller [45]). Consider a spacecurve $\mathbf{x}(t)$ and a second curve $\mathbf{y}(t)$, also parameterised by t, such that $\mathbf{y}(t) = \mathbf{x}(t) + \epsilon\mathbf{v}(t)$, where $\mathbf{v}(t)$ is a vector normal to $\widehat{\mathbf{T}}(t)$ for $t \in [a, b]$ and $\epsilon << 1$. This will naturally wrap itself around $\mathbf{x}$ as shown in Figure 1.13. If ϵ is sufficiently small (usually $\ll 1$) we can assume that $\mathbf{y}$ is disjoint from $\mathbf{x}$, that is $\mathbf{x}$ and $\mathbf{y}$ never cross (Hirsch [53]). Such a construction will be denoted $R(\mathbf{x}, \mathbf{v})(t)$. In choosing $t = s$ it must be noted that s represents the arclength of $\mathbf{x}$ not $\mathbf{y}$. In this thesis both open and closed ribbons

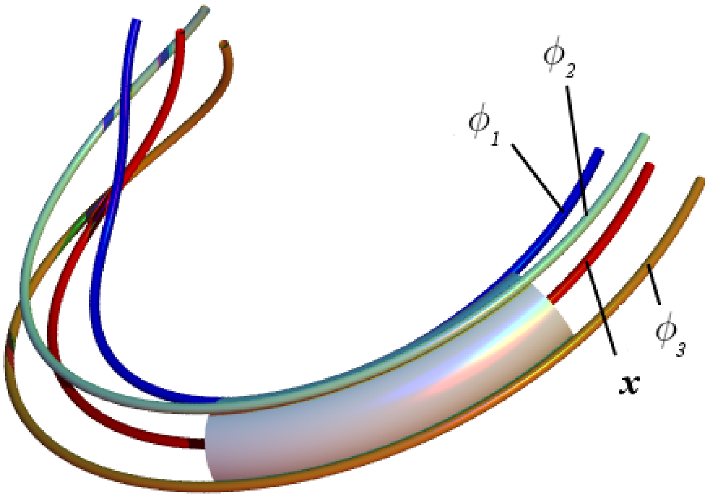

Figure 1.14: An example of a tube. The three curves labelled $\phi_1 = 0$, $\phi_2 = \frac{\pi}{2}$ and $\phi_3 = \pi$ represent differing *framings*, as defined by 1.6.

will be considered. Closed ribbons require $\mathbf{y}$ to be closed over the same period as $\mathbf{x}$.

Tubes

Imagine a circle of radius ϵ centred at $\mathbf{x}(t)$ perpendicular to $\widehat{\mathbf{T}}(t)$. If there is such a circle for each t and ϵ is sufficiently small, a tube centred on $\mathbf{x}(t)$ is obtained, which will not intersect itself. If some curve $\mathbf{y}$ lies on the tube's surface it can be used as the base of a surface parameterisation (t, ϕ), where $\phi = 0$ is taken to be $\mathbf{y}$. If we define a further generating vector $\mathbf{w}$ which is also perpendicular to both $\widehat{\mathbf{T}}$ and $\mathbf{v}$ then the surface parameterisation is given as

$$\mathbf{y}(t, \phi) = \mathbf{x}(t) + \epsilon(\cos\phi\mathbf{v}(t) + \sin\phi\mathbf{w}(t)). \tag{1.6}$$

Here a ribbon has been used to define the surface of a tube[1]. The choice of $\mathbf{y}$ is not unique and is determined by the choice of $\mathbf{v}$. By altering $\mathbf{y}(t)$ we alter the basis of our surface. Such a choice of basis is known as the *framing* (various framings of a tube can be seen in Figure 1.14). Alternatively the tube can be covered with a series of parallel curves which pass through points (t, α) where there is a single curve for each $\alpha \in [0, 2\pi]$. Such a tube is known as a *twisted tube* (see Figure 1.15); when this tube is assigned an energy value it is known as an *isotropic rod* (van der Heijden

---

[1] Fuller [44] referred to this generalisation of the ribbon structure as a "cord"

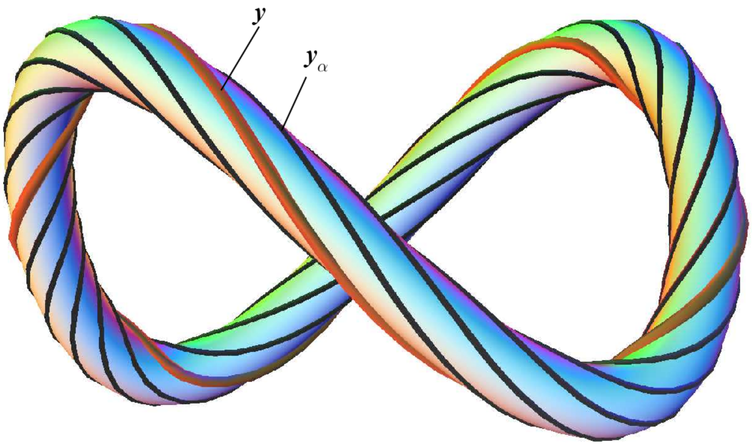

Figure 1.15: An example of a twisted tube. Here the $\mathbf{y}$ is displaced on the tube by a parameter α to produce a set of images of $\mathbf{y}$, an example is labelled $\mathbf{y}_\alpha$.

and Thompson 2000 [113]).

1.2.6 The Frenet frame

The local geometry of $\mathbf{x}$ provides an intrinsic set of basis vectors and coordinates, called the *Frenet frame*. Let

$$\kappa \equiv \left| \frac{\mathrm{d}\widehat{\mathbf{T}}(s)}{\mathrm{d}s} \right| \tag{1.7}$$

be the curvature of $\mathbf{x}$ at s. The *principal normal* vector is defined (where $\kappa \neq 0$) as

$$\widehat{\mathbf{N}} = \frac{1}{\kappa} \frac{\mathrm{d}\widehat{\mathbf{T}}(s)}{\mathrm{d}s}. \tag{1.8}$$

As $\widehat{\mathbf{T}}(s)$ is always a unit vector, $\widehat{\mathbf{N}}(s) \cdot \widehat{\mathbf{T}}(s) = 0$. We can now define a third vector, the *binormal*, as

$$\widehat{\mathbf{B}} = \widehat{\mathbf{T}} \times \widehat{\mathbf{N}}. \tag{1.9}$$

The three vectors $\widehat{\mathbf{T}}, \widehat{\mathbf{N}}, \widehat{\mathbf{B}}$ form a right-handed orthonormal basis, and satisfy the Frenet-Serret equations

$$\frac{\mathrm{d}\widehat{\mathbf{T}}(s)}{\mathrm{d}s} = \kappa \widehat{\mathbf{N}}, \tag{1.10}$$

$$\begin{aligned}\frac{\mathrm{d}\widehat{\mathbf{N}}(s)}{\mathrm{d}s} &= \tau\widehat{\mathbf{B}} - \kappa\widehat{\mathbf{T}}, &(1.11)\\ \frac{\mathrm{d}\widehat{\mathbf{B}}(s)}{\mathrm{d}s} &= -\tau\widehat{\mathbf{N}}, &(1.12)\end{aligned}$$

where τ is the *torsion*.

Of course if $\kappa = 0$ the frame is ill-defined. A further issue encountered in using the Frenet frame is as follows. Consider a helix shaped curve (an open curve) defined as

$$\mathbf{x}(s) = \left\{r\cos(qs/\sqrt{1+(qr)^2}), r\sin(qs/\sqrt{1+(qr)^2}), s/\sqrt{1+(qr)^2}\right\}, \qquad (1.13)$$

where q and r are real constants. The curvature and torsion are constant and given by

$$\begin{aligned}\kappa(s) &= \frac{q^2 r}{1+(qr)^2}, &(1.14)\\ \tau(s) &= \frac{q}{1+(qr)^2}. &(1.15)\end{aligned}$$

As $r \to 0$ the helix becomes a straight line. In this limit the curvature vanishes as expected. The torsion however does not, leaving the problem of a straight line curve which appears to have torsion (Kamien [55]).

This problem, however, does not in general relate to other framings. It is important to note that the writhing expressions introduced in this thesis are invariant of the choice of framing. Further, for curves of $\mathcal{C}^3$ differentiability, there will always be some choice of framing which is non-vanishing. This is a result of the Mermin-Ho relation (Mermin and Ho [73]), which states that, as long as $\widehat{\mathbf{T}}$ is defined everywhere, the geometrical properties of $\mathbf{x}$ are independent of the choice of framing (see Kamien [55] for an introduction).

1.3 Topological invariance

A key property of the linking number is its invariance to a set of transformations of its comprising curves (assuming as stated that they are both closed curves). The technical name for such a set is an *ambient isotopy*. All properties of the link pairings

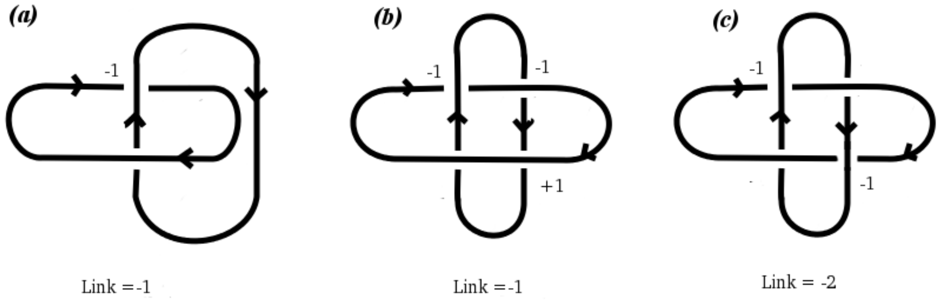

Figure 1.16: (a) represents a simple Hopf link with $\mathcal{L} = -1$. A strand of the horizontal link component is pulled over the vertical curve to produce (b). Such a transformation will not change the planar linking number. Figure (c) is the result of cutting the horizontal link and reconnecting it after threading through the vertical curve. This changes the planar linking evaluation but is not a topologically permitted deformation.

which are left unchanged by such a set of transformations, are known as *topological invariants*. Before proceeding to a strict definition of the term ambient isotopy, a more intuitive definition is introduced to prepare the reader.

The set of deformations of a closed curve (or union of closed curves), which do not allow the curves to pass through either themselves, or any other curve comprising the link, will leave some property of the curve (or union) unchanged. A simple example of such a transformation is depicted in Figure 1.16, in which link diagrams (a) and (b) can be converted into each other by a set of continuous deformations. We see these links have the same $\mathcal{L}$ value despite extra crossings in the second link. The third link (c), cannot be deformed from the other two examples without the comprising curves being passed through each other at any point. This action would change the link by a value of ±1 as prescribed by the rules depicted in Figure 1.8. Proof that the planar linking number is topologically invariant, in terms of its link projection, requires the full set of Reidemeister moves, the planar equivalents of an ambient isotopy. Such detail is beyond the scope of this thesis; this proof is discussed in Cromwell, pages 66-70.

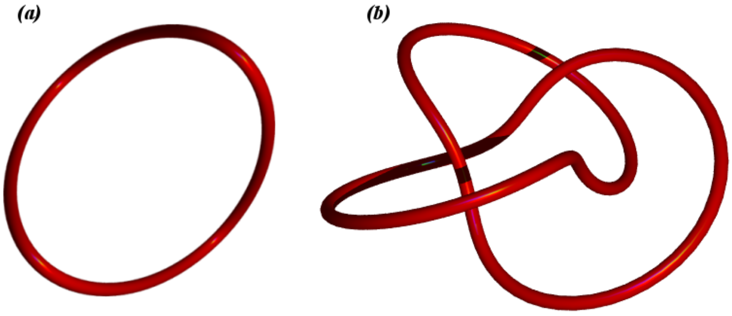

Figure 1.17: Two curves which can be linked by a homeomorphism (note there are no double points on either curve). However there exits no continously linked set of homemorphisms between the two. It is required that at some point figure (b) would have to cross through itself in order to then be deformed continously into (a).

1.3.1 Ambient isotopies and topological invariance

The following definition follows a discussion in Cromwell [33] (pages 3-5). For a more technical definition of a topology conserving transformation, it is necessary start with its basic concept, the *homeomorphism*.

Homeomorphism

A homeomorphism is some function f which represents a continuous bijective map, such that f^{-1} is also continuous. Such a function can represent a mapping between two closed spacecurves $\mathbf{x}_1$ and $\mathbf{x}_2$, $f : \mathbf{x}_1 \mapsto \mathbf{x}_2$. Alternatively this could represent the mapping between two ribbons $f : R_1 \mapsto R_2$. Both curves are restricted from crossing themselves (or each other in the case of ribbons), as this would violate the continuity of f^{-1}.

This condition, however, is not sufficient. We need more tools to define what we mean by topological invariance. For example, there exists a homeomorphism between the two curves depicted in Figure 1.17. However, they could not be deformed smoothly into each other without the curve crossing through itself at a point. It must be required that all closed curves (or ribbons) can be linked by a continuous set of homeomorphisms.

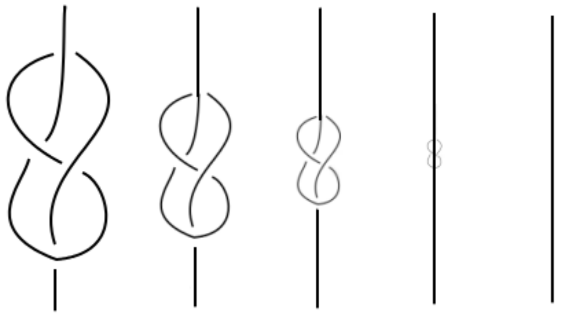

Figure 1.18: A section of a knot being gradually reduced in size (dilated) by a means of a regular isotopy, from left to right. This section could form part of a closed curve. The limit of this sequence is such that the knotted section shrinks to a point and the whole section shrinks until it becomes a straight line section. Such a set of deformations is allowed under isotopic equivalence but not ambient isotopic equivalence.

Isotopy

Two closed curves $\mathbf{x}_1$ and $\mathbf{x}_2$ (or ribbons R_1 and R_2) which can be mapped between each other by a continuous set of homeomorphisms, such that the process is reversible, are said to share an isotopy. This condition states that we must be able to smoothly deform $\mathbf{x}_1$ into $\mathbf{x}_2$ without any self-crossings for knots, or inter-crossings for links.

The isotopy condition is still not sufficient for topological invariance. Under an isotopy all closed curves are isotopic to a circle, this process can be seen in Figure 1.18, which represents a knotted section of curve being shrunk to a point via an isotopy set. In the limit of this sequence the knotted section converges to a point. This point can then be linked by an isotopy to any other curve configuration. In order to prevent this process, it is required that the space surrounding the curve is transformed along with the curve itself.

Ambient isotopy

An ambient isotopy demands that homeomorphic actions act on the space rather than the knot itself. The space is deformed, dragging the knot with it, removing the possibility of shrinking the knot to a single dimensionless point as depicted in 1.18. The remaining set of allowed deformations are smooth non self-crossing deformations of the curve or ribbon.

A definition

A topological invariant ($\mathcal{I}$) of a closed curve $\mathbf{x}$, is some measure $\mathcal{I}(\mathbf{x})$, which is invariant to the full set of ambient isotopies defined for $\mathbf{x}$. The linking number $\mathcal{L}$ is an example of a topological invariant.

1.4 Linking in three dimensions

In the following section the discussion will centre on linking as applied to **closed** ribbons. Many of the properties covered do not hold when the expressions are applied to open ribbons, for reasons which shall be discussed in section 5.1.1. Before introducing the linking number the crossing number is discussed.

1.4.1 Crossing number C

Suppose two curves are projected onto a viewing plane whose normal points along the direction $\hat{n}$. We can also regard a projection angle as a viewing angle. In the projection plane the curves will cross each other a number of times. Let $C(\hat{n})$ count the number of positive crossings minus the number of negative crossings. For two distinct closed curves $C(\hat{n})$ is independent of $\hat{n}$. Counting crossings can be a convenient method of calculating linking and writhe (Orlandini *et al* [81]). Clearly half the total crossing number is equivalent to the planar linking defined earlier.

1.4.2 Linking number $\mathcal{L}$

The extent to which two closed spacecurves $\mathbf{x}(s)$ and $\mathbf{y}(s')$ are linked in $\mathbb{R}^3$, over $s \in [0, L]$ and $s' \in [0, M]$, can be evaluated as a single number as follows,

$$\mathcal{L} \equiv \frac{1}{4\pi} \oint_{\mathbf{x}} \oint_{\mathbf{y}} \frac{\widehat{\mathbf{T}}_{\mathbf{x}}(s) \times \widehat{\mathbf{T}}_{\mathbf{y}}(s') \cdot (\mathbf{x}(s) - \mathbf{y}(s'))}{|\mathbf{x}(s) - \mathbf{y}(s')|^3} \mathrm{d}s \mathrm{d}s'. \tag{1.16}$$

This expression can be applied to open ribbons as well. The properties of link as applied to open ribbons, will be discussed in greater detail in section 5.1.1.

This equation first appears, in this form, in a mathematical notebook belonging to Gauss, which was published in 1867 [47] (as related by Epple [39]). It was linked with Gauss's work on electromagnetic induction by Schering (see [39] for details). However, Epple demonstrates that in 1802 Gauss had considered the problem of the linking of two closed curves in terms of the possible orbits of the Earth and a second celelstial orbit.

$\mathcal{L}$ as an average over all viewpoints

Equation (1.16) represents the average of the planar linking number as averaged over all possible projections. Each projection can be thought of as a particular viewing angle of the link, thus equation 1.16 represents an average, over all viewpoints, of the link's signed crossings. The planar linking number can be shown to be independent of viewing angle (see Langevin [64] for a proof of this). As a result equation 1.16 is equivalent to the planar linking evaluation defined earlier (hence we denote it with the same symbol $\mathcal{L}$). It can be inferred from this that $\mathcal{L}$ must always be of integer value for closed spacecurves. Further, the evaluation of $\mathcal{L}$ is independent of the chosen parameterisations.

1.4.3 Summary of key $\mathcal{L}$ properties, for closed spacecurves

- $\mathcal{L}$ is always of integer value.
- $\mathcal{L}$ is a topological invariant, and will remain unaltered under all ambient isotopies.
- If we allow $\mathbf{x}$ and $\mathbf{y}$ to cross each other, $\mathcal{L}$ changes value line by ±1.
- $\mathcal{L}$ equals half the signed number of crossings of the two curves as seen from any plane projection.

$$\mathcal{L} = \frac{1}{2}C(\hat{n}). \tag{1.17}$$

The above properties are well-established for closed spacecurves. The first property follows from the fact that it is true for planar projection interpretation of $\mathcal{L}$. Alternatively it can be noted that (1.16) represents the degree of the following chord map (see Langevin [64]).

$$\mathbf{m}(s, s') = \frac{\mathbf{x}(s) - \mathbf{y}(s')}{\mid \mathbf{x}(s) - \mathbf{y}(s') \mid}. \tag{1.18}$$

This map is often referred to as the Gauss map, due to its use by Gauss in both his works on orbits and electromagnetism ([39]). When evaluated over all chord combinations $s \in [0, L]$ and $s' \in [0, M]$ it represents the map of the torus to the unit sphere, which is of unit value for closed spacecurves (Langevin [64]). Each chord $\mathbf{m}(s, s')$ is essentially a direction from which $\mathbf{x}$ and $\mathbf{y}$ are seen to cross and will represent a point on the surface of the unit sphere. This leads to a unit sphere interpretation which will be discussed in detail in Section 2.1, where all of the above properties will be demonstrated in terms of the area bound on the surface of the sphere by the mapping (1.18).

The result of $\mathbf{x}$ and $\mathbf{y}$ passing through each other is the change in sign of one planar crossing $\mathcal{S}(\mathcal{C})$. This will result in a change in sign of $\mathcal{L}$ by a value of ±1 as evaluated by (1.3).

$\mathcal{L}$ and ribbons

In addition to the properties detailed above, $\mathcal{L}$ as applied to a ribbon $R(\mathbf{x}, \mathbf{v})(t)$ is invariant to the transformations $t \rightarrow (-t)$ and $s \rightarrow (-s)$. This is a result of both curves reversing orientation simultaneously.

1.5 Writhing in three dimensions

1.5.1 Writhe $\mathcal{W}$

The following definition is for closed spacecurves. The quantity $\mathcal{W}$ has a more complex history than that of $\mathcal{L}$, due partly to the fact the three dimensional description of self-linking cannot be defined by a single planar projection. An overview of the conception and evolution of writhe will be discussed after first introducing the quantity, in order to place the discussion in context. To reiterate; the following writhing definition is distinct from the planar writhe w. By replacing $\mathbf{y}(s)$ with $\mathbf{x}(s')$ in 1.16, where $s, s' \in [0, L]$, we recover an expression representing the self-linking of $\mathbf{x}$ in $\mathbb{R}^3$

$$\mathcal{W} \equiv \frac{1}{4\pi} \oint_{\mathbf{x}} \oint_{\mathbf{x}} \frac{\widehat{\mathbf{T}}_{\mathbf{x}}(s) \times \widehat{\mathbf{T}}_{\mathbf{x}}(s') \cdot (\mathbf{x}(s) - \mathbf{x}(s'))}{|\mathbf{x}(s) - \mathbf{x}(s')|^3} \mathrm{d}s \mathrm{d}s'. \tag{1.19}$$

As with $\mathcal{L}$, equation (1.19) could also be applied to open spacecurves $\mathbf{x}$. Such an interpretation will be discussed in detail in Chapter 4.

Analogous to the linking number, (1.19) measures the average crossing sum of $\mathbf{x}(s)$ with itself over all planar projections. This is discussed by Fuller [44] in which he defines the directional writhing number. Briefly an exact copy of $\mathbf{x}$ is translated along a fixed direction σ by a small amount ϵ, with $\mathcal{W}(\mathbf{x}, \sigma) = \mathcal{L}(\mathbf{x}, \mathbf{x} + \epsilon\sigma)$. The average over all σ with respect to the tantrix sphere equals $\mathcal{W}$ as defined in (1.19). Proof of this can be found in Aldinger *et al* [5] who use a homotopy invariance and the Călugăreanu relation (see Section 1.21); alternatively Pohl [89] provides a demonstration based on the definition of the degree of the $\mathcal{L}$ map (1.18).

1.5.2 Constant conformal invariance

Applying a set of ambient isotopies to a closed curve does not leave $\mathcal{W}$ unchanged, so $\mathcal{W}$ is **not** a topological invariant. However, a set of continuous transformations can be defined, representing a subset of the ambient isotopies, which leave $\mathcal{W}(\mathbf{x})$ unchanged.

Definition *Constant conformal invariance*

For a closed spacecurve $\mathbf{x}(s)$ a constant conformal measure $\mathcal{M}(\mathbf{x})$ is one which is unchanged by the following transformations;

1. Translations, $\mathcal{M}(\mathbf{x}+\mathbf{a}) = \mathcal{M}(\mathbf{x})$ for $\mathbf{a} \in \mathbb{R}^3$.
2. Rotations, $\mathcal{M}(\mathcal{R}(\mathbf{x})) = \mathcal{M}(\mathbf{x})$, where $\mathcal{R}$ is some real valued rotational matrix.
3. Length dilation (applied equally along all three axes), $\mathcal{M}(c\mathbf{x}) = \mathcal{M}(\mathbf{x})$ for $c \in \mathbb{R}$. Except for $c = 0$ which would reduce the curve to a dimensionless point.
4. Any combination of the above.

In essence constant conformal invariance states that any constant conformal invariant $\mathcal{M}$, will be unchanged, as long as the global geometrical inter-relationships of $\mathbf{x}$ remain the same.

Previous notes have denoted $\mathcal{W}$ the property of *conformal invariance* (Fuller [44],Aldinger *et al* [5], Agarwal *et al* 2004 [4]), however in both cases a strict definition of conformal invariance is not given. The above definition of constant conformal invariance is detailed specifically for this thesis, but is not necessarily what is implied by [5] or [4]. Confusion could occur as the term conformal invariance appears in other subjects, in differing forms. For example in differential geometry conformal invariance covers angle preserving changes of metric (Sternberg 1983 [100]). In this thesis the expressions are defined and discussed in terms of simple non curved metric spaces. A discussion of the properties of writhe in curved space is beyond the remit of this thesis. Some of the further writhing expressions introduced are not invariant to the above set of transformations (specifically they are not rotationally invariant), constant conformal invariance is thus used to differentiate between writhing measures which are effectively viewpoint invariant and those which are not.

1.5.3 Properties of $\mathcal{W}$ for closed spacecurves

- $\mathcal{W}$ is **not** generally of integer value.
- $\mathcal{W}$ is a constant conformal invariant but not a topological one, this will be demonstrated in section 2.2 of this thesis.
- $\mathcal{W}$ changes continually under deformations of the spacecurve, except when the spacecurve crosses itself; in such a scenario it jumps by ± 2. This follows from Figure 1.8, as the effect of passing the curve through itself will be the same as viewed from all directions.
- The double integral form of $\mathcal{W}$ has a singularity at $s = s'$. Despite this singularity the integral does not diverge. This issue was covered by Călugăreanu in [24]. Pohl [89] discusses a simpler method of regularising this singularity.
- The $\mathcal{W}$ of a ribbon or tube $R(\mathbf{x}, \mathbf{v})$ depends only on the shape of $\mathbf{x}$. Thus $\mathcal{W}$ is independent of the choice of framing.
- The writhe of a planar spacecurve is zero.

$\mathcal{W}$ and non-smooth curves

As with $\mathcal{L}$, (1.19) is independent of the choice of parametrisation and can be applied to non smooth curves. Starostin [104] discusses the validity (1.19) as applied to curves which are smooth only piecewise. Cantarella [26] evaluates the bounds for the difference between writhing number of a smooth curve and a polygonal representation of this curve (a piecewise linear set of connected line segments). Klenin and Langowski 2000 [58], Cimasoni [30] and Agarwal *et al* [4] discuss the various methods for evaluating of the $\mathcal{W}$ of a polygonal polymer chain. In particular Agarwal *et al* develop an expression for evaluating $\mathcal{W}$ which is less than quadratic with respect to the number of sections n comprising the polygonal curve ($\approx n^{1.6}$, as opposed to being quadratic in n), by equating $\mathcal{W}$ to the winding number of the closed curve, this expression is also valid for open curves.

1.5.4 The Călugăreanu theorem

The integral 1.19 appears to have been first studied by Călugăreanu in 1959 [24] and 1961 [25] (as related by Moffatt and Ricca [75]). Călugăreanu considered two neighbouring closed curves $\mathbf{x}$ and $\mathbf{x}*$ representing the boundaries of a ribbon in the limit $\epsilon \rightarrow 0$; his result can be expressed as

$$\mathcal{L} = \mathcal{W} + \tau + n, \tag{1.20}$$

where τ represents the normalised integrated torsion of $\mathbf{x}$ and n an integer detailing the number of rotations of the unit vector joining the two closed curves, relative to the Frenet pair $(\widehat{\mathbf{N}}, \widehat{\mathbf{B}})$, in one passage around $\mathbf{x}$. The work of Călugăreanu covered spacecurves which were not necessarily smooth, that is some curve $\mathbf{x}(s),\ s \in [0, L]$ for which the tangent vanishes for some arclength value in $[0, L]$ (inflexion points). Pohl [88] discusses the concept of the self-linking number of spacecurves whose curvature did not vanish. Pohl's work was then extended to higher dimensions by White [117]. The term writhe appears to have been coined by Fuller [44], who was asked to study of looped or coiled curves, in response to questions arising from the then burgeoning study of the recently realised structure of DNA molecules. He places the above work in its contemporary form

$$\mathcal{W}(\mathbf{x}) = \mathcal{L}(\mathbf{x}, \mathbf{x} + \epsilon\mathbf{v}) - \mathcal{T}(\mathbf{x}, \mathbf{v}). \tag{1.21}$$

Here $\mathcal{T} \equiv \tau + n$ from Călugăreanu 's work (this is not stated by Fuller but discussed by Moffatt and Ricca [75]). Fuller further states that for any two arbitrary well defined ribbons, based on the generating vectors $\mathbf{v}$ and $\mathbf{v}*$,

$$\mathcal{L}(\mathbf{x}, \mathbf{x} + \epsilon\mathbf{v}) - \mathcal{T}(\mathbf{x}, \mathbf{v}) = \mathcal{L}(\mathbf{x}, \mathbf{x} + \epsilon\mathbf{v}*) - \mathcal{T}(\mathbf{x}, \mathbf{v}*). \tag{1.22}$$

Thus $\mathcal{W}$ is independent of the choice of the ribbon's framing (assuming $\mathbf{x}$ remains the same).

The issue of inflexion points is resolved in the work of Moffatt and Ricca [75] in which $\mathcal{T}$ is shown, using techniques borrowed from fluid dynamics, to be invariant to such occurrences. Specifically they demonstrate that the pair $\tau + n$ change by equal and opposite amounts (± 1 for closed spacecurves), at inflexion points, leaving $\mathcal{T}$ unchanged.

Expression (1.21) has been quoted under a host of names in literature. In 1980

Pohl [89] termed the expression *White's theorem.* Moffatt and Ricca [75] argue that the theorem should be attributed to Călugăreanu as the first author to broach the issue of linking in the limit $\epsilon \to 0$. Other authors have chosen to honour three of the major contributors by labeling this equality the *Călugăreanu -White-Fuller theorem* ([104] [38]). The validity of authorship claim has been discussed in [89] and [75]. However despite controversy over its origin, (1.21) is now a well understood equality for closed ribbons; a nice proof of (1.21) can be found in [89]. Dennis and Hannay [37] discuss the validity of (1.21) in terms of the area bound on the unit sphere's surface by $\mathcal{T}$ and $\mathcal{W}$. This unit sphere methodology is extended in chapter 2 to cover all properties of $\mathcal{W}$, $\mathcal{L}$ and $\mathcal{T}$ detailed in this introductory chapter. In this thesis (1.21) will hereafter be referred to as the Călugăreanu theorem as suggested in [75].

The third quantity comprising the Călugăreanu theorem labelled $\mathcal{T}$, and known as the twist, was given its title by Fuller (1971 [44]). It is itself an interesting geometrical quantity.

1.5.5 Twist

The Călugăreanu theorem defines the relationship between $\mathcal{L}$ and $\mathcal{W}$ as applied to the ribbon $R(\mathbf{x},\mathbf{v})$. Linking occurs between $\mathbf{x}$ and $\mathbf{y}$, while writhing is solely assigned to $\mathbf{x}$. Whilst the Frenet ribbon uses the unit normal as a basis for the generation of $\mathbf{v}$, it is possible to define a ribbon with $\mathbf{x}$ as its spine, but with a different framing vector $\mathbf{v}$. The twist represents the rate of rotation of $\mathbf{v}$ about $\widehat{\mathbf{T}}_{\mathbf{x}}$ and can be characterised as

$$\begin{aligned} \mathcal{T} &\equiv \frac{1}{2\pi}\oint_{\mathbf{x}} \frac{1}{|\mathbf{v}^2(s)|}\widehat{\mathbf{T}}(s)\cdot\mathbf{v}(s)\times\frac{\mathrm{d}\mathbf{v}(s)}{\mathrm{d}s}\,\mathrm{d}s & (1.23)\\ &= \frac{1}{2\pi}\oint_{\mathbf{x}} \widehat{\mathbf{T}}(s)\cdot\widehat{\mathbf{V}}(s)\times\frac{\mathrm{d}\widehat{\mathbf{V}}(s)}{\mathrm{d}s}\,\mathrm{d}s,\ \ \widehat{\mathbf{V}} = \frac{\mathbf{v}}{|\mathbf{v}|}. & (1.24)\end{aligned}$$

As with $\mathcal{L}$ and $\mathcal{W}$, $\mathcal{T}$ can be defined as an average over all viewpoints, as demonstrated by Dennis and Hannay [37]. Consider ribbon $R(\mathbf{x},\mathbf{v})$ viewed from a specific viewpoint. Points at which the ribbon appears "edge on" (Figure 1.19), and which are part of the same local section of the ribbon, are assigned a value ±1, using the crossing rules of Figure 1.8. Now sum over all viewpoints. The average over this sum is shown to be equal to $\mathcal{T}$.

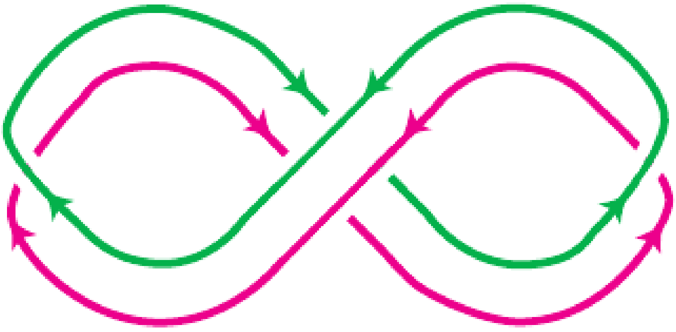

Figure 1.19: A projection of a twisted ribbon. At the left and right-hand side of the diagram the ribbon is "edge-on" to the viewer. Such crossings are local on the ribbon's structure and are right and left handed, for the left and right crossings respectively. These contrast to the crossing which occur in the middle of the diagram (two positive crossings) which are non-local and represent the ribbon crossing over itself. The two left and right crossings contribute to the ribbon's $\mathcal{T}$ as described in [37]. This figure is reproduced from [37].

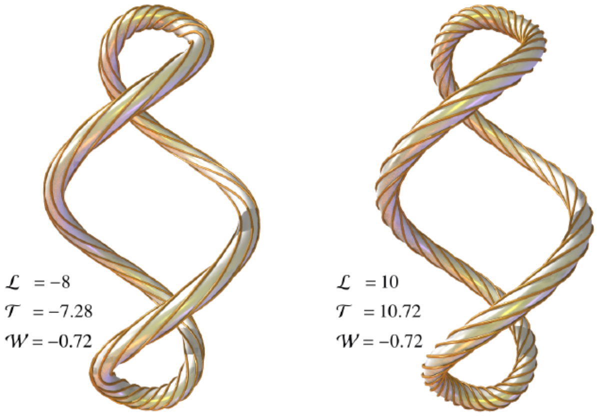

Figure 1.20: Two *twisted tubes* with the same axis curve but differing $\mathcal{T}$ functions (framings). Note that the $\mathcal{W}$ is the same for both tubes.

$\mathcal{T}$ has a very different nature from $\mathcal{W}$ and $\mathcal{L}$. It must be noted that differing choices of **v** represent differing framings of an isotropic tube and will generally have different values of $\mathcal{T}$ (see Figure 1.20).

Properties of $\mathcal{T}$

- $\mathcal{T}$ is a local quantity and thus we can define a local density along the curve.

$$\widehat{\mathbf{T}}(s)\cdot\widehat{\mathbf{V}}(s)\times\frac{\mathrm{d}\widehat{\mathbf{V}}(s)}{\mathrm{d}s}=2\pi\frac{\mathrm{d}\mathcal{T}}{\mathrm{d}s}. \tag{1.25}$$

  As a result $\mathcal{T}$ is an additive quantity. For example if we split a curve $\mathbf{x}$ into two sections $\mathbf{x}_1$ and $\mathbf{x}_2$, $\mathcal{T}(\mathbf{x})\equiv\mathcal{T}(\mathbf{x}_1)+\mathcal{T}(\mathbf{x}_2)$. This further implies that the definition of $\mathcal{T}$ does not depend on whether the ribbon is open or closed.

- $\mathcal{T}$ changes continuously under deformation even when $\mathbf{x}$ and $\mathbf{y}$ cross each other.

- $\mathcal{T}$ is a constant conformal invariant (this will be demonstrated in section 2.3).

- $\mathcal{T}$ is independent of the direction of $\mathbf{x}$. For example, suppose the axis is a vertical straight line, and the secondary a right helix (positive twist). Turning the two upside down will still give a right helix of the same pitch.

The above properties are summarised by Fuller in [44] (with the exception of constant conformal invariance). As discussed earlier Moffatt and Ricca [75] deal with the issue of $\mathcal{T}$ and inflexion points, demonstrating that the presence of such points does not affect $\mathcal{T}$ and its properties.

1.5.6 Alternative $\mathcal{W}$ expressions

The Călugăreanu theorem offers an alternative method for calculating $\mathcal{W}$. For closed spacecurves $\mathcal{L}$ is always an integer quantity. $\mathcal{T}$ is a single integral representing the total rotation of the generating vector **v** about the direction of the ribbon's axis. Thus $\mathcal{W}$ can be evaluated as the subtraction of a single integral quantity from an integer. In 1978 Fuller [45] detailed two new expressions for evaluating the writhe of a closed spacecurve, using the Călugăreanu theorem to replace equation 1.19. The aim was to derive expressions which would be simple to evaluate, i.e. single integral formulae. This work summarised previous work on the concepts of $\mathcal{W}$,

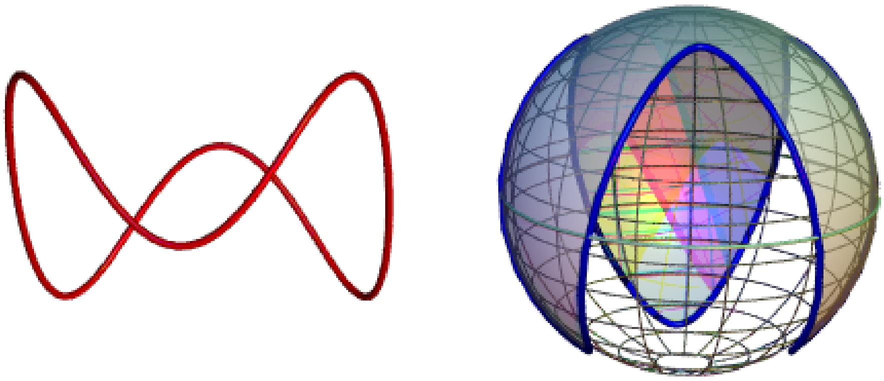

Figure 1.21: The curve $\mathbf{x}(t) = (\sin 2\pi t, \cos 2\pi t, \sin 4\pi t \cos 2\pi t)$ and its tantrix curve lying on the surface of the unit sphere. The area $\mathcal{A}$ bound by $\widehat{\mathbf{T}}_{\mathbf{x}}$ is shown. The magnitude of $\mathcal{A}$ is 2π and is negatively signed. An evaluation by (1.26) will return a $\mathcal{W}$ evaluation of 0 *mod* 2

$\mathcal{L}$ and $\mathcal{T}$ (Crick [31] and Fuller [44]) and included several previously undiscussed properties. Fuller is generally cited as the first to define the following expressions ([40],[104],[114]), together with a partial explanation of their validity. Both of the following expressions can be defined as integrals over a well defined density. This density is defined as the rotation (in terms of increasing parameter value) of an orthonormal framing, defined by the local geometry at all points on the curve. It is for this reason that we choose to call the expressions “local” writhing expressions, in contrast to (1.19) whose density is defined in terms of the geometrical relationship between distinct points on the curve. In terms of the Frenet frame this rotation is its torsion $\tau(s)$.

Fuller theorem 1

For a closed spacecurve $\mathbf{x}(s)$, the tantrix curve $\widehat{\mathbf{T}}_{\mathbf{x}}(s)$ will enclose an area $\mathcal{A}$ on the surface of the unit sphere. This area will be piecewise of class $\mathbf{C}^2$ with respect to s or t and as a consequence of the orientation of $\mathbf{x}$, will be signed (positive or negative). This area can be used to quantify $\mathcal{W}(\mathbf{x})$ as follows,

$$\mathcal{W}(\mathbf{x}) = \frac{\mathcal{A}}{2\pi} - 1 \pmod{2}, \tag{1.26}$$

see Figure 1.21 for example. This expression is independent of parameterisation and can be derived from the Gauss-Bonnet theorem, as demonstrated by Aldinger

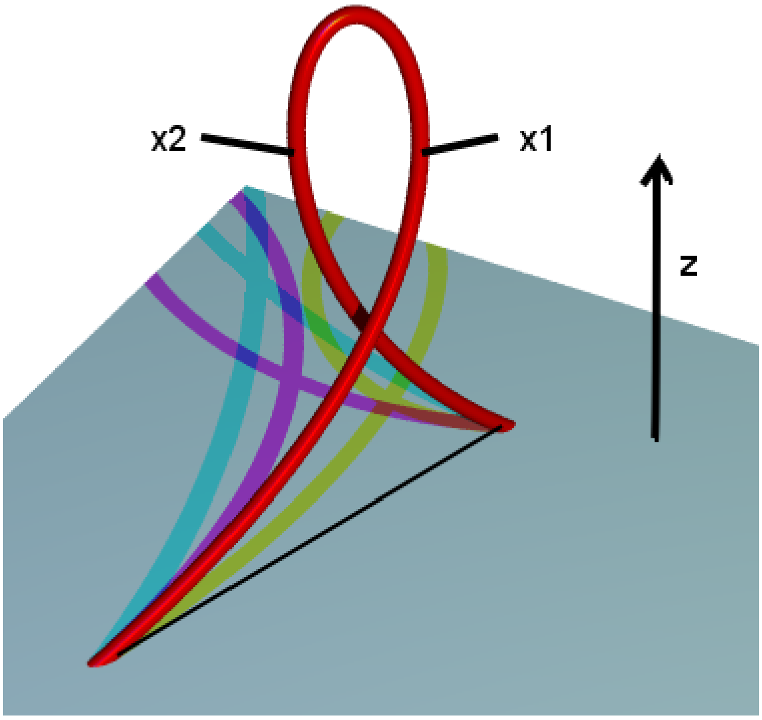

Figure 1.22: A looped section of curve, labelled $\mathbf{x}_1$ and $\mathbf{x}_2$. The two sections of curve which are separated by the local maximum in z, can be seen to wind around each other in the x-y plane. Such contributions to the writhing geometry of the curve are ignored by (1.26).

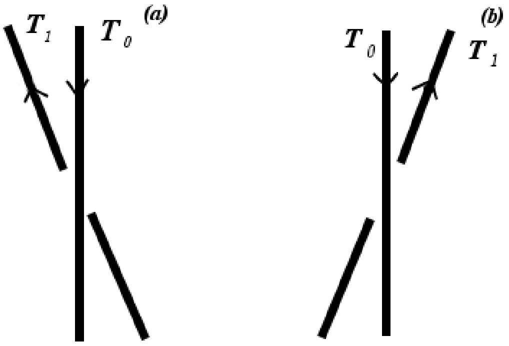

Figure 1.23: By rotating $\widehat{\mathbf{T}}_1$ clockwise, in the page plane, we pass through a configuration for which $\widehat{\mathbf{T}}_0$ and $\widehat{\mathbf{T}}_1$ oppose, in order to reach configuration (b). We note (a) and (b) have planar writhe contributions of opposing sign. We can see at this point the $\mathcal{W}$ has changed non-locally, a fact which is not captured by the local writhing expression 1.27. As $\mathcal{W}$ represents an average over all viewpoints of w we can see this figure provides an intuitive explanation for existence of the non-opposition condition.

et al [5]. It is defined *mod* 2 as the area enclosed on the unit sphere can only be defined *mod* 4π. The modulus condition expresses the fact that (1.26) only tracks the local windings of $\mathbf{x}$. Figure 1.22 shows a section of curve which exhibits both local and non-local windings. Expression (1.19) would take such non-local windings into account, but (1.26) would not. As a consequence of passing $\mathbf{x}$ through itself, $\mathcal{W}$ as evaluated by (1.19) changes by a value ± 2, while (1.26) does not.

Fuller theorem 2

The difference in $\mathcal{W}$ between two non-self-intersecting closed spacecurves $\mathbf{x}_1$ and $\mathbf{x}_0$, linked by an ambient isotopy, with tangents $\widehat{\mathbf{T}}_1$ and $\widehat{\mathbf{T}}_0$, is given by the following equality,

$$\mathcal{W}(\mathbf{x}_1) - \mathcal{W}(\mathbf{x}_0) = \frac{1}{2\pi}\int_0^L \frac{\widehat{\mathbf{T}}_0(s) \times \widehat{\mathbf{T}}_1(s)}{1 + \widehat{\mathbf{T}}_0(s) \cdot \widehat{\mathbf{T}}_1(s)} \cdot (\dot{\widehat{\mathbf{T}}}_0 + \dot{\widehat{\mathbf{T}}}_1)\mathrm{d}s. \tag{1.27}$$

A concise proof of (1.27) appears in Aldinger *et al* [5]. The singularity $\widehat{\mathbf{T}}_0(s) \cdot \widehat{\mathbf{T}}_1(s) = -1$ occurs when the tantrix curves $\widehat{\mathbf{T}}_1$ and $\widehat{\mathbf{T}}_2$ oppose each other (see Figure 1.23). It is this singularity which leads to the restriction that **all** curves comprising the

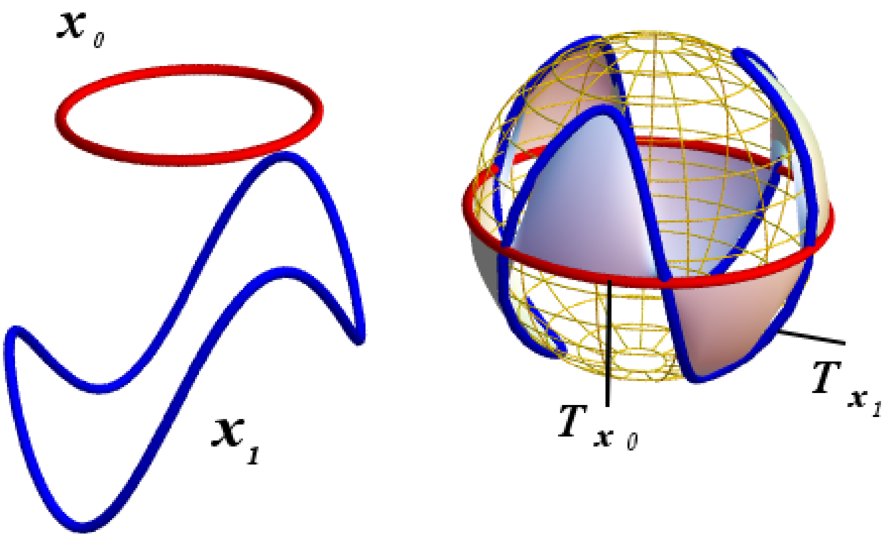

Figure 1.24: On the left are two curves $\mathbf{x}_o(t) = (\sin 2\pi t, \cos 2\pi t, 0)$ and $\mathbf{x}_1(t) = (\sin 2\pi t, \cos 2\pi t, \sin 4\pi t \cos 2\pi t)$. On the right are their tantrix curves $\widehat{\mathbf{T}}_{\mathbf{x}_1}$ and $\widehat{\mathbf{T}}_{\mathbf{x}_0}$ mapped out on the surface of the unit sphere. The spherical area, drawn out as a set of great circle arcs joining $\widehat{\mathbf{T}}_{\mathbf{x}_1}$ to $\widehat{\mathbf{T}}_{\mathbf{x}_0}$ is shown as the shaded region of the sphere. In this case the sections of area in the northern hemisphere are positive, and those in the southern hemisphere are negative. It can be seen that the two will cancel each other exactly, so the difference in $\mathcal{W}$ between $\mathbf{x}_1$ and $\mathbf{x}_0$ is zero. Further as $\mathcal{W}(\mathbf{x}_0)$ is zero (it is a planar curve) $\mathcal{W}(\mathbf{x}_1)$ must also be zero. We note this evaluation of $\mathbf{x}_1$ is the same as that demonstrated in Figure 1.21 by the first Fuller theorem.

ambient isotopy between $\mathbf{x}_1$ and $\mathbf{x}_0$ must never oppose for $s \in [0, L]$. This condition is known as the *non-opposition condition.* As discussed in [5] adherence to the non-opposition condition ensures that the difference in writhing between $\mathbf{x}_0$ and $\mathbf{x}_1$ occurs due to the difference in $\mathcal{T}$. Further Aldinger *et al* demonstrate that a violation of this condition will lead to a change in $\mathcal{W}$ which is an integer multiple of 2 (see Corollary 6 in [5]). This change will not be registered by (1.27). The figures (a) and (b), depicted in Figure 1.23, can be seen to have planar w values differing by a value of 2, a change in non-local writhing, which would be ignored by (1.27). As $\mathcal{W}$ (measured by equation (1.19)), represents an average over all viewpoints of w one can see that requiring the non-opposition be obeyed prevents the non-local jumps in $\mathcal{W}$ which would lead to an incorrect $\mathcal{W}$ evaluation by (1.27). Cantarella [26] interpreted (1.27) in terms of the spherical area enclosed by the great circle arcs joining the end point of $\widehat{\mathbf{T}}_1$ and $\widehat{\mathbf{T}}_0$, see Figure 1.24.

A popular procedure is to define $\mathbf{x}_0(s)$ as a planar spacecurve, known as a *reference curve* ([40],[114],[92],[96]). Planar spacecurves have a $\mathcal{W}$ measure of zero. Thus 1.27 measures $\mathcal{W}(\mathbf{x}_1)$, as long as the non-opposition condition is satisfied for all curves comprising the ambient isotopy linking $\mathbf{x}_1$ and $\mathbf{x}_0$,

$$\mathcal{W}(\mathbf{x}) = \frac{1}{2\pi}\int_0^L \frac{\widehat{\mathbf{T}}_0(s) \times \widehat{\mathbf{T}}_1(s)}{1 + \widehat{\mathbf{T}}_0(s) \cdot \widehat{\mathbf{T}}_1(s)} \cdot (\dot{\widehat{\mathbf{T}}}_0 + \dot{\widehat{\mathbf{T}}}_1)\mathrm{d}s. \tag{1.28}$$

Analytic use of the Fuller expressions

The local nature of the Fuller writhing expressions lends them an analytic tractability which (1.19) does not possess. As such they have been popular in certain subject areas. Fuller was originally asked to provide a quantitative discussion of the properties of $\mathcal{W}$, $\mathcal{L}$ and $\mathcal{T}$ by Vinograd [44], as a result of the interest in such quantities in the field of molecular biology, where the twisting of DNA molecules into superhelical structures provided a need for the study of such geometric quantities. Benham [16] suggested such local formulas could be used to define a model of torsionally deformed elastic polymers. Such a model has become common place in the field of polymer modeling (e.g. [40],[17],[92],[114],[96]).

There is, however, a cost associated with this decrease in complexity. Both expressions (1.26) and (1.27) have limiting conditions which prevent their use in order to obtain full, accurate measures of $\mathcal{W}$ when used in an analytical context. In the case of (1.26) the expression is limited modulo 2 as a result of its inability to calculate the effect of non-local writhings. Thus it only yields a true measure in the case of curves which exhibit very little non-local writhing.

Use of the expression (1.28) is limited by the requirement that the non-opposition condition is satisfied for all curves comprising the ambient isotopy between $\mathbf{x}_1$ and $\mathbf{x}_0$. This restricts its use especially in the case of more complex curves. For example the toroidal trefoil knot (Figure 1.10) has a $\mathcal{W}$ value of -3.52 as evaluated by (1.19), however an evaluation of (1.28) using $\mathbf{x}_{ref} = (\sin 2\pi t, \cos 2\pi t, 0)$ yields a value of 2.48 (note: both are equal modulo 2).

1.6 Open spacecurves

1.6.1 Applications of open writhing and linking

Open polymers

A class of problems concern the geometrical properties of modeling open polymer sections (Fain *et al* [40], Bouchiat and Mézard [17],Rossetto and Maggs [92], van der Heijden *et al* [114],Samuel *et al* [96]), in which the polymer is treated as a ribbon (or rod [114]). The polymers endpoints can often be fixed or controlled in some manner. One such example concerns micromanipulation experiments performed on an isolated open section of DNA molecules ([105],[20]). The molecule is bound at one end, whilst the other end is simultaneously attached to a paramagnetic bead. An appropriate magnetic device can be used to manipulate the molecule by applying both rotational and stretching forces. A theoretical model of this experiment was constructed by Bouchiat and Mézard [17], using an analogy to the quantum model of a symmetric top. A major concern in solving this problem is evaluating the partition function of the allowed configurations the polymer can exhibit,

$$Z(\mathbf{r},\mathcal{L}) = \sum_{\mathcal{C}(\mathcal{L})\in\mathbf{C}(\mathcal{L})} e^{-E(\mathcal{C})/k_bT}. \tag{1.29}$$

Here $\mathbf{r}$ is the separation vector between the molecule endpoints, $\mathcal{L}$ the number of times the bead has been turned (inducing linking into the ribbon), $\mathcal{C}(\mathcal{L})$ is a configuration, of specified $\mathcal{L}$ value, drawn from the full set of possible configurations $\mathbf{C}$; finally $E(\mathcal{C}(\mathcal{L}))$ is its energy and k_b the Boltzmann constant and T the temperature of the substrate containing the molecule. A key issue is defining the set $\mathbf{C}$. If $\mathcal{L}$ can be fixed then $\mathcal{C}$ can be defined (see Samuel *et al* [96] for a brief review of the set of models based on the assumptions applied $\mathcal{L}$). Of course for closed ribbons $\mathcal{L}$ is naturally fixed. However this is not always true for open ribbons.

Open magnetic field structures

Magnetic fields can be viewed as a set of flux tubes carrying flowing magnetic flux (Section 2.9, Priest [90]). An important property of field configurations is their *magnetic helicity* (H). Helicity is a measure of the linked nature of the set of flux tubes comprising the field. The helicity of a single flux tube (net flux Φ) can be evaluated by decomposing the helicity contributions using the Călugăreanu theorem $H = \mathcal{W}\phi^2 + \mathcal{T}\phi^2$, where $\mathcal{W}$ is the writhing of the tubes axis curve and $\mathcal{T}$ measures the average of other field lines (acting as secondary curves), about the axis (Berger and Field [11], Moffatt and Ricca [75]). However, it is often the case that the magnetic field is not fully contained within the region of space in which it is evaluated, that is to say the field structure is open. In this case Berger and Field [11] have shown that the helicity can be measured relative to the minimum-energy vacuum magnetic field. This occurs in the case of the Coronal magnetic field, which lies above the sun's surface (photosphere). Magnetic structures in this region often form helical structures piercing the photospheric layer, as demonstrated in Figure 1.4. This model will form the basis of a study in Chapter 6.

1.6.2 The difficulties surrounding open linking and writhing evaluations

Quantifying the global geometrical properties of open curves is a significantly more complex task than that of closed curves. The major issue affecting the use of $\mathcal{W}$ and $\mathcal{L}$ occurs as a result of the curves endpoints being unconnected. All open curves fitting the criteria of section 1.2.2 can be linked by an ambient isotopy. This loss of topological invariance can be demonstrated for a helical ribbon section such as shown in Figure 1.25(a). It is possible to apply an ambient isotopic deformation such that the curve can be unwound as demonstrated. On the far right of Figure 1.25 is a closed helical structure (c). Such a structure cannot be deformed ambient isotopically, such that its linking is reduced, as with its open counterpart. The consequences for the evaluation of $\mathcal{L}$ are significant.

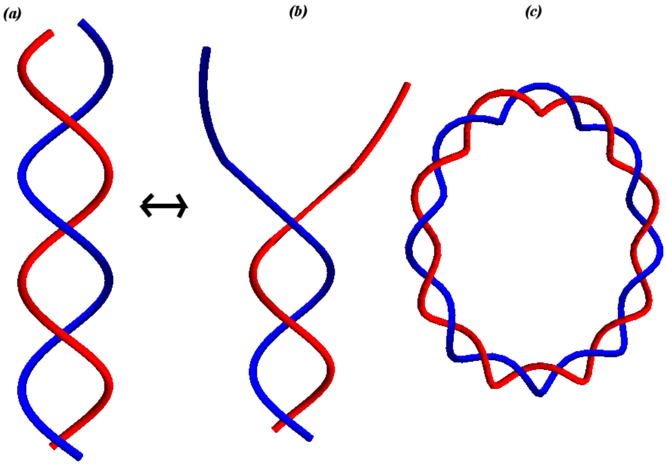

Figure 1.25: Figure (a) is a helical section of a ribbon. An ambient isotopy can be applied to this ribbon to produce (b). This represents an effective un-ravelling of the curve. This procedure could be continued until the curves comprising the ribbon are fully unwound, reducing their linking to zero. Figure (c) represents a closed helical structure. It cannot be unwound in this manner by any set of ambient isotopies

1.6.3 $\mathcal{L}$ and open curves

The $\mathcal{L}$ integral (1.16) can be applied to open ribbons as well as closed ribbons. In this case the integral would be

$$\mathcal{L} \equiv \frac{1}{4\pi}\int_{\mathbf{x}}\int_{\mathbf{y}} \frac{\widehat{\mathbf{T}}_{\mathbf{x}}(s) \times \widehat{\mathbf{T}}_{\mathbf{y}}(s') \cdot (\mathbf{x}(s) - \mathbf{y}(s'))}{|\mathbf{x}(s) - \mathbf{y}(s')|^3} \mathrm{d}s' \mathrm{d}s. \tag{1.30}$$

The absence of topological restriction means open $\mathcal{L}$ is generally of non-integer value and will alter under ambient isotopic transformations. Clearly it is **not** a topological invariant. The loss of topological invariance is a significant issue. As discussed in section 1.6.1, statistical polymer modeling concerns itself with the set of configurations of a collection of intertwined polymers. As discussed in Brereton and Shah [21], Brereton and Vigilis [22] and Samuel *et al* [96], the evaluation of the partition function can be significantly simplified by fixing the linking number, an assumption which cannot be applied generally to open curves for open polymer configurations.

A second example concerns DNA molecules, which can be either closed or open. In the closed case only the action of a set of protein molecules known as Topoisomerases can alter the link of a particular molecule (see Wang [116] for a review of the role of Topoisomerases in cellular biology). For open DNA ribbon structures, various other factors including heat provide a mechanism for altering the molecule inherent linkage (for a review of the role of topology in the study of DNA see Bates and Maxwell [9]).

Two distinct methods for evaluating the open writhing and linking of ribbon type structures have been documented in recent publications.

1.6.4 Local, directional, open writhe

As mentioned in section 1.6.1 Bouchiat and Meźard [17] devised a model for a single elastic polymer (representing a supercoiled DNA molecule) comprising an open ribbon (or rod as it is termed), held in a magnetic trap with its endpoints aligned in a fixed manner along the $\hat{z}$ axis. The motivation was to characterise recent (relative to the publication) experiments on DNA molecules trapped in a magnetic field, which measured charateristics of the relationship between the force applied and elongation of the molecule (Smith *et al* [105], Bustamante *et al* [20]). An expression for the self-contorting nature of the polymer ribbon's backbone was developed, based on work by Fain *et al* on DNA supercoiling [40]. This expression is termed the *local writhe*. It is defined in terms of the Euler angle rotations of an orthonormal reference frame about the $\hat{z}$ axis. An integer ($\mathcal{X}$) representing the degree of linking of the structure about $\hat{z}$ represents the starting point; this is defined in terms of the Euler angle rotations $\theta(s), \phi(s), \psi(s)$,

$$\mathcal{X} = \int_0^L (\psi'(s) + \phi'(s))\mathrm{d}s. \tag{1.31}$$

Using the authors notation, an expression for the twist of the rod in terms of Euler angle rotations is given by

$$\mathcal{T}_w = \int_0^L (\psi'(s) - \phi'(s)\cos\theta(s))\mathrm{d}s. \tag{1.32}$$

A directional equivalent of the Călugăreanu theorem is used to define the local writhe,

$$\mathcal{X}_w = \mathcal{X} - \mathcal{T}_w, \tag{1.33}$$

thus,

$$\mathcal{X}_w = \int_0^L (1 - \cos\theta(s))\phi'(s)\mathrm{d}s. \tag{1.34}$$

Because the Euler angles are discontinuous at $\phi = \pi$ it is necessary that all $\mathbf{x}$, to which this formulation is applied, are restricted from aligning themselves along the negative $\hat{z}$ axis. The Euclidean form of (1.34) demonstrates this explicitly:

$$\mathcal{X}_W = \int_0^L \frac{\hat{z} \cdot (\widehat{\mathbf{T}}_1(s) \times \dot{\widehat{\mathbf{T}}}_t(s))}{1 + \hat{z} \cdot \widehat{\mathbf{T}}_t(s)}\mathrm{d}s. \tag{1.35}$$

Clearly a singularity exists when $\widehat{\mathbf{T}}_{\mathbf{x}} = -\hat{z}$. A naive interpretation of this expression is that it could represent (1.27) with $\mathbf{x}_{ref} = \hat{z}$ (with the factor of $\frac{1}{2\pi}$ taken into account). This appears to be the interpretation expressed in Fain *et al* [40], who specifically label (1.34) as the $\mathcal{W}$ as defined by Gauss (1.19). It is important to make the distinction here that such an assumption would be **false**. Consider a circle lying in the x-y plane. It has a $\mathcal{W}$ value of zero, but (1.34) would denote it a value of $\pm 2\pi$ depending on its orientation. We see the same expression appear in a note by Rosetto and Maggs [92], who express this local writhe formula in its Cartesian form (1.35) with a factor $\frac{1}{2\pi}$, naming it $\mathcal{W}^F$, and state the following relation (without proof or reference),

$$\mathcal{W} - \mathcal{W}^F = 0 \quad (\mathrm{mod}\ 2). \tag{1.36}$$

Section 2.5.2 of this thesis contains a demonstration that

$$\mathcal{W} - (\frac{1}{2\pi}\mathcal{X}_w - 1) = 0 \quad (\mathrm{mod}\ 2), \tag{1.37}$$

as described in terms of the unit sphere interpretation of (1.19) and (1.35). Both [40] and [92] attribute this $\hat{z}$ directional expression to Fuller from his $\mathcal{W}$ discussion in [45]. This would appear to be erroneous. Equation (1.27) which appears in [45], requires that the two constituent curves $\mathbf{x}$ and $\mathbf{x}_{ref}$ are **closed**. This condition is not satisfied by (1.34) or (1.35), as a result of $\hat{z}$ being a single directional vector, and a single point on the unit sphere, rather than a full closed tantrix curve. It is clear the expression proposed by Bouchiat and Meźard is distinct from $\mathcal{W}$ as defined above, as they indeed state in a pair of communications between Rosetto and Maggs 2002 [91] and Bouchiat and Meźard 2002 [18]. It is an expression for the rotation of an orthonormal reference frame of $\mathbf{x}$, about the $\hat{z}$-axis, which does not require $\mathbf{x}$ to be closed.

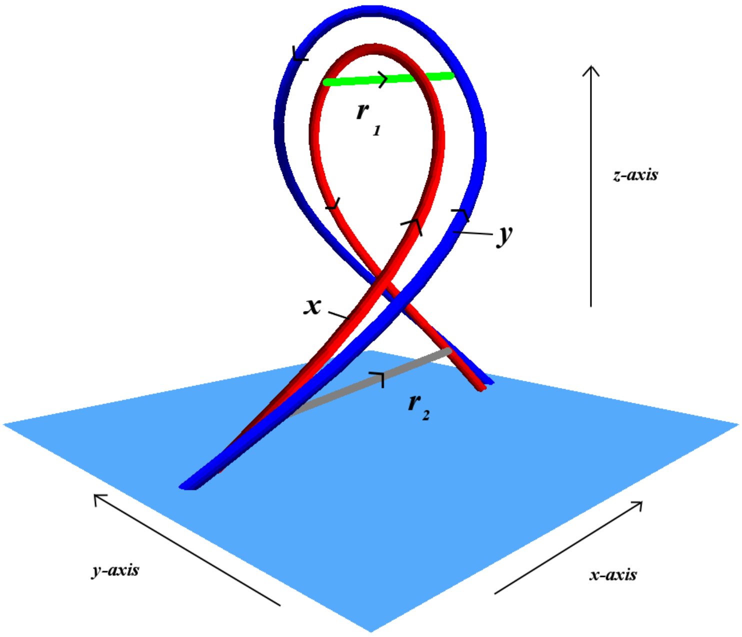

Figure 1.26: A pair of linked curves used to demonstrate the existence of non-local linking and writhing ignored by both (1.31) and (1.34). The chord $\mathbf{r}_1$ links two points on $\mathbf{x}$ and $\mathbf{y}$ which would contribute to the non-local linking. The chord $\mathbf{r}_2$ links two points on $\mathbf{x}$ which would contribute to the non-local winding.

One drawback attributable to expressions (1.34) and (1.35) is that they represent local expressions only. Consider a section of ribbon as seen in Figure 1.26. The local winding formula (1.31) would ignore the contribution due to the sections which share the same z range (see the chord $\mathbf{r}_1$ on 1.26)). This same argument applied to the local writhe expressions would ignore the sections of $\mathbf{x}$ sharing the same z value (an example is marked $\mathbf{r}_2$ on 1.26). This topic will be covered in greater detail in Chapter 3, where a new expression for the directional writhing is developed.

1.6.5 Artificial closures

Several papers have discussed techniques in which an open spacecurve $\mathbf{x}$ is transformed into a closed curve by attaching a curve $\mathbf{x}_c$ to connect the endpoints. This procedure allows the use of the expressions attributed to Fuller (1.26) and (1.27). Both Starostin [104] (following the work of Hannay [51]) and van der Heijden *et al* [114] discuss the modification of these expressions, as applied to curves for which the end tangents $\widehat{\mathbf{T}}_{\mathbf{x}}(0)$ and $\widehat{\mathbf{T}}_{\mathbf{x}}(L)$ lie in the plane containing $\widehat{\mathbf{T}}_0$, $\widehat{\mathbf{T}}_1$ and $\mathbf{x}(L) - \mathbf{x}(0)$. In this scenario it is shown that both (1.26)(Starostin) and (1.27)(van der Heijden et al) can yield evaluations of $\mathcal{W}(\mathbf{x} + \mathbf{x}_c)$ which are equivalent to $\mathcal{W}(\mathbf{x})$. The required closure in such a scenario is a planar section of curve. In terms of the area bound on the unit tangent sphere it is equivalent to joining the two endpoints of the tantrix curve $\widehat{\mathbf{T}}_{\mathbf{x}}(0)$ and $\widehat{\mathbf{T}}_{\mathbf{x}}(L)$, along a geodesic arc. It is important to note that the closure must be such that it is attached smoothly to $\mathbf{x}$ (as discussed in section 1.2.2). Indeed there are two possible geodesic arcs which could close an area on the unit sphere. Starostin [103] demonstrated that it is the arc which conforms to a smooth planar closure which defines the correct area. In section 5.2 we shall define a more general closure which extends this method to a set of open spacecurves whose end points are in general position.

Rossetto and Maggs [92] discuss a closure for the case $\widehat{\mathbf{T}}_{\mathbf{x}(0)} = \widehat{\mathbf{T}}_{\mathbf{x}}(L) = \hat{z}$, as applied to the local writhe (1.35). Briefly, the two endpoints are extended along $\hat{z}$ to $z = -\infty$ and $z = \infty$. A planar section is then smoothly attached to these points to create a closed configuration. In terms of the area covered on the unit sphere this represents the spherical area bound by $\widehat{\mathbf{T}}_{\mathbf{x}}$ and the north pole, noting that it will start and end at the pole.

In general $\mathcal{W}(\mathbf{x})$ of the original open curve is **not** equivalent to that obtained when applying the double integral (1.19) to $\mathbf{x}+\mathbf{x}_c$. This is the result of the non-local interactions between the open curve section and its closure. Rossetto and Maggs [92] show that in addition to the writhe of the open section $\mathbf{x}$, as evaluated in its double integral form, a contribution to the total $\mathcal{W}$ is represented by the winding between the open section and the straight line closure sections. Their work applies to end points whose tangents are parallel (along $\hat{z}$). Starostin [104] details the relationship between the $\mathcal{W}$ of an open section for a more general closure.

1.6.6 The need for a new open writhe expression

We have detailed several methods for evaluating the $\mathcal{W}$ of open spacecurves. Each process however comes with a set of limitations which shall now be discussed, in order to highlight the motivation for deriving a new writhing expression for open spacecurves.

Using artificial closures

The process of creating an artificial closure allows the user to apply the currently existing $\mathcal{W}$ definition to open curves, using single integral expressions. The set of spacecurves to which this formulation can be applied is, however, limited in two ways; the first was discussed in section 1.6.5. This issue we shall show in section 5.2 is not critical, as a sufficient closure can be defined to extend this method to all open spacecurves (of the required smoothness). The second issue relates to the restrictions on the Fuller writhing expressions discussed in section 1.5.6.

Of course one could apply the double integral expression for $\mathcal{W}$ to all open spacecurves, without need for a closure. However, for any applications which strictly require a closure the addition of $\mathbf{x}_c$ will, as discussed in [104] and [92], will alter the value of the $\mathcal{W}$ as evaluated by (1.19).

Open writhing expressions

The expression (1.35) discussed by Bouchiat and Mézard also has issues associated with it. First, as discussed in section 1.6.4 it is a local expression and will not take into account any non-local windings which may affect the physical model.

Secondly (1.35) has an inherent flaw when sections of curve travel in a negative direction along $\hat{z}$. The spherical area interpretation of (1.35) is represented by the area bound between $\widehat{\mathbf{T}}_{\mathbf{x}}$ and the north pole [69]. In Figures (1.27) and (1.28),

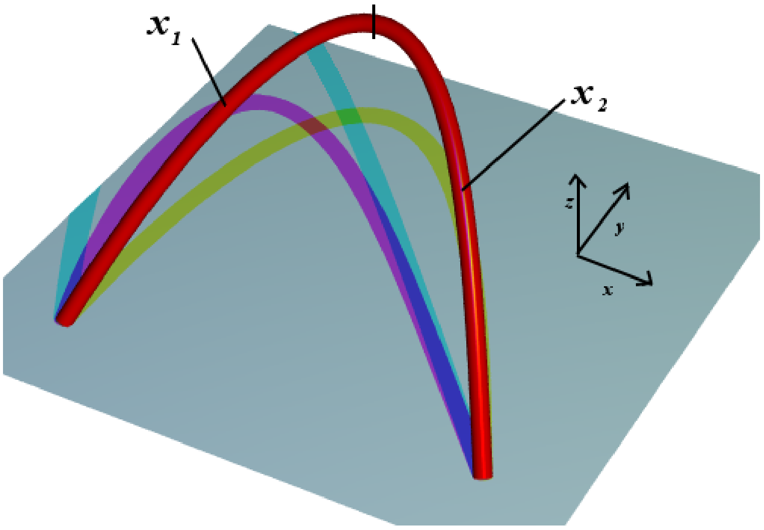

Figure 1.27: The curve $\mathbf{x} = (t, \frac{1}{2}\sin\pi t, 2.5t(1-t))$ evaluated over a period $t \in [0,1]$. This curve can be split, at its peak, into two curve sections. Both curves have the same net torsion.

sections of the curve for which the z component of $\widehat{\mathbf{T}}_{\mathbf{x}}(s)$ is negative (thus lying in the southern hemisphere of the unit sphere) will have a larger contribution to $\mathcal{X}$ than those lying in the northern hemisphere. Sections of curve which exhibit the same total torsion (in absolute terms) should preferably register the same contribution, at least in magnitude, to the total writhe.

Directional bias

In addition to the issues raised above, many physical models will have a strong directional bias. For example, the coronal magnetic field has a natural boundary at the photosphere. Thus the radial direction is naturally distinguished from the two other directions. For structures which are small in comparison to the radius of the sun we can, to a good approximation, model the photosphere as the boundary plane z=0. As a second example, human DNA tends to form open structures bound at either end by the nuclear wall, with the helical structure perpendicular to the wall. This could for example be modelled as a ribbon type structure in the interior of a sphere, or more simply between two planes. As a third example the Bouchiat and Mézard polymer model ([17]) considers a molecule held in a magnetic trap which acts to direct the DNA molecule along a preferred axis ($\hat{z}$ in [17]).

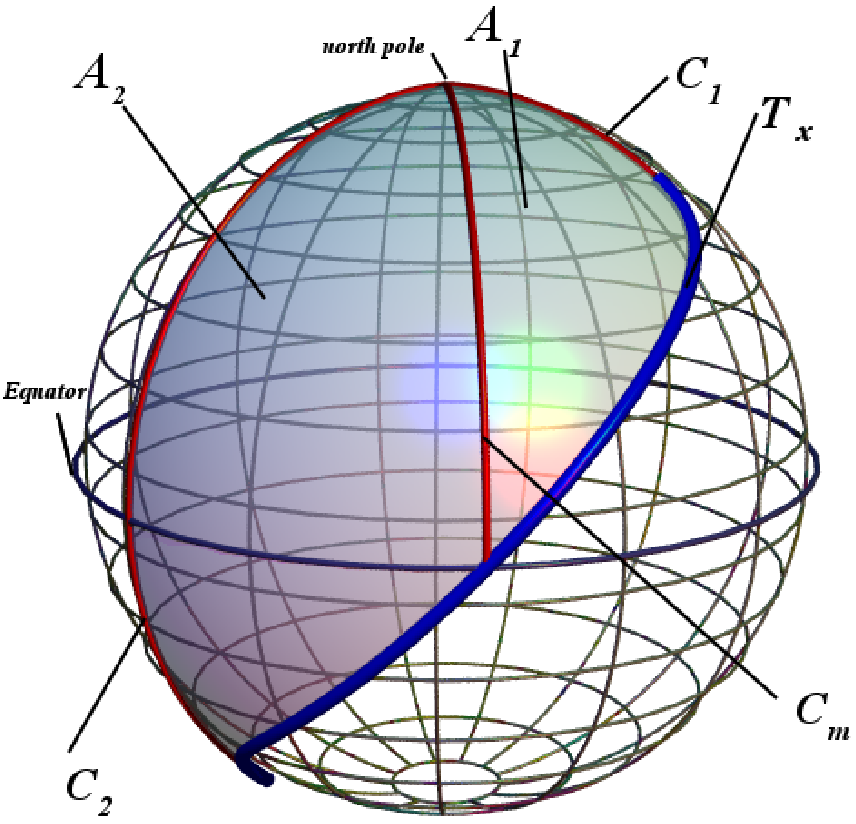

Figure 1.28: The unit sphere area interpretation of the curve $\mathbf{x} = (t, \frac{1}{2}\sin\pi t, 2.5t(1-t))$ (see Figure 1.27) as evaluated using (1.35) over the period $t \in [0,1]$. The area A_1, bound between the tantrix curve $\widehat{\mathbf{T}}_{\mathbf{x}}$ and the two geodesic arcs C_1 and C_m, corresponds to the contribution to $\mathcal{X}_w(\mathbf{x})$ evaluated over the period $t \in [0, 0.5]$. This is the contribution of section $\mathbf{x}_1$ depicted in Figure 1.27. The area A_2 is that bound by C_m, C_2 and $\widehat{\mathbf{T}}_{\mathbf{x}}$ $t \in [0.5, 1]$. This represents the contribution of section $\mathbf{x}_2$ (Figure 1.27) to $\mathcal{X}_w(\mathbf{x})$. It is clear from this figure that the magnitude of A_2 is larger that of A_1, thus the contribution to $\mathcal{X}_w(\mathbf{x})$ from section $\mathbf{x}_2$ is greater than that of $\mathbf{x}_1$. This is despite the magnitude of their torsion being equal.

$\mathcal{W}$ however, is a measure which takes into account all viewpoints. We can view it as an averaging, over all viewpoints of the global geometry of the spacecurve. As such much of the specific directional nature of certain spacecurves or physical models will be lost due to this averaging. It would be preferable if we had a measure of writhing which selectively evaluates the writhing of a spacecurve (local and non-local), along a specific direction, such that only the relevant geometrical information is obtained.

1.6.7 A new open writhe measure

In Chapter 3 we define a new measure of open writhe which is especially applicable to curves in geometries with a special direction. This measure will have the following properties:

- It is a single integral expression defining the writhing of a spacecurve as measured along a preferred direction. Local and non-local contributions, along this direction, are evaluated separately providing an extra dimension of information with regards to the spacecurves directional structure.
- It can be defined for all open spacecurves, without the necessity for the application of an artificial closure.
- Is equal to the $\mathcal{W}$ defined by (1.19) for all closed spacecurves, thus providing a route for quicker numerical evaluation of the writhing of closed spacecurves.
- In general for open spacecurves this measure is different from that of $\mathcal{W}$.

1.7 Outline of thesis

The second chapter demonstrates the properties of the linking and writhing expressions, defined within this introductory chapter, in terms of their interpretation as areas on the unit sphere. This is done by considering their basic geometry rather than relying on theorems extracted from the fields of topology and differential geometry. The aim is to establish a framework for evaluating the properties of writhing and linking expressions which can be applied to open spacecurves. Further the properties of the local directional writhing expression, discussed in section 1.6.4, are established in terms of its unit sphere expression. This is done such that this expression can be compared to the subsequent new writhing expression, developed in chapter 3.

The third chapter concerns the construction of new, consistently defined, expressions for the linking and writhing of open and closed spacecurves. In particular the writhing expression, termed the *polar writhe*, satisfies the set of criteria discussed in section 1.6.6. A directional twisting expression is constructed, and is used to define the polar writhing expression in terms of a directional equivalent of the Călugăreanu theorem. Crucially this expression is shown to be independent of the choice of framing (how the surrounding tube is twisted), in theorem 3.2.3. An expression for the polar writhing is defined in terms of a single Cartesian direction ($\hat{z}$ in this case). The polar writhe is shown to be equivalent to $\mathcal{W}$ for closed spacecurves and interpreted in terms of the unit sphere.

The fourth chapter provides a quantitative comparison of the various writhing expressions, with regards to open spacecurves. A discussion comparing the local directional writhing expression (see section 3.2.3) is used to highlight the advantages inherent to the polar writhe framework, with regards to evaluating the writhing of open spacecurves. The differences are shown to result from its interpretation of non-local windings. A recommendation is made that directionally specific spacecurves are evaluated using the polar writhe expression and non directionally writhing curves evaluated using $\mathcal{W}$. This is based on a series of example spacecurve studies, both directional and non directionally specific cases are considered.

The fifth chapter uses the unit sphere interpretation of the writhing expressions discussed in Chapters 2 and 3 in order to define their properties (or at least a significant number of their properties), with regards to open spacecurves. Further, a new closure is defined for spacecurves whose end tangents have arbitrary orientations, such that local writhing expressions can be defined for the $\mathcal{W}$ of open spacecurves. These expressions, based on the Fuller writhing theorems could be useful for analytic study. Finally a discussion on the choice of direction of evaluation of the polar writhe is discussed.

The sixth chapter is used to provide a physical example of the usefulness of the polar writhe formulation. A simple study of the morphological properties of the coronal magentic field is conducted, using a simple linear force free field model. The polar writhe is used to evaluate various field configurations and its results compared to current assumptions made regarding the morphological properties of such fields. In particular attention is paid to the effect of asymmetry being induced in the field lines, by changing the field line start point, the force free twisting parameter (α) and the Fourier components of the boundary data. The results appear to contradict several common assumptions of the field, relating the fields sigmoidal structure to its writhe and magnetic helicity. Further it demonstrates that the field line behaviour at separatrix surfaces can lead to significant changes in the writhing and helicity of the field lines. Possible directions of further study are provided in a discussion at the chapter's end.

The final chapter gives a brief summary of the main results of the thesis.

Chapter 2

A unit sphere study of linking and writhing

The tantrix sphere provides a simple method for picturing the measure of the quantities $\mathcal{W}$, $\mathcal{L}$ and $\mathcal{T}$ defined in Chapter 1. Visualising an area on the surface of a sphere represents a simpler task than picturing the complex differential geometries which comprise these quantities. As discussed in Chapter 1, several studies have been conducted, defining the properties of these measures for closed spacecurves. Various approaches are applied, generally involving theorems extracted from the fields of differential geometry and topology. These proofs or demonstrations can be tricky to follow for the reader who is not knowledgeable in these fields. It would therefore be desirable to develop simpler methods for analysing quantities such as $\mathcal{W}$ and $\mathcal{L}$, without relying on previous theorems. Hannay [51], Starostin [104], Maggs [69] and Agarwal *et al* [4], discuss the unit sphere area interpretation of $\mathcal{W}$. Dennis and Hannay [37] provide a simple interpretation of the Călugăreanu theorem, in terms of the areas bound on the unit sphere, by demonstrating that $\mathcal{W}$ and $\mathcal{T}$ can be discussed in as mappings which share mutual boundaries. Here this idea will be extended to attempt to explain the properties of all $\mathcal{L}$, $\mathcal{W}$ and $\mathcal{T}$ expressions defined in Chapter 1. The aim is to provide an alternative method for analysing the properties of the various topological and geometrical quantities introduced previously. This will set up a methodology for dealing with the more tricky concept of open $\mathcal{L}$ and $\mathcal{W}$, as applied to spacecurves in the following chapters.

2.1 $\mathcal{L}$ properties interpreted on the unit sphere

As discussed in the introduction $\mathcal{L}(\mathbf{x},\mathbf{y})$ can be defined in terms of the Gauss mapping:

$$\mathbf{m}(s,s') = \frac{\mathbf{x}(s)-\mathbf{y}(s')}{\mid \mathbf{x}(s)-\mathbf{y}(s') \mid} \tag{2.1}$$

To reiterate: each chord $\mathbf{m}(s,s')$ represents a point on the unit sphere. Evaluating $\mathbf{m}$ over all possible pairings for the closed intervals $s \in [0,L]$, $s' \in [0,M]$, will generate a set of points which represent an area $\mathcal{A}_m$ covered on the sphere's surface. This area represnts the degree of the mapping (1.18) and is equal to $\mathcal{L}(\mathbf{x},\mathbf{y})$. Each point is assigned a sign, either positive or negative, which is determined by the scalar triple product $(\frac{\mathrm{d}\mathbf{m}}{\mathrm{d}s} \times \frac{\mathrm{d}\mathbf{m}}{\mathrm{d}s'}) \cdot \mathbf{m}$ [1]. This signed area is the degree of (1.18) and when divided by a factor $\frac{1}{4\pi}$ is equal to the linking number of $\mathbf{x}$ and $\mathbf{y}$ (this is discussed, for example, in Langevin [64]).

$\mathcal{L}$ as a series of continously linked surface curves

Let $\mathbf{o}(\Delta s) = \{\mathbf{m}(s, s+\Delta s), s \in [0,L]\}$ denote a closed curve on the unit sphere. The signed area can be thought of as the area swept out by the set of curves $\mathbf{o}(\Delta s)$, for which Δs ranges from 0 to M, this set shall be denoted $\mathcal{O}_m$. Due to $\mathbf{x}$ and $\mathbf{y}$ being smooth, the set of curves comprising $\mathcal{O}_m$ form a continuously linked set of neighbouring curves $\Delta s = a$ and $\Delta s = a + ds$ (where ds is infinitesimally small), as Δs is varied from 0 to M. All ambient isotopies applied to the pair $\mathbf{x}$ and $\mathbf{y}$ will preserve this neighbouring continuity. In what follows we shall use this set of curves to demonstrate the properties of $\mathcal{L}$ (section 1.4.3).

$\mathcal{L}$ as an integer

The set $\mathcal{O}_m$ will sweep out a signed area $\mathcal{A}_m$ on the sphere's surface. $\mathcal{A}_m$ will be bounded by the curves $\Delta s = 0$ and $\Delta s = M$. These bounding curves $\mathbf{o}(s,0)$ and $\mathbf{o}(s,M)$ are the same curve, as $\mathbf{y}(0) = \mathbf{y}(M)$ (this represents a smooth embedding of the torus in S^2). Thus $\mathcal{A}_m$ must be some multiple of 4π (allowing for negatively signed areas). Any ambient isotopic deformations, applied to $\mathbf{x}$ and $\mathbf{y}$, will naturally

---

[1] This is the pullback of the volume element on S^2 generated by the Gauss map [5]. As the curves are closed (in terms of the definition of cloesd given in section 1.2.2) and we are discussing curves which are non self-intersecting, the inverse is always defined and this measure is well behaved

alter the shape of the curves comprising $\mathcal{O}_m$. However, it will **not** alter the fact that these bounding curves $\Delta s = 0$ and $\Delta s = M$ are equivalent curves. As a result, the area bound by $\mathcal{O}_m$ will always be some multiple of 4π and $\mathcal{L}$ will always be an integer.

Topological invariance

Topological invariance further requires that $\mathcal{L}$ does not alter upon application of an ambient isotopy. In terms of the area $\mathcal{A}_m$, it must be shown that such deformations do not alter its value. As discussed above, all such deformations will alter the bounding curves of $\mathcal{O}_m$ in the exact same manner. Thus $\mathcal{A}_m$ cannot be altered due to $\mathbf{o}(s, 0)$ and $\mathbf{o}(s, M)$, as they will change in exactly the same fashion. The second necessary requirement is that $\mathcal{A}_m$ cannot gain any extra area covered by the set $\mathcal{O}_m$ in between our bounding curves. The requirement that each neighbouring curve belonging to this set be linked homotopically to each other ensures this. The only manner in which area could be added is the appearance of new subset of curves in $\mathcal{O}_m$; such a feat can only be achieved by non ambient isotopic deformations of the link.

$\mathcal{L}$ changes by an amount ± 1 when $\mathbf{x}$ is passed through $\mathbf{y}$

The crossing of $\mathbf{x}$ and $\mathbf{y}$ allows the addition (or subtraction) of a new subset of curves to $\mathcal{O}_m$. This subset will extend an existing subset of $\mathcal{O}_m$ such that its area is increased by an integer (as the neighbouring curves $\mathbf{o}(\Delta s)$ and $\mathbf{o}(\Delta(s+ds)$, bounding this new set, must be identical).

It can be further shown that this subset has an area of 4π, and will hence contribute an value of ± 1 (when sign is taken into account). Consider the links shown in Figure 2.1. Link section (a) can clearly be created from link section (b) by passing $\mathbf{x}$ and $\mathbf{y}$ through each other at their midpoint (a translation in the x-y plane, Figure 2.1). The orientation vectors $\mathbf{m}$, shown in Figure 2.1, represent linking points of mutual z value on $\mathbf{x}$ and $\mathbf{y}$. Section (a) has an extra net rotation of 2π in comparison to that inherent to link section (b), as a result of the reverse of the direction of rotation of $\mathbf{m}(z)$ inherent to b but absent from (a). The reversal in orientation will cause a reversal in sign of the points characterised on the unit sphere. In terms of the unit sphere this extra set of vectors representing $\mathbf{m}(z)$, as evaluated over the full range of z values, will draw out a great circle arc lying on

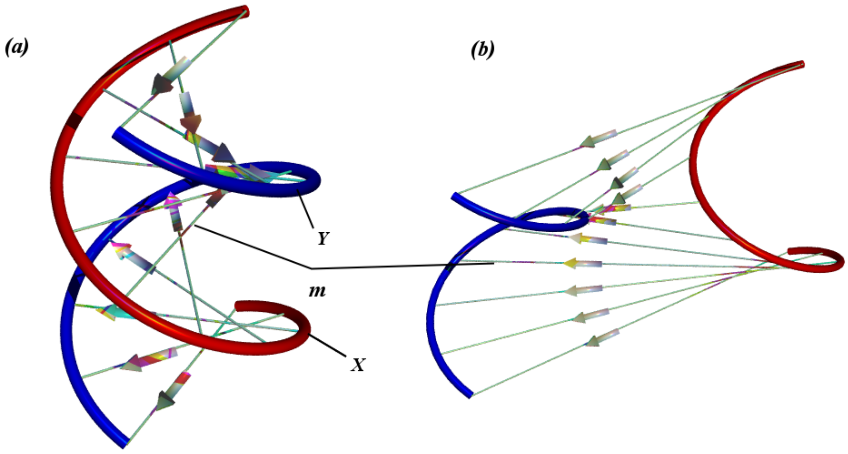

Figure 2.1: A section of link marked (a) is depicted. Vectors, marked $\mathbf{m}$, joining $\mathbf{x}$ and $\mathbf{y}$ at points of mutual z value also shown (that is they lie in the x-y plane), with arrows indicating their orientation. The full set of such vectors form $\mathbf{q}_0$ (section 2.1). Figure (b) represents the same two curves $\mathbf{x}$ and $\mathbf{y}$ except $\mathbf{y}$ has been translated in the x - y plane. This translation necessarily causes $\mathbf{x}$ and $\mathbf{y}$ to pass through each other. It can be seen that the arrows in (a) undergo a full anticlockwise rotation of 2π (over the full set $\mathbf{q}$, moving up in z value). In (b) the arrows begin to rotate in an anticlockwise manner, however this rotation reverses halfway up the ribbon's z range. The bottom and top arrows in the right figure are clearly oriented along the same direction thus the net rotation is zero.

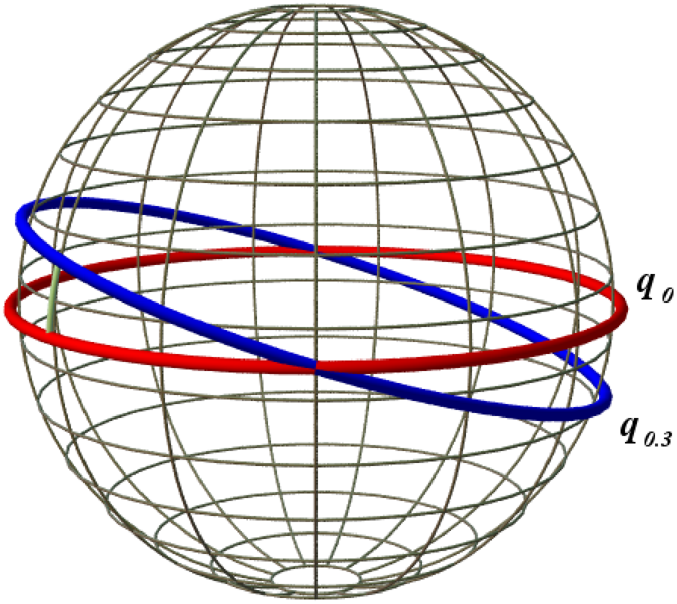

Figure 2.2: Two curves $\mathbf{q}_0$ and $\mathbf{q}_{0.3}$ are mapped out on the unit sphere as a result of viewing link section (a) from Figure 2.1 in the x-y plane ($\mathbf{q}_0$). $\mathbf{q}_{0.3}$ represents viewing (a) in the plane which represents the rotation of the x-y plane about the y-z plane through a polar angle of 0.3.

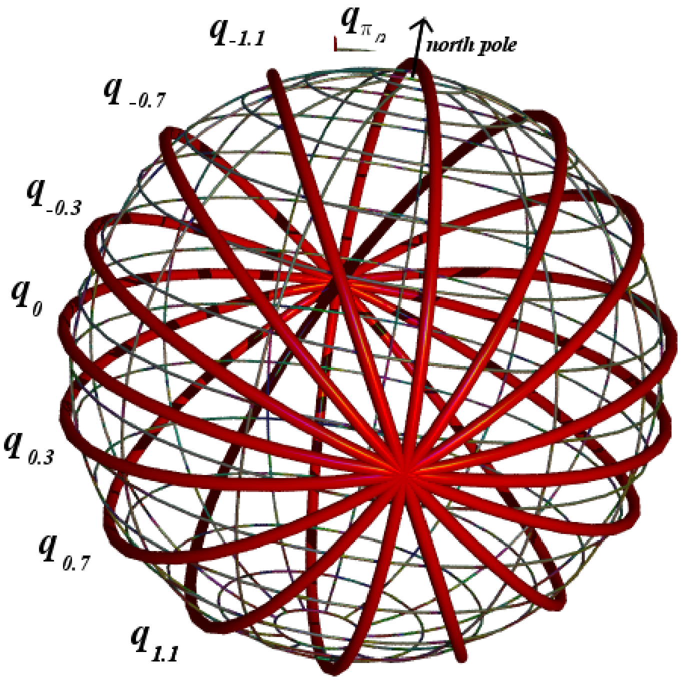

Figure 2.3: A demonstration of the covering of the unit sphere, by the set of curves $\mathbf{q}_\theta$ for $\theta \in (-(\pi/2), \pi/2]$. Note $\mathbf{q}_{\pi/2} = \mathbf{q}_{-\pi/2}$. In the limit in which the full set $\theta \in (-(\pi/2), \pi/2]$ is plotted this set will cover the sphere, in its totality, once.

the equator of the tantrix sphere. For (b) the set of vectors can be split into two halves, each half consisting of the same set of orientations. Due to the opposing direction of rotation of both half sets, they will be of opposing sign and effectively cancel each other out. We can interpret the set of vectors $\mathbf{m}$, as viewing the link from all possible viewing angles in the x-y plane and marking the point at which $\mathbf{x}$ is in front of $\mathbf{y}$ (a similar interpretation is discussed in Dennis and Hannay [37]). Each crossing can be applied a sign in the usual manner. We choose to label this set of vectors $\mathbf{q}_0$.

This same procedure can be performed after rotating the viewing plane through a clockwise angle θ. Due to the directional invariance of $\mathcal{L}$ the interpretation of the difference in net rotation between link sections (a) and (b) will be the same (i.e. differ by 2π). The subset of vectors, drawn from $\mathcal{O}_m$, for which $\mathbf{x}$ will be viewed as covering $\mathbf{y}$ for the set of directions in a plane rotated through θ is labelled $\mathbf{q}_\theta$. The curve drawn out on the unit sphere by $\mathbf{q}_\theta$, will be a great circle rotated through θ, again clockwise (see Figure 2.2). The set of curves drawn out over $\theta \in (-(\pi/2), \pi/2]$, (this will cover all viewing angles), will cover an area of 4π, as depicted in Figure 2.3. For link section (b) the cancellation of orientations will occur for all viewpoints from which the crossing can be seen. For certain viewpoints the crossing will not be seen (for example a viewer directly above (b)), in such cases the net outcome is that no points are marked on the unit sphere. The set of curves $\mathbf{q}_\theta$, $\theta \in (-(\pi/2), \pi/2]$ is appended (or removed), from $\mathcal{O}_m$ upon the crossing of $\mathbf{x}$ and $\mathbf{y}$. Thus the effect of passing $\mathbf{x}$ and $\mathbf{y}$ through each other is the addition or removal of a tantrix area of 4π from the total $\mathcal{A}_m$, or a change in $\mathcal{L}$ of ± 1.

The example shown in Figure 2.1 is exaggerated to demonstrate the principle. We now consider two linked sections $\mathbf{x}$ and $\mathbf{y}$, for both of which $\mathbf{x}$ and $\mathbf{y}$ are separated by an infinitesimal distance at a single pair of points. Further, the two link sections will be such that they can be deformed into each other by a translation which passes $\mathbf{x}$ through $\mathbf{y}$. Even if the two sections are shrunk to an infinitesimal size, the set of vectors $\mathbf{q}_\theta$, $\theta \in (-(\pi/2), \pi/2]$ will still be appended or removed upon crossing.

Topological and non-topological changes

There are effectively two ways of altering the set $\mathcal{O}_m$. First continuous ambient isotopic changes to the whole set. These changes could be termed topological in a sense, as they leave the $\mathcal{L}$ unchanged. The second possibility is the addition or subtraction of a set of curves, to or from $\mathcal{O}_m$. Such changes, by contrast, alter the topology and value of the $\mathcal{L}$, i.e. they are non-topological. $\mathcal{W}$, however, alters under both sets of transformations.

2.2 $\mathcal{W}$ interpreted on the unit sphere

Like the $\mathcal{L}$, $\mathcal{W}$ can be interpreted via a chord mapping between separate points on $\mathbf{x}$,

$$\mathbf{n}(s, s') = \frac{\mathbf{x}(s) - \mathbf{x}(s')}{\mid \mathbf{x}(s) - \mathbf{x}(s') \mid}. \tag{2.2}$$

Evaluating $\mathbf{n}$ over all possible pairings $s \in [0, L]$, $s' \in [0, L]$, will generate a set of points which represent an area $\mathcal{A}_n$ covered on the sphere's surface. Each point is assigned a sign, either positive or negative, which is determined by the scalar triple product $(\frac{\mathrm{d}\mathbf{n}}{\mathrm{d}s} \times \frac{\mathrm{d}\mathbf{n}}{\mathrm{d}s'}) \cdot \mathbf{n}$.

$\mathcal{W}$ as a series of isotopically linked surface curves

Consider the set $\mathcal{O}_n$ of isotopically linked closed spacecurves $\mathbf{p}(\Delta s) = \mathbf{n}(s, s+\Delta(s))$, $s \in [0, L]$ with Δs a constant for each curve $\Delta s \in [0, L]$. $\mathcal{O}_n$ maps out an area $\mathcal{A}_n$ on the surface of the unit sphere. We shall use the set $\mathcal{O}_n$ to demonstrate a unit sphere area interpretation of the properties of$\mathcal{W}$ (section 1.5.1).

$\mathcal{W}$ as a non-integer value

Firstly, consider the case where $\Delta s = (s' - s), \rightarrow 0$. The curve $\mathbf{p}(\Delta s \rightarrow 0)$ traces out the tantrix curve of $\mathbf{x}$. Thus $\mathcal{A}_n$ is bound at one limit by $\widehat{\mathbf{T}}(\mathbf{x})$. In the limit $\Delta s = \rightarrow L$, that is $\mathbf{p}(\Delta s \rightarrow L)$ represents $\widehat{\mathbf{T}}_{\mathbf{x}}$ inverted though the origin of the unit sphere (Figure 2.4), $\mathbf{p}(\Delta s \rightarrow L) = -\widehat{\mathbf{T}}_{\mathbf{x}}$. Excluding any full coverings of the sphere, the surface bound by these two curves $\mathcal{A}_n$ will generally not be a multiple of 4π (note for planar curves (for which $\mathcal{W}$ is zero) $\mathcal{A}_n = 0$). The total area $\mathcal{A}_n$ can be split into two components. The first $\mathcal{A}_n^{frac}$ represents the non-integer or fractional contribution to $\mathcal{W}$. The total area $\mathcal{A}_n$ is completed by some integer number of full-coverings of the unit sphere $\mathcal{A}_n^{int}$.

This argument is similar to a discussion in Dennis and Hannay [37] who consider the behaviour of the mapping (2.2) in terms of what they term a *chord fan*, which

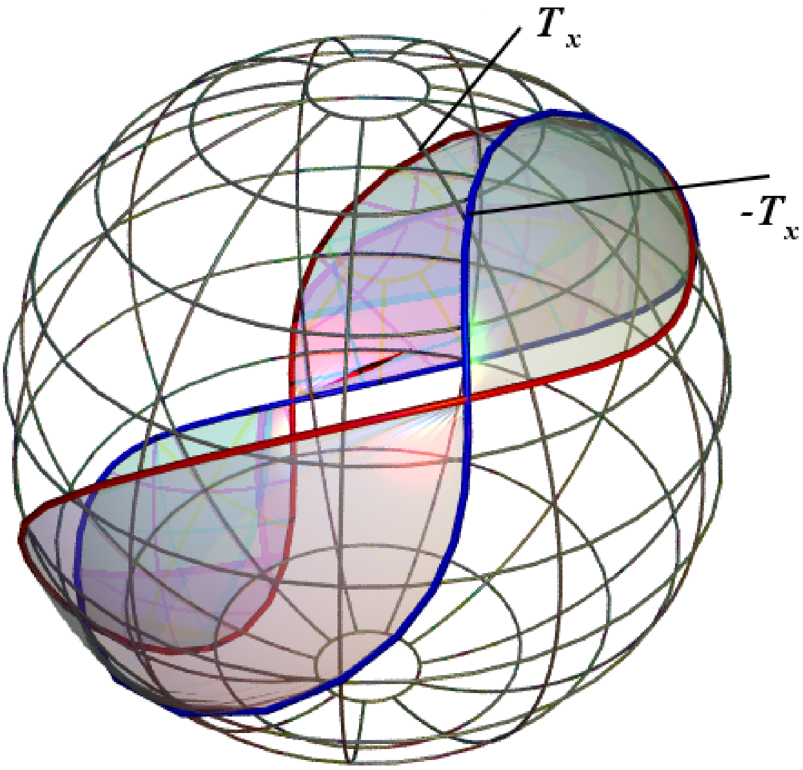

Figure 2.4: The shaded area represents the fractional contribution to $\mathcal{W}$ on the unit sphere . We see marked the tantrix curves $\widehat{\mathbf{T}}_{\mathbf{x}}(s)$ and $-\widehat{\mathbf{T}}_{\mathbf{x}}(s)$, which represents $\widehat{\mathbf{T}}_{\mathbf{x}}$ inverted through the sphere's centre.

is constructed by fixing s and varying s'.

Conformal invariance

Deforming the curve by an ambient isotopy will alter both $\widehat{\mathbf{T}}_{\mathbf{x}}$ and $-\widehat{\mathbf{T}}_{\mathbf{x}}$ smoothly and continuously, thus $\mathcal{A}_n^{frac}$ will alter in a continuous manner also, altering $\mathcal{W}$ in the process. This change has been quantified by Aldinger *et al* [5], who derive an expression for the $\mathcal{W}$ of a curve which is deformed ambient isotopically with respect to a deformation parameter λ,

$$\frac{\mathrm{d}}{\mathrm{d}\lambda}\mathcal{W}(\mathbf{x}_\lambda)(t) = -\frac{1}{2\pi}\oint_a^b \left(\frac{\partial}{\partial\lambda}\widehat{\mathbf{T}}(t,\lambda) \times \widehat{\mathbf{T}}(t,\lambda)\right) \cdot \frac{\partial}{\partial t}\widehat{\mathbf{T}}(t,\lambda)\mathrm{d}t. \tag{2.3}$$

Applying a rotation to $\mathbf{x}$ will not alter $\mathcal{A}_n$ as both $\widehat{\mathbf{T}}_{\mathbf{x}}$ and $-\widehat{\mathbf{T}}_{\mathbf{x}}$ will undergo the same translation about the sphere's surface. A translation will have no affect on the set $\mathcal{O}_n$ as it does not alter the relative orientation of each chords $\mathbf{m}$. The same argument can be made for a scalar dilation, as the set $\mathcal{O}_n$ is normalised. Thus it can be seen that $\mathcal{W}$ is a constant conformal invariant, but not a topological invariant.

$\mathcal{W}$ changes by a value of ± 2 for self-crossings

By analogy with the argument applied to $\mathcal{L}$, the crossing of $\mathbf{x}$ with itself results in addition of a subset of curves to $\mathcal{A}_n$. The subset will cover an area which is some multiple of 4π and hence of integer value. In the case of $\mathcal{A}_n$ the affect is the addition or removal of an area of 8π (i.e. always an even multiple of 4π) as opposed to 4π for $\mathcal{A}_m$. This occurs because the 2π winding is double counted over the whole length of $\mathbf{x}$. For example, returning to Figure 2.1, if we imagine both curves form part of the same curve, the orientation vectors will be drawn in both directions; not just from $\mathbf{x}$ to $\mathbf{y}$ as is the case for $\mathcal{L}$.

Local and non-local components of $\mathcal{W}$

Consider the set of curves $\mathbf{p}(\triangle s)$ belonging to $\mathcal{O}_n$ for which $\Delta s = s' - s$ is very small. Such curves compare the spatial relationship between points which are within some small local radius of each other on our curve. These curves approximately represent the localised contributions to $\mathcal{W}$. However, when Δs is such that the pairs of points are not within each others locality, we tend to extract the non-local, or more distant winding behavior of $\mathbf{x}$. $\mathcal{W}$ can be thought of as a combination of both local and non-local contributions, though they are not evaluated in a distinct manner.

2.3 Twist and the Călugăreanu theorem on the unit sphere

As demonstrated in Dennis and Hannay [37], the $\mathcal{T}$ of a ribbon $R(\mathbf{x}, \mathbf{v})$ can be represented as the area bound on the surface of the unit sphere by the following mapping

2.3.1 $\mathcal{T}$ on the unit sphere

$$\mathbf{l}(s, \theta) = \frac{\widehat{\mathbf{T}}_{\mathbf{x}}(s)\cos\theta + \mathbf{v}(s)\sin\theta}{|\widehat{\mathbf{T}}_{\mathbf{x}}(s)\cos\theta + \mathbf{v}(s)\sin\theta|}. \tag{2.4}$$

When evaluated over $s \in [0, L]$ and $\theta \in [0, \pi]$, this maps out an area which when divided by 2π is equal to the $\mathcal{T}$ of R. As with the $\mathcal{L}$ and $\mathcal{W}$ mappings (1.18) and (2.2) we can define a set $\mathcal{O}_l$ of homeomorphically linked curves $\mathbf{q}(s, \theta_c) = \mathbf{l}(s, \theta_c)$ where θ is held constant (given by a constant value θ_c) and $s \in [0, L]$. These curves form the set $\mathcal{O}_l$ for $\theta_c \in [0, \pi]$, which represents the $\mathcal{T}(R)$ when divided by 2π.

$\mathcal{T}$ as a local property of $R(\mathbf{x}, \mathbf{y})$

Considering the parameter θ gives an insight into the local nature of $\mathcal{T}$ as opposed to the non-local quantities $\mathcal{L}$ and $\mathcal{W}$. In both $\mathcal{O}_n$ and $\mathcal{O}_m$, the second variable Δs is representive of a physical value, specifically a point on the spacecurves $\mathbf{y}$ or $\mathbf{x}$ respectively. In the case of $\mathcal{O}_l$ the second variable θ_c does not represent a physical measurement. Any deformations applied to the ribbon $R(\mathbf{x}, \mathbf{v})$ will not lead to a change in the set $\mathcal{O}_l$ due to θ. As a consequence $\mathcal{T}$ depends only upon s and is local. We cannot add or remove any subsets of the curves $\mathbf{q}$, only alter the existing ones ambient isotopically. The only changes occurring to $\mathcal{T}$ are a result of deformations of $\widehat{\mathbf{T}}_{\mathbf{x}}$ and $\mathbf{v}$, which alter smoothly, so $\mathcal{T}$ reacts similarly.

2.3.2 The Călugăreanu theorem

Dennis and Hannay [37] show the Călugăreanu theorem can be described in terms of the respective unit sphere interpretations of $\mathcal{W}$, $\mathcal{L}$ and $\mathcal{T}$. The following mirrors their argument in terms of the notation introduced previously.

Evaluating the $\mathcal{T}$ area $\mathcal{A}_l$ in the limits $\theta_c = 0$ and $\theta_c = \pi$, the curves representing its limits are $\mathbf{q} = \widehat{\mathbf{T}}_{\mathbf{x}}(s)$ and $\mathbf{q} = -\widehat{\mathbf{T}}_{\mathbf{x}}(s)$ respectively. So $\mathcal{A}_l$ has the same boundary curves as $\mathcal{O}_n$. The amalgamation of $\mathcal{A}_l$ and $\mathcal{A}_n$ will be some integer number of full coverings of the unit sphere. The Călugăreanu theorem tells us that this summed area will be equal to that of $\mathcal{A}_m$. When $\theta = \pi/2$ the twist mapping represents $\mathbf{v}(s)$. This added to the writhe mapping $\mathbf{m}$ gives

$$\mathbf{n}(s,s') + \mathbf{l}(s,\pi/2) = \frac{\mathbf{x}(s) - \mathbf{x}(s') + \mathbf{v}(s')}{\mid \mathbf{x}(s) - \mathbf{x}(s') + \mathbf{v}(s') \mid}, \tag{2.5}$$

which represents the Gauss map $\mathbf{m}(s,s')$. This extension can be approached from both $\theta = 0$ and $\theta = \pi$ which represent the limits $\widehat{\mathbf{T}}_{\mathbf{x}}$ and $-\widehat{\mathbf{T}}_{\mathbf{x}}$, that is to say the $\mathcal{T}$ mapping extends the $\mathcal{W}$ mapping to equal the $\mathcal{L}$ mapping. This is a description rather than a strict proof. Alternatively, Dennis and Hannay show that the link mapping can be used, in appropriate limits to represent both (2.2) and (2.4). Their proof is similar to White's proof (White [117]) though White considered only curves whose curvature was non zero. White's proof is presented in simpler terms by Pohl [89].

2.4 The Fuller $\mathcal{W}$ expressions

The unit sphere interpretations of (1.26) and (1.27) were detailed in section 1.5.6. In this section an alternative demonstration of (1.26) is detailed. This demonstration relies entirely on the unit sphere description of $\mathcal{W}$ detailed in section 2.2. This is in contrast to a strict proof by Aldinger *et al* [5], which relies on the Călugăreanu theorem for its completion. The aim is to further highlight that $\mathcal{W}$ exists as a distinct measurement. A stronger understanding of $\mathcal{W}$ as a measure, without reference to a secondary curve, will benefit its description when we turn our attention to open spacecurves.

2.4.1 The relationship between the two Fuller expressions

One can view the evaluation of $\mathcal{W}$ by (1.26) as the difference between two areas bound on the unit sphere by multiplying the expression by 2π,

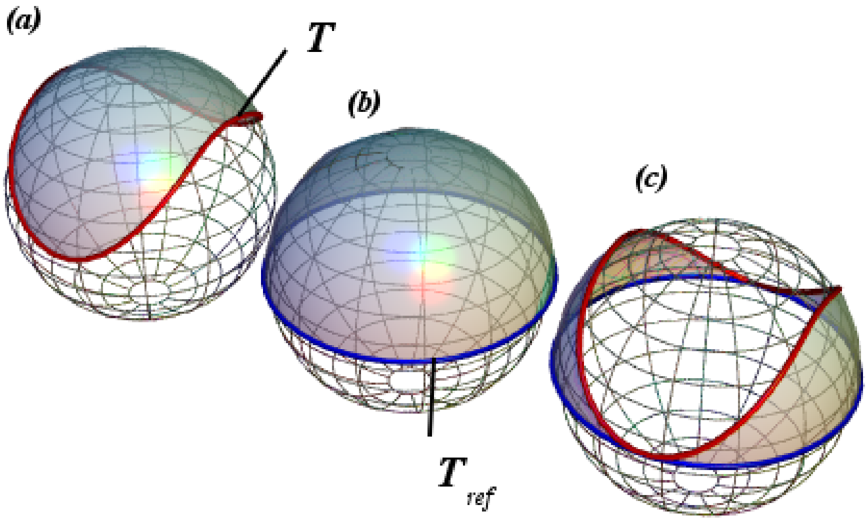

Figure 2.5: Figure (a) represents the (negative) area bound by the tantrix curve of $\mathbf{x}(t) = (\sin 2\pi t, \cos 2\pi t, \sin^2 2\pi t)$. Figure (b) represents the (negative) area bound by $\widehat{\mathbf{T}}_{\mathbf{x}_{ref}}$, where $\mathbf{x}_{ref} = (\sin 2\pi t, \cos 2\pi t, 0)$ is a planar reference curve. Figure (c) shows the area bound by subtracting the second from the first, this is equivalent to an evaluation of (1.27) using the two curves.

$$2\pi\mathcal{W} = \mathcal{A} - 2\pi \pmod{2\pi}. \tag{2.6}$$

This is equivalent to an evaluation using equation (1.27), with $\mathbf{x}_{ref}$ represented by a planar curve lying in the x-y plane. Such a curve will have a tantrix curve $\widehat{\mathbf{T}}_{\mathbf{x}_{ref}}$ which encircles the equator. The remainder of this subtraction is the spherical area drawn out by the great circular arc joining $\mathbf{x}_{ref}$ to $\mathbf{x}$, as required. This equivalence can be demonstrated in Figure 2.5. This description is equivalent to a justification used in Fuller 1978 [45] for (1.26), in which a closed curve, with a helical section, is compared to a planar equivalent in terms of their unit sphere interpretation.

2.4.2 A demonstration of Fuller's first theorem independent of the Călugăreanu theorem

We can demonstrate Fuller's 1st theorem by showing that the unit sphere interpretation of (1.19) satisfies Fuller's 1st theorem, when evaluated modulo 4π. Proof of (1.26) has been detailed in Aldinger *et al* [5]. The authors use the Gauss-Bonnet

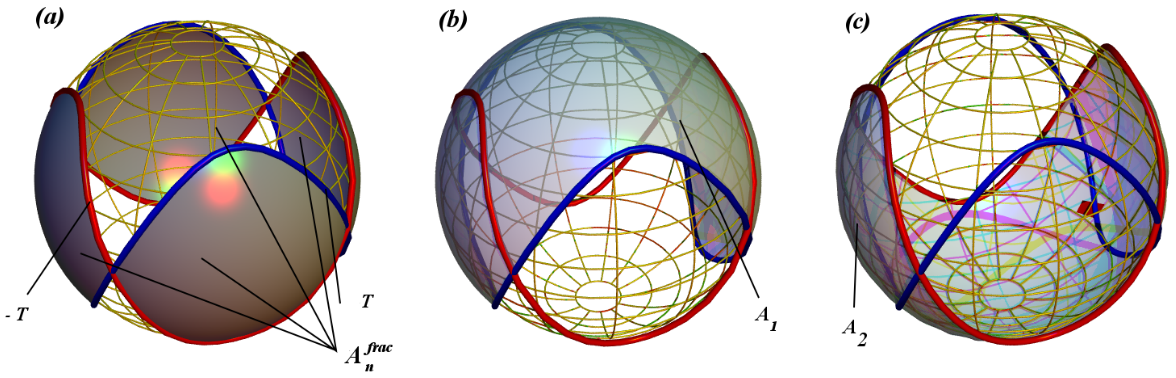

Figure 2.6: .The fractional area $\mathcal{A}_n^{frac}$ is either the area labelled $\mathcal{A}_n^{frac}$ in (a), bound between $\widehat{\mathbf{T}}_{\mathbf{x}}$ and $-\widehat{\mathbf{T}}_{\mathbf{x}}$; or 8π less this shaded area, that is, the two sections of the sphere in (a) unshaded and an extra full 4π covering. This is demonstrated in the text (section 2.4.2). In (b) the area A_1 is bound by $\widehat{\mathbf{T}}$ the tantrix curve and the north pole. In (c) the area, labelled A_2, is bound by $-\widehat{\mathbf{T}}$ and the south pole.

theorem for closed spacecurves and the Călugăreanu thorem. The following demonstration differs in that it makes no assumptions other than the area interpretation of (1.19) defined in section 2.2.

A key component of the demonstration concerns the relative sign of areas on the unit sphere partitioned by $\widehat{\mathbf{T}}$ and $-\widehat{\mathbf{T}}$ ($\mathcal{A}_n^{frac}$). Consider the case in which an area $\mathcal{A}_1$ represents the area bound between $\widehat{\mathbf{T}}$ and the north pole ((b) in Figure 2.6) and $\mathcal{A}_n^{frac}$ (the shaded area of (a) in Figure 2.6). The areas $\mathcal{A}_1$ and $\mathcal{A}_n^{frac}$ will be of opposite sign. To see this we note each area lies on opposite sides of the tantrix curve. Consider two points either side of $\widehat{\mathbf{T}}(t = a)$, at an arbitrary point a on the tantrix curve, displaced along a geodesic longitudinal arc. This equates to two vectors whose directions are rotated up and down (along $\hat{z}$) from $\widehat{\mathbf{T}}$. As such both vectors would require a rotation in opposing directions in order to re-align with $\widehat{\mathbf{T}}(t = a)$. Thus the scalar triple products $(\frac{\mathrm{d}\mathbf{n}}{\mathrm{d}s} \times \frac{\mathrm{d}\mathbf{n}}{\mathrm{d}s'}) \cdot \mathbf{n}$ will be of opposing sign either side of $\widehat{\mathbf{T}}$. This logic could be applied to all directions neighbouring $\widehat{\mathbf{T}}$ to either side in this manner, that is for the set $a \in [0, L]$.

Moving down these longitudinal arcs the directional vector will rotate until it opposes $\widehat{\mathbf{T}}$, that is to say it lies on $-\widehat{\mathbf{T}}$. After this point, which will be in area $\mathcal{A}_2$ (see (c) in Figure 2.6), the sign of the scalar triple product will flip. For example moving down a geodesic arc S_b (see Figure 2.7), the sign flips when the directional

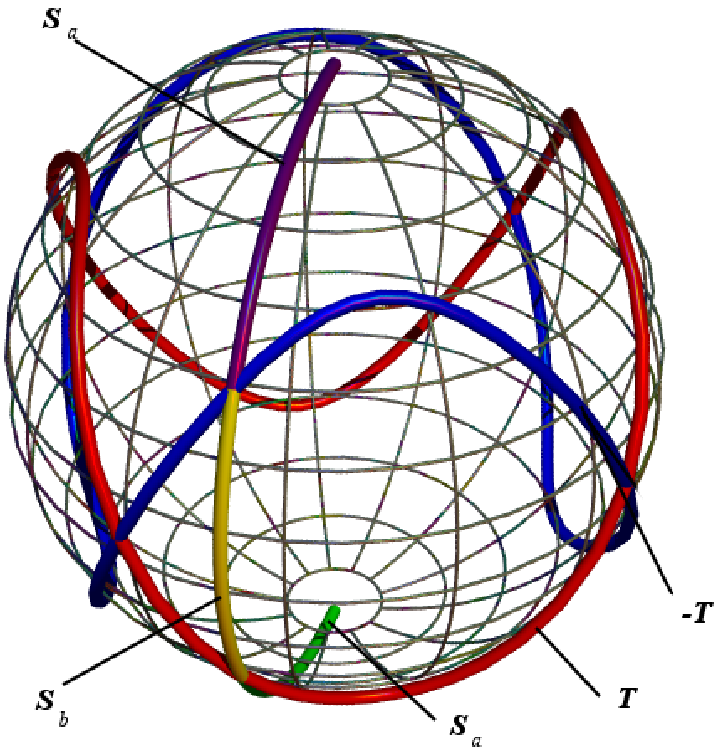

Figure 2.7: A figure demonstrating the possible arcs followed by two opposing possible manifestations of $\mathcal{A}_n^{frac}$ (see Figure 2.6). The arc S_b corresponds to the filled area of figure (a) of 2.6. The arcs S_{a_1} and S_{a_2} form part of the alternative interpretation of $\mathcal{A}_n^{frac}$ (and oppositely signed). They can be joined by an arc section of arc length π joining each pole.

vector passes over $-\widehat{\mathbf{T}}$. So we can say in this case that the areas $\mathcal{A}_1$, bound by $\widehat{\mathbf{T}}$ and the north pole, and $\mathcal{A}_2$ bound by $-\widehat{\mathbf{T}}$ and the south pole ((b) and (c) Figure 2.6), are of the same sign. They will also be of the same magnitude. As such we shall denote both as $\mathcal{A}$, i.e. $\mathcal{A} = \mathcal{A}_1 = \mathcal{A}_2$. Thus the curves $\widehat{\mathbf{T}}$ and $-\widehat{\mathbf{T}}$ are the critical directions. The idea is discussed in Agarwal *et al* [4] who described both curves as the point in which a crossing (in terms of the planar projection), is either lost or gained.

In the case in which $\mathcal{A}_n^{frac}$ represents the area on the sphere covering everything but that shaded in diagram (a) (see Figure 2.6), it will have the same sign as $\mathcal{A}$. Further as demonstrated in Figure 2.7, in contrast to following the arc S_b, $\mathcal{A}^{frac}$ would be defined by the set of arcs $S_{a_1} + \pi + S_{a_2}$ for all a. Following this logic for all points on $\widehat{\mathbf{T}}$ will lead to a set of arc covering an area $\mathcal{A}_1 + 4\pi + \mathcal{A}_2$. Thus in this case $\mathcal{A}_n^{frac} = 2\mathcal{A} \pm 4\pi$, depending on the signs of $\mathcal{A}$ and $\mathcal{A}_n^{frac}$ (if they are positive it will be $+4\pi$ and vice versa). The key point is that in all cases $\mathcal{A}_n^{frac} = 2\mathcal{A}$ when both are evaluated modulo 2. So,

$$\mathcal{A}_n^{frac} - 2\mathcal{A} = \pm 4\pi, \tag{2.7}$$

$$\mathcal{A}_n^{frac} = \pm 4\pi + 2\mathcal{A}. \tag{2.8}$$

Now we can interpret $\mathcal{W}$ (as defined by (1.19)), as

$$\begin{aligned} \mathcal{W} &= \frac{1}{4\pi}(\mathcal{A}_n^{frac} + 8\pi n), && (2.9)\\ &= \pm 1 + \frac{\mathcal{A}}{2\pi} + 2n, && (2.10)\\ &= \frac{\mathcal{A}}{2\pi} - 1 \pmod 2, && (2.11) \end{aligned}$$

which satisfies (1.26).

This represents the full set of possible $\mathcal{A}_{frac}$ contributions, as all other areas bound between $\widehat{\mathbf{T}}_{\mathbf{x}}$ and $-\widehat{\mathbf{T}}_{\mathbf{x}}$ will be complemented by an area of 8π (consider each arc path would have to cover a full 2π to return to its original point). Thus the demonstration is completed.

2.5 The vertically directed writhing expression $\mathcal{W}_z$

The following expression for writhing has appeared in various forms and with various notations,

$$\mathcal{W}_z(\mathbf{x}(s)) = \frac{1}{2\pi}\int_0^M \frac{\hat{z}\cdot(\widehat{\mathbf{T}}_1(s)\times \dot{\widehat{\mathbf{T}}}_t(s))}{1+\hat{z}\cdot\widehat{\mathbf{T}}_t(s)}\mathrm{d}s. \tag{2.12}$$

In Fain *et al* [40], it is defined as an application of (1.27) with $\mathbf{x}_{ref}$ replaced by $\hat{z}$. In this paper this expression is denoted $\mathcal{W}$, which, as we have discussed in section 1.6.4 is erroneous. Bouchiat and Mézard [17] derive the same expression as Fain *et al* but make it clear it is distinct from $\mathcal{W}$ as defined by (1.19). As discussed in section 1.6.4 they develop this expression by detailing directional link and twist expressions in order to define a directionally inclined writhe expression. In van der Heijden *et al* [114] it is introduced, with an arbitrary Cartesian direction. For the sake of clarity we shall chose to label this quantity $\mathcal{W}_z$. Whilst this discussion centres on a choice of direction $\hat{z}$ it could equally have been performed using an arbitrary direction $\hat{a}$.

2.5.1 Properties of $\mathcal{W}_z$

In this section we shall demonstrate the following properties of $\mathcal{W}_z$, using its unit sphere interpretation.

- $\mathcal{W}_z$ is **not** constant conformally invariant (van der Heijden *et al* effectively discuss this in [114]).
- $\mathcal{W}_z$ changes smoothly upon ambient isotopic deformations as long as the curve is restricted from pointing along $-\hat{z}$.
- $\mathcal{W}_z$ changes by a value of ± 2 when $\mathbf{x}$ is deformed such that its tantrix curve passes over the south pole of the unit sphere.
- $\mathcal{W}_z - 1$ is equal to $\mathcal{W}$ when evaluated mod 2.

2.5.2 A comparison of $\mathcal{W}_z$ and $\mathcal{W}$

For a closed spacecurve $\mathbf{x}$ the following can be demonstrated

$$\mathcal{W}(\mathbf{x}) = (\mathcal{W}_z(\mathbf{x}) - 1) \pmod 2. \tag{2.13}$$

To see this we note the unit sphere interpretation of $\mathcal{W}_z$ is the area bound on the surface of the unit sphere by $\widehat{\mathbf{T}}$ and the north pole, divided by 2π. This is of course equivalent to the area $\mathcal{A}$ in our demonstration of 1.26 (section 2.4.2) and thus 2.13 holds using the same logic. Samuel *et al* [96] state this relationship. By contrast Rosetto and Maggs [92] state that $\mathcal{W}(\mathbf{x}) - \mathcal{W}_z(\mathbf{x}) = 0 \; mod \; 2$, where they denote $\mathcal{W}_z$ as $\mathcal{W}^F$. This is of course not true , when we consider a curve in the x-y plane, for example, this relation fails.

Why it is necessary to subtract 1 from $\mathcal{W}_z$ to make the equality (2.13) true? The reason for this could be seen from the following interpretation. $\mathcal{W}_z$ could naively be thought of as the difference in $\mathcal{W}$ between a spacecurve and a straight line directed along the $\hat{z}$ axis using Fuller's second theorem. However, $\hat{z}$ is **not** a closed spacecurve, which (1.27) requires. The -1 in (1.26) represents the minimum curvature inherent to a closed spacecurve, 2π. This is a result of the Frenchel theorem, for an unknotted closed spacecurve,

$$\oint \kappa(s)\mathrm{d}s \geq 2\pi. \tag{2.14}$$

A proof of (2.14) is detailed in Kamien 2002 [55]. The minimum 2π will occur in the case of a closed planar spacecurve whose writhe is zero. Thus the -1 in (2.13) is that which is neglected from $\mathcal{W}_z$ as a result of choosing a reference curve with zero curvature.

2.5.3 $\mathcal{W}_z$ and the south pole

The singularity inherent to (2.12) essentially provides $\mathcal{W}_z$ with an equivalent of the non-opposition condition. The effect of passing the tantrix curve over the south pole is to cause a jump in value of $\mathcal{W}_z$ by ± 2, that is $\mathcal{W}_z$ is effectively now the single critical direction. Consider a circle whose tantrix curve is given by $\widehat{\mathbf{T}}_{\mathbf{x}}(t) = (\sin 2\pi t, \cos 2\pi t, 0)$; this bounds a positive area of 2π with the north pole (see (a) in Figure 2.8). Next we rotate the curve about the $y-z$ plane in a clockwise manner (see (b) in Figure 2.8) though an angle of 1 rad. Clearly the area lost in the western hemisphere is balanced by a gain in the east hemisphere of the same amount, thus the area bound with the north pole is still 2π. However if the rotation is increased

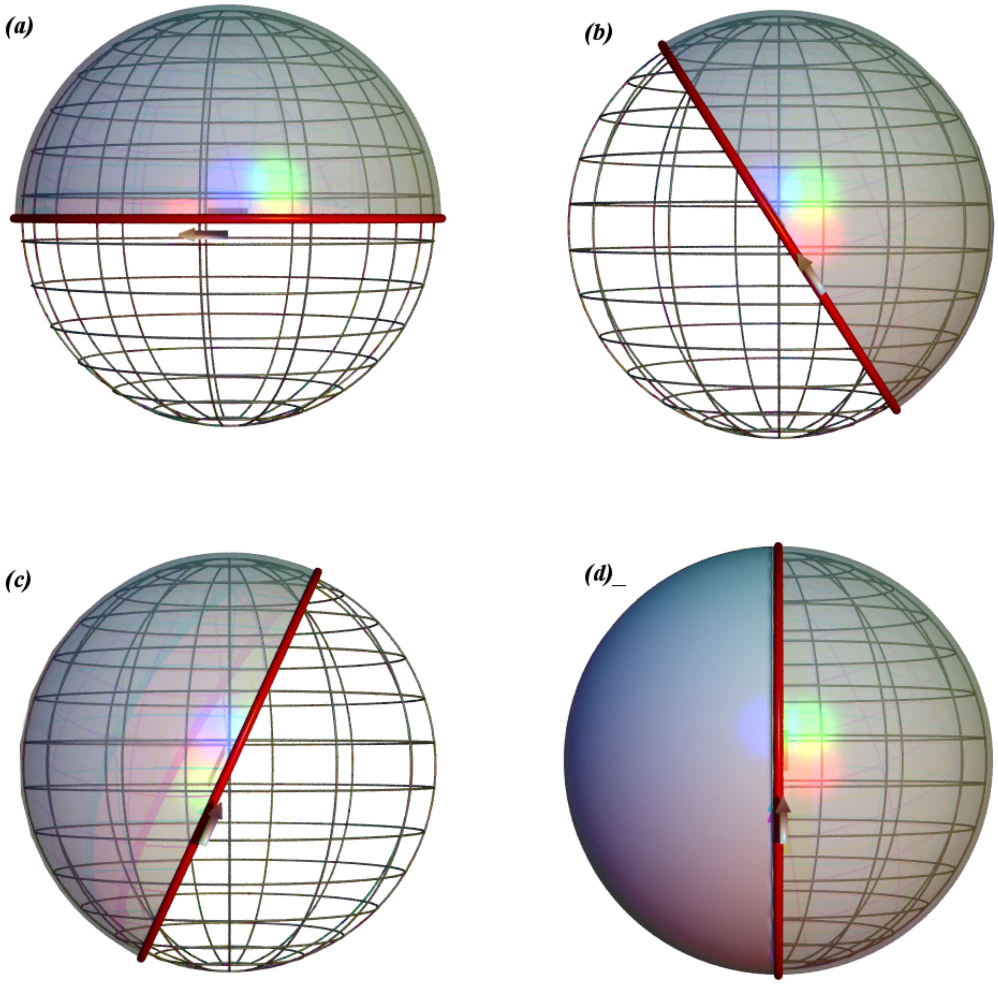

Figure 2.8: Figures (a)-(b) represent the unit sphere interpretations of $\mathcal{W}_z(\mathbf{x})$ for four curves. These examples are used to demonstrate the $\mathcal{W}_z$ which occurs as the tantrix curve $\widehat{\mathbf{T}}_{\mathbf{x}}$ passes thorough the south pole. In (a) $\mathbf{x} = (-\cos 2\pi t, \sin 2\pi t, 0)$ its tantrix curve can be seen to bind an area between the equator and the north pole, an area of 2π. This is area is positively signed and as such $\mathcal{W}_z(\mathbf{x}) = 1$. In (b) $\mathbf{x}$ has been rotated about the y-z plane though and angle of 1 rad. Clearly the area bound is still 2π as the loss of area in the western hemisphere is balanced out by a gain in the eastern hemisphere by the same amount. In (c) $\mathbf{x}$ has been rotated by 2π rad. The curve could either bind a positively signed area in the eastern hemisphere (the transparent area) or a negatively signed area in the western hemisphere (the opaque area). Finally in (d) the area is once gain 2π however now it is negatively signed (note the area is to the left of the tantrix curve rather than on the right as in (a) and (b)).

to $\pi/2$ rad the area bound is now multi valued. As demonstrated in Figure 2.8 (c), the area bound could either be defined by geodesic lines passing through the western (negatively signed) or eastern hemispheres (positively signed), thus the area bound is $\pm 2\pi$. If the rotation is increased further (Figure 2.8(d)) the area once again becomes singularly defined and is now negative (-2π). This we can see the effect of passing the tantrix curve through the south pole is a change in area of 4π, which is equivalent to a change of 2 when the factor $\frac{1}{2\pi}$ is taken into account. This is equivalent to the curve $\mathbf{x}$ being rotated such that it points along $-\hat{z}$ somewhere. This fact also demonstrates that $\mathcal{W}_z$ is not rotationally invariant and hence **not** constant conformally invariant.

Chapter 3

The polar writhe and its associated properties

As demonstrated in section 1.6.6 there is a clear need for the introduction of a consistent and complete measure of writhing and linking which can be applied to open spacecurves. A set of measurements which fit this description has been detailed by Berger and Prior in 2006 [15]. These measures are defined for all open spacecurves, with $\mathcal{C}^3$ differentiability. It is shown in [15] that link, writhe and twist can be defined as sums of single integrals along a preferred direction. As a result all expressions can be applied to open curves without the need for a closure. As with the previous chapter the unit sphere interpretations of the directional linking and writhing expressions will be detailed. Finally it will be shown, in the case of closed spacecurves, that irrespective of direction, these directional measurements are equivalent to the closed $\mathcal{L}$, $\mathcal{T}$ and $\mathcal{W}$ expressions.

3.1 Net winding $\widetilde{\mathcal{L}}$

An alternative to evaluating the linking number using the Gauss integral (1.16), is to calculate a sum of single integrals along a preferred direction, such as the vertical $\hat{z}$ axis (see Figure 3.1). Such a procedure is used to evaluate the Kontsevitch integral for Vassiliev invariants in knot theory (Kontsevitch [60], Berger [14] provides an elementary introduction and Chmutov and Duhzin a thorough treatment [29]). In this section a directional expression for the linking number is defined. This expression shall be used, along with a directional $\mathcal{T}$ expression, to define an equivalent expres-

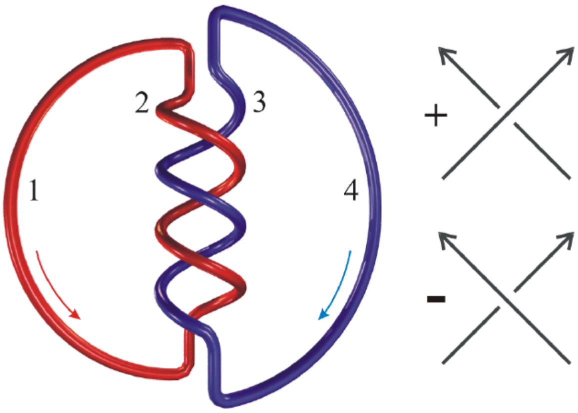

Figure 3.1: Two closed curves with four crossings. All four crossings are negative. The $\mathcal{L}$ in this case is -2. Alternatively, this linking number can be calculated by adding up the winding angles $\Delta\Theta_{ij}$ between pieces of the curves (and dividing by 2π). Here $\Delta\Theta_{13} = \Delta\Theta_{14} = \Delta\Theta_{24} = 0$, while $\Delta\Theta_{23} = -4\pi$.

sion for the self-linking along a preferred direction. As stated, these expressions will be naturally defined for open spacecurves.

Consider two sections of linked spacecurves parameterised by z, $\mathbf{x}(z)$ and $\mathbf{y}(z)$, which are moving only in the positive $\hat{z}$ direction (Figure 3.2), and which have a mutual range $z \in [z_{min}, z_{max}]$. Their winding number can be defined using the vector $\mathbf{r}(z) = \mathbf{y}(z) - \mathbf{x}(z)$, which lies in the x-y plane (see Figure 3.2). Its orientation $\Theta(z)$ is measured relative to the x-axis (Figure 3.2). The rate at which $\Theta(z)$ changes with respect to $\hat{z}$ is given by

$$\frac{\mathrm{d}\Theta(z)}{\mathrm{d}z} = \frac{\hat{z}\cdot\mathbf{r}(z)\times\mathbf{r}'(z)}{\mid \mathbf{r}(z) \mid^2}. \tag{3.1}$$

By integrating over $z \in [z_{min}, z_{max}]$ the net winding number can be evaluated as:

$$\triangle\Theta = \int_{z_{min}}^{z_{max}} \frac{\mathrm{d}\Theta(z)}{\mathrm{d}z}\,\mathrm{d}z = \int_{z_{min}}^{z_{max}} \frac{\hat{z}\cdot\mathbf{r}(z)\times\mathbf{r}'(z)}{\mid \mathbf{r}(z) \mid^2}\,\mathrm{d}z. \tag{3.2}$$

Arbitrary links have turning points in the z axis ($\frac{\mathrm{dx}}{\mathrm{dz}} = 0$). For the full winding of such links it is necessary to split $\mathbf{x}(z)$ into sections using these turning points to divide the curve into sections, for which $\frac{\mathrm{ds}}{\mathrm{dz}} < 0$ and $\frac{\mathrm{ds}}{\mathrm{dz}} > 0$. Consider a curve $\mathbf{x}(z)$ which is split into n sections labelled $i = 1, 2, \ldots n$. Each section straddles a range $z \in [z_i, z_{i+1}]$; σ_i will mark each section as rising or falling in z using the following

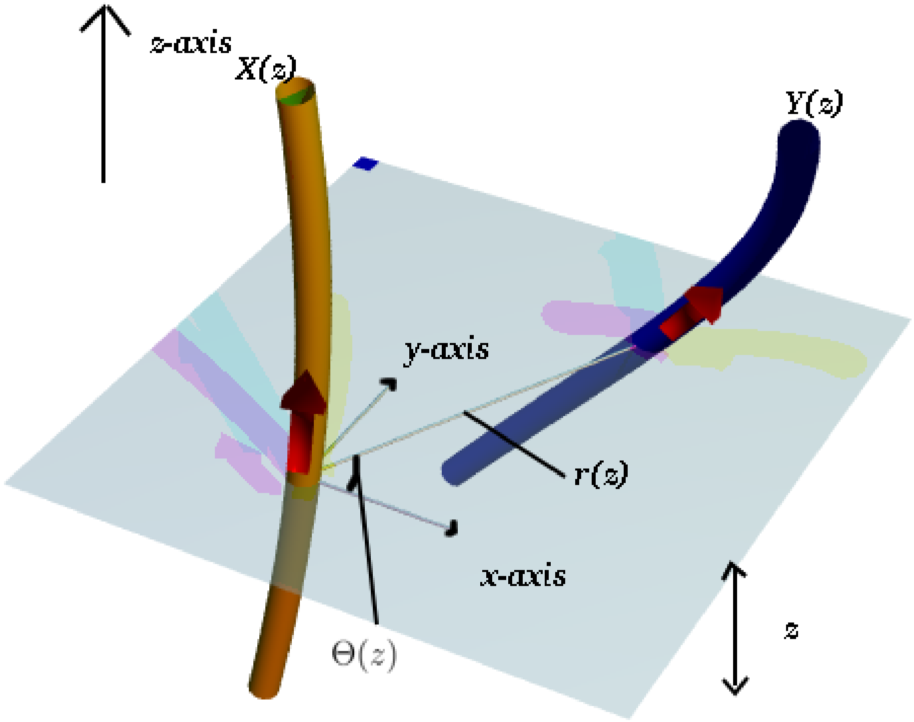

Figure 3.2: Two sections of curves **x** and **y** occupying the same z range. Their linking, along $\hat{z}$, can be defined in terms of the vector $\mathbf{r}(z)$ joining two sections of curve $\mathbf{x}(z)$ and $\mathbf{y}(z)$ in the $x-y$ plane. Also depicted is the angle $\Theta(z)$ which $\mathbf{r}$ makes with the x-axis.

rule set,

$$\sigma_i(z) = \begin{cases} 1, & z \in (z_i, z_{i+1}) \text{ and } \frac{\mathrm{d}s}{\mathrm{d}z} > 0, \\ -1, & z \in (z_i, z_{i+1}) \text{ and } \frac{\mathrm{d}s}{\mathrm{d}z} < 0, \\ 0, & z \notin (z_i, z_{i+1}). \end{cases} \tag{3.3}$$

If further $\mathbf{y}(z)$ is split into sections $j = 1, ..., m$ the total orientation is defined as

$$\Delta\Theta = \sum_{i=1}^{n}\sum_{j=1}^{m}\frac{1}{2\pi}\int_{z_{min}^{ij}}^{z_{max}^{ij}} \sigma_i\sigma_j \frac{\mathrm{d}\Theta_{ij}(z)}{\mathrm{d}z}\,\mathrm{d}z, \tag{3.4}$$

where the numbers z_{max}^{ij} and z_{min}^{ij} represent the extremal z values of two sections which share mutual ranges.

Theorem 1 *Consider two* ***closed*** *spacecurves* $\mathbf{x}$ *and* $\mathbf{y}$. *Let* $\mathbf{x}$ *have sections* $i = 1, ..., n$ *and* $\mathbf{y}$ *have sections* $j = 1, ..., n$. *Let* Θ_{ij} *be the orientation of the vector* $\mathbf{r}_{ij} = \mathbf{y}_j(z) - \mathbf{x}_i(z)$, *linking* $\mathbf{x}_i$ *and* $\mathbf{y}_j$, *in the x-y plane. The* $\mathcal{L}$ *of* $\mathbf{x}$ *and* $\mathbf{y}$ *is given by:*

$$\begin{aligned} \mathcal{L} &= \sum_{i=1}^{n}\sum_{j=1}^{m}\frac{1}{2\pi}\int_{-\infty}^{\infty} \sigma_i\sigma_j \frac{\mathrm{d}\Theta_{ij}(z)}{\mathrm{d}z}\,\mathrm{d}z & (3.5) \\ &= \sum_{i=1}^{n}\sum_{j=1}^{m}\frac{\sigma_i\sigma j}{2\pi}\Delta\Theta_{ij}. & (3.6) \end{aligned}$$

The proof shall be given in the appendix (section A.1). This theorem demonstrates that the linking number can be alternatively evaluated as a sum of single integrals. More specifically this integral is performed over a well-defined density function $\Theta'(z)$. This allows the expression to be applied to open curves as well as closed curves. It must be noted that this evaluation is not local in the sense that the $\mathcal{T}$ is. In order to evaluate $\mathcal{L}$ by either (3.5) or (3.6) it is necessary to split the curve into sections, a process which requires a global knowledge of the link.

This $\mathcal{L}$ measure can be split into two contributions, local sections ($i = j$), and non-local sections ($i \neq j$). In order to do this it is necessary to define the net winding number for non-closed sections of curve.

Definition *Net Winding* $\widetilde{\mathcal{L}}$

Let z_{min} and z_{max} be the maximum and minimum heights both curves reach, and z_0 some value between these limits. The net winding $\widetilde{\mathcal{L}}(z_0)$ of $\mathbf{x}$ and $\mathbf{y}$, below z_0, is given by

$$\widetilde{\mathcal{L}}(z_0) = \int_{-\infty}^{z_0} \frac{\mathrm{d}\widetilde{\mathcal{L}}}{\mathrm{d}z}\mathrm{d}z = \int_{z_{min}}^{z_0} \frac{\mathrm{d}\widetilde{\mathcal{L}}}{\mathrm{d}z}\mathrm{d}z, \tag{3.7}$$

$$\frac{\mathrm{d}\widetilde{\mathcal{L}}}{\mathrm{d}z} = \sum_{i=1}^{n}\sum_{j=1}^{m} \frac{\mathrm{d}\widetilde{\mathcal{L}}_{ij}}{\mathrm{d}z}; \quad \frac{\mathrm{d}\widetilde{\mathcal{L}}_{ij}}{\mathrm{d}z} = \frac{\sigma_i\sigma_j}{2\pi}\frac{\mathrm{d}\Theta_{ij}}{\mathrm{d}z}, \tag{3.8}$$

where $\widetilde{\mathcal{L}}(z_{max}) = \mathcal{L}$ for closed spacecurves.

3.1.1 A restricted sense of topological invariance

Unless $z_0 = z_{max}$, $\widetilde{\mathcal{L}}(z_0)$ is **not** topologically invariant to the full set of ambient isotopies. It will however, be invariant to the subset of such deformations which vanish below z_0.

Theorem 2 *The net winding number $\widetilde{\mathcal{L}}(z_0)$ is an invariant to the restricted set of motions which vanish at $z = z_0$ (such motions do not move the intersection points of the curves with $z = z_0$, nor do they allow other parts of the curve to pass through this plane).*

Proof of Theorem 2

First remember for a closed curve, $\widetilde{\mathcal{L}}(z_{max}) = \mathcal{L}$ is topologically invariant. Secondly the net winding between z_0 and z_{max} will also be invariant as a result of the restriction of motion in this region. Finally

$$\widetilde{\mathcal{L}}(z_0) = \mathcal{L} - \widetilde{\mathcal{L}}(z_0, z_{max}), \tag{3.9}$$

$$\widetilde{\mathcal{L}}(z_0, z_{max}) = \int_{z_0}^{z_{max}} \frac{\mathrm{d}\widetilde{\mathcal{L}}}{\mathrm{d}z}\mathrm{d}z. \tag{3.10}$$

Thus $\widetilde{\mathcal{L}}(z_0)$ is equal to the difference between two quantities, which are unchanged under this restricted set of motions, and must itself be unchanged. Put another way $\widetilde{\mathcal{L}}(R)$ expression is invariant for open ribbons (R) whose endpoints are fixed and which are restricted from self-intersection.

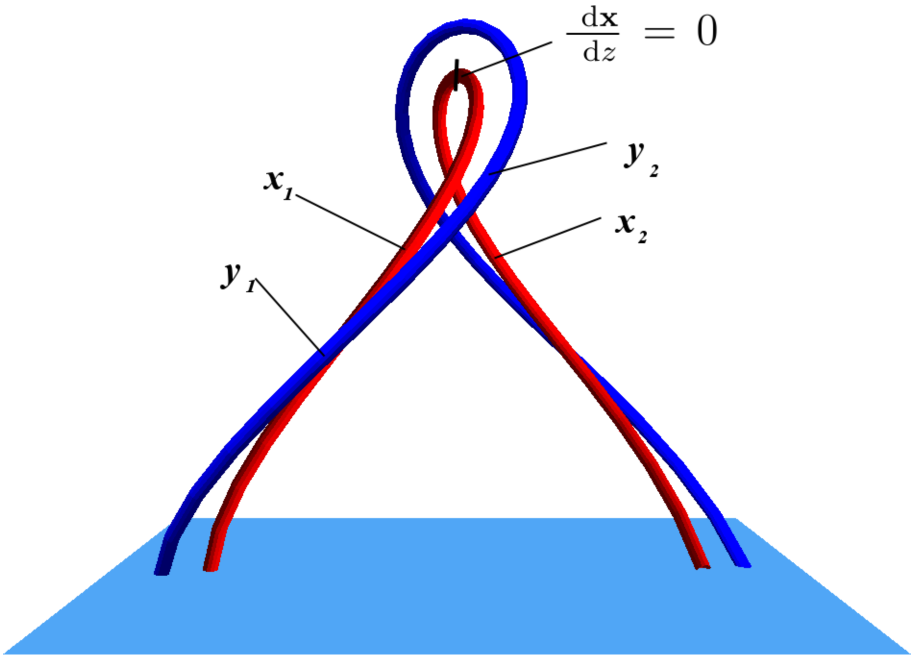

Figure 3.3: A section of ribbon with a turning point in $\mathbf{x}$ marked. There exists non-local winding in the x-y plane, between $\mathbf{x}_1$ and $\mathbf{y}_2$, as well as the local winding between ribbon section 1 with itself, and section 2 with itself.

3.1.2 Local and non-local contributions

The net winding number can be split into local and non-local contributions. Consider the ribbon section depicted in Figure 3.3. The contributions attributable to section $\mathbf{x}_1$ can be split into both local and non-local components. First there is the link between its neighbouring secondary section $\mathbf{y}_1$, which could be termed the local winding. Also there exists a winding contribution between $\mathbf{x}_1$ and $\mathbf{y}_2$ which could be termed a non-local contribution. The net winding density of an arbitrary closed ribbon $R(\mathbf{x}, \mathbf{v})$ can be split into such local and non-local contributions;

$$\widetilde{\mathcal{L}}'(z) = \sum_{i=1}^{n} \widetilde{\mathcal{L}}'(\mathbf{x}_i, \mathbf{y}_j)(z) + \sum_{i=1}^{n}\sum_{j=1}^{n} \widetilde{\mathcal{L}}'(\mathbf{x}_i, \mathbf{x}_j). \tag{3.11}$$

Integrating (3.11) over $z \in [z_{min}, z_{max}]$ will equal $\mathcal{L}(R)$ for closed spacecurves,

$$\mathcal{L}(R) = \frac{1}{2\pi}\sum_{i=1}^{n}\int_{z_{min}}^{z_{max}} \frac{\mathrm{d}\Theta_{ij}}{\mathrm{d}z}\mathrm{d}z + \sum_{i=1}^{n}\sum_{j=1}^{n}\sigma_i\sigma_j\int_{z_{min}}^{z_{max}} \frac{\mathrm{d}\Theta_{ij}}{\mathrm{d}z}\mathrm{d}z. \tag{3.12}$$

3.1.3 A unit sphere interpretation

Equation (3.12) can be interpreted as the total rotation of the orientation vector Θ. For closed ribbons $\Theta(z(0)) = \Theta(z(L))$, thus the total orientation must be some multiple of 2π. In terms of the unit sphere this is equivalent to a half covering of the unit sphere. Take into account the factor of $1/2\pi$ and this equates to an integer. For closed curves this logic is applicable for all choices of direction, not just $\hat{z}$.

If $\mathbf{x}$ and $\mathbf{y}$ are allowed to pass through each other the total rotation will alter $\pm 2\pi$, as detailed in the previous chapter (see Figure 2.1). As a result the tantrix area covered will alter by $\pm 2\pi$ which leads to a change in $\mathcal{L}$ of ± 1. Again this interpretation is view invariant.

3.2 A complete directional writhing expression

Having defined the directional link $\widetilde{\mathcal{L}}(z_0)$ it would be desirable to define an equivalent measure for the twist $\widetilde{\mathcal{T}}(z_0)$. This would enable the definition of a directional writhe measure $\widetilde{\mathcal{W}}(z_0)$ as $\widetilde{\mathcal{W}}(z_0) \equiv \widetilde{\mathcal{L}}(z_0) - \widetilde{\mathcal{T}}(z_0)$. A potential issue with this method of construction is that $\widetilde{\mathcal{L}}(z_0) - \widetilde{\mathcal{T}}(z_0)$ depends on the shape of $\mathbf{y}$ as well as $\mathbf{x}$. This would be undesirable as any equivalent writhing expression should depend only on the shape of the ribbon's axis. However, as shall be demonstrated, the average over the family of secondary curves depends only on $\mathbf{x}$ as required.

We start by defining the following:

$$\widetilde{\mathcal{W}}(z_0) = \int_{z_{min}}^{z_0} \frac{\mathrm{d}\widetilde{\mathcal{W}}(z)}{\mathrm{d}z}\mathrm{d}z, \tag{3.13}$$

$$\widetilde{\mathcal{T}}(z_0) = \int_{z_{min}}^{z_0} \frac{\mathrm{d}\widetilde{\mathcal{T}}(z)}{\mathrm{d}z}\mathrm{d}z, \tag{3.14}$$

$$\tag{3.15}$$

where it is required that, for closed spacecurves, $\widetilde{\mathcal{W}}(z_{max}) = \mathcal{W}$ and $\widetilde{\mathcal{T}}(z_{max}) = \mathcal{T}$.

3.2.1 A directional twisting expression $\widetilde{\mathcal{L}}$

Definition *Directional twist* $\widetilde{\mathcal{T}}$

Consider a ribbon $R(\mathbf{x}, \mathbf{v})$. This ribbon is divided into sections $\mathbf{x}_i$ and $\mathbf{y}_i$ at extrema in z. Along each piece the twist can be evaluated using (1.23), with each contribution labelled $\mathcal{T}_i$. Section i covers a range $z \in [z_{min}, z_{max}]$. Recall that σ_i gives the sign of $\frac{\mathrm{d}s}{\mathrm{d}z}$ (so if $\sigma_i = +1$, $s = s_i^{min}$ at $z = z_i^{min}$), then

$$\mathcal{T}_i = \int_{s_i^{min}}^{s_i^{max}} \frac{\mathrm{d}\mathcal{T}_i}{\mathrm{d}s}\mathrm{d}s = \int_{z_i^{min}}^{z_i^{max}} \frac{\mathrm{d}\mathcal{T}_i}{\mathrm{d}s}\left|\frac{\mathrm{d}s}{\mathrm{d}z}\right|\mathrm{d}z, \tag{3.16}$$

and thus

$$\widetilde{\mathcal{T}}_i'(z) = \frac{\mathrm{d}\mathcal{T}_i}{\mathrm{d}s}\left|\frac{\mathrm{d}s}{\mathrm{d}z}\right| = \frac{\sigma_i}{2\pi}\widehat{\mathbf{T}}_i(z)\cdot\widehat{\mathbf{V}}(z)\times\widehat{\mathbf{V}}'(z). \tag{3.17}$$

3.2.2 A directional writhing expression $\widetilde{\mathcal{W}}$

Now $\widetilde{\mathcal{L}}$ and $\widetilde{\mathcal{T}}$ have been defined it is possible to construct an expression for $\widetilde{\mathcal{W}}$. It is important to note that $\widetilde{\mathcal{T}}$ is an entirely local quantity and thus the local contribution to the $\widetilde{\mathcal{W}}$ density will be

$$\widetilde{\mathcal{W}}_i'(z) = \widetilde{\mathcal{L}}_i' - \widetilde{\mathcal{T}}_i', \tag{3.18}$$

where $\widetilde{\mathcal{L}}_i' = \widetilde{\mathcal{L}}(\mathbf{x}_i, \mathbf{y}_i)$, and the non-local density contribution $\widetilde{\mathcal{W}}_{ij}$,

$$\widetilde{\mathcal{W}}_{ij}' = \widetilde{\mathcal{L}}_{ij}' \tag{3.19}$$

where $\widetilde{\mathcal{L}}'_{ij}(z) \equiv \widetilde{\mathcal{L}}'(\mathbf{x}_i, \mathbf{y}_j)$. The non-local contribution would present issues as $\widetilde{\mathcal{L}}'_{ij}$ depends on both $\mathbf{x}$ and $\mathbf{y}$. However as we can choose the distance ϵ to be much smaller than the distance between sections i and j, it can be said that

$$\widetilde{\mathcal{L}}'(\mathbf{x}_i, \mathbf{y}_j) = \widetilde{\mathcal{L}}'(\mathbf{x}_i, \mathbf{x}_j) \equiv \widetilde{\mathcal{L}}'_{ij}. \tag{3.20}$$

In what follows it will often be convenient to decompose the tangent vector $\widehat{\mathbf{T}}$ into its z component $\widehat{\mathbf{T}}_z$ and its perpendicular components $\widehat{\mathbf{T}}_\perp$. Suppose $\widehat{\mathbf{T}}$ is oriented at an angle θ with respect to the $\hat{z}$ axis. We will define

$$\begin{aligned} \lambda &= \cos\theta = \widehat{\mathbf{T}}_z = \frac{\mathrm{d}\mathbf{x}_z}{\mathrm{d}s}, & (3.21) \\ \mu &= \sin\theta = |\widehat{\mathbf{T}}_\perp|. & (3.22) \end{aligned}$$

3.2.3 The local contribution to $\widetilde{\mathcal{W}}$

It is necessary to average $\widetilde{\mathcal{L}}(z) - \widetilde{\mathcal{T}}(z)$ over all secondary curve choices inherent to a twisted tube, in order to ensure the $\widetilde{\mathcal{W}}$ measures depends solely on the axis curves geometry.

Theorem 3 *Let the rate of directional writhing of a segment i of $\mathbf{x}$, be defined as*

$$\widetilde{\mathcal{W}}'_i(z) = \langle \widetilde{\mathcal{L}}'(z) - \widetilde{\mathcal{T}}'(z) \rangle, \tag{3.23}$$

where $\langle\ \rangle$ denotes the average over all secondary curves in the surface of the twisted tube. Then $\widetilde{\mathcal{W}}'(z)$ is independent of framing, and its local writhing contribution (that of the specific section) can be determined by integrating the following

$$\widetilde{\mathcal{W}}'_i(z) = \frac{1}{2\pi} \frac{1}{(1 + |\lambda_i|)} (\widehat{\mathbf{T}}_i \times \widehat{\mathbf{T}}'_i)_z. \tag{3.24}$$

The proof of (3.23) is somewhat detailed and is left for the appendix (section A.2). A natural choice for the framing, given that directional expressions have been defined along the $\hat{z}$ axis, is such that $\widehat{\mathbf{V}}$ is always in the x-y plane.

At each point on the axis, we define three orthonormal vectors $\{\widehat{\mathbf{T}}, \widehat{\mathbf{f}}, \widehat{\mathbf{g}}\}$ starting with the tangent vectors

$$\widehat{\mathbf{f}} = \frac{\hat{z}\times\widehat{\mathbf{T}}}{\mu}, \tag{3.25}$$

$$\widehat{\mathbf{g}} = \widehat{\mathbf{T}}\times\widehat{\mathbf{f}}. \tag{3.26}$$

Points where $\widehat{\mathbf{T}}$ is parallel to the z axis do not cause any real difficulty, as alternative framings can be employed near them, which do not change the final result (remembering it has been demonstrated $\widetilde{\mathcal{W}}'(z)$ is independent of framing). Setting $\widehat{\mathbf{V}} = \widehat{\mathbf{f}}$ and substituting into (3.17) gives

$$\begin{aligned} 2\pi\widetilde{\mathcal{T}}_i'(z) &= \frac{\sigma_i}{\mu_i^2}\widehat{\mathbf{T}}_i\cdot(\hat{z}\times\widehat{\mathbf{T}}_i)(\hat{z}\times\widehat{\mathbf{T}}_i'), & (3.27)\\ &= \frac{\sigma_i}{\mu_i^2}\widehat{\mathbf{T}}_z(\widehat{\mathbf{T}}_i\times\widehat{\mathbf{T}}_i')_z, & (3.28)\\ &= \frac{|\lambda_i|}{\mu_i^2}\hat{z}\cdot\widehat{\mathbf{T}}_i\times\widehat{\mathbf{T}}_i'. & (3.29)\end{aligned}$$

As a result of the choice of framing the winding of $\mathbf{r}(z) = \mathbf{y}_i(z) - \mathbf{x}_i(z)$ can be characterised in terms of $\widehat{\mathbf{f}}$, where $\mathbf{r}(z) = \epsilon\widehat{\mathbf{f}}$. Substituting this into 3.11 gives

$$\begin{aligned} 2\pi\widetilde{\mathcal{L}}_i' &= \frac{\mathrm{d}\Theta}{\mathrm{d}z} = \hat{z}\cdot\widehat{\mathbf{f}}_i\times\widehat{\mathbf{f}}_i', & (3.30)\\ &= \frac{1}{\mu_i^2}(\widehat{\mathbf{T}}_i\times\widehat{\mathbf{T}}_i')_z. & (3.31)\end{aligned}$$

Taking the difference between the directional link and twist densities leaves the directional writhe density $\widetilde{\mathcal{W}}'(z)$,

$$2\pi\widetilde{\mathcal{W}}' = \frac{1-|\lambda_i|}{\mu_i^2}(\widehat{\mathbf{T}}_i\times\widehat{\mathbf{T}}_i')_z = \frac{1}{1+|\lambda_i|}(\widehat{\mathbf{T}}_i\times\widehat{\mathbf{T}}_i')_z, \tag{3.32}$$

as required.

It is now possible to define an expression for $\mathcal{W}$ as a single integral summation of both the local and non-local contributions, which shall be labelled $\widetilde{\mathcal{W}_l}$ and $\widetilde{\mathcal{W}_{nl}}$ respectively. So for closed spacecurves we have

$$\mathcal{W} = \widetilde{\mathcal{W}_l} + \widetilde{\mathcal{W}_{nl}}, \tag{3.33}$$

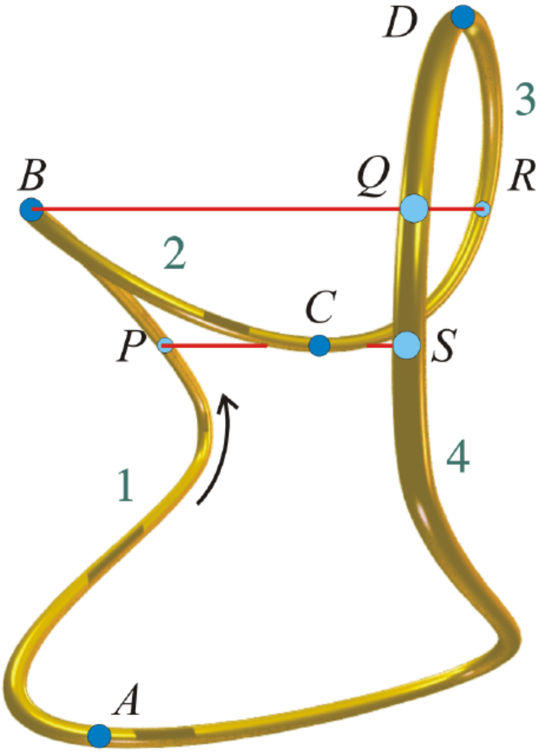

Figure 3.4: The axis of the above curve is a heart shaped curve with maxima points B and D, and minima at points A and C. For this example $z_D > z_B > z_C > z_A$. The points C, P and S area at height z_C while B, Q and R are at height z_B. Section 1 goes from A to B, section 2 from B to C, section 3 from C to D and section 4 from D to A.

$$\widetilde{\mathcal{W}}_l = \frac{1}{2\pi}\sum_{i=1}^{n}\int_{z_{min}}^{z_{max}} \frac{1}{1+|\lambda_i|}(\widehat{\mathbf{T}}_i \times \widehat{\mathbf{T}}_i')_z \mathrm{d}z, \tag{3.34}$$

$$\widetilde{\mathcal{W}}_{nl} = \sum_{i=1}^{n}\sum_{j=1}^{n}\frac{\sigma_i\sigma_j}{2\pi}\int_{z_{ij}^{min}}^{z_{ij}^{max}} \Theta_{ij}'(z)\mathrm{d}z. \tag{3.35}$$

3.2.4 The non-local contribution to $\widetilde{\mathcal{W}}$

http://news.bbc.co.uk/sport1/hi/football/8389683.stm

As an example we will consider a simple heart shaped curve (see Figure 3.4). The curve divides into four pieces, so there will be six pairs going into the double sum. First,

$$\widetilde{\mathcal{W}}_{12} = -\frac{1}{2\pi}\int_{z_C}^{z_B} \Theta_{12}'(z)\mathrm{d}z. \tag{3.36}$$

Let ϕ_B be the orientation of the tangent vector at B in the x-y plane, i.e. $\tan\phi_B = \widehat{\mathbf{T}}_{B_y}/\widehat{\mathbf{T}}_{B_x}$. Also let Θ_{PC} be the orientation of the vector pointing from P to C. Then Θ_{12} starts out pointing in the direction ϕ_B and ends pointing in the direction Θ_{PC}. Thus

$$\widetilde{\mathcal{W}}_{12} = (\Theta_{PC} - \phi_B + 2\pi w_{12}), \tag{3.37}$$

for some integer w_{12} (which keeps track of complete turns).

The remaining possibilities work in the same way, except for Θ_{14} which starts out pointing in the *opposite* direction to ϕ_A. Thus

$$\begin{aligned}
\widetilde{\mathcal{W}}_{13} &= (\Theta_{BQ} - \Theta_{PC} + 2\pi w_{13}), & (3.38)\\
\widetilde{\mathcal{W}}_{14} &= ((\phi_A \pm \pi) - \Theta_{BR} + 2\pi w_{13}), & (3.39)\\
\widetilde{\mathcal{W}}_{23} &= (\phi_c - \Theta_{BQ} + 2\pi w_{23}), & (3.40)\\
\widetilde{\mathcal{W}}_{24} &= (\Theta_{BR} - \Theta_{CS} + 2\pi w_{24}), & (3.41)\\
\widetilde{\mathcal{W}}_{34} &= (\Theta_{CS} - \phi_D + 2\pi w_{34}). & (3.42)
\end{aligned}$$

Remembering that $\widetilde{\mathcal{W}}_{21} = \widetilde{\mathcal{W}}_{12}$, the sum is

$$\widetilde{\mathcal{W}}_{nl} = \frac{1}{\pi}(\phi_A - \phi_B + \phi_C - \phi_D) + 2w \pm 1, \quad w = \sum_{i<j} w_{ij} \tag{3.43}$$

Without calculating the winding numbers w_{ij} (or worrying about the dependence of ϕ_A, ϕ_B, etc, on the position of the branch cut), it can be seen that,

$$\widetilde{\mathcal{W}}_{nl} = \frac{1}{\pi}(\phi_A - \phi_B + \phi_C - \phi_D) - 1 \pmod 2. \tag{3.44}$$

3.2.5 A generalised mod 2 expression for evaluating $\widetilde{\mathcal{W}}_{nl}$

Consider a closed spacecurve $\mathbf{x}$ which can be split into n sections, by its turning points in z, where each section covers a range $z \in [z_{min}, z_{max}]$. Note that all minima and maxima will be labelled twice, for example if section i has $\mathrm{d}s/\mathrm{d}z > 0$ then $z_i^{max} = z_{i+1}^{max}$,

Theorem 4 *Let $\phi(z_i^{min})$ and $\phi(z_i^{max})$ be the angles with respect to the x-axis of the tangent vectors $\widehat{\mathbf{T}}(z_i^{min})$ and $\widehat{\mathbf{T}}(z_i^{max})$, then*

$$\widetilde{\mathcal{W}}_{nl} = \frac{1}{2\pi}\sum_{i=1}^{n}(\phi(z_i^{min}) - \phi(z_i^{max})) - 1 \pmod 2. \tag{3.45}$$

Proof of Theorem 4 Consider the double sum of non-local terms. Some of the terms may vanish because pieces i and j may not exist at the same height z (i.e. $\sigma_i\sigma_j = 0$ everywhere). Suppose two pieces i and j do overlap in z, from some height z_{ij}^{min} up to some height z_{ij}^{max}. When we integrate over this overlap, we obtain the difference between two angles. Let Θ_{ij}^{min} and Θ_{ij}^{max} be the orientations of the relative position vectors $\mathbf{r}_{ij}(z_{ij}^{\text{min}})$ and $\mathbf{r}_{ij}(z_{ij}^{\text{max}})$ between the points $\mathbf{x}_i$ and $\mathbf{x}_j$ on the curves at these two heights. Note that $i < j$ and $\mathbf{r}_{ij}$ points from piece i to piece j. Also note that for adjoining pieces, one of the angles will be the orientation of the tangent vector at the join (for example, in Figure 3.4, $\Theta_{12}^{\text{min}} = \Theta_{PC}$ and $\Theta_{12}^{\text{max}} = \phi_B$).

With this notation

$$\widetilde{\mathcal{W}}_{ij} = \frac{\sigma_i\sigma_j}{2\pi}\int_{z_{ij}^{\text{min}}}^{z_{ij}^{\text{max}}} \Theta'_{ij}(z)\,\mathrm{d}z = \frac{\sigma_i\sigma_j}{\pi}\left(\Theta_{ij}^{\text{max}} - \Theta_{ij}^{\text{min}}\right) + w_{ij}. \tag{3.46}$$

Suppose Θ_{ij}^{max} is not a tangent vector. At least one of the points $\mathbf{x}_i^{\text{max}}$ or $\mathbf{x}_j^{\text{max}}$ is at a local maximum in z, say $\mathbf{x}_i^{\text{max}}$. This point joins piece i with either piece $i-1$ or $i+1$. Suppose it is $i+1$. Consider $\widetilde{\mathcal{W}}_{(i+1)j}$. From the previous equation, this will involve the angle $\Theta_{(i+1)j}^{\text{max}}$. This angle is measured with the same point $\mathbf{x}_i = \mathbf{x}_{i+1}$, so $\Theta_{(i+1)j}^{\text{max}} = \Theta_{ij}^{\text{max}}$. But $\sigma_{i+1} = -\sigma_i$; consequently

$$\sigma_{i+1}\sigma_j\Theta_{(i+1)j}^{\text{max}} = -\sigma_i\sigma_j\Theta_{ij}^{\text{max}} \tag{3.47}$$

and the two terms cancel.

The same would hold true if the maximum were between $i-1$ and i, or if it involved j instead of i. Also, the cancellation of Θ terms occurs at minima as well. As a result, all of the angles cancel except for the tangent vectors connecting adjoining pieces. (These do not cancel because they only appear once.)

Now, for adjoining pieces $\sigma_i\sigma_{i+1} = -1$. Let $\alpha_i = -1$ if the end of piece i is a maximum and $\alpha_i = +1$ if it is a minimum. Also the angles Θ become the orientations ϕ of tangent vectors. More precisely, except for the point joining piece 1 with the last piece $i = 2m = n$, we can write $\Theta_{i(i+1)} = \phi_{i(i+1)}$. Note that the point joining piece 1 with piece m has $\mathbf{r}_{1n}$ reversed with respect to the tangent vector. Thus $\Theta_{1n} = \phi_{n1} \pm \pi$.

Thus the non-local terms (including the winding numbers w_{ij}) sum to

$$\begin{aligned}
\widetilde{\mathcal{W}}_{nonlocal} &= \frac{1}{\pi}\sum_{i=1}^{n-1}\alpha_i\Theta_{i(i+1)} + \frac{1}{\pi}\alpha_n\Theta_{1n} + 2w && (3.48)\\
&= \frac{1}{\pi}\sum_{i=1}^{n-1}\alpha_i\phi_{i(i+1)} + \frac{1}{\pi}\alpha_n(\phi_{n1} \pm \pi) + 2w. && (3.49)
\end{aligned}$$

Now at minima $\alpha_i\phi_{i(i+1)} = \phi(z_i^{min}) = \phi(z_{i+1}^{min})$ and at maxima $\alpha_i\phi_{i(i+1)} = -\phi(z_i^{max}) = -\phi(z_{i+1}^{max})$. Taking into account the double counting,

$$\widetilde{\mathcal{W}}_{nonlocal} = \frac{1}{2\pi}\sum_{i=1}^{n}(\phi(z_i^{min}) - \phi(z_i^{max})) + (2w \pm 1). \tag{3.50}$$

Calculating mod 2 completes the theorem.

In section 5.3.4 a similar procedure is used to develop a general expression for the non-local writhing as applied to open spacecurves.

3.3 The polar writhe $\mathcal{W}_p$

Whilst $\widetilde{\mathcal{L}}$, $\widetilde{\mathcal{T}}$ and $\widetilde{\mathcal{W}}$ have been defined as quantities varying along the $\hat{z}$ axis, the above work could have been applied to an arbitrary direction $\mathbf{a}$ and still been accurate. Further, as the densities $\widetilde{\mathcal{L}}'(z)$ and $\widetilde{\mathcal{W}}'(z)$ have been consistently defined, these directional writhing and linking expressions can be applied to all open spacecurves in terms of single integrals for $z \in [z_{min}, z_{max}]$. Of particular interest in this thesis will be the directional writhing $\widetilde{\mathcal{W}}$. We make directional dependence specific by writing $\widetilde{\mathcal{W}}(a_0) = \widetilde{\mathcal{W}}(a_0, \hat{a})$ as the directional writhing of a curve $\mathbf{x}$, below a_0, along the direction $\hat{a}$. We choose to call this framework for evaluating writhing the *Polar writhe*, which relates to the unit sphere interpretation of this quantity. We shall cover the unit sphere interpretations in section 3.3.1 for closed curves, and section 5.3 for open curves. Of course the term directional writhe may well have been more appropriate, however this term was used by Fuller in [45] for the quantity defined in section 1.5.1.

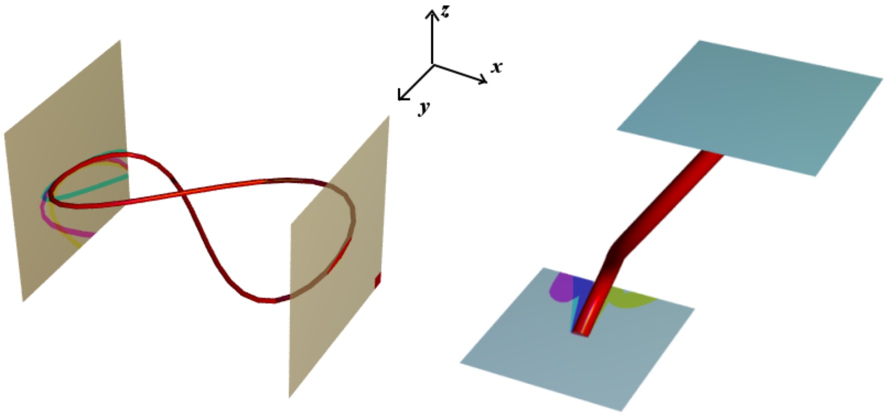

Figure 3.5: Examples of both closed and open curve sections bound between parallel planes. The closed curve is parameterised as $\mathbf{x}(t) = (-6\cos 2\pi t, 3\sin 4\pi t, \sin 2\pi t)$ and can be bound between planes at $x = -1$ and $x = 1$. The open curve is parameterised as $\mathbf{x}(t) = (4t^2, \sin 2\pi t, 4e^t)$, and is bound between planes at $z = 0$ and $z = 4e$.

In this thesis all open, finite, curves can be defined as lying in between two parallel planes, along a specific direction. For example the closed curve depicted in Figure 3.5 can be bound between two planes $x = x_{min}$ and $x = x_{max}$, representing the minimum and maximum x values obtained by the curve. The open curve is bound between two planes of minimum and maximum z values.

Definition *Polar writhe* $\mathcal{W}_p$

The polar writhe of a curve $\mathbf{x}$ (open or closed), is defined along a direction $\hat{a}$. Suppose the curve has minimum and maximum values along a of a_{min} and a_{max}. Then,

$$\mathcal{W}_p(\mathbf{x}, \hat{a}) = \widetilde{\mathcal{W}}(a_{min}, a_{max}, \hat{a}) = \widetilde{\mathcal{W}}(a_{max}, \hat{a}) - \widetilde{\mathcal{W}}(a_{min}, \hat{a}). \tag{3.51}$$

This expression can be split into its local $\mathcal{W}_{pl}$ and non-local components $\mathcal{W}_{pnl}$

$$\begin{aligned} \mathcal{W}_p(\mathbf{x}, \hat{a}) &= \mathcal{W}_{pl}(a_{min}, a_{max}, \hat{a}) + \mathcal{W}_{pnl}(a_{min}, a_{max}, \hat{a}), && (3.52) \\ \mathcal{W}_{pl} &= \frac{1}{2\pi}\sum_{i=1}^{n}\int_{a_{min}}^{a_{max}} \frac{1}{1+|\lambda_i^a|}(\widehat{\mathbf{T}}_i \times \widehat{\mathbf{T}}_i')_a \mathrm{d}a, && (3.53) \\ \mathcal{W}_{pnl} &= \sum_{i=1}^{n}\sum_{j=1}^{n}\frac{\sigma_i\sigma_j}{2\pi}\int_{a_{ij}^{min}}^{a_{ij}^{max}} \Theta_{ij}'(a)\mathrm{d}a, && (3.54) \end{aligned}$$

where $\lambda^a = \widehat{\mathbf{T}}_a\ (\hat{a} \cdot \widehat{\mathbf{T}})$,

$$\Theta'_{ij}(a) = \frac{\mathrm{d}\Theta}{\mathrm{d}a} = \frac{\hat{a} \cdot \mathbf{r}_{ij}(a) \times \mathbf{r}'_{ij}(a)}{|\mathbf{r}_{ij}|^2}, \tag{3.55}$$

and $\mathbf{r}_{ij}(a) = \mathbf{y}(a) - \mathbf{x}(a)$.

This notation will hereafter replace $\widetilde{\mathcal{W}}$ for all spacecurves, both open and closed. Further, the majority of discussion concerning the polar writhe will use $\hat{z}$ as the default choice of direction, thus $\mathcal{W}_p(\mathbf{x}) \equiv \mathcal{W}_p(\mathbf{x}, \hat{z})$, will be used as short hand notation.

3.3.1 Properties of the polar writhe of closed spacecurves

The polar writhe, as applied to a closed spacecurves $\mathbf{x}$, has the following properties.

- $\mathcal{W}_p$ is equivalent to $\mathcal{W}$ (as defined by (1.19)) and hence has all its properties.
- Because of the modulus in the denominator of (3.53), $\mathcal{W}_p$ does not suffer a singularity.
- $\mathcal{W}_{pl}$ will register the same value for a section $\mathbf{x}_i$ upon a reversal of orientation.

These properties can be demonstrated using the tantrix sphere interpretations of $\mathcal{W}_p$, $\mathcal{W}_{pl}$ and $\mathcal{W}_{pnl}$. As a default the discussion will employ the directional choice $\hat{z}$ and refer to other directions when necessary.

3.3.2 Unit sphere interpretation of $\mathcal{W}_{pl}$

$\mathcal{W}_{pl}$ represents the area enclosed by the tantrix curve $\widehat{\mathbf{T}}_{\mathbf{x}}$ and one of the tantrix sphere poles. If the section of curve has a positive $\hat{z}$ gradient, the area will be that enveloped by the section's tantrix curve, which is bound between the points $\widehat{\mathbf{T}}_{z_{ij}^{min}}$ and $\widehat{\mathbf{T}}_{z_{ij}^{max}}$, and two geodesic lines joining these points to the north pole (see Figure 3.6 for an example). Any sections of negative gradient will be those bound between the tantrix curve and the south pole (see Figure 3.6), that is

$$\mathcal{W}_{pl} = \sum_{i=1}^{n} \frac{1}{2\pi} \int_{z_{ij}^{min}}^{z_{ij}^{max}} (1 - \mid \cos\theta(z) \mid) \frac{\mathrm{d}\phi(z)}{\mathrm{d}z} \mathrm{d}z. \tag{3.56}$$

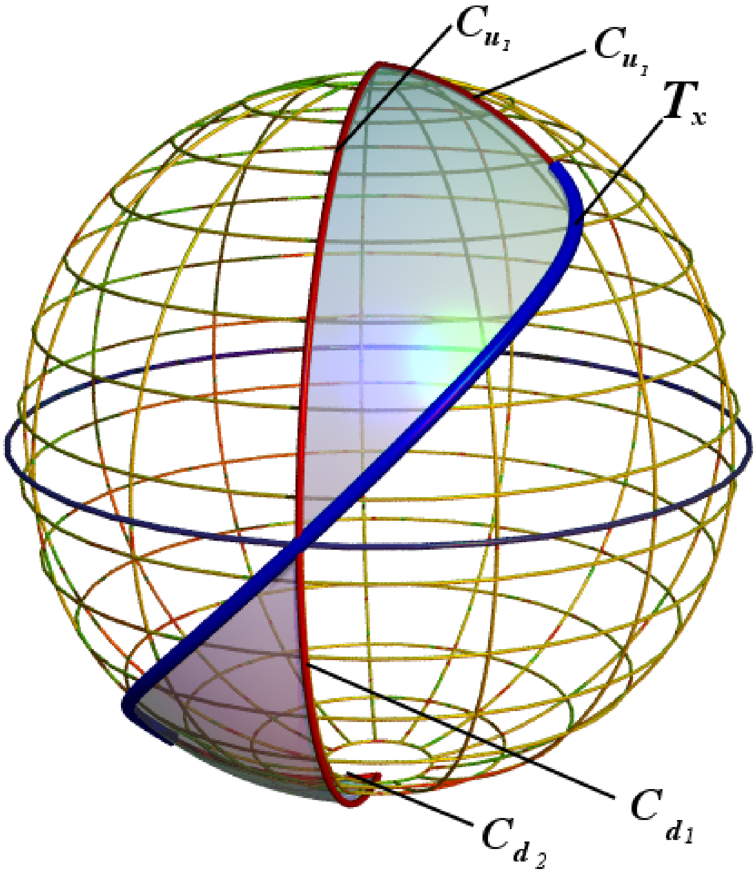

Figure 3.6: The unit sphere interpretation of $\mathcal{W}_{pl}(\mathbf{x})$ for the curve $\mathbf{x} = (t, \frac{1}{2}\sin \pi t, 2.5t(1-t))$ (depicted in Figure 1.27). The tantrix curve is depicted on the sphere's surface. For $t \in [0, 0.5]$ the tantrix curve lies in the northern hemisphere, and $\mathcal{W}_{pl}(\mathbf{x})$ represents the spherical area bound by the geodesic curve sections $\mathcal{C}_{u_1}$ and $\mathcal{C}_{u_2}$, joining $\widehat{\mathbf{T}}_{\mathbf{x}}(0)$ and $\widehat{\mathbf{T}}_{\mathbf{x}}(0.5)$ to the north pole. For the period $t \in [0.5, 1]$, $\mathcal{W}_{pl}(\mathbf{x})$ is represented as the area bound by the tantrix curve and geodesic arcs joining $\widehat{\mathbf{T}}_{\mathbf{x}}(0.5)$ and $\widehat{\mathbf{T}}_{\mathbf{x}}(1)$ to the south pole ($\mathcal{C}_{d_1}$ and $\mathcal{C}_{d_1}$ respectively).

This can be demonstrated by considering a single section of spacecurve $\mathbf{x}$ for which $\frac{\mathrm{d}s}{\mathrm{d}z} > 0$. Recalling that $T_z = \lambda = \cos\theta$; thus θ gives the co-latitude of the tantrix sphere.

$$\widehat{\mathbf{T}}'\mathrm{d}z = \mathrm{d}\widehat{\mathbf{T}} = \mathrm{d}\theta\ \hat{\theta} + \sin\theta\mathrm{d}\phi\ \hat{\phi}. \tag{3.57}$$

Also $\hat{z} \times \widehat{\mathbf{T}} = \sin\theta\ \hat{\phi}$ giving

$$(\widehat{\mathbf{T}} \times \widehat{\mathbf{T}}') \cdot \hat{z}\mathrm{d}z = \hat{z} \times \widehat{\mathbf{T}} \cdot \widehat{\mathbf{T}}'\mathrm{d}z = \sin^2\theta\mathrm{d}\phi, \tag{3.58}$$

and so (3.53) gives

$$\begin{aligned} 2\pi\mathcal{W}_{pl}' &= \frac{1}{(1+|\cos\theta|)}\sin^2\theta\frac{\mathrm{d}\phi}{\mathrm{d}z} && (3.59)\\ &= (1-|\cos\theta|)\frac{\mathrm{d}\phi}{\mathrm{d}z}; && (3.60)\\ \Rightarrow 2\pi\mathcal{W}_{pl} &= \int_{z_0}^{z_1}(1-|\cos\theta|)\frac{\mathrm{d}\phi}{\mathrm{d}z}\mathrm{d}z. && (3.61) \end{aligned}$$

Clearly for $\theta < \pi/2$ the area is bound with the north pole, and for $\theta < \pi/2$ the area is anchored at the south pole.

Consider a section of spacecurve $\mathbf{x}_i(z)$. Reversing the orientation of this curve will lead to the same $\mathcal{W}_{pl}$ evaluation. This is because the $\cos(\theta)$ contribution is of absolute value, rendering $\mathcal{W}_{pl}$ invariant to the transformation $s \rightarrow -s$. Compare this to the tantrix interpretation of $\mathcal{W}_z$ (2.12); where $\cos(\theta)$ is not of absolute value. As a result southern polar contributions hold greater weight for $\mathcal{W}_z$. It is clear this lack of directional bias, inherent to $\mathcal{W}_{pl}$, is a desirable property. The local writhing should be the same for sections of curve with the same degree of torsion (in terms of the Frenet frame), of the direction it travels along $\hat{z}$.

3.3.3 A unit sphere interpretation $\mathcal{W}_{pnl}$

The interpretation of $\mathcal{W}_{pnl}$ is very similar to that of $\widetilde{\mathcal{L}}$ except that each turning point orientation $\phi(z_i)$ is counted twice (with the same sign). With this in mind $\mathcal{W}_{pnl}$ can be interpreted as the sum of areas bound between the longitudinal lines at $\phi = \phi(z_i^{min})$ and $\phi = \phi(z_i^{max})$. This area can either cover an area containing the tantrix curve lying in the northern hemisphere, or alternatively the southern hemisphere. This choice may seem arbitrary, but as will be demonstrated in the following section, it will be useful in making comparisons between $\mathcal{W}_p$ and $\mathcal{W}$.

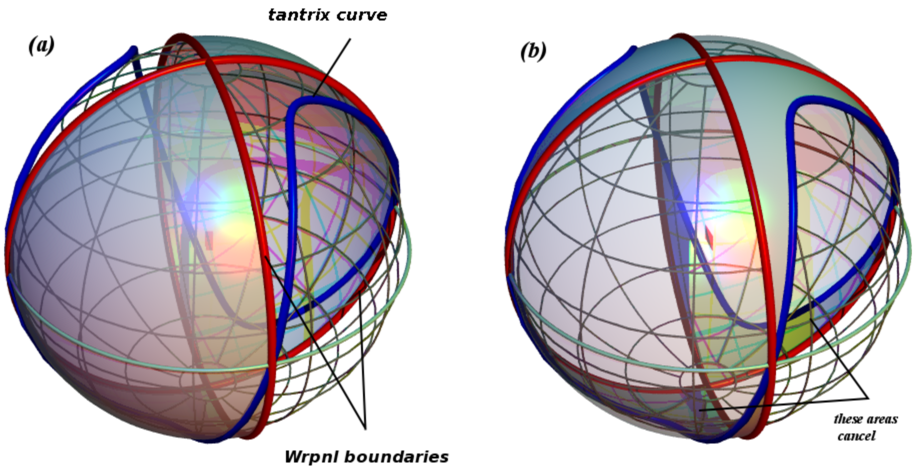

Figure 3.7: Figure (a) is an example of a tantrix curve and its geometric $\mathcal{W}_{pnl}$ contribution (assuming we confine it to the southern hemisphere). On the right the opaque areas mark out the contributions to $\mathcal{W}_{pl}$. Mapped onto this as a transparent area is the $\mathcal{W}_{pnl}$ contributions from the left figure. We note, as the two cancel where they meet, the area left is that bound between the tantrix curve and the north pole.

3.3.4 A comparison between the polar writhe and Fuller writhing expressions

$\mathcal{W}_p$ and Fuller's 1st theorem

It can be demonstrated, with a little effort, that the tantrix sphere interpretation of $\mathcal{W}_p$ matches that of (1.26), as long as $\mathcal{W}_p$ is evaluated mod 2. In evaluating $\mathcal{W}_{pl}$ the tantrix sphere interpretation is split into single-hemispherical sections by the turning points of $\mathbf{x}(z)$, which lie on the equator. These points are also the geodesic boundaries of the $\mathcal{W}_{pnl}$ contributions. We choose the $\mathcal{W}_{pnl}$ areas to correspond to the tantrix curve lying in the southern hemisphere. These areas will be of opposite sign and thus where they meet will cancel each other out. As demonstrated in Figure 2.2 the product of this cancellation is the area bound between $\widehat{\mathbf{T}}_{\mathbf{x}}$ and the north pole. This will be equivalent to $\mathcal{A}$ in (1.26) when evaluated mod 4π. Taking into account the -1 in (3.45), which represents the full non-local winding of the curve between its start and end points, we have thus matched the geometrical interpretation of $\mathcal{W}_p$ to that of (1.26).

Further if we ignore the non-local winding between the start and end points, we are left the area bound by the tantrix curve and the north pole, the unit sphere interpretation of $\mathcal{W}_z$. Thus it can be concluded that

$$\mathcal{W}_p(\mathbf{x}) \equiv \mathcal{W}_z(\mathbf{x}) - 1 \pmod 2. \tag{3.62}$$

These two results hold for an arbitrary directional parameterisation. For an arbitrary orientation $\hat{a}$ the boundary between *northern* and *southern* polar contributions are rotated from the equator such that the new boundary is defined by the plane perpendicular to $\hat{a}$. The poles to which the geodesic closures point are altered by the same transformation. The new tantrix curve can be obtained from $\widehat{\mathbf{T}}_{\mathbf{x}}(z)$ by rotating it through the same transformation which maps the new equator from the standard one. Thus we see the overall $\mathcal{W}_p$ interpretation for an arbitrary direction $\hat{a}$ can be defined by rotating the corresponding $\hat{z}$ area through the set of Euler angles required to map $\hat{z}$ to $\hat{a}$. Thus we can conclude the total signed area bound on the sphere's surface is the same as that of the $\hat{z}$ parameterisation.

A comparison between $\mathcal{W}_p$ and Fuller's second theorem

Consider a ribbon or tube, it may be desirable to define the $\mathcal{W}_p$ of $\mathbf{y}$ (lying on the tubes surface) along the direction of the axis $\mathbf{x}$. We can attempt to define such a measurement by replacing the arbitrary fixed direction $\hat{a}$ with the variable direction $\hat{b}$ which is defined by $\widehat{\mathbf{T}}_{\mathbf{x}}(s)$. Such a calculation however would prove exceptionally complicated when attempting to define $\mathcal{W}_{pnl}$. The direction of evaluation is constantly changing, thus turning points and hence regions for which non-local writhe exists is also constantly changing, making the consistent definition of self-winding sections difficult. The evaluation of $\mathcal{W}_{pl}$ however is not so complex and can be represented by a single integral expression. Further this expression shall be shown to be identical to (1.27) (when the non-opposition condition is satisfied) and represents the difference between $\mathcal{W}(\mathbf{y})$ and $\mathcal{W}(\mathbf{x})$. This, coupled with (3.62) demonstrates that the Fuller writhing expressions arise as a local subset of the polar writhe structure, at least for closed spacecurves. First we present a simple unit sphere demonstation (section 3.3.4). Then a more rigorous derivation, in terms of a *tertiary ribbon* is detailed.

A unit sphere interpretation

Consider a single point on the ribbon $R(\mathbf{x}, \mathbf{y})$ at $t = c$. The direction of $\mathbf{x}$ at this point is given by $\widehat{\mathbf{T}}_{\mathbf{x}}(c)$ and the direction of $\mathbf{y}$ is given by $\widehat{\mathbf{T}}_{\mathbf{y}}(c)$. Next consider a point

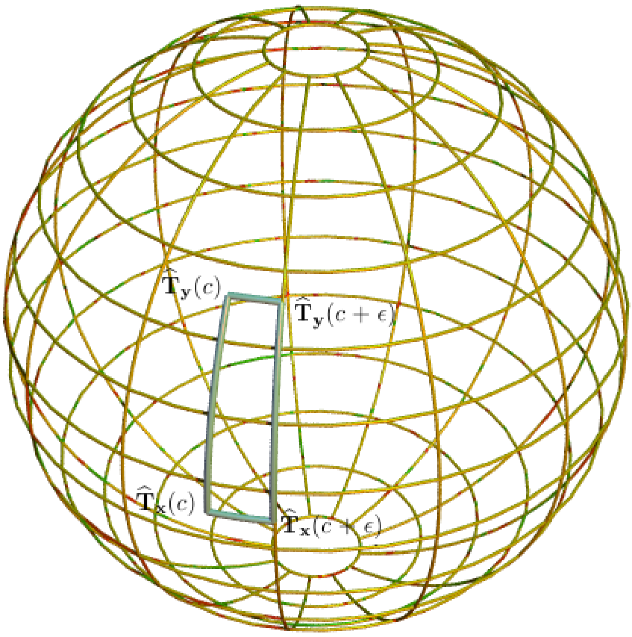

Figure 3.8: A representation of the area bound, on the unit sphere surface, between points $\widehat{\mathbf{T}}_{\mathbf{x}}(c)$, $\widehat{\mathbf{T}}_{\mathbf{y}}(c)$, $\widehat{\mathbf{T}}_{\mathbf{x}}(c+\epsilon)$ and $\widehat{\mathbf{T}}_{\mathbf{y}}(c+\epsilon)$. In the limit $\epsilon \to 0$ this area tends to the geodesic arc joining $\widehat{\mathbf{T}}_{\mathbf{x}}(c)$ to $\widehat{\mathbf{T}}_{\mathbf{y}}(c)$.

$c+\epsilon$, giving the direction of $\mathbf{x}$ as $\widehat{\mathbf{T}}_{\mathbf{x}}(c+\epsilon)$ and the direction of $\mathbf{y}$ is $\widehat{\mathbf{T}}_{\mathbf{y}}(c+\epsilon)$. The four points bound a spherical area on the surface of the unit sphere as demonstrated in Figure 3.8. In the limit $\epsilon \rightarrow 0$ this area will tend to a great arc section of curve joining $\widehat{\mathbf{T}}_{\mathbf{y}}(c)$ to $\widehat{\mathbf{T}}_{\mathbf{x}}(c)$, which is equivalent to an instantaneous measurement of the polar writhe of the curve at c along the direction $\widehat{\mathbf{T}}_{\mathbf{x}}$. Applying this logic over $t \in [0, L]$ will leave an area drawn out by the set of great arc sections joining $\widehat{\mathbf{T}}_{\mathbf{y}}$ to $\widehat{\mathbf{T}}_{\mathbf{x}}$. This interpretation matches (1.27) as required.

It is interesting to note this interpretation holds true for non-closed tubes or ribbons. This idea has been considered by van der Heijden *et al* [114], who discuss a planar closure, for a ribbon, which allows (1.27) to be applied to a subset of open spacecurves. Our new result would suggest a closure could be constructed for an increased set of open spacecurves (those which can be closed using a non planar curve section), which would lead to a consistent definition of $\mathcal{W}$ (assuming the non-opposition condition is not violated). Such a closure will be detailed in section 5.2.

A more rigorous demonstration

Consider a ribbon $R(\mathbf{x}, \mathbf{v})$. We wish to evaluate the local writhing of $\mathbf{y}$ along the directional vector $\hat{b}$, where $\hat{b} = \widehat{\mathbf{T}}_{\mathbf{x}}(t)$. In order to do this a tertiary curve $\mathbf{z}(t)$ is defined, which surrounds $\mathbf{y}$ as shown in Figure 3.9. Defining $\mathbf{z}$ in terms of t as $\mathbf{z}(t) = \mathbf{y}(t) + \mathbf{v}_{\mathbf{y}}(t)$ we create a second ribbon $R(\mathbf{y}, \mathbf{v}_{\mathbf{y}})$ which we shall use to develop an expression for $\mathcal{W}_{pl}(\mathbf{x}, \hat{b})$. We start by defining $\mathbf{v}_{\mathbf{y}}$

$$\mathbf{v}_{\mathbf{y}}(t) = \hat{b}(t) \times \widehat{\mathbf{T}}(t), \tag{3.63}$$

$$\mathbf{v}'_{\mathbf{y}}(t) = \hat{b}(t) \times \widehat{\mathbf{T}}'(t) + \hat{b}'(t) \times \widehat{\mathbf{T}}(t). \tag{3.64}$$

When defining $\mathcal{W}_p$ along a specific Cartesian direction we note that the term $\hat{b}'(t) \times \widehat{\mathbf{T}}(t)$ would equate to zero. However this is not the case when the direction itself changes smoothly. Substituting (3.63) and (3.64) into (1.23) we can obtain an expression for $\mathcal{T}(R(\mathbf{y}, \mathbf{v}_{\mathbf{y}}), \hat{b})$

$$\widetilde{\mathcal{T}}(R(\mathbf{y}, \mathbf{v}_{\mathbf{y}}), \hat{b}) = \frac{1}{2\pi}\int_{t_1}^{t_2} \frac{\widehat{\mathbf{T}}_{\mathbf{y}}(t) \cdot (\hat{b}(t) \times \widehat{\mathbf{T}}_{\mathbf{y}}(t)) \times (\hat{b}(t) \times \widehat{\mathbf{T}}'_{\mathbf{y}}(t))}{\mid \hat{b}(t) \times \widehat{\mathbf{T}}_{\mathbf{y}}(t) \mid^2} \mathrm{d}t \tag{3.65}$$

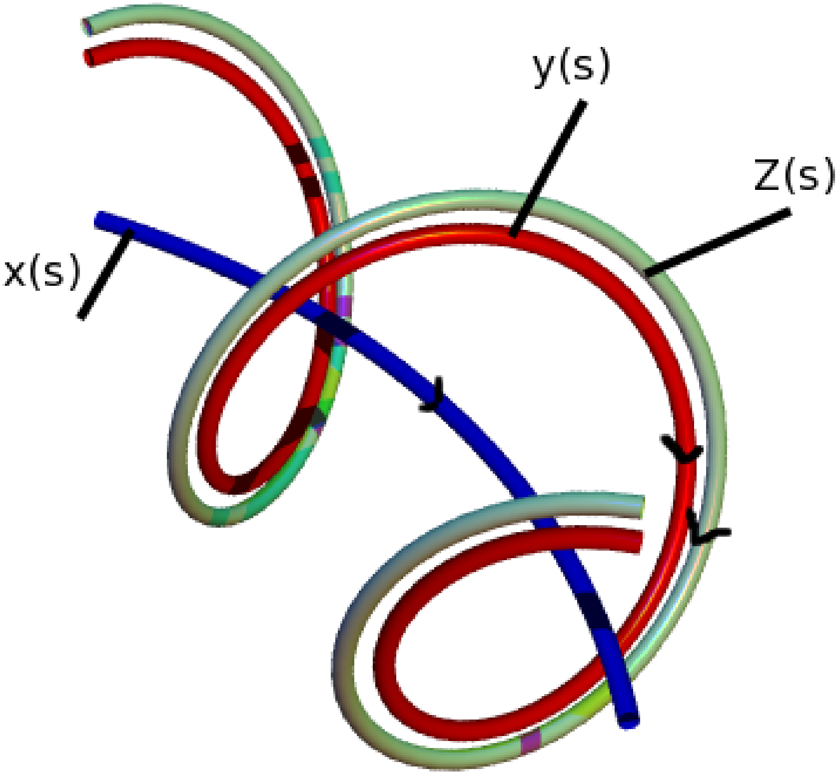

Figure 3.9: The "tertiary ribbon" used to define $\mathcal{W}_{pl}(\mathbf{y}, \widehat{\mathbf{T}}_{\mathbf{x}})$.

$$
\begin{aligned}
+ &\quad \frac{1}{2\pi}\int_{t_1}^{t_2} \frac{\widehat{\mathbf{T}}_{\mathbf{y}}(t)\cdot(\hat{b}(t)\times\widehat{\mathbf{T}}_{\mathbf{y}}(t))\times(\hat{b}'(t)\times\widehat{\mathbf{T}}_{\mathbf{y}}(t))}{\mid \hat{b}(t)\times\widehat{\mathbf{T}}_{\mathbf{y}}(t)\mid^2}\mathrm{d}t, \quad (3.66)\\
= &\quad \frac{1}{2\pi}\int_{t_1}^{t_2} \frac{(\widehat{\mathbf{T}}_{\mathbf{y}}(t)\cdot\hat{b}(t))(\hat{b}(t)\cdot\widehat{\mathbf{T}}_{\mathbf{y}}(t)\times\widehat{\mathbf{T}}'_{\mathbf{y}}(t))}{\mid \hat{b}(t)\times\widehat{\mathbf{T}}_{\mathbf{y}}(t)\mid^2}\mathrm{d}t \quad (3.67)\\
- &\quad \frac{1}{2\pi}\int_{t_1}^{t_2} \frac{(\widehat{\mathbf{T}}_{\mathbf{y}}(t)\cdot\hat{b}(t)\times\hat{b}'(t))}{\mid \hat{b}(t)\times\widehat{\mathbf{T}}_{\mathbf{y}}(t)\mid^2}\mathrm{d}t. \quad (3.68)
\end{aligned}
$$

Substituting (3.63) and (3.64) into (3.2) we obtain an expression for $\widetilde{\mathcal{L}}_{local}(R(\mathbf{y},\mathbf{z}),\hat{b})$

$$
\begin{aligned}
\widetilde{\mathcal{L}}_{local}(R(\mathbf{y},\mathbf{z}),\hat{b}) &= \frac{1}{2\pi}\int_{t_1}^{t_2} \frac{\hat{b}(t)\cdot(\hat{b}(t)\times\widehat{\mathbf{T}}_{\mathbf{y}}(t))\times(\hat{b}(t)\times\widehat{\mathbf{T}}_{\mathbf{y}}(t))}{\mid \hat{b}(t)\times\widehat{\mathbf{T}}'_{\mathbf{y}}(t)\mid^2}\mathrm{d}t \quad (3.69)\\
&+ \frac{1}{2\pi}\int_{t_1}^{t_2} \frac{\hat{b}(t)\cdot(\hat{b}(t)\times\widehat{\mathbf{T}}_{\mathbf{y}}(t))\times(\hat{b}'(t)\times\widehat{\mathbf{T}}_{\mathbf{y}}(t))}{\mid \hat{b}(t)\times\widehat{\mathbf{T}}_{\mathbf{y}}(t)\mid^2}\mathrm{d}t, \quad (3.70)\\
&= \frac{1}{2\pi}\int_{t_1}^{t_2} \frac{(\hat{b}(t)\cdot\widehat{\mathbf{T}}_{\mathbf{y}}(t)\times\widehat{\mathbf{T}}'_{\mathbf{y}}(t))}{\mid \hat{b}(t)\times\widehat{\mathbf{T}}_{\mathbf{y}}(t)\mid^2}\mathrm{d}t \quad (3.71)\\
&- \frac{1}{2\pi}\int_{t_1}^{t_2} \frac{(\hat{b}(t)\cdot\widehat{\mathbf{T}}_{\mathbf{y}}(t))(\widehat{\mathbf{T}}(t)\cdot\hat{b}(t)\times\hat{b}'(t))}{\mid \hat{b}(t)\times\widehat{\mathbf{T}}_{\mathbf{y}}(t)\mid^2}\mathrm{d}t. \quad (3.72)
\end{aligned}
$$

Substituting these expressions into (3.18), and integrating, gives

$$
\begin{aligned}
\mathcal{W}_{pl}(\mathbf{y}) &= \widetilde{\mathcal{L}}_{local}(R(\mathbf{y},\mathbf{z}),\hat{b}) - \widetilde{\mathcal{T}}(R(\mathbf{y},\mathbf{v}_{\mathbf{y}}),\hat{b}), \quad (3.73)\\
&= \frac{1}{2\pi}\int_{t_1}^{t_2} \frac{(1-\widehat{\mathbf{T}}_{\mathbf{y}}(t)\cdot\hat{b}(t))(\hat{b}(t)\cdot\widehat{\mathbf{T}}_{\mathbf{y}}(t)\times\widehat{\mathbf{T}}'_{\mathbf{y}}(t))}{\mid \hat{b}(t)\times\widehat{\mathbf{T}}_{\mathbf{y}}(t)\mid^2}\mathrm{d}t \quad (3.74)\\
&+ \frac{1}{2\pi}\int_{t_1}^{t_2} \frac{(1-\hat{b}(t)\cdot\widehat{\mathbf{T}}_{\mathbf{y}}(t))(\widehat{\mathbf{T}}_{\mathbf{y}}(t)\cdot\hat{b}(t)\times\hat{b}'(t))}{\mid \hat{b}(t)\times\widehat{\mathbf{T}}_{\mathbf{y}}(t)\mid^2}\mathrm{d}t. \quad (3.75)
\end{aligned}
$$

This can be rearranged to the following single expression

$$
\mathcal{W}_{pl}(\mathbf{y}(t),\hat{b}) = \frac{1}{2\pi}\int_{t_1}^{t_2} \frac{(1-\hat{b}(t)\cdot\widehat{\mathbf{T}}_{\mathbf{y}}(t))((\hat{b}(t)\times\widehat{\mathbf{T}}_{\mathbf{y}}(t))\cdot(\hat{b}'(t)+\widehat{\mathbf{T}}'_{\mathbf{y}}(t)))}{\mid \hat{b}(t)\times\widehat{\mathbf{T}}_{\mathbf{y}}(t)\mid^2}\mathrm{d}t. \quad (3.76)
$$

Noting that

$Ref.[112]”DNAsupercoilingaglobaltranscriptionalregulatorfor > enterobacterialgrowth?” > -$

and substituting this into (3.76) we recover the required expression:

$$\begin{aligned}\mathcal{W}_{pl}(\mathbf{y},\hat{b}) &= \frac{1}{2\pi}\int_{t_1}^{t_2}\frac{(1-\hat{b}(t)\cdot\widehat{\mathbf{T}}_{\mathbf{y}}(t))(\hat{b}(t)\times\widehat{\mathbf{T}}_{\mathbf{y}}(t))\cdot(\hat{b}'(t)+\widehat{\mathbf{T}}'_{\mathbf{y}}(t))}{1-(\hat{b}(t)\cdot\widehat{\mathbf{T}}_{\mathbf{y}}(t))^2}\mathrm{d}t \quad (3.79)\\ &= \frac{1}{2\pi}\int_{t_1}^{t_2}\frac{(\hat{b}(t)\times\widehat{\mathbf{T}}_{\mathbf{y}}(t))\cdot(\hat{b}'(t)+\widehat{\mathbf{T}}'_{\mathbf{y}}(t))}{1+(\hat{b}(t)\cdot\widehat{\mathbf{T}}_{\mathbf{y}}(t))}\mathrm{d}t. \quad (3.80)\end{aligned}$$

The right hand side of (3.79) is identical to (1.27) (with $\widehat{\mathbf{T}}_0 = \mathbf{b}$ and $\widehat{\mathbf{T}}_1 = \widehat{\mathbf{T}}_y$). This suggest that $\mathcal{W}_{pl}(\mathbf{y},\widehat{\mathbf{T}}_{\mathbf{x}}) = \mathcal{W}(\mathbf{y}) - \mathcal{W}(\mathbf{x})$. It is important to state, however, this is only true if non-opposition condition is satisfied for the full set of ambient isotopies linking $\mathbf{x}$ and $\mathbf{y}$.

An evaluation of $\mathcal{W}(\mathbf{x})$ can be obtained by choosing a planar reference curve as the smoothly altering direction of evaluation. Consider a closed spacecurve $\mathbf{x}$ and a reference curve $\mathbf{x}_{ref}$ (planar such that $\mathcal{W}(\mathbf{x}_{ref}) = 0$). Assuming the non-opposition condition is satisfied, for the full set of ambient isotopies linking $\mathbf{x}_{ref}$ to $\mathbf{x}$, the following is true

$$\mathcal{W}(\mathbf{x}) = \mathcal{W}_{pl}(\mathbf{x},\widehat{\mathbf{T}}_{\mathbf{x}_{ref}}). \quad (3.81)$$

3.3.5 Conclusions regarding the polar writhe and closed spacecurves

Ref.[112] "DNA supercoiling a global transcriptional regulator for ¿ enterobacterial growth?" ¿ -¿ "DNA supercoiling - a global transcriptional regulator for ¿ enterobacterial growth?" ¿ Remove the comma after "Rev". To summarise, for closed spacecurves we can conclude the following for the writhing of closed curves

$$\begin{aligned}\mathcal{W}_p(\mathbf{x},\hat{a}) &= \mathcal{W}(\mathbf{x}), \quad (3.82)\\ \mathcal{W}_p(\mathbf{x}) &= \mathcal{W}_z(\mathbf{x}) - 1 \pmod{2}), \quad (3.83)\end{aligned}$$

which is true for all $\hat{a}$.

$\mathcal{W}_p$ and $\mathcal{W}$

The polar writhe formulation has several advantages over $\mathcal{W}$ (as evaluated by (1.19)), as applied to closed curves. The first is simply that $\mathcal{W}_p$ is a single integral calculation, as opposed to the double integral (1.19). The calculation is of the order $(n + nl^2)$ where l represents the number of sections in to which the curve is split and n the number of evaluation points. This will in general represent an improvement on the Agarwal *et al* [4] method which is of the order $\approx n^{1.6}$. $\mathcal{W}_p$ can then be used as a numerically efficient method for evaluating $\mathcal{W}$.

Secondly by splitting the polar writhe into local and non-local components an extra degree of information is obtained. It is possible to imagine a curve whose $\mathcal{W}$ is zero, for which $\mathcal{W}_{pl} = \mathcal{W}_{pnl}$. Using a simple $\mathcal{W}$ evaluation it is impossible to discern between a curve with a great amount of local and non-local writhing and a planar curve. Applying the polar writhe framework this discrepancy will become apparent. For example consider the curve depicted in Figure 5.5. If the planar section of curve lying below the plane marked in the diagram is made arbitrarily small then the contribution to $\mathcal{W}_p$ from the section below the plane reduces to zero (see section 4.6 for details). For a specific height h the local and non-local components of $\mathcal{W}_p$ are equal and opposite thus $\mathcal{W}_p = 0$ (see section 5.3.5). In such a scenario the $\mathcal{W}$ of the fully closed curve will also be zero, however by employing the polar writhe methodology we have gained an extra level of insight of the curve's nature.

$\mathcal{W}_p$ and the local writhing expressions

Here by local writhing expression we mean both the Fuller writhe expressions (1.26) and (1.27), as well as $\mathcal{W}_{fz}$.

The one obvious major advantage is that the polar writhe is equal to $\mathcal{W}$ exactly, not mod 2. Secondly $\mathcal{W}_p$ does not suffer the existence of a limitation equivalent to the non-opposition condition.

However there is one very important point which must be highlighted. The polar writhe does not, in general, represent an analytically tractable expression. The need for an algorithm which breaks the curve into sections by its turning points prevents this. The analytical tractability inherent to the local writhing expressions is key to their popularity in statistical mechanical models (Bouchiat and Mézard [17], van der Heijden *et al* [114], Samuel *et al* [96]).

Chapter 4

A comparison of writhing expressions for open spacecurves

In the previous chapters we detailed the properties of $\mathcal{W}$, $\mathcal{W}_z$ and $\mathcal{W}_p$, for closed spacecurves. In this chapter we show, using a set of example curves, that these three expressions generally give different answers for open spacecurves. Using both the unit sphere interpretation, and a set of instructive example studies, it will be demonstrated that none of the writhing expressions share a consistent quantitative relationship. Instead a set of qualitative relationships are outlined. We will emphasise the importance of the degree of directionality of the curve. Further $\mathcal{W}_z$ is shown to be generally an inappropriate measure of the writhing of open spacecurves.

Before proceeding we note that Rossetto and Maggs [92] and van der Heijden al [114] have already demonstrated that for open spacecurves, $\mathcal{W}_z$ and $\mathcal{W}$ are not, in general, equal. So we consider only the relationships between $\mathcal{W}_p$ and the two alternate expressions.

In what follows several example curve studies will be detailed. The writhing of these curves will be evaluated as dsicretised approximations to the actual parameterised curves, with each curve split into 1000 equal length, piecewise linear sections. Details of the algorithms used to perform these evaluations for each writhing expression can be found in the appendix (sections B.1-B.3)

4.1 A comparison between $\mathcal{W}_p$ and $\mathcal{W}_z$

Using the notation defined in section 3.2.2, we can re-write (2.12) as

$$\mathcal{W}_z = \frac{1}{2\pi}\int \frac{1}{1+\lambda(t)}(\widehat{\mathbf{T}}(t)\times\widehat{\mathbf{T}}'(t))\mathrm{d}t, \tag{4.1}$$

where $\lambda = \cos\theta = \widehat{\mathbf{T}}_z$. This result looks superficially similar to (3.53) with $\hat{a} = \hat{z}$, with the difference being the absolute value of $|\lambda|$ not present in (4.1). For sections of tantrix curve lying in the northern hemisphere, the two interpretations will be equivalent: both measure the spherical area between the tantrix curve and the north pole. The difference manifests itself for sections of tantrix curve traversing the southern hemisphere. In such regions $\mathcal{W}_z$ still evaluates the spherical area bound between the tantrix curve and the northern hemisphere. For $\mathcal{W}_{pl}$ the absolute sign ensures it is the area bound between the tantrix curve and the south pole. As a result $\mathcal{W}_z$ will give greater weighting to sections of curve which are traveling downwards in comparison to $\mathcal{W}_{pl}$. This can be seen by comparing Figures 1.28 and 3.6, which represent unit sphere interpretations of $\mathcal{W}_{pl}$ and $\mathcal{W}_z$ for the same curve.

The difference becomes most apparent if we consider an almost vertical section of curve with small wiggles. For upwards travelling curves the tantrix curve will be close to the north pole and hence sweep out a small area inbetween. Both expressions will agree in this case. But what if the wiggles are such that the curve has sections which point almost vertically downwards ? The local contribution to $\mathcal{W}_{pl}$ writhe will still report a small contribution, assuming the wiggles are small. $\mathcal{W}_z$ however will assign such sections a large contribution to the overall measure. Maggs 2001 [69] an Rossetto and Maggs 2003 [92] have shown that statistical distributions of $\mathcal{W}_z$, can be strongly affected by fluctuations near the south pole. A further issue results from the non-local windings of $\mathcal{W}_{pnl}$ which are ignored by $\mathcal{W}_z$. The following case study highlights this issue.

Case study: a vertically contorted curve

We wish to consider a section of curve which evolves from pointing vertically along $\hat{z}$, such that a kink forms at its middle section (in terms of its height). This will coax its tantrix curve to venture into the southern polar regions. This will allow us to characterise the behavior of $\mathcal{W}_p$ and $\mathcal{W}_z$ under such conditions, emphasising the effect of non-local windings. We can define such a curve (which we call it *polcv*, short for polar curve, as its endpoints always point along $\hat{z}$), using the following parametric set

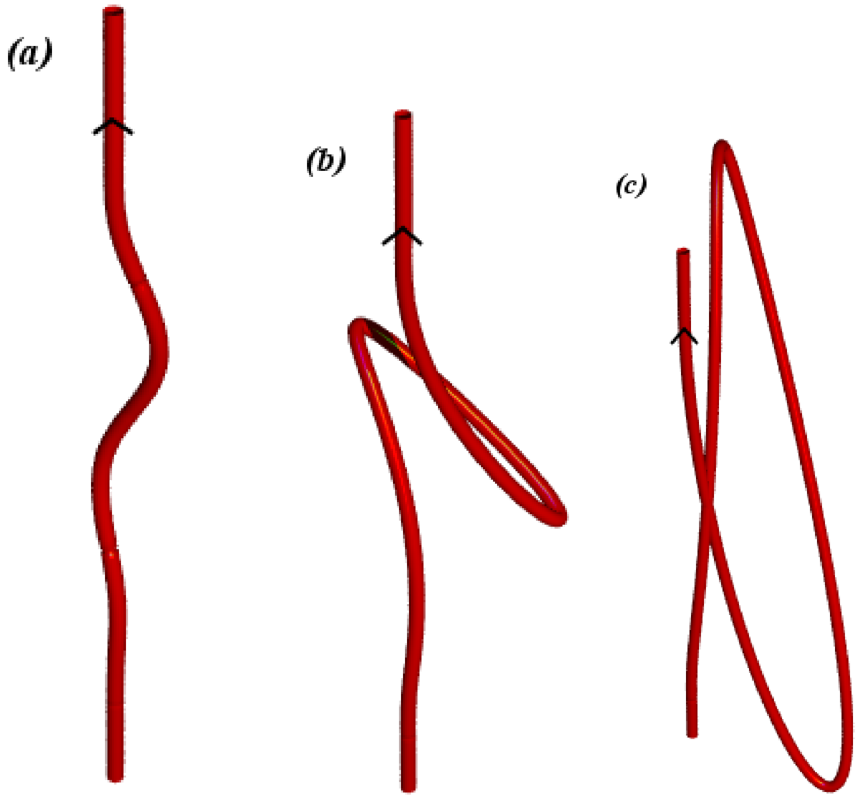

Figure 4.1: The curve $polcv(t)$, equation(4.2), evaluated over a period $t \in [-1,1]$, for values of $a = 0.2$ (a), $a = 0.8$ (b) and $a = 1.16$ (c) respectively (note the z component has been multiplied by a factor of 10 for the sake of aesthetics). In (a) the curve has developed a small sigmoidal kink about its midriff. This kink develops such that the curve develops $\mathcal{W}_{pnl}$ contributions about its middle section. In (c) the curves actually intersect, forming a double point. For $a > 1.1.6$ the curve will have passed through itself leading to a change in its non-local writhing of $+2$ (Figure 4.2).

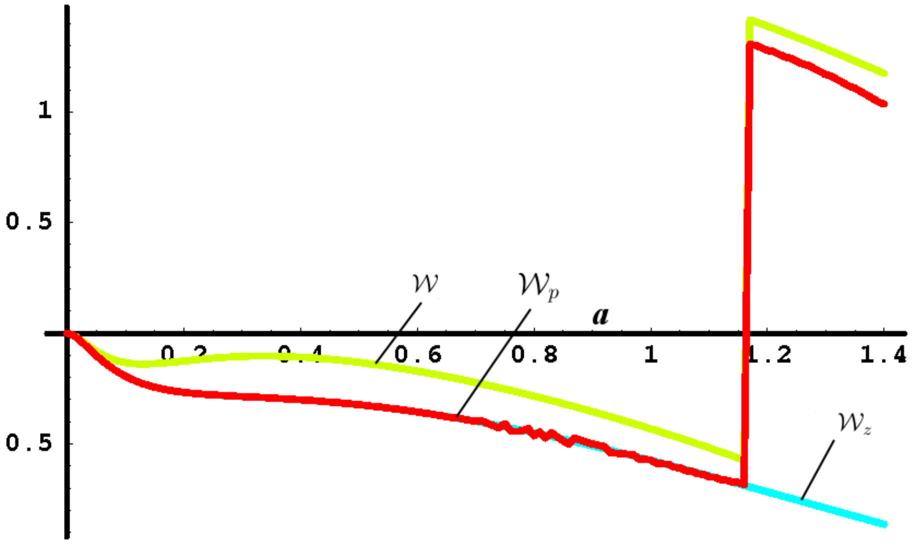

Figure 4.2: Plots of $\mathcal{W}$, $\mathcal{W}_z$ and $\mathcal{W}_p$ against t for the curve $polcv(t)$, evaluated over a period $t \in [-1, 1]$, over a range of a values $a \in [0, 1.4]$. For $a \approx [0, 1.175]$ $\mathcal{W}_p$ and $\mathcal{W}_z$ agree in their evaluations. However at $a \approx 1.75$ there is a jump in value of both $\mathcal{W}$ and $\mathcal{W}_p$ as the curve crosses itself. This jump does not occur for $\mathcal{W}_z$.

$$erf(t) = \frac{2}{\sqrt{\pi}} \int_0^t e^{-t'^2} \mathrm{d}t', \tag{4.2}$$

$$\begin{aligned} polcv(t) = (a7.5(erf(-2t^2) + 1) \sin 2\pi t \\ , 2a(erf(-2t^2) + 1) \\ , 5(t + a5erf(-2t^2) + 1)(t(t-a)(t+a))), \end{aligned} \tag{4.3}$$

where a is a constant which controls the contortion of the polymer. Increasing a causes a kink to form about the curves midpoint. It then develops non-local windings about this section as demonstrated in Figure 4.1. Note that the end tangents always point smoothly along $\hat{z}$ irrespective of a. The curve (a) occurs for a value $a = 0.2$, it is devoid of non-local windings about $\hat{z}$, so the tantrix curve will not enter the southern hemisphere. At $a = 0.8$ (curve (b) in Figure 4.1), a kink has formed and the tantrix curve has passed into the southern hemisphere. The curve $a = 1.16$ (curve (c) in Figure 4.1), is an extreme case of the deformation in which the curve actually crosses itself. We shall see this leads to a jump of +2 for $\mathcal{W}$ and $\mathcal{W}_p$, but not $\mathcal{W}_z$.

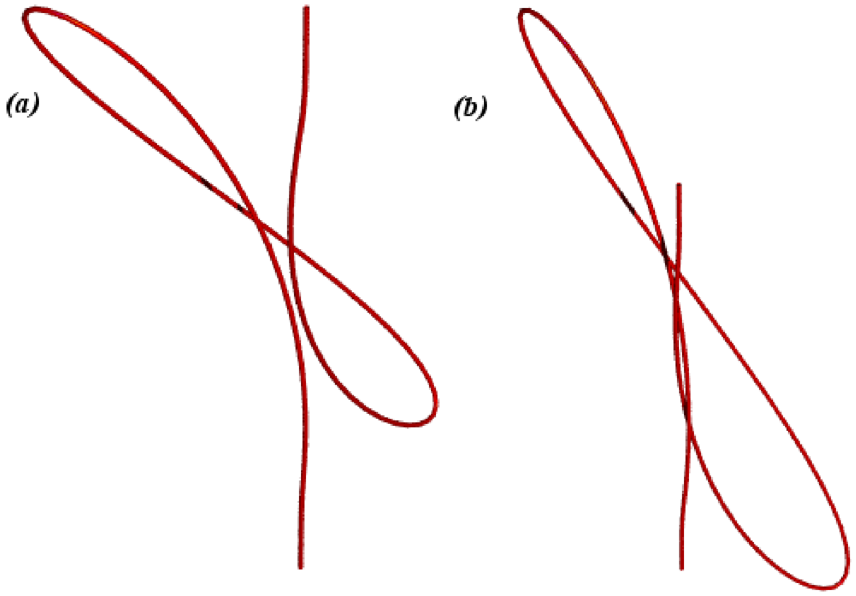

Figure 4.3: Figure (a) represents $polcv(t)$ (4.2), plotted over a range $t \in [-1, 1]$, with $a = 1.1$. It represents an example of the curve before it has passed through itself (we would expect $\mathcal{W}_p$ and $\mathcal{W}_z$ to return the same measure, and they do (Figure 4.2). (b) is the same curve with $a = 1.2$; the curve has passed through itself.

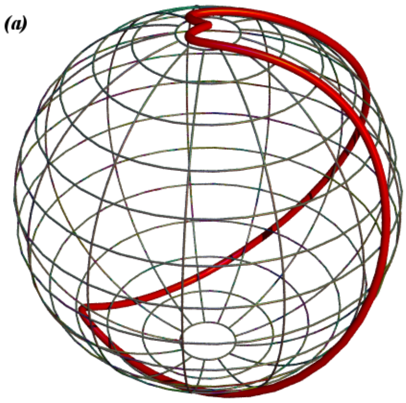

Figure 4.4: Figures (a) and (b) are the corresponding tantrix curves of the $polcv(t)$ examples (a) and (b) depicted in Figure 4.3. The tantrix curves have three important features. First the end points are at the north pole, thus the end points of $polcv(t)$ are seen to be pointing along $\hat{z}$. Second the curves can be connected by a continous transformation (for $a \in [1.1, 1.2]$) which will not pass through the south pole. Third there is very little difference in the area bound by the tantrix curve and the north pole. This indicates that $\mathcal{W}_z(polcv)$ has only changed by a small value (as seen in Figure 4.2).

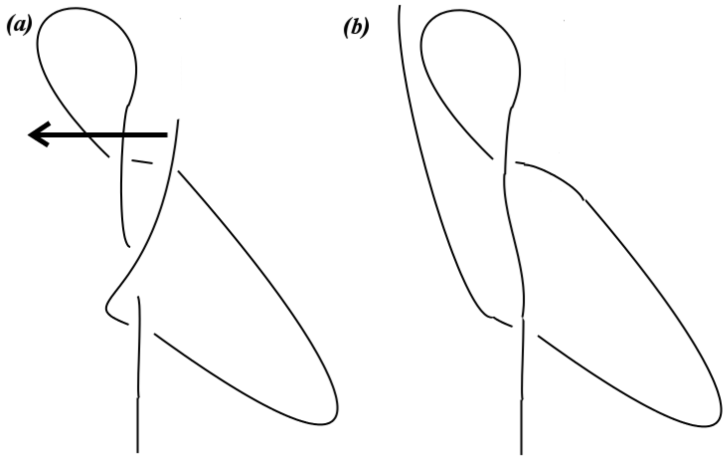

Figure 4.5: . Figures (a) and (b) depict a mechanism by which the curve defined by (4.2) for $a = 1.14$ (depicted as (b) in Figure 4.3), can be linked to a straight line configuration by an ambient isotopy. (a) represents this particular curve. An ambient isotopy indicated by an arrow links it to (b). This ambient isotopy would at no point require that the set of curves linking (a) and (b) points along $\hat{z}$. Next (b) can clearly then be deformed by an ambient isotopy back to a straight line (always with its endpoints pointing along $\hat{z}$).

Figure 4.2 details the results for $\mathcal{W}_p(\mathbf{x}(t))$, $\mathcal{W}_z(\mathbf{x}(t))$ and $\mathcal{W}(\mathbf{x})$, as evaluated over the period $t \in [-1, 1]$, for $a \in [0, 1.4]$. Here $\mathcal{W}$ is evaluated using (1.19) in order to further highlight the effect of non-local writhings. There is an agreement in the writhing interpretations of $\mathcal{W}_z$ and $\mathcal{W}_p$ up until a value of $a = 1.16$. This includes the period in which non-local windings are formed. This can be understood using the tantrix sphere description from section 3.3.4, where the $\mathcal{W}_{pnl}$ contributions can be seen to cancel those of $\mathcal{W}_{pl}$, leaving to the area bound by the tantrix sphere and the north pole.

After $a = 1.16$ there is a jump in the values of $\mathcal{W}$ and $\mathcal{W}_p$ of $+2$, as a result of the curve passing through itself. Note that the curve can be deformed ambient isotopically from a straight line curve section pointing along $\hat{z}$ to configurations either side of this crossing (see Figure 4.5). $\mathcal{W}_p$ and $\mathcal{W}$ detect the crossing by registering a jump of $+2$. $\mathcal{W}_z$ on the other hand recognises only a small difference in writhing between two such states. We see the potential for $\mathcal{W}_z$ to drastically underestimate the writhing contributions, as a result of its ignorance towards non-local windings.

4.1.1 Polar writhe and $\mathcal{W}_z$ conclusions

We can conclude there are several advantages to employing the polar writhe formulation over $\mathcal{W}_z$.

- There is no requirement of smooth, never anti-poloidal, deformation from a reference curve.
- The local writhe formula is more balanced: upward and downward travelling curves (with corresponding northern and southern tantricies), have integrands identical in magnitude. This is especially desirable as the total polar writhe does not change on reversal $s \to -s$.
- The behaviour of equation (4.1) near the south pole can magnify experimental and numerical errors, and affect statistical analyses (Maggs [69]): the integral is heavily weighed toward small southern wiggles.
- The polar writhe displays the influence of non-local windings unlike $\mathcal{W}_z$.

4.2 A comparison of $\mathcal{W}$ and $\mathcal{W}_p$ for open space-curves

A clear difference between the definition of writhing as defined by the double integral (1.19) and the polar writhe is the sense of directionality, inherent to $\mathcal{W}_p$ and absent from $\mathcal{W}$. We have already seen how the choice of $\hat{a}$ affects the nature of the polar writhe interpretation. The writhing, as evaluated by $\mathcal{W}$, is affected by the relative orientations of the curve with itself, as averaged over **all** viewpoints.

This difference will often manifest itself in terms of the non-local writhing, as evaluated by each expression. A $\mathcal{W}$ evaluation will **always** detect the presence of non-local writhings for a curve with any degree of writhing (although it may be cancelled out under certain circumstances by positive and negative components in equal quantity). The polar writhe will only register non-local windings if they occur about the direction of evaluation.

The pertinent question would be: can we identify any quantitative relationship between the two measures for arbitrary open curves ? This would seem unlikely given the complex nature of the non-local windings inherent to the polar writhe (this shall be discussed in greater detail in section 5.3.4). The following investigation will proceed via a set of instructive example calculations. The procedure will involve tracking the evolution of $\mathcal{W}$ and $\mathcal{W}_p$, as applied to a set of curves over a period $[0, t]$, as t is increased.

Case 1 - the helix

Figure 4.6 depicts the result of evaluating $\mathcal{W}$ and $\mathcal{W}_p$ of a helix ($\mathbf{x}(t) = (\sin 4\pi t, \cos 4\pi t, t)$), as it evolves over $t \in [0, 1]$. We see a marked difference in the writhe interpretation of each measure (note that the results for $\mathcal{W}_p$ in this case would be the same as $\mathcal{W}_z$). Specifically $\mathcal{W}_p$ increases linearly with t. $\mathcal{W}$ increases slower at first until it starts to increase linearly after roughly $t = 0.4$. The reason for this difference derives from their interpretation of non-local writhing. $\mathcal{W}_p(\mathbf{x})$ in this scenario records no non-local writhing, over the full parameterisation range. $\mathcal{W}(\mathbf{x})$ however records non-local windings from all possible view points, thus will record the helix as exhibiting non-local windings, which may not be relevant to the physics of the model under evaluation. For example in section 6.2.4 we define an expression for the linked nature of coronal magnetic field lines (the magnetic helicity), the polar writhe formulation

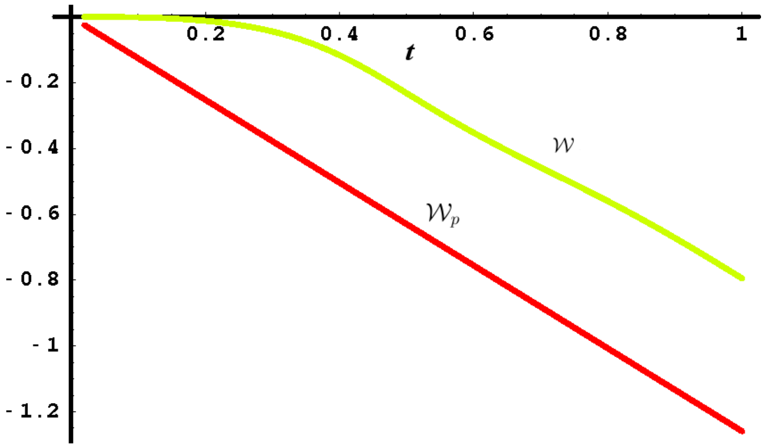

Figure 4.6: A plot of $\mathcal{W}(\mathbf{x})$ and $\mathcal{W}_p(\mathbf{x})$, where $\mathbf{x} = (\sin 4\pi t, \cos 4\pi t, t)$, evaluated over $[0,t]$ for $t \in [0,1]$. The $\mathcal{W}_p$ plot is linear, the $\mathcal{W}$ becomes linear after $t \approx 1.4$.

is shown to be the correct formulation in this case.

Case 2 - the open trefoil knot

A trefoil knot tied into an infinite string can be parameterised by

$$tref(t) = \left(t^3 - 3t, t^4 - 4t^2, t^5 - 10t\right). \tag{4.4}$$

In Figure 4.8 we compare the evolution of $\mathcal{W}_p$ and $\mathcal{W}$ over $t \in [-2.2, 2.2]$. In this scenario $\mathcal{W}$ and $\mathcal{W}_p$ agree exactly. It must be stressed this is a fairly unique case with regards to the set of all open curves. It is important to note this curve is symmetric about its mid-point height (marked on 4.4), that is if one where to place a mirror in the x-y plane at this point the curve would be re-created. This is of course the plane in which $\mathcal{W}_p(tref, \hat{z})$ will register non-local windings. It is a result of this symmetry, occurring along the appropriate direction, that the two measurements agree.

Case 3 - the twisted parabola

We consider a parabola which is twisted (about the x-y plane), via a rotation, causing it to form a loop type structure. This deformation causes smooth fluctuations in both $\mathcal{W}_{pl}$ and $\mathcal{W}_{pnl}$. The points representing the maximum and minimum z values

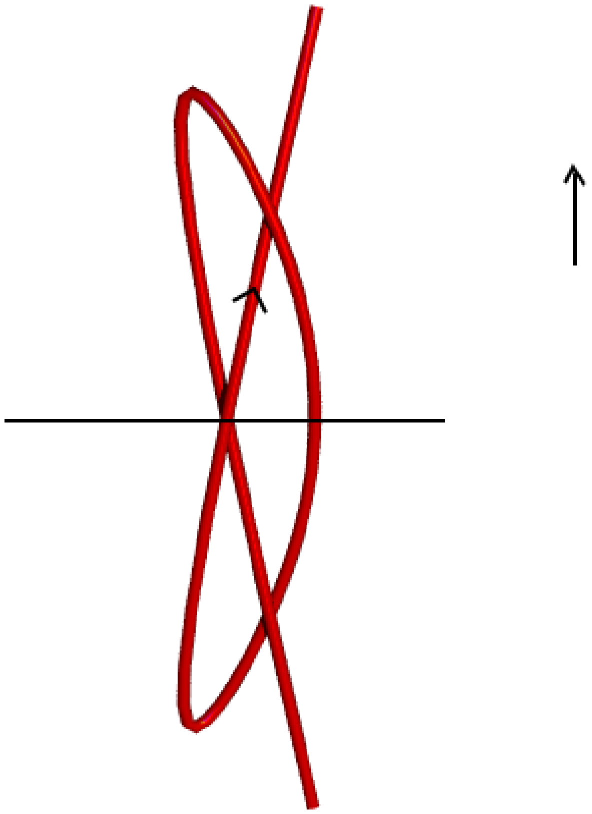

Figure 4.7: The open trefoil (4.4) evaluated over a period $t \in [-2.2, 2.2]$. This is view along the $\hat{z}$ axis. A line is drawn along the middle of the curve indicating its symmetry about the y axis.

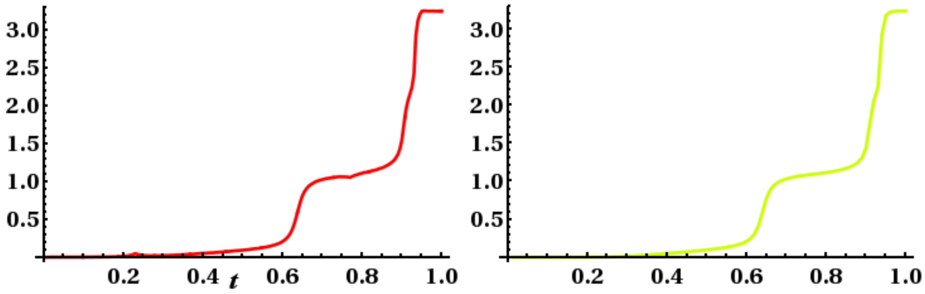

Figure 4.8: Plots of $\mathcal{W}_p(tref(t'))$, on the left and $\mathcal{W}(tref(t'))$ evaluated over a period $t' \in [-2.2, t]$ where $t \in [-2.2, 2.2]$. We note they agree for all t values.

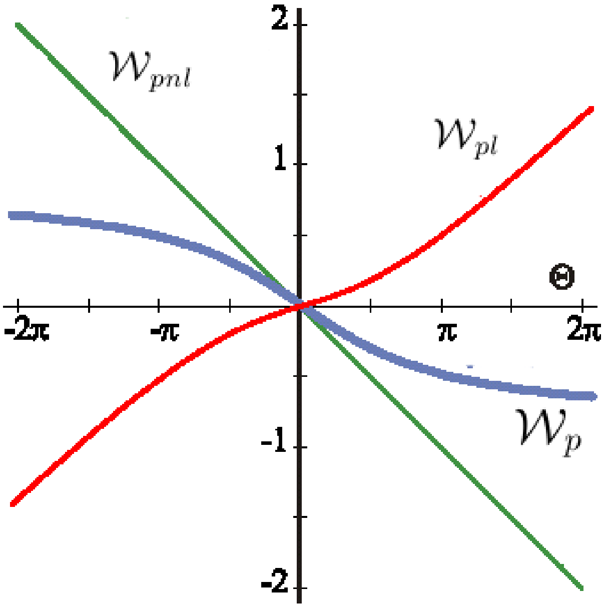

Figure 4.9: A plot of $\mathcal{W}_p[parab(t)]$, $\mathcal{W}_{pl}[parab(t)]$ and $\mathcal{W}_{pnl}[parab(t)]$ ($parab(t)$ is given by 4.6), evaluated over a period $t \in [0,1]$, plotted as a function of Θ for the twisted parabola (equation (4.6)). We note that $\mathcal{W}_{pl}$ and $\mathcal{W}_{pnl}$ are always of opposite sign

of the parabolic shape are fixed [1]. This restricts $\mathcal{W}_{pnl}$ to a smoothly altering value, due entirely to the tangential direction of its maximum point, avoiding the discontinuous jumps encountered when evaluating the polar writhe of the helix. As such we would expect $\hat{z}$ to be the optimal choice of evaluation direction. The parabola is parameterised as follows

$$\begin{aligned} z(t) &= 4ht(1-t), && (4.5)\\ parab(t) &= \left((t-\frac{1}{2})\cos\frac{\Theta z(t)}{h}, (t-\frac{1}{2})\sin\frac{\Theta z(t)}{h}, z(t)\right), && (4.6)\end{aligned}$$

---

[1] Altering the footpoints will, in general, alter the $\mathcal{W}_p$ value (both $\mathcal{W}_{pl}$ and $\mathcal{W}_{pnl}$). Here we choose not to do so. In chapter 6 we will be studying Coronal magetic field structures which are very similar to this twisted parabola. In that study we shall observe the effect, on $\mathcal{W}_p$, of altering the structures footpoints.

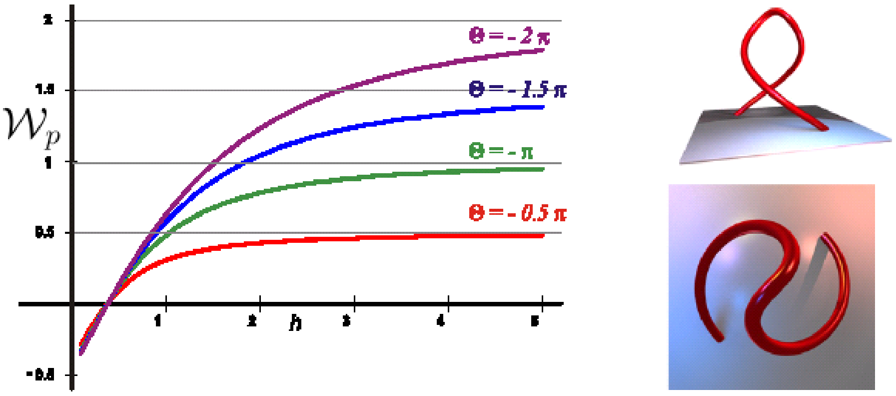

Figure 4.10: Demonstrating the relationship between $\mathcal{W}_p$ and h for various values of Θ, we see an apparent point where all curves cross the h-axis (this will be shown to be a small range in section 6.3.4).

where $t \in [0, 1]$. The parameter Θ controls the twist applied to the curve [2]. $\Theta = 0$ will leave us with a basic parabola. As Θ is increased the curve begins to twist about its midpoint. As a result of the $(t - \frac{1}{2})$ function, contributing to $x(t)$ and $y(t)$, this rotation drops to zero at the peak and base of the parabola. For global windings $\mathcal{W}_{pnl} = -\Theta/\pi$ and is independent of the parabola's start height. Figure 4.10 demonstrates that $\mathcal{W}_{pl}$ is dependent on the parabola's height h and also of opposite sign to $\mathcal{W}_{pnl}$. Specifically as h is increased the relative contribution of $\mathcal{W}_{pl}$ decreases. The geometrical dynamics of the twisted parabola are relevant to a particular set of coronal magnetic field models, a topic which will be covered in Chapter 6.

As a consequence the $\mathcal{W}_{pl}$ contribution controls the sign of $\mathcal{W}_p$ with respect to the starting height (see Figure 4.10). Decreasing or increasing h can cause a change in sign of $\mathcal{W}_p$.

We now compare the evolution of $\mathcal{W}_p[parab(t)]$ to $\mathcal{W}[parab(t)]$ over the range of twisting angles $\Theta \in [0, 4\pi]$. It can be seen in Figure 4.11 $\mathcal{W}[parab(t)]$ is much closer to $\mathcal{W}_p[parab(t)]$ in comparison to the $\mathcal{W}_z$ evaluation, and specifically both lead to lower writhing measures. This is not unexpected as we have already seen the non-local contributions tend to be opposite in sign to local ones, also the twisting

---

[2] Note this is the same symbol as used for the orientation of the rotation vector $r(z)$ in (3.1). This is not a coincidence as here Θ is zero when the parabola's peak is oriented along the x-axis. As Θ is increased the peak tangent orientation will rotate with Θ, clockwise if positive and anticlockwise if neagtive. So Θ (the rotation in 4.6) entirely determines the $\mathcal{W}_{pnl}$ contribution.

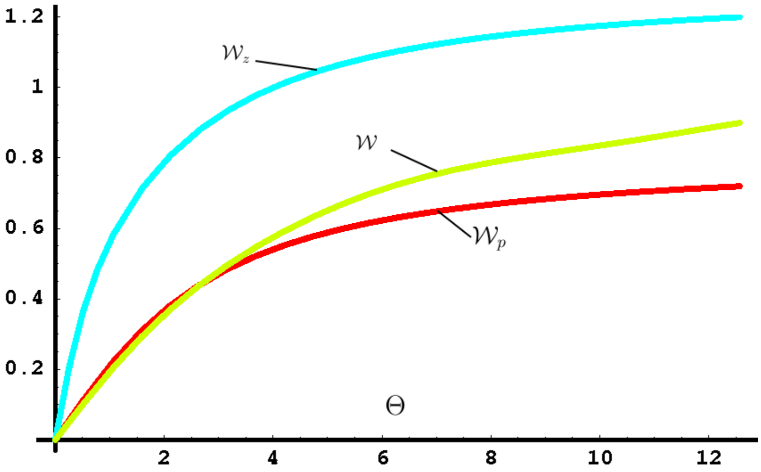

Figure 4.11: A plot of $\mathcal{W}_z$, $\mathcal{W}$ and $\mathcal{W}_p$ measures of *parab*(t) (see equation 4.6), for a period $t \in [0,1]$ for twisting angles $\Theta \in [0, 4\pi]$. Both the $\mathcal{W}$ and $\mathcal{W}_p$ evaluations differ significantly from $\mathcal{W}_z$. As Θ increases the difference between the $\mathcal{W}$ and $\mathcal{W}_p$ evaluations are seen to diverge.

occurs about a preferred axis ($\hat{z}$) leading to much of the non-local writhing to occur about this axis. The discrepancy between $\mathcal{W}$ and $\mathcal{W}_p$ is a result of $\mathcal{W}$ measuring non-local windings about all viewpoints not just the x-y plane. This discrepancy becomes more marked as the degree of twisting increases. This is in contrast to the previous study (section 4.2), in which $\mathcal{W}$ and $\mathcal{W}_p$ were identical. This suggests, as expected, that there is no exact relationship between the two.

4.3 Directionality in open spacecurves

The three studies conducted so far suggest some kind of relationship between $\mathcal{W}_p$ and $\mathcal{W}$, but not $\mathcal{W}_z$. This relationship would appear unlikely to be one which can be expressed as a simple quantitative relationship such as is the case for closed spacecurves. All three curves studied in section 4.2, had a strong sense of directionality. It would seem wise at this point to split open spacecurves into two categories.

- Non-directionally coiled spacecurves. These curves have a significant degree of writhing (as measure by all expressions), which display no bias towards a particular direction.

- Directionally-coiled spacecurves, curves such as the helix and the parabola which tend to wind in both local and non-local manners with bias towards a specific direction.

4.3.1 Non-directionally coiled spacecurves

Such curves will by their nature always exhibit a strong degree of non-local writhing. In such cases we can immediately rule out the use of $\mathcal{W}_z$ as a coherent writhing measure. Thus we are left with $\mathcal{W}_p$ and $\mathcal{W}$ which both measure the effects of non-local winding. As stated the difference is that $\mathcal{W}_p$ evaluates this non-local winding about a specific direction. $\mathcal{W}$ on the other hand essentially measures non-local relationships for all directions, and will display the full spectrum writhing behavior inherent to non-directional spacecurves. This averaging means it will not empahsise the specific directional nature of the non-local writhing of such curves. On this basis we must consider $\mathcal{W}$ as a more appropiate for evaluating such curves. Of course we have seen that there can exist a great amount of correlation between $\mathcal{W}_p$ and $\mathcal{W}$ (section 4.2). Even in these cases however the $\mathcal{W}_p$ evaluation changes in a non smooth manner whilst the $\mathcal{W}$ measures changes smoothly.

Case Study 4 - trefoil knot

We consider the torus trefoil knot. This knot exhibits a great deal of non-local coiling, which shows no particular trend to a specific cartesian direction, it is parameterised as follows

$$\begin{aligned}
\mathbf{x}(u) &= (\cos 2\pi u, \sin 2\pi u, 0), && (4.7)\\
\mathbf{v}(u,v) &= (\cos 2\pi u \cos 2\pi v, \sin 2\pi u \cos 2\pi v, \sin 2\pi v), && (4.8)\\
\mathbf{y}(u,v) &= \mathbf{x}(u) + \mathbf{v}(u,v), && (4.9)\\
tref(t) &= \mathbf{y}(2t, 3t). && (4.10)
\end{aligned}$$

We see in Figure (4.12), $\mathcal{W}_z$ offers a substantially different interpretation of the writhing to that of $\mathcal{W}_p$ and $\mathcal{W}$, to such an extent that they generally differ in sign. The measurements $\mathcal{W}$ and $\mathcal{W}_p$ however are subject to a far more interesting relationship. We see the $\mathcal{W}_p$ curve displays the same general trend as that of $\mathcal{W}$. This relationship is however not exact. The $\mathcal{W}$ curve changes continuously, whilst $\mathcal{W}_p$ changes erratically and tends to jump above and below $\mathcal{W}$. This supports our

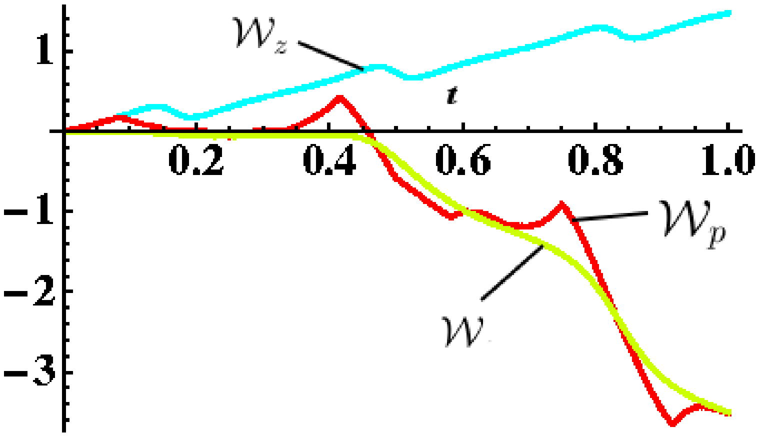

Figure 4.12: Plots of our three writhe measurements for the trefoil curve $tref(t)$, equation 4.10, evaluated from 0 to t for a period $t \in [0,1]$. The $\mathcal{W}_z$ measure is significantly different to $\mathcal{W}$ and $\mathcal{W}_p$. $\mathcal{W}$ and $\mathcal{W}_p$ appear to agree approximately in their evaluations of the curves writhing. However, the $\mathcal{W}$ evaluation changes in a smoother, more consistent manner.

assumption that $\mathcal{W}$ represents the most consistent and coherent measurement of the curves writhing nature, in the case that it is not directionally specific.

4.3.2 Directionally coiled spacecurves

Depending on the direction $\hat{a}$ in which the polar writhe is evaluated, the effect of $\mathcal{W}_{pnl}$ could range from non-existence to dominance (this shall be discussed in more detail in section 5.3.5). However, the $\mathcal{W}$ is a measurement taken over all viewpoints. A logical conclusion would be that $\mathcal{W}$ is simply not the correct definition needed to establish the directional nature of the curve's shape. Instead $\mathcal{W}_p$ emerges as the appropriate expression, due to its status as the only directionally specific expression which analyses non-local writhing.

Case Study 5 - Vertically coiling curve (*vcc*)

We define a curve (depicted in Figure 4.3.2), which begins as a curve winding locally along $\hat{z}$. The coiled section then drops back over its axis leading to non-local winding of the curve about itself. This winding occurs about $\hat{z}$. This curve is parameterised as follows,

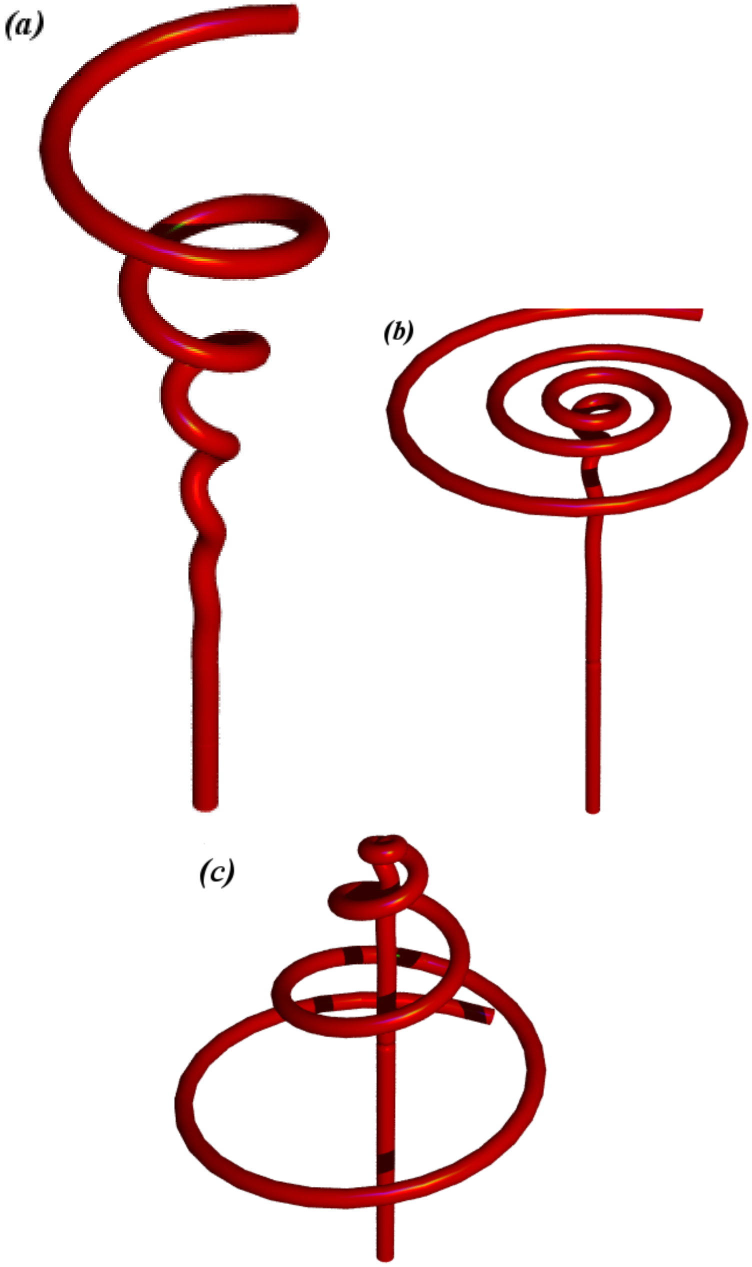

Figure 4.13: Looping curves $loop(t)$ evaluated over a period $t \in [-1, 1]$ for cases $a = 1$, 2.3 and 8, from top left, clockwise. In (a) the curve has only local windings. In (b) the curves spiral section is tending to a coil lying in the x-y plane, marking the threshold of non-local winding. In (c) the spiral section winds around the straight line section.

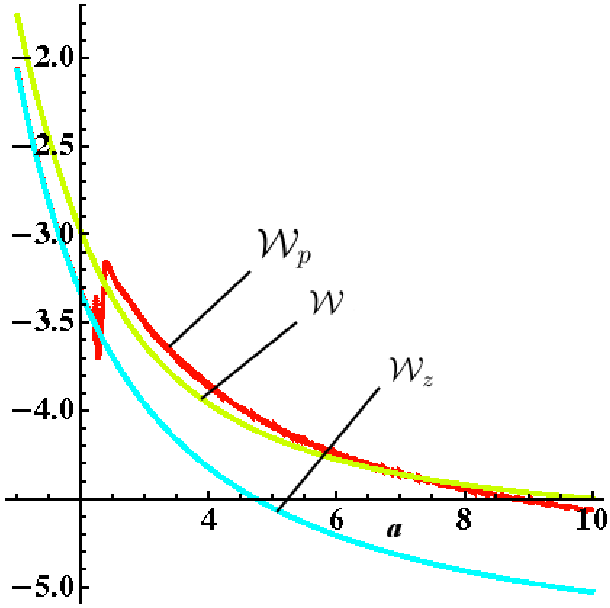

Figure 4.14: A plot showing the evaluation of $\mathcal{W}_p$, $\mathcal{W}_z$ and $\mathcal{W}$, of the curve $vcc(t)$ (equation (4.11)), evaluated over the period $t \in [0,1]$ for a varied over the range of $a \in [0.1, 10]$. Up until $a \approx 2.3$ the $\mathcal{W}_z$ and $\mathcal{W}_p$ evaluations agree. After this point the curve develops non-local windings and the $\mathcal{W}_p$ evaluation jumps in value; the same is not true of $\mathcal{W}_z$. After this point, in contrast to lower a values, $\mathcal{W}_p$ and $\mathcal{W}$ roughly agree in their evaluations.

$$vcc(t) = \left\{a/2t^5 \sin 16\pi t, a/2t^5 \cos 16\pi t, 5t(t-1/2) + a\sin \pi t\right\}. \qquad (4.11)$$

The results for $\mathcal{W}(vcc(t))$, $\mathcal{W}_p(vcc)$ and $\mathcal{W}_z(vcc(t))$ are demonstrated in Figure 4.14. Starting at $a = 1$, the curve coils locally along $\hat{z}$ (left figure in 4.3.2) $\mathcal{W}_z$ and $\mathcal{W}_p$ are in agreement; $\mathcal{W}$ however is significantly different. As with the helix study $\mathcal{W}$ gives a differing interpretation, by measuring non-local windings, as evaluated over all viewpoints. At $a \approx 2.3$ the coils align along a mutual z-value (the middle Figure in 4.3.2). At this point the $\mathcal{W}_p$ measurement jumps in value, as a result of the curve beginning to wind about itself non-locally. Further, we note $\mathcal{W}_z$ does not register this jump as a result of its inability to correctly evaluate non-local windings. From $a \approx 2.5$ to $a = 10$ (which covers the middle figure of 4.3.2 deformed ambient isotopically into the third figure), we see $\mathcal{W}$ and $\mathcal{W}_p$ now roughly agree. $\mathcal{W}_p$ is the only expression which has captured the transition of $vcc(t)$ from a locally winding curve to one which has both local and non-local components. The fact that $\mathcal{W}_p$ can jump in a disjoint manner due to $\mathcal{W}_{pnl}$ is in fact an advantage, representing the transition in a manner which is not replicated by $\mathcal{W}_z$ and $\mathcal{W}$.

Conclusions

We can distill the conclusion of this chapter into the following set of observations.

- $\mathcal{W}_z$ is generally a poor measure of open spacecurves, especially when they exhibit any sort of non-local writhing or winding.
- In general $\mathcal{W}$ and $\mathcal{W}_p$ are not equal.
- For spacecurves which exhibit a significant degree of non-local writhing but which do not have a preferred direction, the writhing of the curve will be measured in a more consistenet manner by $\mathcal{W}$ than $\mathcal{W}_p$.
- For curves which display a marked directional preference, the polar writhe will capture the directionally specific aspect of the curves geometry; whereas the averaging over all viewpoints, inherent to the calculation the non local $\mathcal{W}$ measure will not explicitly demonstrate this behaviour. For example we have seen in figure 4.14 that the polar writhe is the only measure which captures

the transistion as the curves helically winding section changes from spiralling upwards to spiralling downwards (see figure 4.3.2).

Chapter 5

The writhing of open spacecurves

Many of the properties of $\mathcal{W}$ and $\mathcal{W}_p$ do not exist for open spacecurves, due to their ability to unwind without the curve passing thorough itself. This chapter will perform a review of the properties of both expressions with regards to open curves. Particular attention is paid to the unit sphere interpretation (which was discussed for closed spacecurves in Chapter 2). Two key issues have particular relevance.

The first issue is the artificial closure of the curve (or ribbon) discussed in section 1.6.5. Closures can be used to mimic a set of physical constraints placed upon a particular physical system, such as fixed or clamped end points (van der Heijden *et al* [114]). Previous notes regarding this topic have tended to apply a planar closure, with the assumption that the end tangents ($\widehat{\mathbf{T}}(0)$ and $\widehat{\mathbf{T}}(L)$) either point along a fixed direction (Rossetto and Maggs [92]), or can be closed smoothly by a planar section of curve (Starostin [104] and van der Heijden *et al* [114]). In this chapter more general closures are introduced, and their effect on the various writhe measures discussed. One such closure, detailed in section 5.2, will be unique to this thesis and can be applied to the full set of open spacecurves (of at least $\mathcal{C}^3$ smoothness). The closure can be used to apply the Fuller writhing expressions (1.26) and (1.27).

Secondly, an important issue is the choice of evaluation direction, inherent to the polar writhe framework. It is shown, in contrast to the case for closed curves, that the choice of direction can greatly affect the interpretation of the $\mathcal{W}_p$ measure obtained. This effect is shown to be particularly driven by changes in non-local writhing.

Closures

For this chapter we must fix a number of conditions upon the set of allowed closures, relating to the need for the closures to join in a smooth and continuous manner. For a spacecurve $\mathbf{x}(s)$, $s \in [0, L]$ and closure curve section $\mathbf{x}_c(s), s \in [L, M]$ we require that

$$\begin{aligned}
\mathbf{x}(L) &= \mathbf{x}_c(L) \qquad (5.1)\\
\mathbf{x}(0) &= \mathbf{x}_c(M) \qquad (5.2)\\
\widehat{\mathbf{T}}_{\mathbf{x}}(L) &= \widehat{\mathbf{T}}_{\mathbf{x}_c}(L)) \qquad (5.3)\\
\widehat{\mathbf{T}}_{\mathbf{x}}(0) &= \widehat{\mathbf{T}}_{\mathbf{x}_c}(M) \qquad (5.4)
\end{aligned}$$

These conditions will be assumed for all closures defined in this chapter. Note the above set of equalities must also hold for $\mathbf{x}(t)$, $t \in [a, b]$ and $\mathbf{x}_c(t)$, $t \in [b, c]$ (where a and b and c are parameters corresponding to 0, L,and M respectively). Applying these conditions we shall be able to glue $\mathbf{x}$ and $\mathbf{x}_c$ together in a smooth manner such that they form the smooth closed curve union $\mathbf{x} + \mathbf{x}_c$. We require the same conditions to hold for a ribbon i.e. for $\mathbf{y} + \mathbf{y}_c$ as well as $\mathbf{x} + \mathbf{x}_c$. This is not always strictly necessary (Hannay [51], Starostin [103]) but is always possible so we shall assume for all closed ribbons continuity is held.

5.1 The Gauss integral and open spacecurves

It is entirely possible to perform the $\mathcal{L}$ and $\mathcal{W}$ integrations, as defined by (1.16) and (1.19), on open spacecurves. However, the geometrical descriptions, and hence properties of $\mathcal{W}$ and $\mathcal{L}$, differ from their non-closed counterparts.

5.1.1 Open $\mathcal{L}$

We define open $\mathcal{L}$ to be the same double integral (1.16) applied to an open ribbon.

Properties of $\mathcal{L}$ as Applied to Open Curves

- $\mathcal{L}$ is not topologically invariant when applied to open spacecurves. But $\mathcal{L}$ is still constant conformally invariant.

- $\mathcal{L}$ can no longer be calculated by a single planar projection.
- $\mathcal{L}$ changes continually upon deformation, except when two curves cross each other, which causes a jump in value of ± 1.
- In general if a closed ribbon R is split into two separate open links R_1 and R_2, then $\mathcal{L}(R) \neq \mathcal{L}(R_1) + \mathcal{L}(R_2)$ (Fuller 1978 [45]). Thus the closed linking number of an artificially closed open curve may not equal the sum of the $\mathcal{L}$ values from the curve and its closure.

The loss of topological invariance

Comparing the surfaces covered by the mapping (1.18) for open and closed spacecurves, the major difference is that the area bound on the unit sphere will no longer be a multiple of 4π. Consider the set $\mathcal{O}_m$ of curves $\mathbf{o}(\Delta s)$ defined in section 2.1. Each curve ($s \in [0, L]$ for a constant Δs), no longer represents a closed curve (in general), on the sphere's surface. Thus there is no guarantee that the total area ($\mathcal{A}_m$), enclosed on the tantrix sphere, is some integer multiple of 4π. Also as $\mathbf{y}(0) \neq \mathbf{y}(L)$ the two bounding curves will in general not be the same, reinforcing the non integer nature of the open measurement. In a sense $\mathcal{L}$ of open curves behaves in a similar manner to $\mathcal{W}$ for open spacecurves: both can change continuously upon deformation. Both the shape of the constituent curves and the difference between bounding curves alter continuously upon application of ambient isotopic deformations. If the ribbon being evaluated is continuously contorted, until both sections of the ribbon align themselves along a common straight line, $\mathcal{A}$ will reduce to zero. This occurs as a result of the curves $\mathbf{o}(\Delta s)$ shrinking to a point.

As with the closed spacecurve case, the result of the ribbon crossing through itself is the addition or subtraction of a full 4π area from $\mathcal{A}_m$. This argument follows from the discussion in section 2.1. Specifically the description of the change evoked by crossing $\mathbf{x}$ and $\mathbf{y}$ was applied to an open section of the full ribbon, and is thus applicable to open curves as well.

Consider $\mathcal{O}_m$ to represent the set of observed crossing directions contributing to $\mathcal{L}(R)$. Evaluating the link of a closed ribbon R as separate ribbon sections R_1 and R_2 (where $R_1 + R_2 = R$), ignores the non-local contributions present in the $\mathcal{L}$ evaluation of the closed ribbon R. A subset of the directions represented will thus be removed from $\mathcal{O}_m$. We can think of the set as being split into three parts $\mathcal{O}_{m_1}$ representing

$\mathcal{L}(R_1)$, $\mathcal{O}_{m_2}$ representing $\mathcal{L}(R_2)$ and $\mathcal{O}_{m_{lost}}$ representing $\mathcal{L}(R) - (\mathcal{L}(R_1) + \mathcal{L}(R_2))$.

The open ribbon section $R(\mathbf{x}, \mathbf{y})$, $s \in [0, L]$, can be extended with a suitable closed ribbon $R(\mathbf{x}, \mathbf{y})_c$, $s \in [L, M]$, such that the closure conditions, defined for this chapter (section 5), are satisfied. The newly defined link $(R + R_c)(s)$ will have an integer $\mathcal{L}$ value, which is topologically confined and possesses the properties defined for closed ribbons. The closure extends each curve of the set $\mathcal{O}_m$ to form closed curves. Secondly the set itself is extended such that it covers some integer multiple of 4π. However closures are not unique; one can apply an infinite number of increasingly complicated closures, which will lead to differing integer linking numbers. Geometrically the areas covered by the mapping (1.18) will differ by an integer number of full coverings of the tantrix sphere.

5.1.2 Open $\mathcal{W}$

As with the $\mathcal{L}$ of open curves, the $\mathcal{W}$ of an open spacecurve is defined by evaluating (1.19) over $\mathbf{x}$ for $s,\ s' \in [0, L]$ (where we replace $\oint_0^L$ with $\int_0^L$). The same question applied to our general parameterisation t, all properties discussed are independent of the choice of parameterisation.

Properties of $\mathcal{W}$ as applied to open curves

- $\mathcal{W}$ is constant conformally invariant.
- $\mathcal{W}$ changes continually under the set of ambient isotopies. The result of a section of curve crossing through itself is a change in value of ±2.
- In general if a closed curve $\mathbf{x}$ is split into two separate open curves $\mathbf{x}_1$ and $\mathbf{x}_2$, then $\mathcal{W}(\mathbf{x}) \neq \mathcal{W}(\mathbf{x}_1) + \mathcal{W}(\mathbf{x}_2)$.
- A $\mathcal{W}$ evaluation of an open spacecurve and its artificially closed compatriot will not, in general, be equal.

As with the open $\mathcal{L}$ discussion, the set of curves comprising the map $\mathcal{O}_n$ (2.2) will no longer be closed on themselves. This leads to a further loosening of the conditions placed upon the allowed set of $\mathcal{W}$ values. As with the closed curve case open $\mathcal{W}$ is theoretically free to gain an unlimited amount of writhing, or reduce to zero for each existing open curve, except now the set of allowed ambient isotopies has been expanded, such that **all** curves can be smoothly deformed into each other.

The result of curves crossing each other is the same as the closed curve case (two full coverings of the sphere being removed or added).

That the $\mathcal{W}$ is not additive follows from an argument mirroring that of the $\mathcal{L}$ case. We split $\mathcal{O}_n$ into sets $\mathcal{O}_{n_1}$, $\mathcal{O}_{n_2}$ and $\mathcal{O}_{n_{lost}}$. If the set $\mathcal{O}_{n_{lost}}$ provides no contribution to $\mathcal{W}(\mathbf{x})$ then the $\mathcal{W}$ evaluation becomes linear. This is true of the (full) curve depicted in Figure 5.2.

One can always define a suitable closure $\mathbf{x}_c$ for a spacecurve $\mathbf{x}$, again noting this is not a unique choice. The area on the tantrix sphere, enclosed by evaluating the mapping (2.2) will be the set of open curves $\mathbf{p}(\triangle s)$, where $s \in [0,l]$ and $\triangle s \in [0,L]$. The closure extends each of these curves such that they are closed for s and $\triangle s' \in [0,M]$. We can now apply all the relations defined for $\mathcal{W}$ for closed spacecurves to the $\mathbf{x}+\mathbf{x}_c(s)$ combination. As with the linking number the writhe is not invariant to the choice of closure. The relationship between the $\mathcal{W}$ of the open curve $\mathbf{x}$, and the $\mathcal{W}$ of a closed union $\mathbf{x}+\mathbf{x}_c$, is discussed by both Rossetto and Maggs [92] and Starostin [104].

Specific closures - aligned end tangent closure

Rossetto and Maggs [92] consider the set of curves for which $\widehat{\mathbf{T}}(0)$ and $\widehat{\mathbf{T}}(L)$ are aligned along unique direction, specifically $\hat{z}$. The paper details a ribbon which is closed at infinity by the extra sections s_1, s_2 stretching off to infinity in both directions and closed by an infinite semi circular section c. The expression for the ribbon and its closure is split into two separate components. The $\mathcal{W}$ of $\mathbf{x}$ is calculated by evaluating the spherical area swept out by the mapping (2.2). The contribution of $\mathbf{x}_c$ is parameterised by two arclength parameters s, which covers $\mathbf{x}$ and s', which covers the extension R_c stretching out to ∞ along the direction $\hat{z}$. The mapping used to define the $\mathcal{W}$ attributable to the section s_1 is $\hat{u}(s) = \mathbf{m}(s,s')$, where s' is fixed, represents a closed spherical curve (as the end tangents of $\mathbf{x}$ are fixed to point along $\hat{z}$). Letting s' vary from 0 to ∞ the mapping will sweep out a spherical area between $\hat{u}(s)$ and the north pole of the tantrix sphere. The same logic is applied to the section s_2 with $s' \in [0,\infty]$, which returns the same integral. The sum of these contributions gives the expression for $\mathbf{x}+\mathbf{x}_c$,

$$\mathcal{W}(\mathbf{x}+\mathbf{x}_c) = \mathcal{W}(\mathbf{x}) + \frac{1}{\pi}\hat{z}\cdot\int\frac{\hat{u}\times\hat{u}'}{1+\hat{z}\cdot\hat{u}}\mathrm{d}s. \tag{5.5}$$

The expressions covering s_1 and s_2 sum to twice the area bound by $\widehat{\mathbf{T}}_{\mathbf{x}}$ and the north pole.

General case

Starostin [104] considers a general case for which the end tangents are not aligned. In a similar manner to that described by Rossetto and Maggs [92], the end tangents are extended with sections of curve s_1 and s_2 which are extended to infinite length. They are then joined by a section c, which is not in general planar. This section contributes an extra term to the overall $\mathcal{W}$ (termed the *squint*).

5.2 The Fuller writhing expressions and closures

As discussed in section (1.6.5) several papers have applied an artificial closure in order to define expressions for the $\mathcal{W}$ of open spacecurves, using the Fuller expressions (1.26) and (1.27). This work has been applied to curves whose endpoints are aligned along a mutual plane, specifically when the endpoints are in the same plane as the vector $\mathbf{x}(L) - \mathbf{x}(0)$. As demonstrated in section 3.3.5 these expressions are, given the correct circumstances, equivalent to a measure of $\mathcal{W}_{pl}(\mathbf{x}, \widehat{\mathbf{T}}_{\mathbf{x}_{ref}})$, where $\mathbf{x}_{ref}$ represents an planar curve. In the following section a new closure is detailed for curves whose end tangents are randomly aligned.

5.2.1 The alternative closure $\mathbf{x}_{cr}$

Rotating a spacecurve $\mathbf{x}$ through an angle of π radians, about an arbitrary axis of rotation L_{axis}, will not alter the $\mathcal{W}$ of a curve. If further we re-parameterise this rotated curve, such that its start point is the equivalent end point of the original curve, **and** the parameterisation direction is reversed ($s \to -s$), the $\mathcal{W}$ will still remain unaltered. By connecting $\mathbf{x}$ to this rotated image, via a set of planar extensions, we create a closed, smoothly oriented spacecurve $\mathbf{x}_{cr}$, whose $\mathcal{W}$ measurement will be $2\mathcal{W}(\mathbf{x})$. This occurs because the non-local contributions between the two connected curves, comprising $\mathbf{x}_{cr}$, are equal and opposite. This closure is possible for all spacecurves defined within this thesis, as long as they are at least $\mathcal{C}^3$ differentiable.

In order to fix these curves together we attach a planar section of spacecurve, $\mathbf{a}_1$ to $\mathbf{x}(L)$ which will orient its endpoint to have a tangent anti-parallel to the start point tangent ($\widehat{\mathbf{T}}_{\mathbf{x}_0}$), where $\mathbf{a}_1$ will attach to $\mathbf{x}(L)$. This concatenated curve

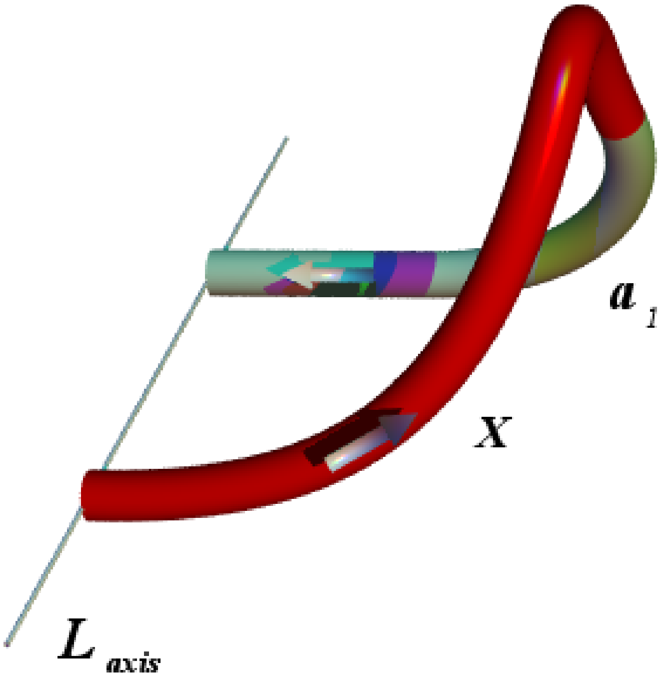

Figure 5.1: The darker (red) section of spacecurve represents an arbitrary open spacecurve $\mathbf{x}$ which we intend to close. We choose the axis of rotation (L_{axis}) to be perpendicular to the tangent at $\mathbf{x}(0)$. The curve is extended with a planar section $\mathbf{a}_1$ such that it joins to L_{axis}. The curve shown is parameterised as $\mathbf{x}(t) = \left((t-2)(t+2)t, t/2, e^{-0.2\frac{t^2}{2}}\right), \, t \in [-5, 2]$.

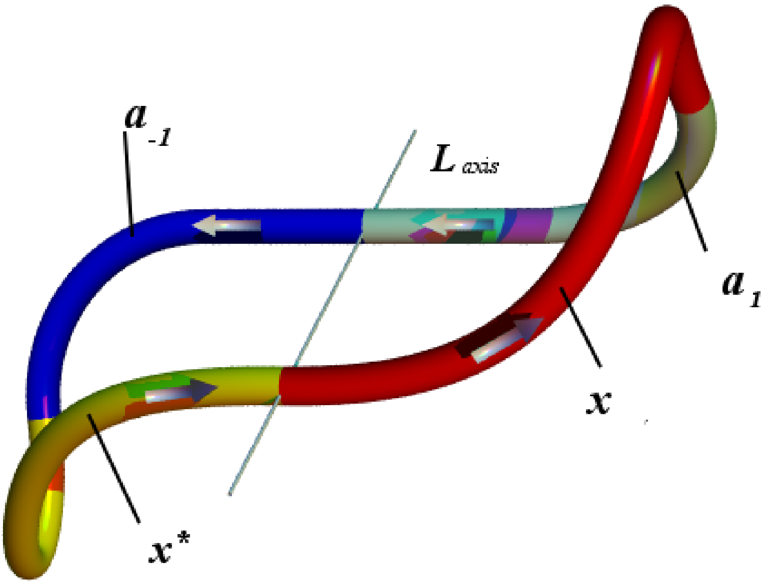

Figure 5.2: The full closure $\mathbf{x}_{cr}$ (defined in section 5.2.1), with orientations marked by arrows. $\mathbf{x}_{orig}$ ($\mathbf{x}$ $+\mathbf{a}_1$) has been rotated through an angle of π rad about the axis of rotation (L_{axis}), to produce $\mathbf{x}_{image}$ ($\mathbf{x}^*$ $+\mathbf{a}_{-1}$, where $\mathbf{x}^*$ is the rotated image of $\mathbf{x}$), whose orientation has been adjusted to ensure the curve is oriented in a consistent manner. This second half attaches smoothly to the first half to form a fully closed spacecurve twice the writhe of $\mathbf{x}$. This figure represents the completion of the closure started in Figure 5.1.

$\mathbf{x} + \mathbf{a}_1$ shall be denoted $\mathbf{x}_{orig}$. We define the axis of rotation L_{axis} as the vector joining $\mathbf{x}_{orig}(0)$ to the endpoint of $\mathbf{a}_1$ (see Figure 5.1). The next step is to rotate the $\mathbf{x}_{orig}$ through π rad about L_{axis} to produce an image $\mathbf{x}_{image}$. We note this image is constructed from $\mathbf{x}$ rotated through π ($\mathbf{x}_{rot}$) and its planar section $\mathbf{a}_1$ also rotated in this manner ($\mathbf{a}_{-1}$). So $\mathbf{x}_{image} \equiv \mathbf{a}_{-1} + \mathbf{x}_{rot}$. By reversing the orientation of this image we create a closed spacecurve $\mathbf{x}_{cr}$, where $\mathbf{x}_{orig} + \mathbf{x}_{image} \equiv \mathbf{x}_{cr}$ as depicted in Figure 5.2. Its $\mathcal{W}$ is $2\mathcal{W}(\mathbf{x})$ as required.

Geometrically $\mathbf{x}_{cr}$ will map out a closed spacecurve $\widehat{\mathbf{T}}_{\mathbf{x}_{cr}}$. Again we note this will have a continuous and consistent orientation. Starting with the original spacecurve $\mathbf{x}$ and its planar closure, the unit tangent of this curve will map out a section of tantrix curve $\widehat{\mathbf{T}}_{\mathbf{x}_{orig}}$ on the unit sphere (remembering its tangents are aligned), its endpoints will be points which can be connected by a spherical chord on the sphere which follows a geodesic arc. $\mathbf{x}_{image}$ will also map out a closed tantrix curve $\widehat{\mathbf{T}}_{\mathbf{x}_{image}}$, which will be the same shape as $\widehat{\mathbf{T}}_{\mathbf{x}}$. It will be displaced on the sphere's surface through a combination of Euler angle rotations, defined by the direction about which $\mathbf{x}$ is rotated to produce $\mathbf{x}_{image}$. For instance if this rotation occurs about the x-axis, the displacement would be a rotation through π radians about the polar angle θ. So we are left with two sections of tantrix curve which combine to form a fully closed and well oriented tantrix curve, see Figure 5.3 for an example.

For each Fuller writhe expression we can use the above closure, in order to generate an expression for $\mathcal{W}(\mathbf{x})$ which is potentially applicable to the full set of open spacecurves.

5.2.2 A generalised definition of open $\mathcal{W}$ using Fuller's theorems

Open $\mathcal{W}$ as measured by Fuller's first theorem

Applying the new general closure, the closed tantrix curve $\widehat{\mathbf{T}}(\mathbf{x}_{rc})$ will map out a signed area $\mathcal{A}_{cr}$ on the tantrix sphere. Using 1.26 we can evaluate $\mathcal{W}(\mathbf{x}_{rc})$ as

$$\mathcal{W}(\mathbf{x}_{rc}) = \frac{\mathcal{A}_{cr}}{2\pi} - 1 \pmod{2}. \tag{5.6}$$

$\mathcal{A}_{cr}$ can be split symmetrically into two areas, $\mathcal{A}_{orig}$ and $\mathcal{A}_{image}$. The first area represents the tantrix curve $\widehat{\mathbf{T}}(\mathbf{x}_{orig})$ and a geodesic curve ($\mathbf{g}$) joining its endpoints. $\mathcal{A}_{image}$ covers the area bound by $\widehat{\mathbf{T}}(\mathbf{x}_{image})$ and $\mathbf{g}$. Both areas will be of equal

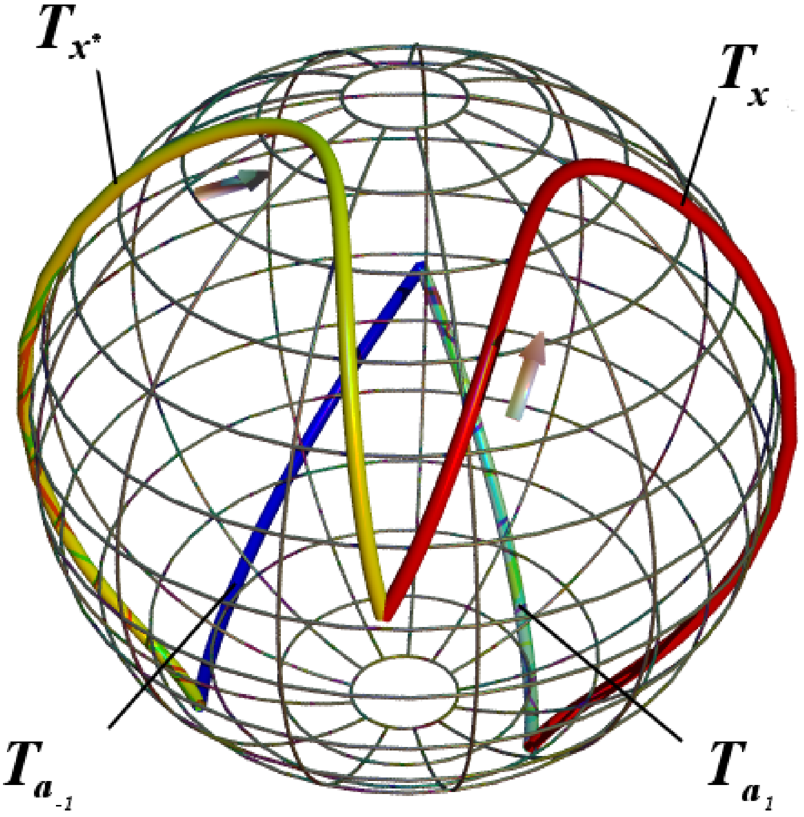

Figure 5.3: The tantrix curve of the fully closed curve $\mathbf{x}_{cr}$, based on an original curve $\mathbf{x}(t) = ((t-2)(t+2)t, t/2, e^{-0.2\frac{t^2}{2}})$, $t \in [-5, 2]$, which is depicted in 5.2. The various sections are marked and their coloring matches that in 5.2. The two sections $\widehat{\mathbf{T}}_{\mathbf{x}_{image}}$ and $\widehat{\mathbf{T}}_{\mathbf{x}_{orig}}$ can be separated by a geodesic section of curve joining the points at which they meet which would form two seperate areas of equal magnitude and sign.

magnitude and sign, hence

$$\mathcal{W}(\mathbf{x}) = \frac{1}{2}\mathcal{W}(\mathbf{x}_{rc}) = \frac{1}{2}(\frac{\mathcal{A}_{cr}}{2\pi} - 1) \pmod{1}. \tag{5.7}$$

Open $\mathcal{W}$ as measured by Fuller's second theorem

Consider a planar spacecurve $\mathbf{x}_{ref}(t)$, closed over the interval $t \in [a, c]$, which can be linked to the closure $\mathbf{x}_{rc}$, also $t \in [a, c]$. $\mathbf{x}_{rc}$ is built in the manner described in section 5.2.1 from the open spacecurve $\mathbf{x}(t), t \in [a, b]$, two planar sections of curve $\mathbf{a}_1(t)$, $t \in [b, b_e]$ and $\mathbf{a}_{-1}(t)$, $t \in [b_e, c_e]$, and the rotated image $\mathbf{x}_{rot}$, $t \in [c_e, c]$; where $a < b < b_e < c_e < c$. Assuming the non-opposition condition can be satisfied, the difference in $\mathcal{W}$ is given by (1.27) as

$$\mathcal{W}(\mathbf{x}_{rc}) - \mathcal{W}(\mathbf{x}_{ref}) = \frac{1}{2\pi}\int_a^c \frac{\widehat{\mathbf{T}}_{ref}(t) \times \widehat{\mathbf{T}}_{\mathbf{x}_{rc}}(t)}{1 + \widehat{\mathbf{T}}_{ref}(t) \cdot \widehat{\mathbf{T}}_{\mathbf{x}_{rc}}(t)} \cdot (\widehat{\mathbf{T}}'_{ref}(t) + \widehat{\mathbf{T}}'_{\mathbf{x}_{rc}}(t))\mathrm{d}t. \tag{5.8}$$

This can be split into two separate integrals. Noting $\mathcal{W}(\mathbf{x}_{ref}) = 0$,

$$\begin{aligned} \mathcal{W}(\mathbf{x}_{rc}) &= \tfrac{1}{2\pi}\int_a^{b_e} \tfrac{\widehat{\mathbf{T}}_{ref}(t)\times\widehat{\mathbf{T}}_{\mathbf{x}_{rc}}(t)}{1+\widehat{\mathbf{T}}_{ref}(t)\cdot\widehat{\mathbf{T}}_{\mathbf{x}_{rc}}(t)} \cdot (\widehat{\mathbf{T}}'_{ref}(t) + \widehat{\mathbf{T}}'_{\mathbf{x}_{rc}}(t))\mathrm{d}t \\ &+\tfrac{1}{2\pi}\int_{b_e}^{c} \tfrac{\widehat{\mathbf{T}}_{ref}(t)\times\widehat{\mathbf{T}}_{\mathbf{x}_{rc}}(t)}{1+\widehat{\mathbf{T}}_{ref}(t)\cdot\widehat{\mathbf{T}}_{\mathbf{x}_{rc}}(t)} \cdot (\widehat{\mathbf{T}}'_{ref}(t) + \widehat{\mathbf{T}}_{\mathbf{x}_{rc}}(t))\mathrm{d}t. \end{aligned} \tag{5.9}$$

Suppose we compare $\widehat{\mathbf{T}}_{\mathbf{x}_{orig}}(t)$ and $\widehat{\mathbf{T}}_{\mathbf{x}_{image}}(t')$ for $t \in [a, b_e]$ and $t' \in [b_e, c]$. We see that both $\widehat{\mathbf{T}}_{\mathbf{x}_{image}}(t')$ and $\widehat{\mathbf{T}}_{ref}(t'))$ have gone through the same transformation (the rotation of π) from $\widehat{\mathbf{T}}_{\mathbf{x}_{orig}}(t)$ and $\widehat{\mathbf{T}}_{ref}(t)$, so for $t' = c - t$,

$$\begin{aligned} &\widehat{\mathbf{T}}_{ref}(t) \times \widehat{\mathbf{T}}_{\mathbf{x}_{orig}}(t) \cdot (\widehat{\mathbf{T}}'_{ref}(t) + \widehat{\mathbf{T}}'_{\mathbf{x}_{orig}}(t)) \\ &= \widehat{\mathbf{T}}_{ref}(t') \times \widehat{\mathbf{T}}_{\mathbf{x}_{image}}(t') \cdot (\widehat{\mathbf{T}}'_{ref}(t') + \widehat{\mathbf{T}}'_{\mathbf{x}_{image}}(t')), \end{aligned} \tag{5.10}$$

and

$$\widehat{\mathbf{T}}_{ref}(t) \cdot \widehat{\mathbf{T}}_{\mathbf{x}_{orig}}(t) = \widehat{\mathbf{T}}_{ref}(t') \cdot \widehat{\mathbf{T}}_{\mathbf{x}_{image}}(t'), \tag{5.11}$$

for all $t \in [a, b_e]$, noting that $b_e - a = c - b_e$). Thus,

$$\begin{aligned} &\tfrac{1}{2\pi}\int_a^{b_e} \tfrac{\widehat{\mathbf{T}}_{ref}(t)\times\widehat{\mathbf{T}}_{\mathbf{x}_{rc}}(t)}{1+\widehat{\mathbf{T}}_{ref}(t)\cdot\widehat{\mathbf{T}}_{\mathbf{x}_{rc}}(t)} \cdot (\widehat{\mathbf{T}}'_{ref} + \widehat{\mathbf{T}}'_{\mathbf{x}_{rc}}(t))\mathrm{d}t = \\ &\tfrac{1}{2\pi}\int_{b_e}^{c} \tfrac{\widehat{\mathbf{T}}_{ref}(t)\times\widehat{\mathbf{T}}_{\mathbf{x}_{rc}}(t)}{1+\widehat{\mathbf{T}}_{ref}(t)\cdot\widehat{\mathbf{T}}_{\mathbf{x}_{rc}}(t)} \cdot (\widehat{\mathbf{T}}'_{ref}(t) + \widehat{\mathbf{T}}'_{\mathbf{x}_{rc}}(t))\mathrm{d}t. \end{aligned} \tag{5.12}$$

So we can rewrite 5.9 as

$$\mathcal{W}(\mathbf{x}_{rc}) = \frac{1}{\pi}\int_a^{b_e} \frac{\widehat{\mathbf{T}}_{ref}(t) \times \widehat{\mathbf{T}}_{\mathbf{x}_{rc}}(t)}{1 + \widehat{\mathbf{T}}_{ref}(t) \cdot \widehat{\mathbf{T}}_{\mathbf{x}_{rc}}(t)} \cdot (\widehat{\mathbf{T}}'_{ref}(t) + \widehat{\mathbf{T}}'_{\mathbf{x}_{rc}}(t))\mathrm{d}t. \tag{5.13}$$

As $\mathbf{a}_1$ and $\mathbf{a}_{-1}$ are planar sections of the spacecurve they will contribute nothing to the calculation (van der Heijden *et al* [114]). So we return to an expression for $\mathcal{W}$, applied to the closed curve $\mathbf{x}_{rc}$, which can be shown to depend entirely on the geometry of the open spacecurve $\mathbf{x}(t)$,

$$\mathcal{W}(\mathbf{x}_{rc}) = \frac{1}{\pi}\int_a^{b} \frac{\widehat{\mathbf{T}}_{ref}(t) \times \widehat{\mathbf{T}}_{\mathbf{x}}(t)}{1 + \widehat{\mathbf{T}}_{ref}(t) \cdot \widehat{\mathbf{T}}_{\mathbf{x}}(t)} \cdot (\widehat{\mathbf{T}}'_{ref}(t) + \widehat{\mathbf{T}}'_{\mathbf{x}}(t))\mathrm{d}t. \tag{5.14}$$

Finally we know that $\mathcal{W}(\mathbf{x}_{rc}) = 2\mathcal{W}(\mathbf{x})$, so we have an expression for the open $\mathcal{W}$ of $\mathbf{x}$

$$\mathcal{W}(\mathbf{x}) = \frac{1}{2\pi}\int_a^{b} \frac{\widehat{\mathbf{T}}_{ref}(t) \times \widehat{\mathbf{T}}_{\mathbf{x}}(t)}{1 + \widehat{\mathbf{T}}_{ref}(t) \cdot \widehat{\mathbf{T}}_{\mathbf{x}}(t)} \cdot (\widehat{\mathbf{T}}'_{ref}(t) + \widehat{\mathbf{T}}'_{\mathbf{x}}(t))\mathrm{d}t. \tag{5.15}$$

We conclude that the above expression can be applied to any open spacecurve $\mathbf{x}$ of $\mathcal{C}^3$ differentiability, as long as the non-opposition condition is satisfied for all ambient isotopies linking $\mathbf{x}_{ref}$ to $\mathbf{x}_{rc}$.

In terms of the unit sphere this equation has the same interpretation as that of its closed curve counterpart i.e., the spherical area enclosed by the great circle arcs joining the end point of $\widehat{\mathbf{T}}_1$ and $\widehat{\mathbf{T}}_0$. The only difference in this case is that both curves are open on the unit sphere. If the non-opposition is adhered to this is equivalent to the Gauss mapping for a curve $\mathbf{x}$.

Reference curves and the non-opposition condition

The expression (5.15) has an explicit dependence on $\mathbf{x}_{ref}$. However, as long as the non-opposition condition is satisfied, and $\mathbf{x}_{ref}$ is planar, this will have no effect on the value of $\mathcal{W}(\mathbf{x})$. The reference curve does however cause this open writhe measure to have a restricted sense of rotational invariance. If both the reference curve and $\mathbf{x}_{rc}$ are both subject to the same rotation the measure will remain constant and will satisfy the non-opposition condition. However if only $\mathbf{x}_{rc}$ is rotated there will in general be some set of rotations which violate the non-opposition condition. For example consider the reference curve starting in the plane perpendicular to $\mathcal{L}_{axis}$ and oriented such that its tantrix curve is parallel to the tantrix curve of $\mathbf{x}_{rc}$ on the axis itself. Such a pairing would satisfy the non-opposition condition. If $\mathbf{x}_0$ is then rotated about its plane through π rad it will then violate the non-opposition at both points on $\mathcal{L}_{axis}$. This conclusion is similar to that of van der Heijden *et al* [114], where their discussion concerns a planar closure.

5.3 Polar writhe and open spacecurves

The polar writhe framework is well-defined for all open curves $\mathbf{x}$. However, the open curve properties of $\mathcal{W}_p(\mathbf{x}, \hat{a})$ are not in general the same as those for closed curves.

5.3.1 Properties of $\mathcal{W}_p$ for open spacecurves

- One can define closures which can be applied to all spacecurves and will not affect the evaluation of $\mathcal{W}_p$.
- $\mathcal{W}_p$ is **not** rotationally invariant [1] and hence **not** constant conformally invariant. It is, however, invariant to both translations and homogeneous dilations (except those which reduce $\mathbf{x}$ to a point).
- $\mathcal{W}_p$ does not change continually upon deformation due to the disjoint nature of $\mathcal{W}_{pnl}$.
- $\mathcal{W}_{pl}$ is invariant to the reversal $s \to -s$.
- $\mathcal{W}_{pnl}$ changes by a value of ± 2 when the curve is passed through itself.

5.3.2 Polar writhe closures

It is not necessary to apply a closure in order to evaluate $\mathcal{W}_p$. However, in some cases closures do exist where $\mathcal{W}_p(\mathbf{x})$ is equivalent to the writhe of the closed curve, i.e. $\mathcal{W}(\mathbf{x} + \mathbf{x}_c) \equiv \mathcal{W}_p(\mathbf{x})$.

A curve stretching between two planes

Consider an arbitrary open spacecurve $\mathbf{x}(s)$ for which $\mathrm{d}s/\mathrm{d}z > 0$. We attach two planar segments of spacecurve $\mathbf{a}_1$ and $\mathbf{a}_{-1}$, to $\mathbf{x}(L)$ and $\mathbf{x}(0)$ respectively. These

---

[1] The question of what averaging the polar writhe over all possible evaluation direction is an open question. It is not immediately clear if such a measure is even itself rotationally invariant.

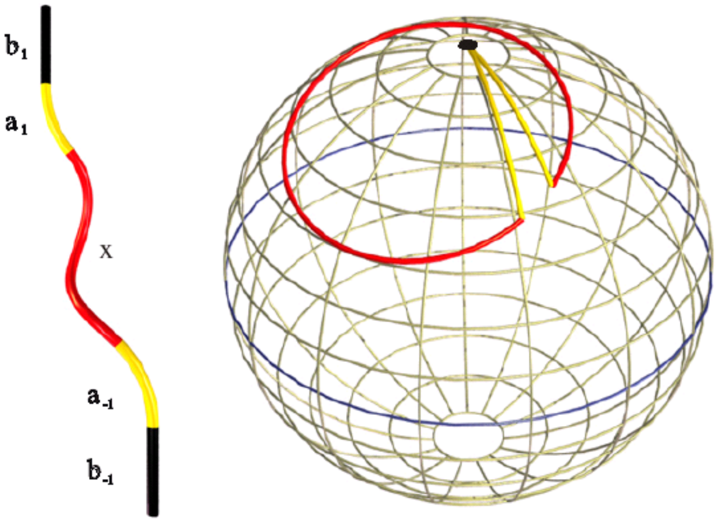

Figure 5.4: An open curve $\mathbf{x}$ has been extended by adding circle segments $\mathbf{a}_1$ and $\mathbf{a}_{-1}$, then vertical lines $\mathbf{b}$ and $\mathbf{b}_{-1}$. This curve is a helix inclined by a small angle with respect to the vertical (so the tantrix does not centre on the north pole). The helix winds through a phase of 1.9π. For this curve, the polar writhe is $\mathcal{W}_p = -0.145$. The associated tantrix curve is also shown.

sections extend the curve smoothly, such that its end tangents will align with $\hat{z}$ and oppose it respectively. The closure is then extended to ∞ and $-\infty$, via straight line sections $\mathbf{b}_1(s)$ and $\mathbf{b}_{-1}(s)$, parallel and anti-parallel to $\hat{z}$. Thus the curve is closed at infinity, with the extensions (see Figure 5.4) contributing nothing to $\mathcal{W}_z$ as they are planar.

Alternatively rather than extend $\mathbf{b}_1(s)$ and $\mathbf{b}_{-1}(s)$ to $\pm\infty$ they can be connected, with a planar section of curve (again denoted $\mathbf{c}$), to form a finite closed curve. It is required that, for the period in which the z range of $\mathbf{c}$ is equal to that of the curve $\mathbf{x}(z)$, $\mathbf{c}$ is oriented such that there is no net non-local winding between the two.

The unit sphere interpretation in both cases is the area between the tantrix curve (of axiscurve) and two geodesic arcs joinig the tantrix curves endpoints to the north pole (see Figure 5.4). If we applied Fuller's first theorem, to this closure, the area $\mathcal{A}$ in equation (1.26) would be the same.

A curve whose end points lie on the same plane

Such a curve, as depicted in Figure 5.5, in which both end points lie on a mutual plane $z = z_{min}$, can be closed by extending its endpoints with two planar curve

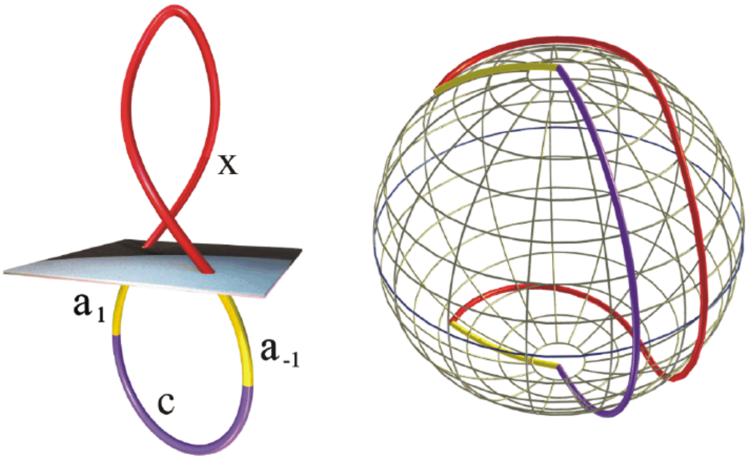

Figure 5.5: An open curve $\mathbf{x}$ in the form of a loop with endpoints on the same horizontal plane, has been extended by adding circle segments $\mathbf{a}_1$ and $\mathbf{a}_{-1}$, then a semicircle $\mathbf{c}$. The associated tantrix curve is also shown. This curve is a representation of the twisted parabola curve, defined by equation (4.6) with $\Theta = 3\pi/4$ and $h = 1.5$. It has a polar writhe measure of $\mathcal{W}_p = 0.55$.

sections $\mathbf{a}_1(0) = \mathbf{x}(L)$ and $\mathbf{a}_{-1} = \mathbf{x}(0)$. These sections extend the curve below z_{min}, in a smooth manner, such that they the both point along $\hat{z}$ at a mutual height $z < z_{min}$. This can then be joined by a semi-circular section of curve $\mathbf{c}$ as depicted in Figure 5.5. In order to reduce the $\mathcal{W}_p$ measure to that of the original curve $\mathbf{x}$, $\mathbf{a}_1$ and $\mathbf{a}_{-1}$ are made arbitrarily small and will as such accumulate a negligible $\mathcal{W}_{pnl}$ measure.

The unit sphere interpretation of this construct is depicted in Figure 5.5. It is represented by two geodesic lines joining $\widehat{\mathbf{T}}_{\mathbf{x}}(0)$ and $\widehat{\mathbf{T}}_{\mathbf{x}}(L)$ to both the north and south poles respectively. If at $\widehat{\mathbf{T}}_{\mathbf{x}}(0)$, $\mathrm{d}s/\mathrm{d}z > 0$, it will be joined to the north pole, and thus $\widehat{\mathbf{T}}_{\mathbf{x}}(L)$ joined to the south pole, or vice versa (note both endpoints will always lie in opposite hemispheres). The area is completed by a great circle arc joining the poles. The orientation of this great circle arc is such that its azimuthal angle ϕ matches the orientation in the x-y plane of the semi-circular closure section $\mathbf{c}$.

5.3.3 Open $\mathcal{W}_{pl}$

The tantrix sphere interpretation of $\mathcal{W}_{pl}$, applied to open spacecurves, is almost the same as that for closed spacecurves. The only difference is that the start and end

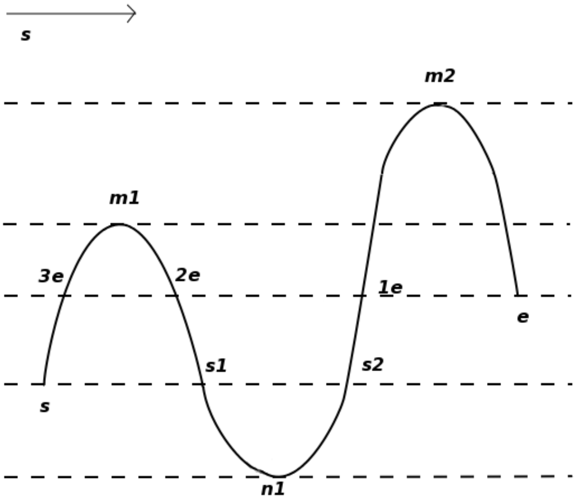

Figure 5.6: A plot of $\mathbf{x}_z(s)$ against s of an open spacecurve $\mathbf{x}(s)$. Marked on the diagrams are the local maxima (m_1 and m_2) and minima (n_1), the start (s) and end points (e), and all points which share z values with s (s_1, s_2) and e (e_1, e_2 and e_3).

points $\widehat{\mathbf{T}}_{\mathbf{x}}(0)$ and $\widehat{\mathbf{T}}_{\mathbf{x}}(L)$ do not necessarily lie on the equator of the unit sphere.

As discussed in section 3.3.2 $\mathcal{W}_{pl}$ is invariant to the transformation $s \rightarrow -s$.

5.3.4 Open $\mathcal{W}_{pnl}$

Measuring the non-local winding of open spacecurves is a more complex undertaking that the equivalent closed curve measure. As shall be demonstrated, this is a congruence of the differing start and end tangents $\widehat{\mathbf{T}}_{\mathbf{x}}(0)$ and $\widehat{\mathbf{T}}_{\mathbf{x}}(L)$.

Theorem 5 *Consider an open spacecurve* $\mathbf{x}(s)$, $s \in [0, L]$, *which has m local maxima in the* $\hat{z}$ *direction, and n local minima. We label its start and end points* $\mathbf{x}_s(s=0)$ *and* $\mathbf{x}_e(s=L)$ *respectively. All l points on the curve which share a z value with* $\mathbf{x}_s$ *will be labelled* $\mathbf{x}_{s_1}, \mathbf{x}_{s_2}, ...\mathbf{x}_{s_l}$ *in* ***ascending*** *order of s from* $\mathbf{x}_s$*. All k points on the curve which share a z value with* $\mathbf{x}_e$ *will be labelled* $\mathbf{x}_{e_1}, \mathbf{x}_{e_2}, ...\mathbf{x}_{e_k}$ *in* ***descending*** *order of s from* $\mathbf{x}_e$*. We define* $\phi(\mathbf{x}_{n/m})$ *as the tangent angle of orientation at turning point n/m (n/m indicates n or m not a fraction),* Φ_{s,s_v} *represents the total angle of orientation (inclusive of sign) between* $\mathbf{x}_s$ *and the vth* ($v = 1, 2, ...l$) *point* $\mathbf{x}_{s_i}$ *and* Φ_{e,e_w} *as the total angle of orientation (inclusive of sign) between the wth* ($w = 1, 2, ...k$) $\mathbf{x}_{e_w}$ *and* $\mathbf{x}_e$*. The open non-local polar writhe* $\mathcal{W}_{pnl}$ *of* $\mathbf{x}$ *can be* *defined as.*

$$2\pi \mathcal{W}_{pnl}(\mathbf{x}) = \sum_{i=1}^{m} \phi(\mathbf{x}_m) - \sum_{j=1}^{n} \phi(\mathbf{x}_n) + \sum_{v=1}^{l} \Phi_{s,s_v} + \sum_{w=1}^{k} \Phi_{e,e_w} \tag{5.16}$$

Where the signs prefixed to Φ_{s,s_v} and Φ_{e,e_w} are given by,

$$\mathcal{W}_{pnl}(s/e) = \begin{cases} \sum_{v=1}^{l} (-1)^{l+1}\Theta_{s,s_v} + \sum_{w=1}^{k} (-1)^{k}\Theta_{e,e_w} \text{ if } \widehat{\mathbf{T}}_s(0) \geq 0 \text{ and } \widehat{\mathbf{T}}_e(L) \geq 0 \\ \sum_{v=1}^{l} (-1)^{l}\Theta_{s,s_v} + \sum_{w=1}^{k} (-1)^{k}\Theta_{e,e_w} \text{ if } \widehat{\mathbf{T}}_s(0) \leq 0 \text{ and } \widehat{\mathbf{T}}_e(L) \geq 0 \\ \sum_{v=1}^{l} (-1)^{l}\Theta_{s,s_v} + \sum_{w=1}^{k} (-1)^{k+1}\Theta_{e,e_w} \text{ if } \widehat{\mathbf{T}}_s(0) \geq 0 \text{ and } \widehat{\mathbf{T}}_e(L) \leq 0 \\ \sum_{v=1}^{l} (-1)^{l+1}\Theta_{s,s_v} + \sum_{w=1}^{k} (-1)^{k+1}\Theta_{e,e_w} \text{ if } \widehat{\mathbf{T}}_s(0) \leq 0 \text{ and } \widehat{\mathbf{T}}_e(L) \leq 0. \end{cases} \tag{5.17}$$

Proof of Theorem 5 In order to assess all contributions to $\mathcal{W}_{pnl}$ we must consider the four possible individual contributions to $\mathcal{W}_{pnl}$.

- Those whose calculation involve a tangent angle of a turning point $\phi(\mathbf{x}_k)$
- Those which involve either the start or end points.
- Those which do not involve a tangent angle of $\phi(\mathbf{x}_k)$, or a start/end point, but do involve a turning point $\mathbf{x}_k$.
- those which involve none of the above

N.b., contributions involving both a tangent angle and a start/end point contribution have no special role here. Their behaviour is captured by the first two possibilities.

If we consider first the case in which there are no distinct points (non-critical contributions) involved in the calculation. We see such an example in Figure 5.7. The contribution $\mathcal{W}_{pnl}(\mathbf{x}_i, \mathbf{x}_j)$ is

$$\mathcal{W}_{pnl}(\mathbf{x}_i, \mathbf{x}_j) = \sigma_i \sigma_j (\Theta_{(i+1)(j-1)} - \Theta_{i,j} + \omega_{ij}). \tag{5.18}$$

Here ω_{ij} is some integer number of full windings between $\Theta_{(i+1),(j-1)}$ and $\Theta_{i,j}$. In this scenario there will always be a contribution due to curve sections between $\mathbf{x}_i$ and $\mathbf{x}_j$ which involve a turning point (that is, if the contribution of $\mathbf{x}_i$ and $\mathbf{x}_j$ has no critical contributions itself). In this particular case it will occur in the calculation $\mathcal{W}_{pnl}(\mathbf{x}_{(i+1)}, \mathbf{x}_{(j-1)})$

$$\mathcal{W}_{pnl}(\mathbf{x}_{(i+1)}, \mathbf{x}_{(j-1)}) = \sigma_{i+1} \sigma_{j-1} (\phi_{(i+2)} - \Theta_{(i+1)(j-1)} + \omega_{(i+1)(j-1)}). \tag{5.19}$$

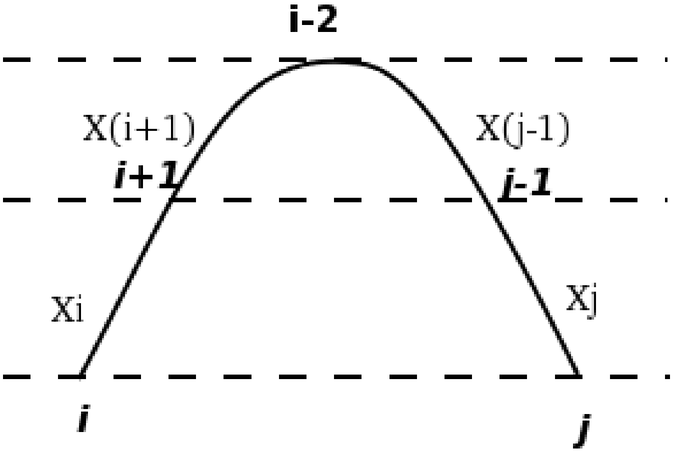

Figure 5.7: A section of curve $\mathbf{x}_z(s)$ belonging to a spacecurve $\mathbf{x}(s)$. The $\mathcal{W}_{pnl}$ of this curve section is split into two contributions $\mathcal{W}_{pnl}(\mathbf{x}_i, \mathbf{x}_j)$ (which includes no turning points or start/ end orientations) and $\mathcal{W}_{pnl}(\mathbf{x}_{(i+1)}\mathbf{x}_{(j-1)})$ (which includes a turning point contribution).

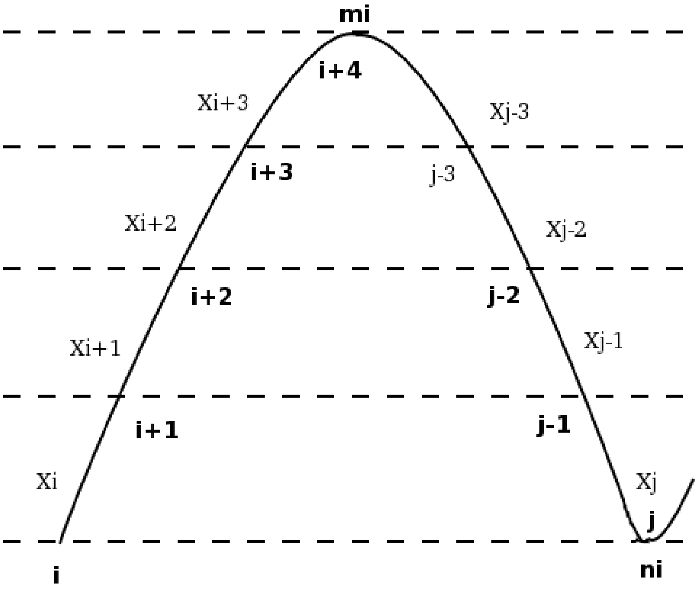

Figure 5.8: A section of curve $\mathbf{x}_z(s)$ belonging to a spacecurve $\mathbf{x}(s)$, which has several $\mathcal{W}_{pnl}$ contributions is shown. The middle contributions $\mathcal{W}_{pnl}(\mathbf{x}_{(i+1)}, \mathbf{x}_{(j-1)})$ and $\mathcal{W}_{pnl}(\mathbf{x}_{(i+2)}, \mathbf{x}_{(j-2)})$ can be shown to cancel out over the total $\mathcal{W}_{pnl}(\mathbf{x})$ calculation.

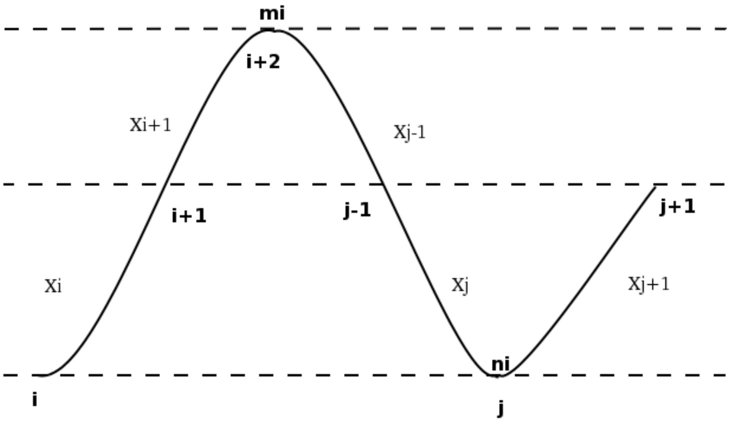

Figure 5.9: A section of $\mathbf{x}_z(s)$ used to demonstrate that all orientations involving a turning point, except the tangent of the turning point, will cancel.

We note the following

$$\sigma_{i+1} = \sigma_i, \tag{5.20}$$

$$\sigma_{j-1} = \sigma_j. \tag{5.21}$$

There are two contributions in (5.18) and (5.19), involving $\Theta_{(i+1),(j+1)}$, which are prefaced by opposing signs, thus canceling. The same analysis can be applied for sections of $\mathbf{x}$ for which there are many non-critical contributions (contributions from $(\mathbf{x}_{(i+1)}, \mathbf{x}_{(j-1)})$ and $(\mathbf{x}_{(i+2)}, \mathbf{x}_{(j-2)})$ depicted in Figure 5.8). All contributions bar the top and bottom, which both involve turning point orientations, will cancel. The same logic can be applied to local minima. Thus all non-critical contributions will cancel.

It can also be shown orientations which involve a turning point will cancel. Consider a contribution $\mathcal{W}_{pnl}(\mathbf{x}_i, \mathbf{x}_j)$ as depicted in Figure 5.9). We see $\mathbf{x}_j$ is linked to a turning point.

$$\mathcal{W}_{pnl}(\mathbf{x}_i, \mathbf{x}_j) = \sigma_i \sigma_j (\Theta_{(i+1),(j-1)} - \Theta_{i,j} + \omega_{ij}). \tag{5.22}$$

Now let us consider the contribution $\mathcal{W}_{pnl}(\mathbf{x}_i, \mathbf{x}(j+1))$ (Figure 5.9)

$$\mathcal{W}_{pnl}(\mathbf{x}_i, \mathbf{x}_{(j+1)}) = \sigma_i \sigma_{j+1} (\Theta_{(i+1),(j+1)} - \Theta_{i,j} + \omega_{i(j+1)}). \tag{5.23}$$

However, $\sigma_{j+1} = -\sigma_j$, so again there are two contributions from $\Theta_{i,j}$ which, when combined, will cancel each other out. This logic can be applied to the other three possibilities in which the turning point is found at i, $(i+1)$ and $(j-1)$, thus all orientations which involve a turning point, but which are not a tangent, will not appear in the overall calculation.

So far we have shown all contributions except those of the turning point tangents ϕ and any orientations involving the start or end points, cancel. As with the closed curve case (section 3.2.5) all ϕ will be counted twice in any calculation. Local maxima will always be prefaced with a positive sign and local minima a negative sign. So their contribution to $\mathcal{W}_{pnl}$ can be summed as follows

$$2(\sum_{i=1}^{m}\phi(\mathbf{x}_m) - \sum_{j=1}^{n}\phi(\mathbf{x}_n)). \tag{5.24}$$

It can further be shown all start or end point contributions will not cancel, and be counted twice. $\mathbf{x}_s$ and $\mathbf{x}_e$ essentially act like turning points in $\mathcal{W}_{pnl}$, in the sense that they mark z values about which non-local winding occurs. In the case of turning points there are always two sections of spacecurve attached either side of the turning point (see Figure 5.9). As we saw in the case of orientations involving turning points, which were not tangents themselves, the second section, to the right of the curve, provided an orientation vector which cancels the same vector from the left hand curve section. In the case of start and end points the second cancelling curve branch does not exist. Thus we see orientation anchored at the start and end points will not be removed from the $\mathcal{W}_{pnl}$ evaluation. Further these contributions will be counted twice.

With regards to the start point orientations, the relative signs prefacing Θ_{s,s_n} depend on the initial gradient as $\mathbf{x}(s)$. If the tangent of $\mathbf{x}(s)_z$ has a positive gradient then the start point orientation Θ_{s,s_v} will supply the negatively signed component of the evaluation $\mathcal{W}_{pnl}(\mathbf{x}_{s_v})$ (see Figure 5.10). This is because the contributions will be evaluated over ranges $z \in [z_{min}, z_{max}]$ for which z_{min} will always be the height of s. The tangent at $\mathbf{x}_{s_1}$ will have a negative gradient, so $\sigma_s\sigma_{s_1} = -1$. This will leave Θ_{s,s_1} with a positive sign. Moving on the tangent at $\mathbf{x}_{s_2}$ has a positive gradient, thus $\sigma_s\sigma_{s_2} = 1$. So Θ_{s,s_2} will be prefaced by a $-$ sign. This pattern will repeat itself for all Θ_{s,s_v} with the prefacing sign alternating as $(-1)^{(l+1)}$.

Alternatively if the tangent at $\mathbf{x}_s$ has a negative gradient Θ_{s,s_1} will always supply the positive part of $(\Theta_{(i+1),j} - \Theta_{i,(j+1)})$. Applying the same logic the sign prefacing Θ_{s,s_l} will alternate as $(-1)^l$.

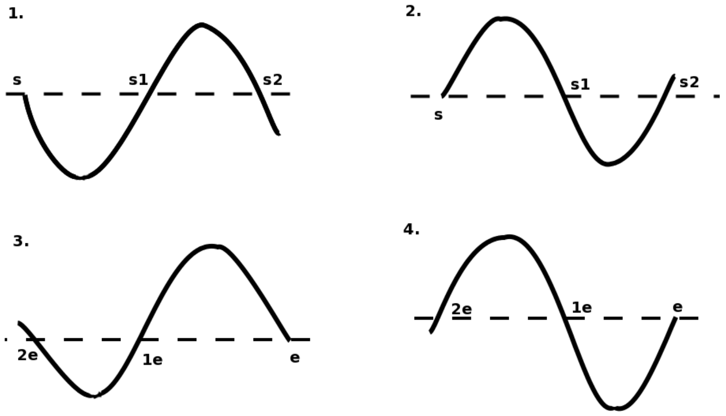

Figure 5.10: The four figures represent $\mathbf{x}_z(s)$ of a general curve. Figures 1 and 2 represent the two possibilities from the start point of the curve and 3 and 4 the two possible end point cases (in tems of the maxima/minima ordering). Using these four diagrams we can infer the pattern of the sign which prefaces both start and end point contributions $\Theta_{s/e,s/e_n}$, for all n. The top two demonstrate the cases for start point orientations which have both a positive and negative initial gradient. The bottom diagrams do the same for the end point contributions

For $\mathbf{x}_e$ contributions the sign patterns swap. So if the tangent at $\mathbf{x}_e$ has a positive gradient the prefacing sign for all Θ_{e,e_w}, as we move away from e, will alternate as $(-1)^k$ and for a negative gradient $(-1)^{(k+1)}$, thus,

$$\mathcal{W}_{pnl}(s/e) = \begin{cases} \sum_{v=1}^{l}(-1)^{l+1}\Theta_{s,s_v} + \sum_{w=1}^{k}(-1)^{k}\Theta_{e,e_w} \text{ if } \widehat{\mathbf{T}}_s(0) \geq 0 \text{ and } \widehat{\mathbf{T}}_e(L) \geq 0 \\ \sum_{v=1}^{l}(-1)^{l}\Theta_{s,s_v} + \sum_{w=1}^{k}(-1)^{k}\Theta_{e,e_w} \text{ if } \widehat{\mathbf{T}}_s(0) \leq 0 \text{ and } \widehat{\mathbf{T}}_e(L) \geq 0 \\ \sum_{v=1}^{l}(-1)^{l}\Theta_{s,s_v} + \sum_{w=1}^{k}(-1)^{k+1}\Theta_{e,e_w} \text{ if } \widehat{\mathbf{T}}_s(0) \geq 0 \text{ and } \widehat{\mathbf{T}}_e(L) \leq 0 \\ \sum_{v=1}^{l}(-1)^{l+1}\Theta_{s,s_v} + \sum_{w=1}^{k}(-1)^{k+1}\Theta_{e,e_w} \text{ if } \widehat{\mathbf{T}}_s(0) \leq 0 \text{ and } \widehat{\mathbf{T}}_e(L) \leq 0. \end{cases} \tag{5.25}$$

By designating Φ_{s,s_v} and Φ_{e,e_w} the sign-inclusive orientations, which take into account any full windings ω_{s,s_v} or ω_{e,e_w} we can rewrite this as a single equation;

$$2(\sum_{v=1}^{l}\Phi_{s,s_v} + \sum_{w=1}^{k}\Phi_{e,e_w}). \tag{5.26}$$

So by combining (5.26) and (5.24) we obtain the right hand side expression for $\mathcal{W}_{pnl}(\mathbf{x})$. Finally we note, as with the closed curve case, each orientation will be double counted leading to the factor of 2π (rather than 4π) on the left hand side of

(5.16).

A unit sphere interpretation of open $\mathcal{W}_{pnl}$

In contrast to the closed curve case, using the above definition of $\mathcal{W}_{pnl}$ (5.16), it is necessary to consider the contributions of orientations anchored by the start ($\mathbf{x}(0)$) and end points ($\mathbf{x}(L)$), denoted $\Phi_{s,s_{i_l}}$ and $\Phi_{k_e,e}$, as well as the turning point contributions.

Considering first the turning point contributions. As with the closed curve the double counting of each contribution means we can pair neighbouring turning point $n = m$ to give the area bound between the longitudinal lines ϕ_m and ϕ_n. The first departure we see from the closed curve case is the possibility of unpaired turning points ($i \neq j$).

Similarly the start and end point contributions can be paired up. A logical choice would be to pair all contributions $v = w$ i.e. Φ_{s,s_1} and Φ_{e,e_1}, Φ_{s,s_2} and Φ_{e,e_2} etc., to form contributions $\pm\frac{2}{2\pi}(\Phi_{s,s_1} - \Phi_{e,e_1})$, Φ_{s,s_2} and Φ_{e,e_2} etc. Depending on the start and end gradients the geometrical interpretation of such pairings would be the area bound between the longitudinal lines representing Φ_{s,s_1} and Φ_{e,e_1}. Such an area can always be chosen to be positive. Again there may be an imbalance in the number of start and end contributions.

The total number of contributions to $\mathcal{W}_{pnl}$ from all counted orientations in 5.16 is always even. Thus by pairing a single turning point contributions with a start or end orientation one can always obtain a pairing and hence a longitudinally bound area interpretation.

Helices and their $\mathcal{W}_p$ unit sphere interpretation

Consider the following helical curve

$$\mathbf{x}(t) = \{\sin 2\pi t, \cos 2\pi t, t\}, \tag{5.27}$$

depicted in Figure 5.3.4, which wraps itself about the $\hat{z}$ axis. Evaluating the polar writhe of the helix curve along this axis ($\mathcal{W}_p(\mathbf{x}(t))$), leads to a measure consisting of only local writhing. As shown in Figure 5.3.4 this translates to a tantrix area bounded by $\widehat{\mathbf{T}}_{\mathbf{x}}$ and the north pole.

An evaluation of $\mathcal{W}_p(\mathbf{x}, \hat{y})$ is vastly different. In terms of $\hat{y}$ the curve reaches a

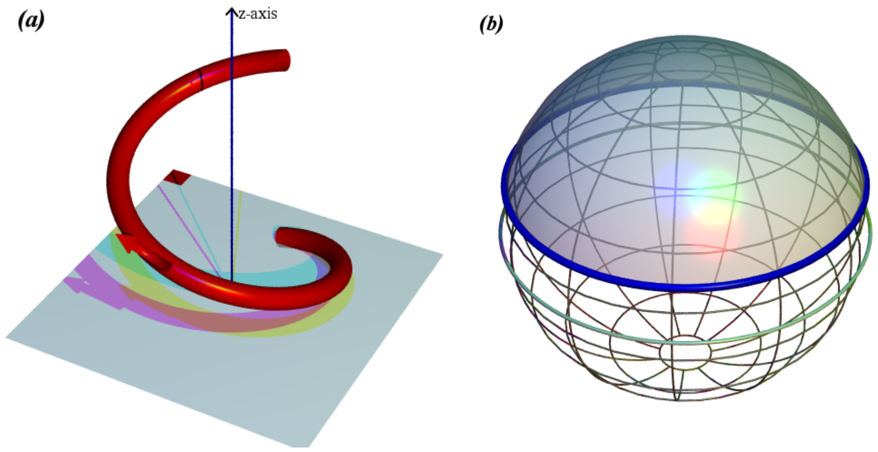

Figure 5.11: (a) represents helix $\mathbf{x}(t) = \{\sin 2\pi t, \cos 2\pi t, t\}$ evaluated over the period $t \in [0, 1]$. (b) is its tantrix curve $\widehat{\mathbf{T}}_{\mathbf{x}}$ representation. This curve has a $\mathcal{W}_{pl}$ measure of -0.842823 and no $\mathcal{W}_{pnl}$.

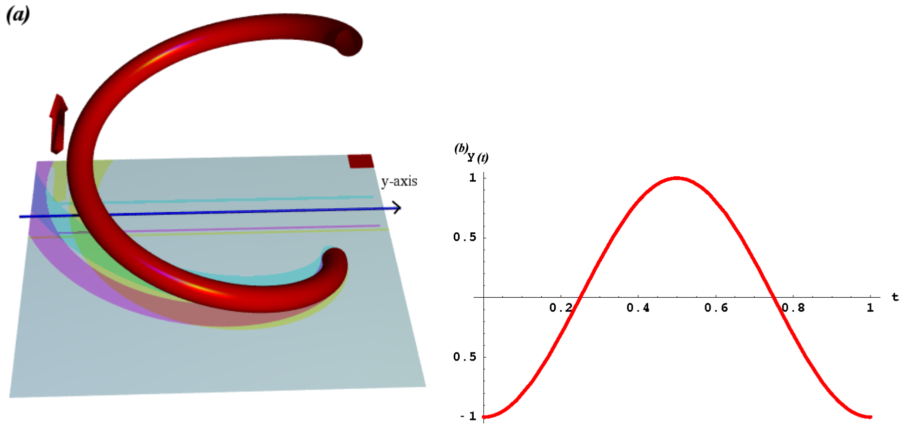

Figure 5.12: (a) represents the helix $\mathbf{x}(t) = \{\sin 2\pi t, \cos 2\pi t, t\}$ evaluated over the period $t \in [0, 1]$ as viewed by an observer perpendicular to the $\hat{y}$ axis. (b) is a plot of the $y(t)$ as viewed along the $\hat{y}$ direction. Its $\mathcal{W}_p$ value is -1.6967.

maximum at $t = 0.5$ and is minimal at $t = 0$ and $t = 1$ (Figure 5.12), thus the helix must exhibit non-local writhing about $\hat{y}$. We expect a single contribution to $\mathcal{W}_{pnl}$ between $\phi_{0.5}$ and $\Phi_{0,1}$ of

$$\mathcal{W}_{pnl}(\mathbf{x}) = \frac{1}{\pi}(1)(-1)\left(\phi(\mathbf{x}(0.5)) - \Phi_{0,1}\right), \tag{5.28}$$

which in this case gives us $\mathcal{W}_{pnl}(\mathbf{x}) = -1.80381$. We also expect two contributions to $\mathcal{W}_{pl}(\mathbf{x})$ from the periods $t \in [0, 0.5]$ and $t \in [0.5, 1]$, which will be $\mathcal{W}_{pl} = 0.107129$.

The unit sphere area interpretation of $\mathcal{W}_p(\mathbf{x}, \hat{y})$ is depicted in Figure 5.13. The two areas representing $\mathcal{W}_{pl}$ and $\mathcal{W}_{pnl}$ can be seen to coincide. Also the $\mathcal{W}_{pnl}$ area is of opposite sign to that of the $\mathcal{W}_{pl}$ contribution, and they will cancel leaving an area which is generally not simply connected. This area would be difficult to use as a tool of comparison with the $\mathcal{W}$ and $\mathcal{W}_z$ measures which are generally bound by a single (piecewise smooth) boundary curve. The helix represents one of the simpler non trivial open curves. More complex curves would lead to unit sphere diagrams which will be very difficult to interpret. This is a result of the existence of the start/end point contributions which do not tend to coincide with $\widehat{\mathbf{T}}_{\mathbf{x}}$ crossing the equator in the neat manner we saw for closed spacecurves. One benefit of the tantrix diagrams was their relative ease of interpretation. In Chapter 2 the tantrix areas bound by the various writhe measurements were used as a means for comparing and contrasting each measurement. For open spacecurves the unit sphere diagrams, associated with $\mathcal{W}_p$, will not always represent an effective tool for analysis. Unless that is, the curve under consideration has a strong directional bias and an appropriate direction of evaluation is chosen. In the following we will explore the relationship between $\mathcal{W}_p(\mathbf{x}, \hat{a})$ and $\hat{a}$ by way of a set of example studies.

5.3.5 Selecting the direction of evaluation of $\mathcal{W}_p(\mathbf{x}, \hat{a})$

We have seen that the choice of viewpoint can affect the evaluation produced by $\mathcal{W}_p$. By tracking the evolution of $\mathcal{W}_p(\mathbf{x}, \hat{a})$, $\mathcal{W}_{pl}(\mathbf{x}, \hat{a})$ and $\mathcal{W}_{pnl}(\mathbf{x}, \hat{a})$ as $\hat{a}$ is rotated, from $\hat{z}$, about the y-z axis, through an angle $\theta \in [0, 2\pi]$, we may be able to gain an insight into the effect of changing $\hat{a}$. The non-smoothly altering nature of $\mathcal{W}_p$ is demonstrated in Figure 5.14. $\mathcal{W}_p$ stays constant up until a value of $\theta \approx 0.4$. Up until this point the only contribution to $\mathcal{W}_p$ is $\mathcal{W}_{pl}$ (Figure 5.14). Once this critical angle has been reached, there is a gradual decrease of $\mathcal{W}_{pl}$ and increase of $\mathcal{W}_{pnl}$, though there exists no obvious consistent relationship between their rates of change.

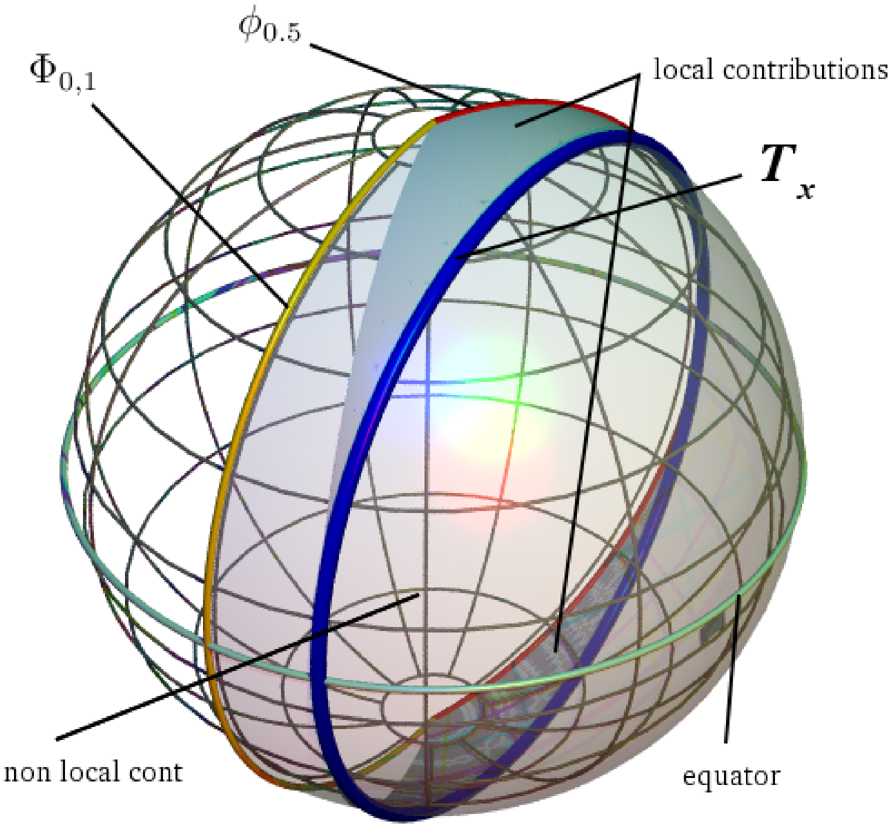

Figure 5.13: The unit sphere area interpretation of $\mathcal{W}_p(\mathbf{x}, \hat{y})$. Note, the pole here represents the $\hat{y}$ direction. We see two types of areas superimposed on each other. The transparent area represents $\mathcal{W}_{pnl}$ and the solid area $\mathcal{W}_{pl}$. Also marked are the geodesic longitudinal lines representing $\phi_{0.5}$ (the turining point tangent orientation at $t = 0.5$) and $\Phi_{0,1}$ (the startpoint to endpoint and orientation). As the two contributions are oppositely signed they will cancel where they coincide, leaving a non-simply connected area.

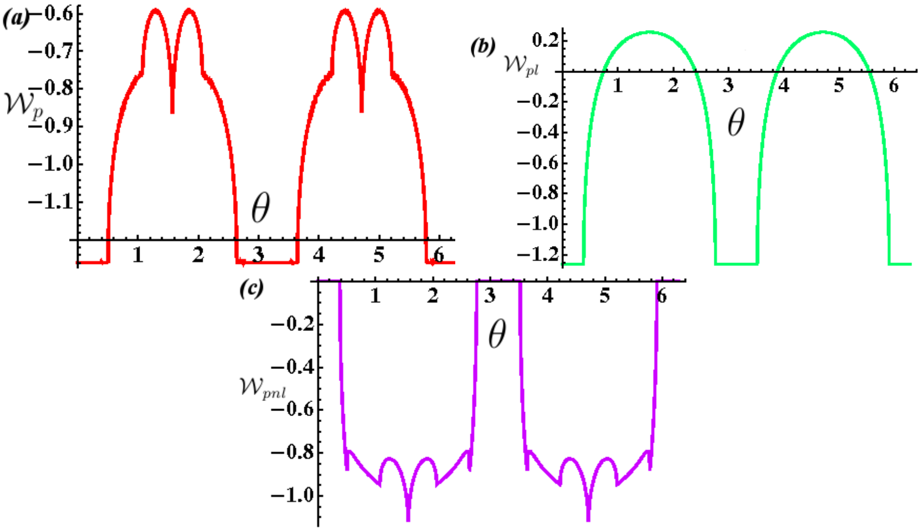

Figure 5.14: Plots of $\mathcal{W}_p(\mathbf{x}(t))$ (a), $\mathcal{W}_{pl}(\mathbf{x}(t))$ (b) and $\mathcal{W}_{pnl}(\mathbf{x}(t))$ (c), for $t \in [0,1]$, $\mathbf{x}(t) = (\sin 4\pi t, \cos 4\pi t, t)$ against θ, for $\theta \in [0, 2\pi]$. Here θ represents the viewing direction of the curve about the z-y plane, with the viewpoint set at $\hat{z}$ for $\theta = 0$ and $\theta = 2\pi$ and $\theta = \pi \equiv -\hat{z}$.

Careful observation of figure 5.14 shows the discontinuous changes in $\mathcal{W}_p$ coincide with those of $\mathcal{W}_{pnl}$, with the changes of $\mathcal{W}_{pl}$ being generally smooth whilst $\mathcal{W}_{pnl}$ is being registered. Clearly the non smooth fluctuations of $\mathcal{W}_p$ occur as a result of the interpretation of the non-local writhing attributed to a spacecurve. The propensity of $\mathcal{W}_{pnl}$ and $\mathcal{W}_p$ to change, suddenly and drastically, advises the user to exercise great caution when applying a polar writhe evaluation for a spacecurve.

The pertinent question is what information is required or expected to be seen from the calculation? If this helix were in fact an electric coil with current flowing through the helix (along the direction of increasing arclength), where the helices central axis is directed along $\hat{z}$, the magnetic field lines would flow down the middle of the coil. This is a consequence of the local coiling of the electric field about the obvious symmetry axis. In such a scenario it would be prudent to choose $\hat{z}$ as a direction of evaluation, as this points directly along the magnetic field lines path and will register only local writhing. Using an informed choice the measurement, $\mathcal{W}_p$ can accurately capture the **relevant** local and global geometrical behavior of the system. In this case the non-local windings of the coil, implied by alternative viewpoints, are essentially redundant data not relevant to the physics of the system. Should the coil be shaped such that it has both local and non-local windings, for

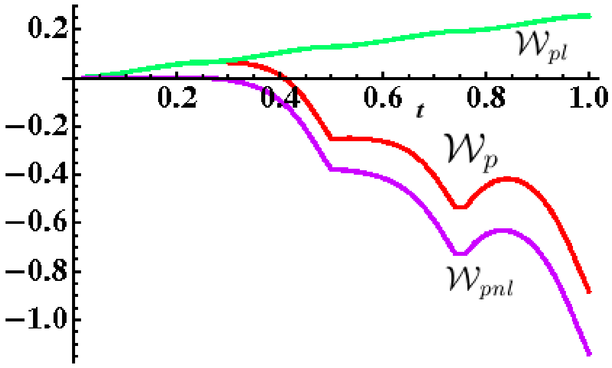

Figure 5.15: Plots of $\mathcal{W}_p(\mathbf{x},\hat{y})$, $\mathcal{W}_{pl}(\mathbf{x},\hat{y})$ and $\mathcal{W}_{pnl}(\mathbf{x},\hat{y})$ against parameter t, for the helix, over a period $t \in [0,1]$, with the choice of direction of evaluation of $\mathcal{W}_p$ lying along the y-axis. We see as the helix develops the behavior is dominated, in a coherent fashion, by the $\mathcal{W}_{pnl}$ contributions.

instance if the coil is bent around its axis, it would be necessary to consider a viewpoint which encapsulates the non-local winding in an appropriate manner. It must be stressed that the choice of direction is a **key** factor when using the polar writhe measure. Further, as we shall discuss in section 6.2.4, it ($\mathcal{W}_p$) can be shown to be the **correct** measurement the case of coronal magentic field structures.

Case study - rotated helices

It has been demonstrated that altering the viewpoint $\hat{a}$ of a curve $\mathbf{x}$ changes the nature and value $\mathcal{W}_p(\mathbf{x},\hat{a})$ evaluation. By evaluating $\mathcal{W}_p(\mathbf{x},\hat{a})(t)$ as a function of t (i.e over the period $[a,t]$, where $t \in [a,b]$), the changing value of $\mathcal{W}_p$, with regards to its local and non-local components, can be observed.

First we choose to view the helix along the y-axis. We saw in the previous section an evaluation of $\mathcal{W}_p(\mathbf{x},\mathbf{y})$ has local and non-local components of significantly differing value. Figure 5.15 shows the results of the evaluation as the helix is drawn out through increasing t. Up until $t \approx 0.28$ the evaluations of $\mathcal{W}_p$ and $\mathcal{W}_{pl}$ agree. However after this point the curve reaches a turning point along the y-axis and the helix exhibits non-local winding about $\hat{y}$. As t increases the contribution of $\mathcal{W}_{pnl}$ begins to dominate and we see a coherence between $\mathcal{W}_{pnl}$ and $\mathcal{W}_p$ in this range.

We now choose a viewpoint in which one might expect to see an equally balanced contribution of $\mathcal{W}_{pl}$ and $\mathcal{W}_{pnl}$ to $\mathcal{W}_p$, that is a rotation of the viewpoint from $\hat{z}$ of $\theta = \pi/4$. The results are depicted in Figure 5.16. The pattern of $\mathcal{W}_{pl}$ shows much

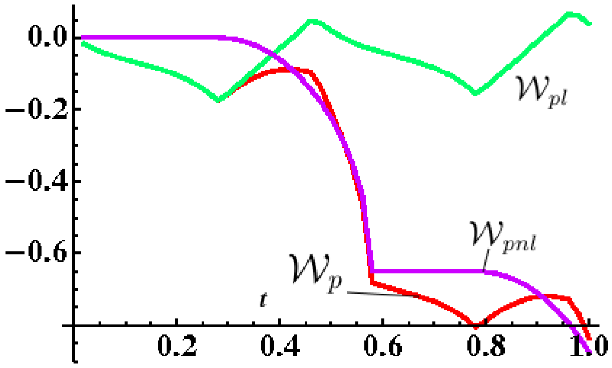

Figure 5.16: Plots of $\mathcal{W}_p$, $\mathcal{W}_{pl}$ and $\mathcal{W}_{pnl}$ against parameter t for the helix, evaluated over a period $t \in [0, 1]$, with the choice of direction of evaluation of $\mathcal{W}_p$ drawn along a polar angle of $\pi/4$ along the $y - z$ plane. We see between $t = 0$ and $t \approx 0.3$ an agreement between $\mathcal{W}_p$ and $\mathcal{W}_{pl}$. After this point the curve begins to exhibit non-local windings and as the parameter increases $\mathcal{W}_{pnl}$ begins to dominate the evaluation of $\mathcal{W}_p$.

greater variation than seen in the previous case (Figure 5.15). As a result whilst $\mathcal{W}_{pnl}$ tends to dominate the value of $\mathcal{W}_p$, the coherent relationship depicted in Figure 5.15 is not present.

This set of results help to further highlight the fact that there generally exists no easily quantifiable relationship between the choice of $\hat{a}$ in $\mathcal{W}_p(\mathbf{x}, \hat{a})$, and the interactions between $\mathcal{W}_p$, $\mathcal{W}_{pl}$ and $\mathcal{W}_{pnl}$. In the case of $\mathcal{W}_p(\mathbf{x}, \hat{y})$ a clear, coherent, relationship between $\mathcal{W}_p$ and $\mathcal{W}_{pnl}$ developed, which was not present in the second example.

Case Study 2 - a twisted parabola

What happens if we evaluate $\mathcal{W}_p(parab(t))$ (where $parab$ is given by equation 4.6), along a different direction? For example evaluating the parabola along the y-axis ($\mathcal{W}_p(parab, \hat{y})$). We see in Figure 5.17 the polar writhe measurement becomes erratic as a result of the disjoint behavior of both $\mathcal{W}_{pl}$ and $\mathcal{W}_{pnl}$. The comparison is made, in figure 5.17, with the far more regular $\mathcal{W}(\mathbf{x})$ curve (where this measure of $\mathcal{W}$ is the double integral (1.19)). The $\hat{z}$ viewpoint is clearly the preferable direction for evaluation of the twisted parabola. This is a result of the twist (controlled by Θ) being applied in the x-y plane.

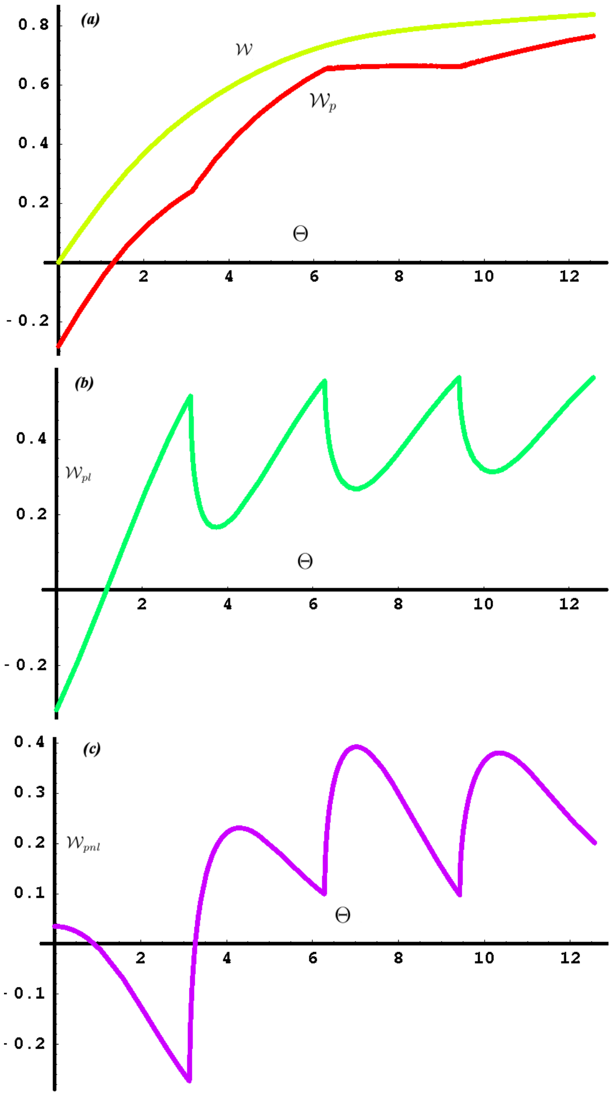

Figure 5.17: Plots of $\mathcal{W}_p(parab, \hat{y})$ (a), $\mathcal{W}_{pl}(parab, \hat{y})$ (b) and $\mathcal{W}_{pnl}(parab, \hat{y})$ (c), of $parab(t)$ (4.6) all over the period $t \in [0, 1]$. All three graphs are plotted for a set of rotations $\Theta \in [0, 4\pi]$. We note that both $\mathcal{W}_{pl}$ and $\mathcal{W}_{pnl}$ do not alter smoothly, leading to a $\mathcal{W}_p$ curve which is less coherent that the $\mathcal{W}$ evaluation (a).

Chapter 6

Coronal loop morphology

A topic of great interest in solar physics is the attempt to model or reconstruct the Coronal magnetic field. The Corona is the outer layer of the sun's atmosphere and is connected to the chromosphere by a thin transition layer (Priest 1982 [90]), see Figure 6.1. The solar coronal region is well recognised as being dominated by its magnetic field (Priest Chapter 3 [90]), playing a crucial role in phenomena such as solar flares, coronal mass ejections, prominences and coronal heating. Observational techniques in this region are limited because direct measurement of the magnetic field in the corona is very difficult (Aschwanden [8]). As a consequence theoreticians have attempted to reconstruct the field by extrapolation techniques, either from the magnetic data available at the photosphere (See Gary [46] and Amari *et al* [3], and references within both), or by attempting to match the model to observed phenomena (Rust and Kumar [93], Titov and Démoulain [108], Moore *et al* [76], Low and Berger [67], Török and Kliem [110]). The general procedure is to use photospheric data and/or a set of assumptions regarding the magnetic field's behavior in the coronal region. Combining this information, a boundary value problem can be formed whose solution is the expected field line configuration.

Observations of the coronal region reveal the existence of S-shaped features. They are considered to result from enhanced dissipation that accumulates hot plasma along correspondingly shaped field lines (Green *et al* [50]). These structures were termed *sigmoids* by Rust and Kumar [93], and are generally seen to occur in both forward and reverse S shapes (termed Z sigmoids by Low and Berger [67]); examples are shown in Figure 6.2. Nakagawa *et al* [79] explained the origin of such structures by describing the magnetic fields in sun spot regions as twisted flux ropes. The sug-

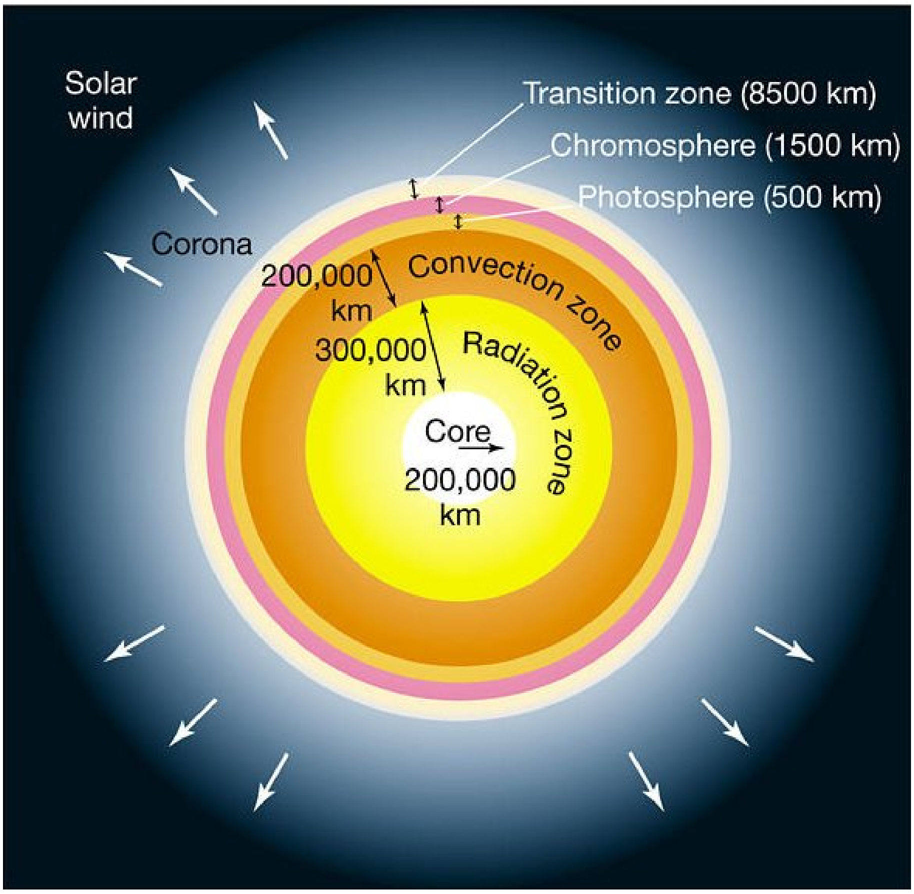

Figure 6.1: A schematic diagram of the sun's various layers. We see the sun's atmosphere which is composed of the photosphere, the chromosphere and a transition layer leading to the coronal region. The diagram is reproduced from the High Altitude Observatory website (*www.hao.ucar.edu*).

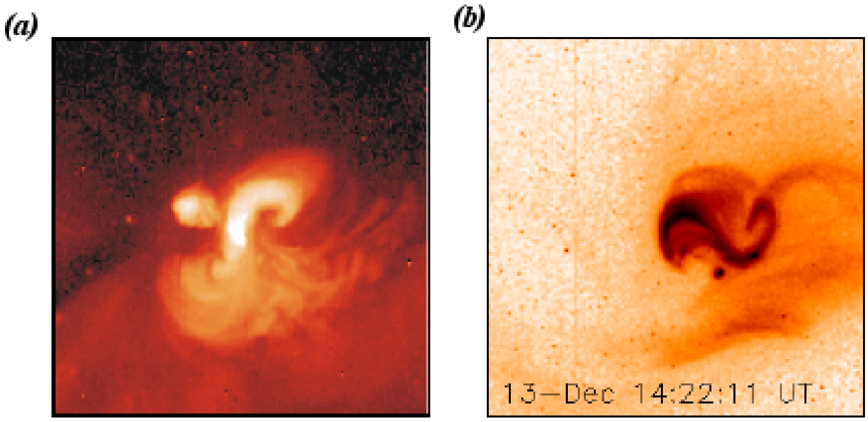

Figure 6.2: The sigmoid depicted in (a) is a sigmoid before an eruption. Observed on 8 June 1998 15:19 UT, as a Solar X-ray image from the Yohkoh Soft X-Ray Telescope. (b) is an example of a reverse S sigmoid (the date of its observation is on the figure), viewed as a Solar X-ray image from the Yohkoh Soft X-Ray Telescope. Both are reprinted from the Montana state university solar physics department website (*solar.physics.montana.edu*).

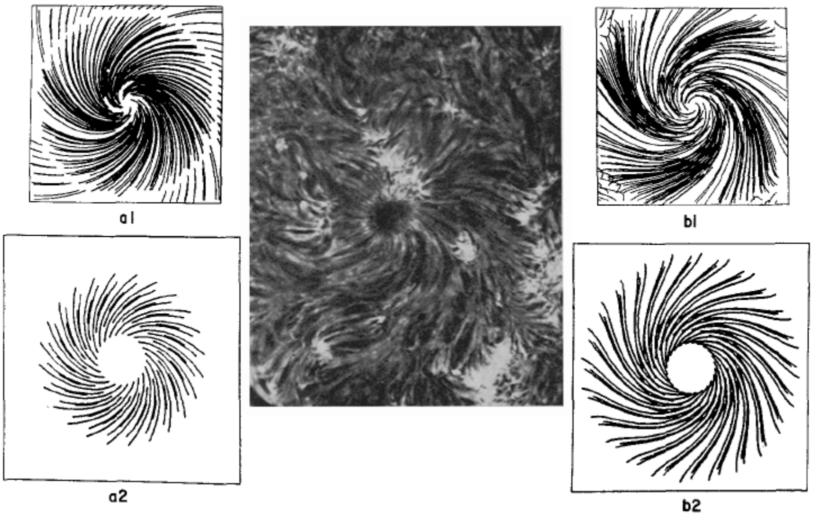

Figure 6.3: The central figure is an Hα observation demonstrating the spiral topology of filaments near a sun spot (from the Big Bear Observatory 9 September 1970). Figure a_1, a_2, b_1 and b_2 represent force free magnetic field models with a spiral angle of 45°. The field is right handed, in terms of its chirality and causes a clockwise rotation of the fibrils surrounding the centre of the sun spot. A left handed field would cause fibril rotation in the opposite direction. This figure is reproduced from Nakagawa *et al* [79].

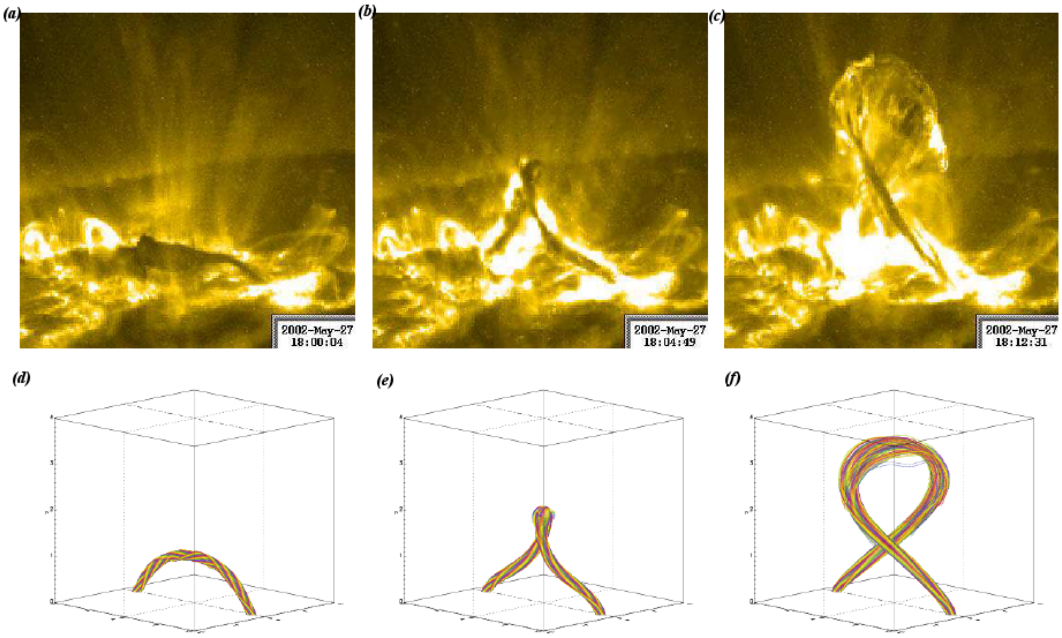

Figure 6.4: The top row of figures are images of a confined filament eruption on 2002 May 27, shown in extreme extraviolet light by the TRACE satellite. The right image shows the filament after it has reached its maximum height. The bottom figures represent the evolution of a kink-unstable flux rope, from a simulation performed by Török and Kliem 2005 [109] and are reprinted here.

gestion was that the direction of curvature of the sigmoidal structures was related to the sense of twist in the magnetic field. So a field with right handed twist (positive chirality) would cause the sigmoidal structure to rotate in a clockwise direction during its evolution (Figure 6.3), with left handed twist causing an anticlockwise rotation (negative chirality).

Attempts to model the onset of sigmoidal brightenings generally involve magnetic flux ropes (Green *et al* [50] review the existing set of models). A flux rope can be thought of as a set of magnetic field lines which bunch together to create a twisted flux bundle with a mutual general axis (See Figure 1.4). There is an interest in the global geometrical properties of the flux rope configurations generated by the various models (Titov and Démoulin [108],Canfield *et al* [23], Low and Berger [67], Rust [94], Green *et al* [50], Pevstov [86]). Flux rope shapes are helical in their nature (see Figure 6.4 for example) with the structure anchored in the x-y plane at $z = 0$, which is taken to be the sun's surface (Gary [46] Amari *et al* [3], Titov and Démoulin [108]).

Previous studies concerning the morphological characteristics of flux ropes applied to cases which were cylindrically symmetric and of uniform twist (Titov and Démoulin [108],Low and Berger [67], Fan and Gibson [41], Török and Kliem [110]); these simulations have tended to develop symmetrical sigmoidal structures. Specifically the field lines can be split into two halves at a centrepoint; each half can be obtained from the other by rotating thorough 180° in the x-y plane (the parabola viewed from above in Figure 4.9 is indicative of such symmetrical shapes). The morphological properties of such shapes are fairly predictable with the height controlling the sign of the $\mathcal{W}_p$ measure (we shall see in section 6.2.4 $\mathcal{W}_p$ is the correct measure in such cases), through the interplay of the $\mathcal{W}_{pnl}$ and $\mathcal{W}_{pl}$ components (see section 6.3.3). It is not clear from observational data however that such symmetry is the norm (see Figure 6.5). Further the effects of asymmetry on the writhing (and helicity) of a helical field line configurations have not been examined in detail, to the best of our knowledge.

In the following section we use a simple force free model of the active coronal field to analyse the morphology of asymmetric field line structures. This analysis is the result of a series of numerical experiments. Following Berger and Prior [15] an expression for the magnetic helicity of helical field lines, which can be bound between two planes, is shown to be equivalent to the $\widetilde{\mathcal{L}}$ formulation defined in section 3.1. The field lines generated could, for example, represent the axis of a coronal flux tube.

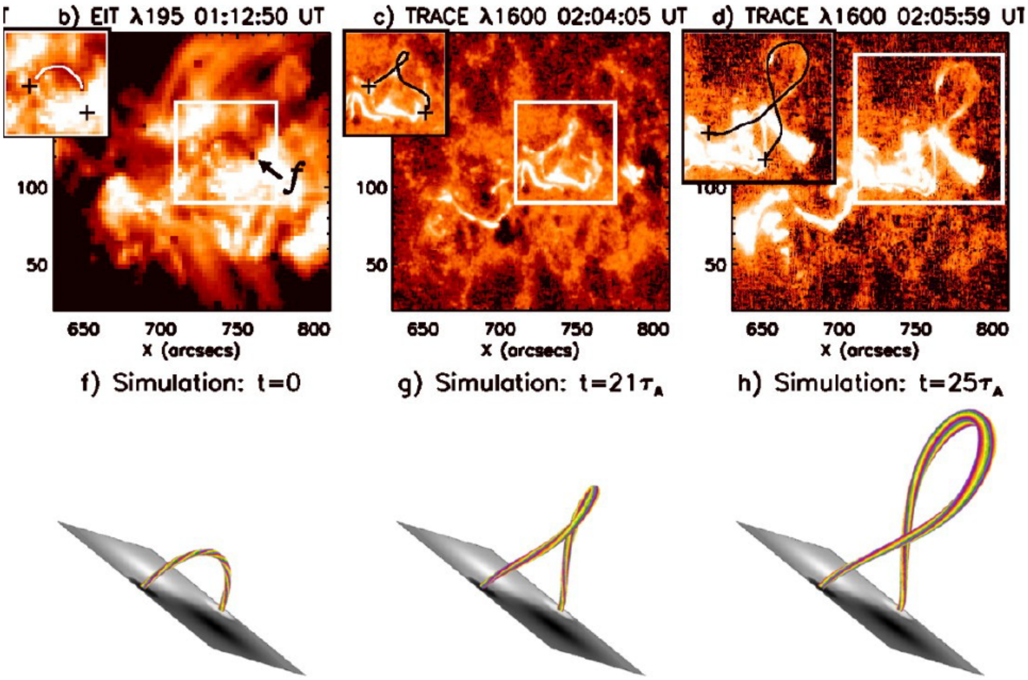

Figure 6.5: Figures b,c and d depict a Filament eruption and coronal mass ejection on October 10th 2004 in the NOAA active region 10696.The images are TRACE 1600 images. Figures f-h are MHD simulations form a numerical simulation performed by Török and Kliem [109]. The times marked on the figures are Alfvén times. Figures b-d would appear to suggest a shape which is not fully symmetric (about its maximum height (apex)), whilst the simulation flux rope does. This figure is reprinted from Green *et al* [50].

The results demonstrate that, even with a simple field model, the range of global geometrical behavior is both varied and complex. The interplay between the local and non-local polar writhing contributions has a significant effect on the sign of the field line's writhing (which is represented by $\mathcal{W}_p$). In general $\mathcal{W}_{pl}$ and $\mathcal{W}_{pnl}$ are of opposite sign and alter with differing rates under a gradual transformation of the field lines shape. One conclusion is that symmetric field configurations do not represent the full set of morphological possibilities available to field line structures. Further, we demonstrate that an accurate measure of the flux rope helicity requires an intimate knowledge of its full three dimensional structure as opposed to observations made from two dimensional imaging techniques and line of sight imaging. This leads to the further conclusion that current methods of inferring the writhe and helicity of single field lines or flux ropes, from currently available data, could lead to false assumptions regarding their sign and value.

6.1 Simple coronal field models

The various regions of the sun's atmosphere are generally modelled as ideal electrically neutral plasma (Priest Chapter 2 [90]). Such plasmas are treated as a continuum which is in thermodynamic equilibrium. In general this continuum is a single isotropic fluid (Priest Chapter 2 [90]). The equation of plasma motion and its subsidiary equations are

$$\begin{aligned} \rho(\frac{\partial \mathbf{v}}{\partial t} + \mathbf{v}\cdot\nabla\mathbf{v}) &= -\nabla p + \mathbf{j}\times\mathbf{B} + \eta\mathbf{g}, && (6.1)\\ \mathbf{j} &= \nabla\times\mathbf{B}/\mu, && (6.2)\\ \nabla\cdot\mathbf{B} &= 0, && (6.3) \end{aligned}$$

where $\mathbf{v}$ is the plasma velocity, t represents time, $\mathbf{B}$ the magnetic field, $\mathbf{j}$ the current and $\mathbf{g}$ the gravitational force. The scalar quantities ρ, p, η and μ are the mass density, plasma pressure, *magnetic diffusivity* and *magnetic permeability*, respectively. From left to right the three contributions to the R.H.S of (6.1) come from the plasma pressure gradient, the Lorentz force and the gravitational force. If the plasma is in equilibrium then the plasma's motion can be considered to be zero, thus equation (6.1) becomes

$$\mathbf{0} = -\nabla p + \mathbf{j} \times \mathbf{B} + \eta \mathbf{g}, \tag{6.4}$$

where $\mathbf{0}$ is a null vector. The assumption made for (6.4) to hold is that the sources of the magnetic field in the photosphere are moving slowly enough that the system can relax to its equilibrium state. To be more specific, the magnetic field has time to relax if the plasma velocity is much smaller than the speed with which information is transmitted along field lines (the Alfvén speed). In the coronal region the field structures are stable on the timescale of hours to days and the conditions required for (6.4) are considered to hold (Gary [46]).

In the coronal region the plasma pressure and gravitational force are small relative to the magnetic pressure (Priest Chapter 3 [90]); as a result of this they may be ignored for equilibrium fields, thus the Lorentz force will tend to dominate in this region.

6.1.1 Potential field

Potential fields give the most basic models with a well defined boundary-value problem (Schmidt [98], Altsulter and Newkirk [2]). The assumption is made that there exists no current in the coronal region. Using this assumption (6.4) reduces to the following set of differential equations, concerning the coronal magnetic field $\mathbf{B}(x, y, z)$

$$\nabla \times \mathbf{B} = 0, \;\; \nabla \cdot \mathbf{B} = 0. \tag{6.5}$$

So this field is both current free and divergenceless. Taking the curl of (6.5) and coupling with (6.3) gives

$$\nabla^2 \mathbf{B} = 0. \tag{6.6}$$

This implies the magnetic field is potential. Thus there exists a scalar function ψ, called the *scalar magnetic potential* defined by,

$$\mathbf{B} = \nabla \psi, \tag{6.7}$$

a conservative field, which satisfies

$$\nabla^2 \psi = 0. \tag{6.8}$$

We can solve (6.8) in order to determine the vector field lying in the plane above $z = 0$, based on the normal field components at this point. Note that this problem is equivalent to solving the Laplace equation with Neumann boundary conditions (see Chiu and Hilton [28] for a review of this problem).

6.1.2 Force free field

The assumptions for potential fields will often not hold in the corona, particularly in active regions. Observations have demonstrated conclusively the existence of currents running in the solar atmosphere (Gary [46]). A good alternative to potential fields are force free fields. If the height of the region of interest is much less than the scale height (the vertical distance in which the pressure falls by a factor e) and the ratio

$$\beta = \frac{2\mu_0 p_0}{B_0^2}, \tag{6.9}$$

of the plasma to magnetic pressure (where p_0 and B_0 are the base pressure and magnetic field), is much less than unity, then the magnetic field dominates and (6.4) becomes

$$\mathbf{j} \times \mathbf{B} = 0. \tag{6.10}$$

This implies that the current flows along magnetic field lines. We may write (6.10) as

$$\nabla \times \mathbf{B} = \alpha \mathbf{B}, \tag{6.11}$$

with

$$\mathbf{B} \cdot \nabla \alpha = 0, \tag{6.12}$$

where α is some function of position (Priest Chapter 3 [90]).

6.1.3 Linear force free fields

For the simplest family of solutions to (6.11) we consider α to be a scalar constant (the same for all field lines in the region), this is the linear force free model (See Priest sections 3.5-3.53 for a discussion and general solutions and Gary [46] for an introduction to re-creating force free models based on observational data). In this scenario (6.11) is equivalent to the Helmholtz equation

$$(\nabla^2 + \alpha^2)\mathbf{B} = 0. \tag{6.13}$$

Using the linear model, the field can be reconstructed above $z = 0$, for a specified α value, from a reading of the normal value of $\mathbf{B}$ value at the coronal surface. Readings can be gained from magnetographs. Methods for solving (6.13) include using either a Fourier transform (Nakagawa *et al* 1972 [80], Gary 1989 [46]) or Greens function (Chiu and Hilton [28], Semel [99]). However, such solutions can be shown ([28]) to be non-unique. Further studies suggest that the use of more than one $\mathbf{B}$ component could solve such issues. Gary [46] suggested the use of two components, and Kress (1989 [62]) used all three $\mathbf{B}$ components. In the following work we are considering theoretical configurations of the coronal field and will be specifying the magnetic field entirely.

The linear approximation is shown to suffer from a number of inconsistencies. One important issue is the lack of a limit on the field's energy value on the unbounded domain (see Gary [46] for a discussion on this issue). The second factor is its failure to match observational data, showing electric currents are not uniformly distributed as the model requires (Hagyard [52]). Despite this the linear force free model is still widely used in current research. Of particular interest to this is its use in flux rope modeling. Linear force free models of cylindrically symmetric flux ropes have been used as a start point for the study of flux rope formations (Titov and Démoulin [108], Low and Berger [67], Fan and Gibson [41]). These start configurations are then developed using MHD simulations which attempt to replicate the time varying behavior of active region fields (Fan and Gibson [41],Török and Kliem [109]).

The aim of this particular study is to explore the various global geometric properties of a wide variety of possible configurations. Use of the linear force free model provides us with a compromise between physical accuracy and numerical efficiency with regards to evaluation. As much of the morphological study of helicity and writhing involve linear force free flux rope models as their base, this simplification can be justified. More complex models are beyond the scope of this study. They include non linear force free models (α varies but is constant along specific field lines) and MHD models, in which the pressure and gravitational terms are included. Amari *et al* [3] discuss the different mathematical problems associated with various coronal magnetic field models, including non-linear and MHD cases.

6.2 Flux tubes and magnetic helicity and field line morphology

6.2.1 Magnetic flux tubes

A magnetic field line is a curve whose tangent is in the direction of $\mathbf{B}$. A magnetic flux tube is the volume enclosed by a set of field lines which intersect a surface bounded by a simple closed curve. The strength F of such a flux tube may be defined as the amount of flux, crossing a cross sectional area S of the tube, as

$$F = \int_S \mathbf{B} \cdot \mathrm{d}\mathbf{S}, \tag{6.14}$$

Because $\nabla \cdot \mathbf{B} = 0$, this strength is constant along the tube's length (Priest section 2.92 [90]). Of particular interest are cylindrically symmetric flux tubes, whose field components depend only on the tubes radius (Priest section 3.2 [90], contains an introduction to the properties of such tubes). The global geometrical properties of such uniformly twisted tubes can be defined in terms of the ribbon surface parameterisation defined in section 1.2.5 (Berger 1999 [13]).

6.2.2 Magnetic helicity

Magnetic helicity quantifies various aspects of magnetic field structure. Examples of fields possessing helicity include twisted, kinked, knotted or linked flux tubes. It is very useful measure in magnetic field modeling as it allows for the comparison of fields of differing geometries, avoiding the use of parameters specific to one model (Berger [13]). Magnetic helicity is conserved in ideal MHD (Woltjer [118]). Taylor conjectured that for plasmas with a high Reynolds number it is conserved during field line reconnection (Taylor [106], [107]). Berger [10] defined rigorous limits on magnetic helicity dissipation in the solar corona demonstrating that, to a good degree of approximation, helicity could be considered conserved in solar coronal field structures.

A definition

Consider first two interlinked closed flux tubes. It has been shown by (Moffatt [74] and Arnold [6]) that the magnetic helicity (H) is simply the linking number (as characterised by (1.16)) multiplied by the amounts of flux Φ_1 and Φ_2 running through the tubes,

$$H = \Phi_1\Phi_2\mathcal{L} = \frac{\Phi_1\Phi_2}{4\pi}\oint_{\mathbf{x}}\oint_{\mathbf{y}} \frac{\mathrm{d}\mathbf{x}(s)}{\mathrm{d}s}\cdot\frac{\mathbf{r}}{r^3}\times\frac{\mathrm{d}\mathbf{y}}{\mathrm{d}s'}\mathrm{d}s\mathrm{d}s'. \tag{6.15}$$

Here 6.15 represents an alternate form of the Gauss linking integral (1.16) multiplied by the flux values (note $\mathbf{r} = \mathbf{y} - \mathbf{x}$). If we now consider a system of N closed flux tubes, the helicity is simply the sum of all interlinkings $\mathcal{L}_{ij}$ multiplied by their fluxes [6],

$$H = \sum_i^N\sum_j^N \Phi_i\Phi_j\mathcal{L}_{ij}. \tag{6.16}$$

A magnetic field contains an infinite number of flux tubes, which, in this limit, become field lines (spacecurves). Thus in the limit $N \to \infty$ with $\Phi_i \to 0$[1],

$$H = \frac{1}{4\pi}\int\int \mathbf{B}(\mathbf{x})\cdot\frac{\mathbf{r}}{r^3}\times\mathbf{B}(\mathbf{y})\,\mathrm{d}^3\mathbf{x}\,\mathrm{d}^3\mathbf{y}, \tag{6.17}$$

To simplify we can employ the Coulomb gauge vector potential

$$\mathbf{A}(\mathbf{x}) = -\frac{1}{4\pi}\int\frac{\mathbf{r}}{r^3}\times\mathbf{B}(\mathbf{y})\,\mathrm{d}^3\mathbf{y}, \tag{6.18}$$

to reduce H to

$$H = \int \mathbf{A}\cdot\mathbf{B}\,\mathrm{d}^3\mathbf{x}. \tag{6.19}$$

This expression assumes that the entire field is contained within a volume $\mathcal{V}$, bound by a surface $\mathcal{S}$, for which $\mathbf{B}\cdot\mathbf{n}|_S = 0$ holds at $\mathcal{S}$. That is to say it is a union of closed flux tubes.

6.2.3 Mutual and self helicity

We can split the helicity into *mutual* and *self* components (Berger and Field [11], Berger [13]). If we consider a set of n intertwined flux tubes each labelled $1, 2, \dots n$, the mutual helicity of a pair of separate tubes (i, j) can simply be determined by (6.15). All $i = j$ components, contributing to (6.16), can be termed the *self*-

---

[1] The quantity $N\Phi_i$ will stay constant in this limit, as it represents the net flux in the tube. Arnold has shown that this is true even if the tubes are not closed [6].

helicities. Suppose all field lines within the tube twist about a central axis. The self-helicity has two components. The first relates to the axis of the tube, for closed curves this is of course the writhe, as defined by (1.19). The second relates to the twisting inside the tube and can be characterised by the $\mathcal{T}(R(\mathbf{x},\mathbf{v}))$. So we can conclude that the helicity of a flux tube, of flux Φ, can be given by the Călugăreanu theorem, $H = (\mathcal{W} + \mathcal{T})\Phi^2$.

6.2.4 Open field structures

It is often the case that the magnetic field is not closed in the volume of interest. The coronal region magnetic field is one such example, with its field lines terminating at the photospheric surface. In such cases the helicity can be measured relative to the minimum energy vacuum field (Berger and Field [11]). A second definition for the open writhing of such fields was first detailed by Berger and Prior [15] and is reproduced here. Following [11] we see that the open magnetic helicity when a space can be divided into subvolumes by parallel planes can be considered as the sum of helicity contributions form each section, with the minimum energy relative measure. Suppose we slice space into a set of layers separated by parallel planar boundaries at $z = z_0, z_1, ...$, then the helicity of all space will equal the sum of helicities of each layer, with the vacuum contribution in each case zero (see [11]). Using this construction one can compute the helicity as an integral in z, corresponding to (3.1), averaged over all pairs of field lines. Thus we can write the helicity of a section of a flux tube between planes z_i and z_j, as

$$H(z_i, z_j, \hat{z}) = \widetilde{\mathcal{T}}(z_i, z_j)\Phi^2 + \mathcal{W}_p(z_i, z_j)\Phi^2. \tag{6.20}$$

Where we define the net directional twisting ($\widetilde{\mathcal{T}}(z_i, z_j)$) of a curve, which can be split into n pieces by $n-1$ turning points along $\hat{z}$, as

$$\widetilde{\mathcal{T}}(z_i, z_j) = \sum_{i=1}^{n} \int_{z_1}^{z_2} \widetilde{\mathcal{T}}_i'(z), \tag{6.21}$$

where $\widetilde{\mathcal{T}}'(z)$ is as defined in (3.17). As a result we can state that the helicity as applicable to coronal field models is defined along a specific direction rather than an average over all viewing angles as it would be for closed volume field structures.

6.2.5 Observing helicity

Deriving information on the helicity of coronal field from observational data is a difficult task as current observational methods do not provide full specifications of the field lines three dimensional structure. TRACE imaging (Handy *et al* [49]), and Michelson Doppler Imager MDI (Scherrer *et al* [97]), can be used for line of sight coronal images. The Yohkoh soft X ray telescope (Tsuneta *et al* [112]) is used to follow the evolution of structures in the corona. More recently two satellite missions have been launched, in order to offer superior resolution of the coronal magnetic field structure. The Hinode satellite has a solar optical telescope as well as X ray and EUV (ultraviolet emission) capabilities (Kosugi *et al* [61]). The recent NASA launched STEREO satellite mission employs two identical observatory satellite, one ahead of the earth's orbit and one behind. The aim is to provide stereoscopic measurements of the corona ([54]). The STEREO mission may be able to offer a three-dimensional picture of the coronal field structure allowing more accurate measurements of the field line morphology.

Rust [94] for example discussed the writhe of filament using a line-of-sight TRACE images. Discussing the confined eruption TRACE image (c) shown in Figure 6.4, the author states that field depicted has a writhe value of ≈ 1. As this image essentially represents a particular viewpoint of the field structure with the filament image projected onto a plane, we should really state that the planar writhe w depicted in this figure is 1 (though technically the planar writhe is usually defined for closed projections), rather than the $\mathcal{W}$ as defined by (1.19). This figure (6.4) could be approximated by the twisted parabola (4.6) discussed in section see in Figure 3.50 if $\Theta \approx \pi$ then as h increases). As shown in section 6.2.4 however, the correct writhing expression for coronal fields would be $\mathcal{W}_p$, which will generally give a different number. For example, this figure (6.4) could be approximated by the twisted parabola (4.6) discussed in section 5.3.5. We see in Figure 4.10 if $\Theta \approx \pi$, then as h increases $\mathcal{W}_p$ **will** approach 1. Of course even if this field line were representable as symmetric twisted parabola, it is not immediately clear from this figure what value Θ parameter would take on. So it would seem a risky to assume the level of writhing, based on a single line of sight image.

Various other methods for extrapolating measures of the helicity present in coronal field have been suggested.

- The z component of current helicity, a different quantity from magnetic helicity

(Abramenko *et al* 1996 [1], Pevstov and Latushko [84]).

- Helicity flow through the photosphere (Kusano *et al* [63], Démoulin *et al* [32], Démoulin and Berger [35], Chae *et al* [27]).
- The α best fit model for linear force free models. Using magnetographic data, a best fit linear force free field model is constructed, and the value of α is used as a proxy for helicity (Pevstov *et al* 1997 [83], Démoulin *et al* [34]).

Démoulin and Pariat [36] have recently performed a review of the various methods for evaluating the flow of magnetic helicity through the photosphere into the corona. The models involve the injection of helicity into an active region zone of the corona. In this particular study we are interested in the helicity of specific field line configurations rather than the total helicity in a particular region. The interested reader is directed to this ([36]) and the above references ([63],[35],[27]) for more information.

An assumption regarding helicity is that the dominant helicity sign in the northern/southern hemisphere is positive/negative (Pevstov, Canfield and Mclaymont [83], Burnette, Canfield, and Pevstov 2004 [19]) with both studies using the α-best method for estimating helicity. Pevstov (Pevstov [86]) states that the α coefficient has the same sign as the magnetic helicity, a statement echoed by Green *et al* [50]. This is true of closed volume helicity measures (closed curves) (Pevstov [86]). However, we shall see in the following work that this assumption will not always hold for field lines in the corona; at least based on the linear force free model used in this study.

6.3 Sigmoid orientation and writhe

Soft x-ray imaging (SXR), taken during the Skylab and Yokoh missions give strong evidence that the shape of the magnetic field in active coronal regions is helical (Green *et al* [50]). Further, Hα imaging has demonstrated that active regions of the corona often contain collections of such helical loops. These loop structures can be split into two main categories forward S shapes and reverse Z shapes.

6.3.1 A simplified picture

The sigmoids are known to occur with strong preferentiality in the Northern hemisphere (Z shapes) and Southern hemispheres (S shapes) respectively (Rust and Kumar [93], Pevstov *et al* [85]). A simplified picture, based on a set of morphological assumptions, has emerged.

- For field lines, or flux rope axes which trace out forward S shapes the writhe will be positive, if the aspect ratio is > 0.4 and negative otherwise (Green *et al* [50]). Note this is the writhe of the flux tubes axis. For Z shaped sigmoids this relationship is reversed. Török and Kliem [110] simulate a confined flux tube eruption (indicative of an active region), whose height ranges from 1-4, where by height they are referring to the height divided by the footpoint width (we shall call this aspect ratio) and the height measure has no units.

- For rising flux ropes, the rope's middle section take a Z shape for fields of positive chirality and an S shape for field of negative chirality (Fan and Gibson [41], Kliem, Titov and Török [59], Green *et al* [50]). Note the chirality is determined by the sign of α for force free fields.

Simulations of sigmoidal field models have tended to generate symmetrical helical field lines and flux ropes (see section 6.3.3 for a discussion on what we mean by symmetric), for examples see (Titov and Démoulin [108], Berger and Low [67], Fan and Gibson [41], Török and Kliem [109]).

Low and Berger [67] describe flux rope field models which raise the possibility that field lines in such active regions may dip at their central point leading to Z shaped field lines in regions for which S shaped field lines dominate, that is for fields of positive chirality. Such cases have been found in simulations (Magara and Longcope 2001 [72], [71], Kliem *et al* [59]).

6.3.2 Our findings, in brief

Further analysis in this chapter gives a more complicated picture regarding the morphology of sigmoidal field lines. The following results are demonstrated.

- For field lines of significant size the $\mathcal{W}_p$ measure of S shaped sigmoidal structures is generally positive rather than negative, except in a small number of cases (section 6.4.4).

- Field lines can be shown to change sign from positive to negative over a varying range of heights (sections 6.4.3, 6.4.4 and section 6.4.5).
- Field lines whose central section appear to trace out a Z shape, and which show no dip at their centre, can be produced using positive α values. These field lines generally have positive $\mathcal{W}_p$ values. Such fields could be misinterpreted as having negative chirality and thus assumed to have the wrong helicity (section 6.4.6).

We begin our analysis by first discussing the general characteristics of sigmoidal field lines.

6.3.3 Characteristics of a sigmoidal field line

In what follows the field lines generated will all have mutual characteristics, which we will use to analyse and compare the morphology of the subsequent shapes formed. We shall be concentrating in single field lines (in MHD field lines often have physical meaning as field lines are related to the physics properties of plasma, Longcope [66]) and use a simple dipole linear force free field model to generate a large set of field lines.

The simplest linear force free field lines (for two point field line topologies) are parabolic in their nature (Priest section 3.5.2 [90]), (a) in Figure 6.6. The start and end footpoints of the field line will lie in the $z = 0$ plane and the field lines lie in the x-y plane. The orientation between the start and end points $\Theta(z = 0)$ forms one part of the $\mathcal{W}_{pnl}$ calculation. The *apex* represents the point on the curve which represents the maximum field line height (see (a) in Figure 6.6), the orientation at this point is $\Theta(z = z_{max})$. We note in what follows all curves generated will have only one maximum in z, a global maximum so the $\mathcal{W}_{pnl}$ contribution is $\frac{1}{\pi}(\Theta(z = z_{max}) - \Theta(z = 0))$. Of course in this simple planar case $\Theta(z = z_{max}) = \Theta(z = 0)$, and indeed $\mathcal{W}_p$ will be zero. Finally when we discuss the aspect ratio it shall be understood to be the apex height divided by the footpoint width.

Increasing α in magnitude causes the field lines to develop $\mathcal{W}$, by developing helical type structures (Nakagawa *et al* [79], Gary [46]), see (b) and (c) in Figure 6.6. Projecting these field lines onto the x-y plane can be thought of as equivalent to viewing the field from above. We note in (c) (Figure 6.6) the loop forms an S shaped structure, as seen from above. The sigmoidal shape in Figure (6.6) has a

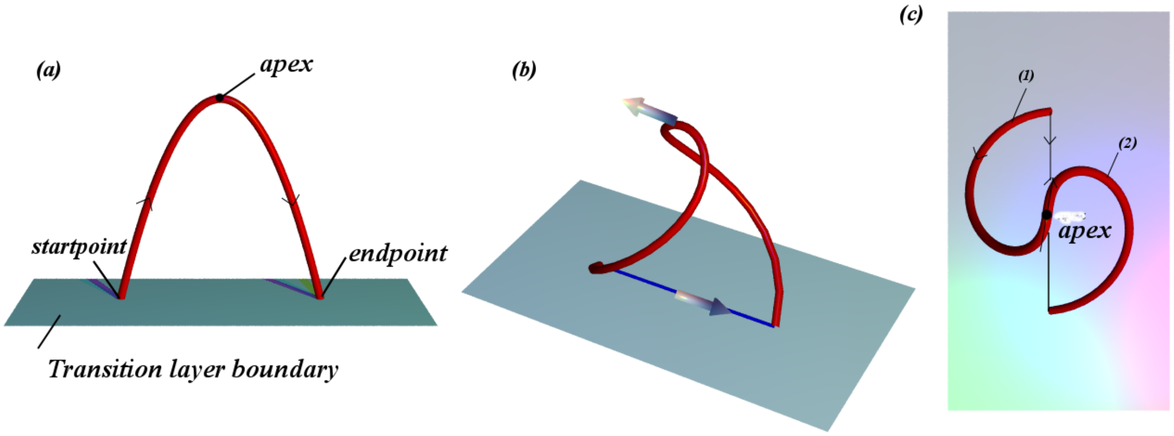

Figure 6.6: (a) to (c) are representative of the type of field lines morphologies present in magnetic flux rope sigmoid models. (a) is an example of a field with no writhe, it draws out a parabolic shape in the y-z plane (it can be generated using equation 4.6 with $\Theta = 0$). Its maximum height (apex) and footpoints are marked. (b) is a helical field structure which could be representative of the axis of a sigmoidal flux tube (generated using equation (4.6) with $\Theta = \pi - 0.2$). Arrows mark the orientations between the footpoints and the orientation at the apex point. The orientations of these vectors, $\Theta(z_{min})$ and $\Theta(z_{max})$ respectively, represent the contributions to $\mathcal{W}_{pnl}$ of the field line. (c) is the view from above of (b). We can clearly see the sigmoidal nature of the field line from this view. Further (c) can be used to estimate the contribution of $\mathcal{W}_{pnl}$, as the angle made between the footpoint joining vector and the apex tangent vector (in this case the angle is $\pi - 0.2$). This assumes there are no full windings of the vector $r(z)$ over $z \in [z_{min}, z_{max}]$. Figure 4.9 depicts and example of a Z shape sigmoidal structure (generated with a twist of $\Theta = -\pi$).

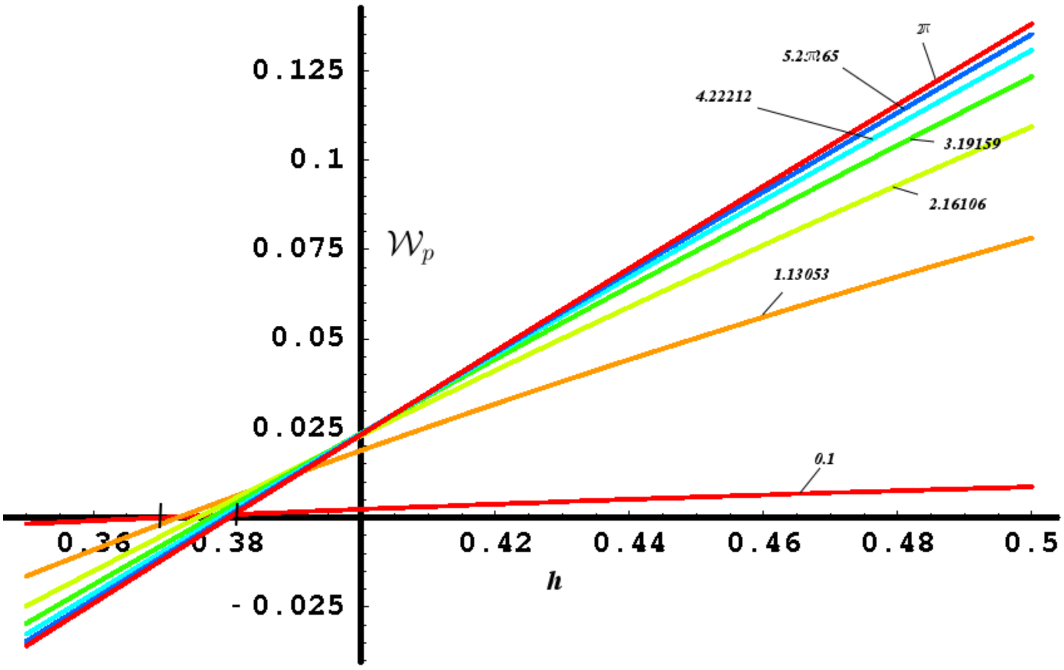

Figure 6.7: A set of curves of fixed Θ values $\Theta \in [0.1, 0.1 + \frac{1(2\pi-0.1)}{6}, 0.1 + \frac{2(2\pi-0.1)}{6}, 0.1+\frac{3(2\pi-0.1)}{6}, 0.1+\frac{4(2\pi-0.1)}{6}, 0.1+\frac{5(2\pi-0.1)}{6}, 2\pi]$. Plotted is $\mathcal{W}_p[parab(t)]$, $t \in [0,1]$) in each case for a range of h values $h \in [0.35, 0.5]$. It can be seen that all curves cross the x-axis (switch from negative to positive $\mathcal{W}_p$) over a short range of values between $x \in [0.37, 0.38]$ (marked on the diagram).

degree of symmetry about the curves apex. Section 1 (marked on Figure 6.6) can be rotated clockwise or anticlockwise, using the apex as a pivot, through an angle of π radians to superimpose onto section 2. The same is true of the Z shape depicted in Figure 4.9. When we talk about symmetry and asymmetry in what follows it is with respect to this rotation (about the apex).

6.3.4 The twisted parabola and sigmoids

The twisted parabola discussed in section 4.2 forms twisted helical loops characteristic of the coronal active region (Figure 4.10). Figure 6.7 represents a set of evaluations of $\mathcal{W}_p(parab(t))$, $t \in [0,1]$ (parab(t) is defined by (4.6)), over a range of starting heights $h \in [0.35, 0.5]$, for a series of positive Θ values (forming Z shapes). The results clearly show, for a wide range of twist values Θ, the parabola changes from negative to positive $\mathcal{W}_p$ values over a very small range of heights ($x \approx [0.37, 0.38]$).

We note the footpoint width will always be 1 here, so the height is equivalent to the aspect ratio. This result is discussed in Green *et al* [50] (page 6),

> "Berger and Prior (2006) have recently shown that a curve (e.g the axis of a flux rope), anchored at both ends in the same plane, with positive (negative) writhe can exhibit a forward (reverse) S shape, if the apex height is less than roughly 0.4 times the footprint separation. The situation is, however, not relevant for the evolved phase of solar eruptions we focus on in the present study."

This result can be understood from the fact that $\mathcal{W}_{pl}$ and $\mathcal{W}_{pnl}$ go in opposite directions when we vary h. The $\mathcal{W}_{pnl}$ contribution can be seen to occur as a result of the parabola apex rotating (remembering the endpoints are fixed) and changes linearly. In the case of actual coronal fields, as seen by observational techniques (see section 6.2.5), it is very difficult to gauge an accurate measure of this local writhing from a two dimensional image, though it is possible to attain a reasonable estimation the $\mathcal{W}_{pnl}$ contribution using soft x-ray imaging (Rui *et al* [65]).

In the following section we demonstrate that a relationship between field line apex height and the sign of its writhe (as measured by $\mathcal{W}_p$) is not limited to the symmetric twisted parabola example. Further the difference in rate of changes of $\mathcal{W}_{pl}$ and $\mathcal{W}_{pnl}$ is shown to account for the possibility of both forward and reverse S structures with both writhing signs, over a range of apex heights.

6.4 Results

6.4.1 The model

A divergenceless field can be split into scalar poloidal and toroidal components (Morse and Feshbach pg 1767 [78]). As the linear force free field model represents an example of such a field we can separate the solution ($\mathbf{B}$) of (6.13) in this fashion (Mackay *et al* [68]). We choose to specify our field using a simple Fourier method. Using Cartesian coordinates a simple solution is

$$P = \frac{1}{k^2}\sin(mx+ny)e^{-\gamma z}, \tag{6.22}$$

$$T = \alpha P. \tag{6.23}$$

Here P and T represent the poloidal and toroidal field components, m and n represent the frequency components, $k = \sqrt{m^2 + n^2}$ and $\gamma = \sqrt{k^2 - \alpha^2}$ (with α the force free parameter). Now

$$\mathbf{B}(x, y, z, m, n, \alpha) = L.T + \nabla \times \mathbf{L}P, \tag{6.24}$$

where $\mathbf{L} = \hat{z} \times \nabla$ is the angular momentum operator. Substituting (6.22) and (6.23) into (6.24) we find

$$B(x, y, z) = \left(\frac{n\alpha - m\gamma}{k^2} \cos(mx + ny), -\frac{m\alpha + n\gamma}{k^2} \cos(mx + ny), \sin(mx + ny) \right) e^{-\gamma z} \tag{6.25}$$

This satisfies both field equations for a linear force free model, see appendix section C. Using inputted values for $\mathbf{B}_i,\ i = x, y, z$ we use a simple second order Runge-Kutta algorithm (See Press *et al* [87] for example) to generate the set of points lying above the plane $z = 0$.

A two component field was used in order that the model be simple and numerically quick to calculate but have sufficient complexity to develop asymmetric solutions. We found by experimentation that values of $m = 3$ and $n = 4$ satisfied these criteria. We specify the field at the photospheric boundary ($z = 0$) to be

$$\mathbf{B}(x, y, \alpha) = a_1 \mathbf{B}_1(x, y, 0, 3, 4, \alpha) + a_2 \mathbf{B}_2(x, y, 0, 3, -4, \alpha), \tag{6.26}$$

where a_1 and a_2 are real constants (we shall vary these to develop asymmetry in the solutions in section 6.4.5). Note that if the α value is positive we would expect, in general, a forward S shape. In the following study we alter variously the start x coordinates of the field, α (note we will only get real solutions to 6.26 for $\alpha < 5$), and the weighting of each Fourier component (a_1 and a_2), in order to develop various degrees of asymmetry and scale in our field line solutions. In what follows unless stated it is to be assumed that $a_1 = a_2 = 1$, indeed it is only in section 6.4.5 that we change the values of the Fourier component weighting.

6.4.2 Preliminary results

Evaluations of $\mathcal{W}_p(\mathbf{B})$ values were performed; obtained over startpoint ranges of $x \in [2.2, 3]$ and $y \in [0.01\pi, 0.03\pi]$ (these ranges were found by trial and error to

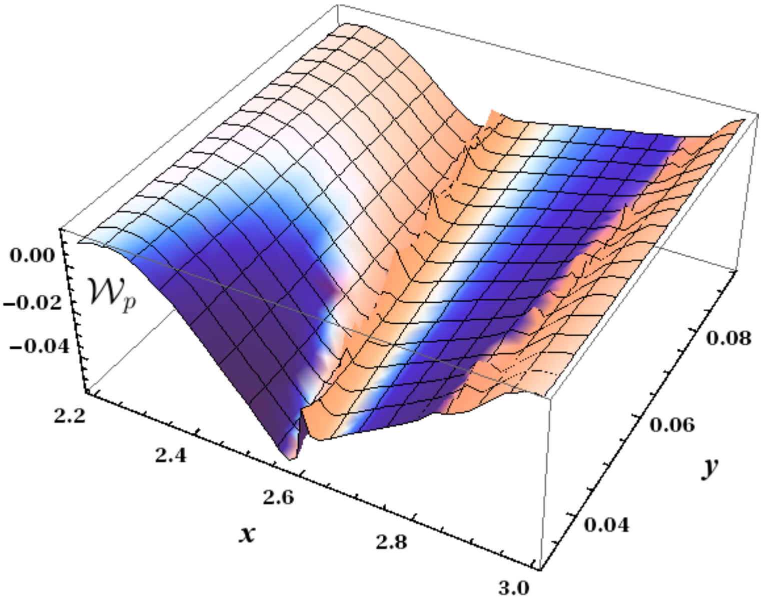

Figure 6.8: A surface plot of $\mathcal{W}_p(\mathbf{B})$, where $\mathbf{B}$ is generated using equation 6.26 with $\alpha = 2$. The ranges $x \in [2.2, 3]$ and $y \in [0.01\pi, 0.03\pi]$ were used. Starting from $x = 2.2$ The $\mathcal{W}_p$ value decreases positive to negative as x is increased, reaching a minimum point. After this minimum point $\mathcal{W}_p$ increases with x. We note this behaviour is consistent across the y range, with the most extreme $\mathcal{W}_p$ values occurring for $y = 0.01\pi$.

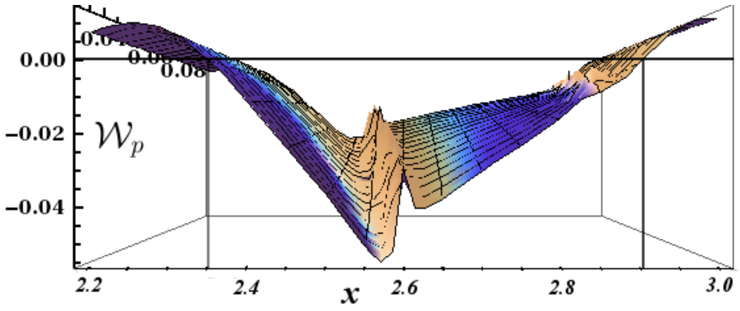

Figure 6.9: The surface plot depicted in Figure 6.8 viewed along the $\hat{y}$ direction. The cross section curve nearest the viewer is that of $y = 0.01\pi$. Marked on the figure are the x values for which $\mathcal{W}_p \approx 0$. These values are $x \approx 2.35$ and $x \approx 2.9$. We see a higher percentage of the field configurations have negative $\mathcal{W}_p$.

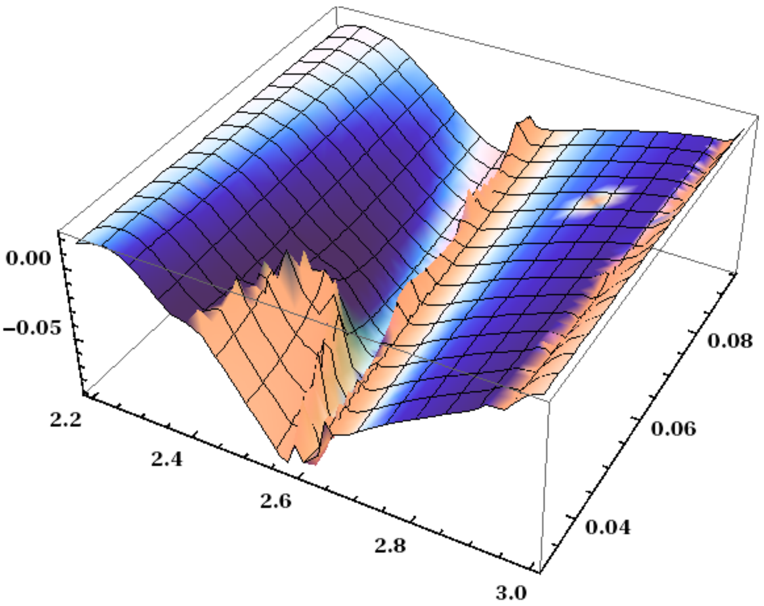

Figure 6.10: A surface plot of $\mathcal{W}_p(\mathbf{B})$, where $\mathbf{B}$ is generated using equation (6.26), with $\alpha = 3$. The ranges $x \in [2.2, 3]$ and $y \in [0.01\pi, 0.03\pi]$ were used (ranges found to consistently produce real field lines). Starting from $x = 2.2$ the $\mathcal{W}_p$ value decreases positive to negative as x is increased, reaching a minimum point. After this minimum point $\mathcal{W}_p$ increases with x. We note this behavior is consistent across the y range, with the most extreme differences in $\mathcal{W}_p$ occurring for $y = 0.01\pi$. The behaviour is similar to that of $\alpha = 1$ with the $\mathcal{W}_p$ values reaching greater extremes.

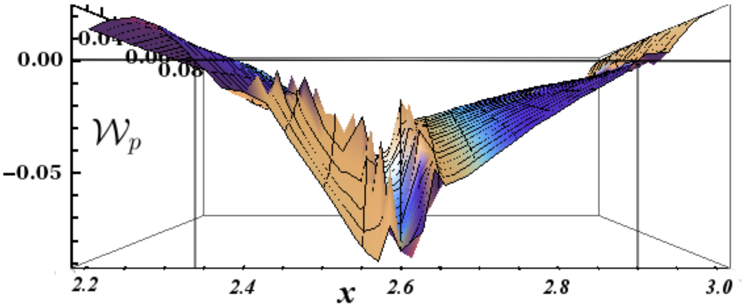

Figure 6.11: The surface plot depicted in Figure 6.10 viewed along the $\hat{y}$ direction. The cross section curve nearest the viewer is that of $y = 0.01\pi$. Marked on the figure are the x values for which $\mathcal{W}_p \approx 0$. These values are $x \approx 2.34$ and $x \approx 2.9$. We see a higher percentage of the field configurations have negative $\mathcal{W}_p$.

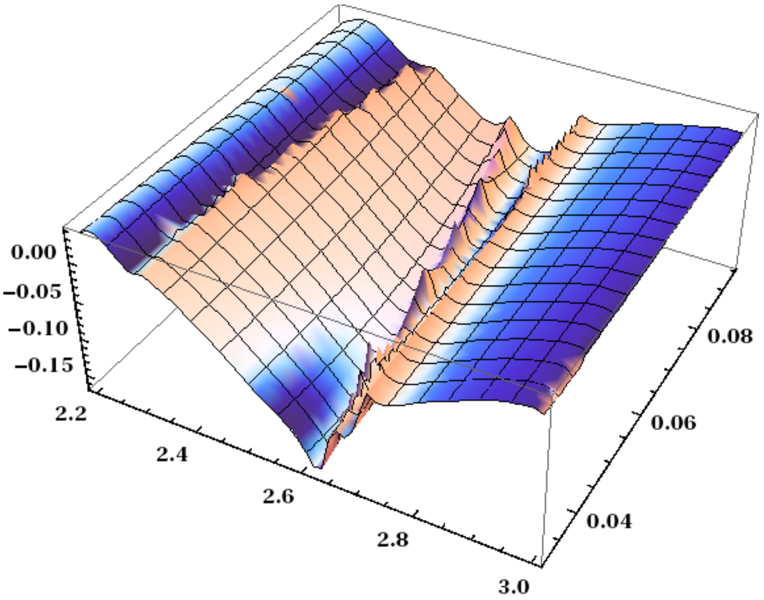

Figure 6.12: A surface plot of $\mathcal{W}_p(\mathbf{B})$, where $\mathbf{B}$ is generated using equation (6.26), with $\alpha = 4$. The ranges $x \in [2.2, 3]$ and $y \in [0.01\pi, 0.03\pi]$ were used. Starting from $x = 2.2$ The $\mathcal{W}_p$ value decreases positive to negative as x is increased, reaching a minimum point. After this minimum point $\mathcal{W}_p$ increases with x. We note this behavior is consistent across the y range, with the most extreme differences in $\mathcal{W}_p$ occurring for $y = 0.01\pi$. The behavior is similar to that of $\alpha = 1$ and 3 with the $\mathcal{W}_p$ values reaching greater extremes.

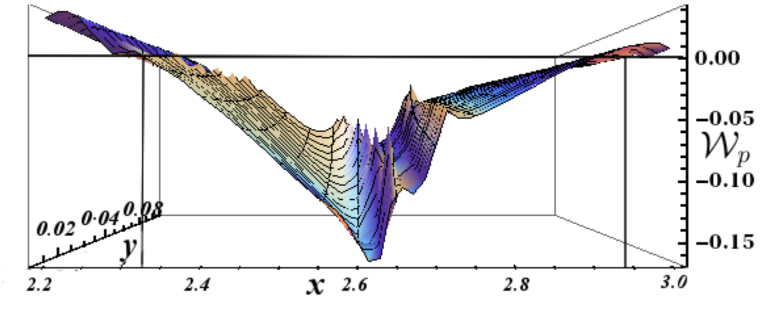

Figure 6.13: The surface plot depicted in Figure 6.12 viewed along the $\hat{y}$ direction. The cross section curve nearest the viewer is that of $y = 0.01\pi$. Marked on the figure are the x values for which $\mathcal{W}_p \approx 0$. These values are $x \approx 2.33$ and $x \approx 2.94$. We see a higher percentage of the field configurations have negative $\mathcal{W}_p$.

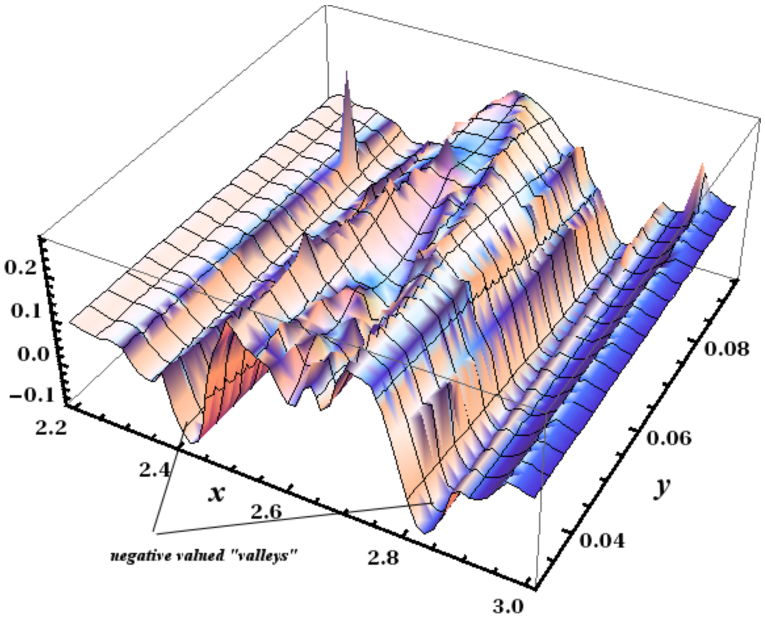

Figure 6.14: A surface plot of $\mathcal{W}_p(\mathbf{B})$, where $\mathbf{B}$ is generated using equation 6.26, with $\alpha = 4.9$.The ranges $x \in [2.2, 3]$ and $y \in [0.01\pi, 0.03\pi]$ were used . In contrast to the smaller alpha values (Figures 6.8, 6.10 and 6.12) $\mathcal{W}_p$ is generally positive. Instead there are two small "valleys" of negative $\mathcal{W}_p$ marked on the figure which are consistent across all y values.

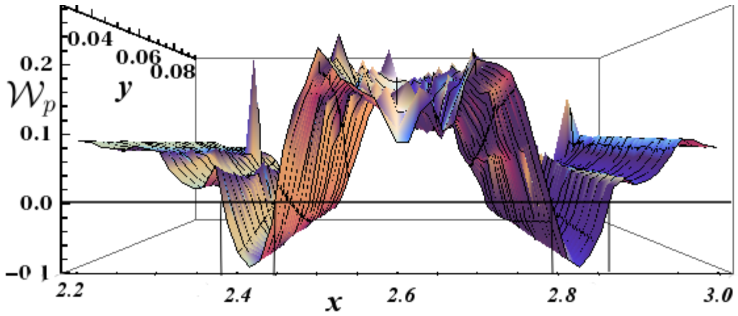

Figure 6.15: The surface plot depicted in Figure (6.14) viewed along the $\hat{y}$ direction. The cross section curve nearest the viewer is that of $y = 0.01\pi$. Marked on the figure are the x values for which $\mathcal{W}_p \approx 0$. These values are $x \approx 2.38$, $x \approx 2.45$, $x \approx 2.79$ and $x \approx 2.86$. We see a higher percentage of the field configurations have positive $\mathcal{W}_p$.

produce consistent results), with $z = 0$, $\alpha = 2$ (Figure 6.8), $\alpha = 3$ (Figure 6.10) , $\alpha = 4$ (Figure 6.12) and $\alpha = 4.9$ (Figure 6.14). These surfaces are also shown viewed from the $\hat{y}$ axis, $\alpha = 2$ (Figure 6.9), $\alpha = 3$ (Figure 6.11) , $\alpha = 4$ (Figure 6.13) and $\alpha = 4.9$ (Figure 6.15). We see, in the cases of $\alpha = 2$, 3 and 4 the field lines $\mathcal{W}_p$ can take on both positive and negative values. By contrast the in the $\alpha = 4.9$ case the $\mathcal{W}_p$ field values are generally of positive value, except for two dipped section of the $\mathcal{W}_p$ surface (marked on Figures 6.14 and 6.15). We further note that the more extreme variations occur for a y value of 0.01π. It is this value which shall be used for the following work.

The following results, depicted in Figures 6.8-6.15, will be of interest in the following study:

- For α values in the range $\approx [1, 4]$ there appears to be a small x range $x \approx [2.33, 2.35]$ at which the $\mathcal{W}_p$ values is zero, and which marks the points at which $\mathcal{W}_p$ switches from positive to negative values. We shall see in section 6.4.3 this is true over a range of α values (to a good degree of approximation). We shall see this change, and indeed the zero value, result form the differing magnitudes of $\mathcal{W}_{pl}$ and $\mathcal{W}_{pnl}$, which are generally of opposite sign (see sections 5.3.5 and 6.3.4).
- The extreme $\alpha = 4.9$ case clearly shows differing $\mathcal{W}_p$ behavior from the lower α cases, it is generally positive. We shall see these field lines correspond to S shaped sigmoids have significant aspect ratios (> 1). This result would appear to contradict the assumptions of Green *et al* [50] (section 6.3.1).

6.4.3 Fixed start position, changing α

In section 6.4.2 we found the apparent existence of an x value (≈ 2.35) for which the polar writhe measure changed sign from positive to negative, for a positive α value. In this section we fix a start point and investigate whether this phenomenon persists over a range increasing α values. Figure 6.16 details the $\mathcal{W}_p$, $\mathcal{W}_{pl}$ and $\mathcal{W}_{pnl}$ values for field lines with start point ($x = 2.35, y = 0.01\pi, z = 0$) over a range of α values $\alpha \in [0.5, 5]$. For the domain $\alpha \in [0.5, 3]$ the $\mathcal{W}_{pl}$ and $\mathcal{W}_{pnl}$ measures are equal and opposite (to a good degree of approximation). As α is increased above 3, $\mathcal{W}_p$ oscillates between very small positive and negative values, with two periods of slightly increased $\mathcal{W}_p$ oscillations for $\alpha > 4.7$ and $3.5 < \alpha < 3.7$). With regards

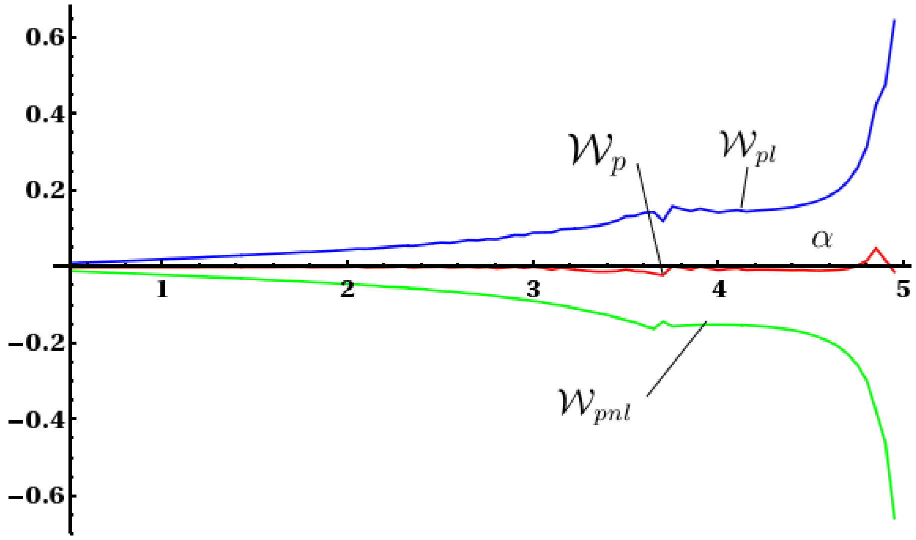

Figure 6.16: Plots of field line $\mathbf{B}$ $\mathcal{W}_p$, $\mathcal{W}_{pl}$ and $\mathcal{W}_{pnl}$ values for a start point $(x = 2.35, y = 0.01\pi)$, plotted over a range $\alpha \in [0.5, 5]$. It can be seen that for range of roughly $\alpha \in [0.5, 3]$ the $\mathcal{W}_p$ value is very close to zero as a result of $\mathcal{W}_{pl}$ and $\mathcal{W}_{pnl}$ being equal and opposite in size. After this range the $\mathcal{W}_p$ value oscillates very close to zero between a small range of $\mathcal{W}_p$ values (except $\alpha > 4.7$ and $3.5 < \alpha < 3.7$).

to $\alpha > 4.7$ shall see in section 6.4.4 that high α values cause field configurations with a higher degree of writhing and asymmetry. We shall see in this section that the discontinuity between $3.5 < \alpha < 3.7$ corresponds to the field lines crossing a separatrix surface.

In Figures 6.17 and 6.18 we see plots of the various polar writhe measures for curves with fixed start points $(x = 2.19, y = 0.01\pi, z = 0)$ and $(x = 2.5, y = 0.01\pi, z = 0)$, where α is varied over the range $\alpha \in [0.5, 5]$. Looking back to Figures 6.8-6.12, these start points, in particular their x values, are either side of the zero $\mathcal{W}_p$ configuration and generate field lines with $\mathcal{W}_p$ values of opposing sign. In Figures 6.17 and 6.18 we see that in both cases the sign of $\mathcal{W}_p$ remains consistent whilst the magnitude increases slowly (barring the extreme values of α in Figure 6.18). So in the case of $x = 2.19$ the magnitude of the $\mathcal{W}_{pl}$ contribution is always greater than that of the $\mathcal{W}_{pnl}$ contributions, and vice versa for the $x = 2.5$ case (again excluding some of the extreme α values). This would suggest that there is some degree of consistency in the global geometry of the field lines with increasing α, in the sense that the relative magnitudes of local and non-local contributions are roughly conserved.

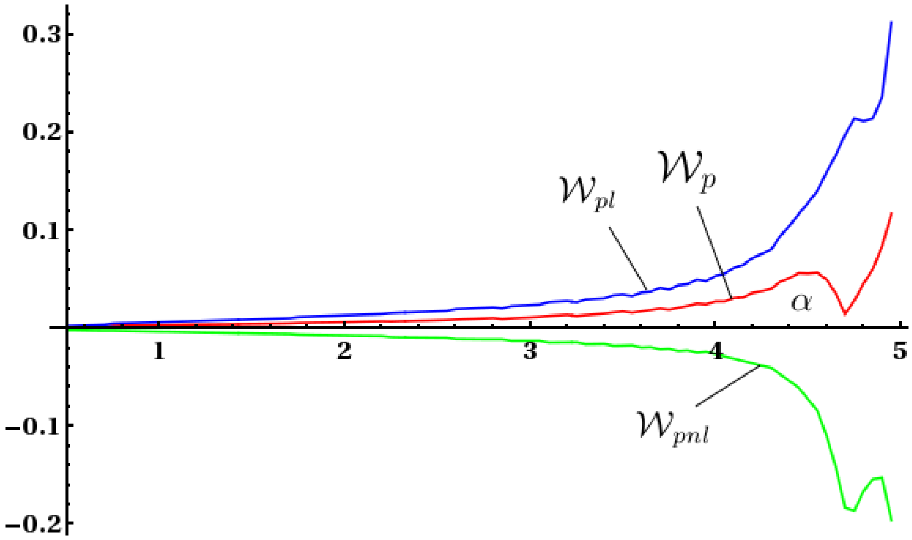

Figure 6.17: Plots of field line **B** $\mathcal{W}_p$, $\mathcal{W}_{pl}$ and $\mathcal{W}_{pnl}$ values for a start point $(x = 2.19, y = 0.01\pi)$, plotted over a range $\alpha \in [0.5, 5]$. It can be seen, for the full range of α values, the $\mathcal{W}_p$ measure remains positive and increases gradually, except after $\alpha \approx 4.6$ where the non local contribution begins to decrease in magnitude. The sudden decrease in $\mathcal{W}_p$ after $\alpha \approx 4.6$ is an interesting phenomenon. At this point the field lines aspect ratio shows a marked increase (see figure 6.19). There may be some reason this occurs, we also see a sharp changes in $\mathcal{W}_p$, in this α range, in Figures 6.16 and 6.18. This issue is not covered in this study but would merit further investigation.

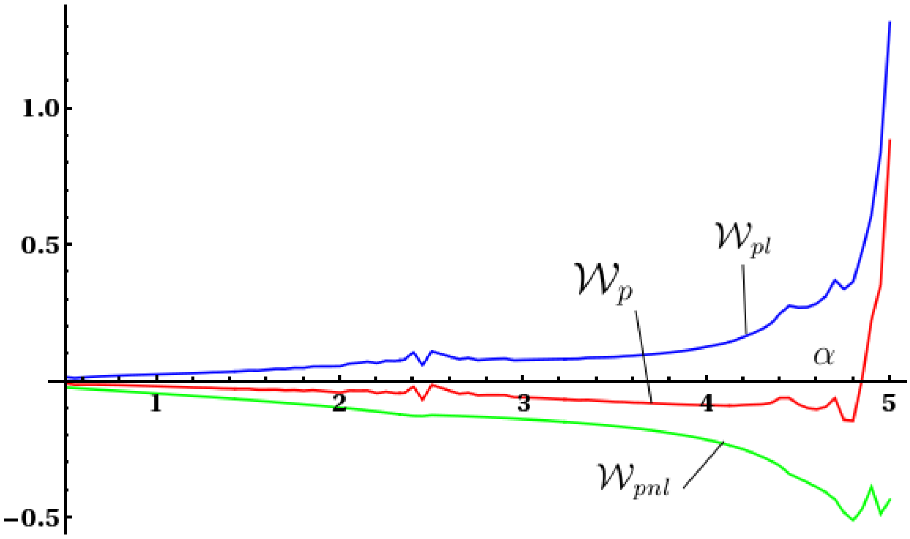

Figure 6.18: Plots of field line $\mathbf{B}$ $\mathcal{W}_p$, $\mathcal{W}_{pl}$ and $\mathcal{W}_{pnl}$ values for a start point ($x = 2.5, y = 0.01\pi$), plotted over a range $\alpha \in [0.5, 5]$. It can be seen, for the full range of α values, the $\mathcal{W}_p$ measure remains negative and increases gradually (except after $\alpha \approx 4.6$ and $2.4 < \alpha < 2.5$). This is clearly a result of $\mathcal{W}_{pnl}$ being greater in magnitude and opposite in sign to the $\mathcal{W}_{pl}$ contributions.

Aspect ratio and shape

In section 6.4.3 we demonstrated a degree of consistency with regards to the structure of field lines, in terms of their $\mathcal{W}_p(\mathbf{B})$ measures (at specific fixed starting points), over a range of α values. In this section we study the geometrical aspects of the field configurations over the same range of input values. Starting with ($x = 2.35, y = 0.01\pi, z = 0$), for which $\mathcal{W}_p$ results are depicted in Figure 6.16 (for a range $\alpha \in [0.5, 5]$). Figure 6.19 depicts the field line aspect ratio over this α range. For $x = 2.35$ the aspect ratio remains constant (≈ 0.35) over a range of values $\alpha \approx [0.5, 3.5]$. It then increases slightly to approximately 0.4 and is close to constant constant up until $\alpha \approx 4.8$, suggesting an increase in height in this alpha range is twinned with an increase in footpoint width. We shall see later the jump at $\alpha \approx 3.5$ corresponds to the field lines crossing a separatrix surface (Figure 6.23). Figure 6.19 demonstrates that the aspect ratios of solutions $x = 2.5$ and $x = 2.19$ remain close to constant over ranges of α which are larger and smaller respectively. Further the aspect ratios of the $x = 2.5$ and $x = 2.19$ are larger and smaller, respectively, than the $x = 2.35$ case. This suggests, at least over the range of configurations we have focused on, a

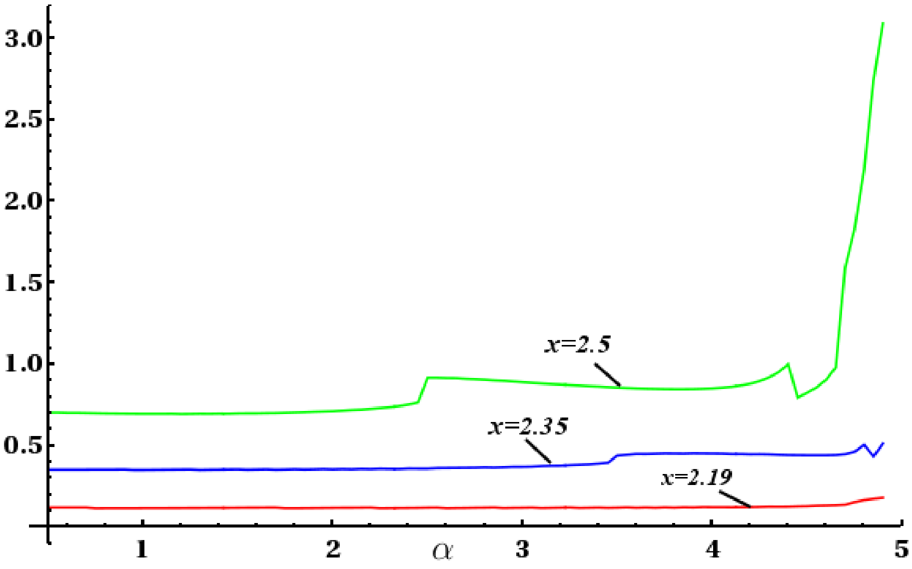

Figure 6.19: Plots of field aspect ratio for $\alpha \in [0.5, 4.9]$. The three plots represent field generated with start points $(x = 2.35, y = 0.01\pi)$, $(x = 2.19, y = 0.01\pi)$ and $(x = 2.5, y = 0.01\pi)$. For each plot the aspect ratio appears to stay constant for a range of α values for each plot. There is a sudden increase in aspect ratio around $\alpha \approx 3$ and for $x = 2.5$, $\alpha \approx 3.5$ for $x = 2.35$ and $\alpha \approx 4.85$ for $x = 2.19$. For more extreme α values there is only a significant change in aspect ratio for $x = 2.5$.

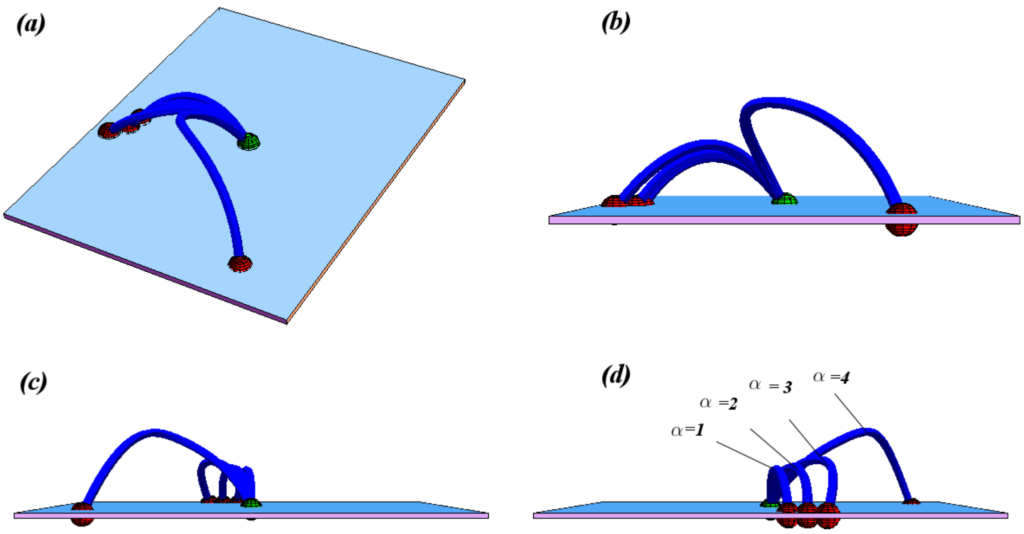

Figure 6.20: (a) to (d) represent field configurations generated using start points ($x = 2.35, y = 0.01\pi, z = 0$). The respective α values are $\alpha = 1$ ($\mathcal{W}_p = 4.02 \times 10^{-4}$), $\alpha = 2$ ($\mathcal{W}_p = 1.1 \times 10^{-3}$), $\alpha = 3$ ($\mathcal{W}_p = -4.76 \times 10^{-3}$), $\alpha = 4$ ($\mathcal{W}_p = 7.638 \times 10^{-3}$). (b) represents the view from the y axis, (c) and (d) represent the viewpoints of observers at the start point (($x = 2.3545, y = 0.01\pi, z = 0$)) and endpoints of the curves respectively. It is clear for the curves $\alpha = 1$, $\alpha = 2$, $\alpha = 3$ that there is both an increase in height and apex-region rotation with increasing α. The field line generated for $\alpha = 4$ appears at first sight to be different in nature to those of $\alpha = 1$, $\alpha = 2$ and $\alpha = 3$. However we shall see its shape has similar $\mathcal{W}_{pl}$ and $\mathcal{W}_{pnl}$ values to the other three configurations. The $\alpha = 4$ field line can be said to belong to a different separatrix surface.

similar relationship between aspect ratio and $\mathcal{W}_p$ sign as that found in the symmetric field configurations (section 6.3.4). That is, there is an aspect ratio (or small range of aspect ratios), over which the sign of $\mathcal{W}_p$ changes (at least for non extreme α values).

A second observation is that for extreme alpha values ($\alpha > 4.8$) the field configurations can show a drastic increase in aspect ratio (Figure 6.19). This may be more indicative of active field regions.

Figure 6.20 depicts the field line configurations generated using a start point ($x = 2.35, y = 0.01\pi, z = 0$) for α values $\alpha \in 1, 2, 3, 4$. We see that increasing α causes an increase in asymmetry of the field line configurations, manifested through a rotation of the apex position. We note the endpoint $\alpha = 4$ configuration shows a drastic

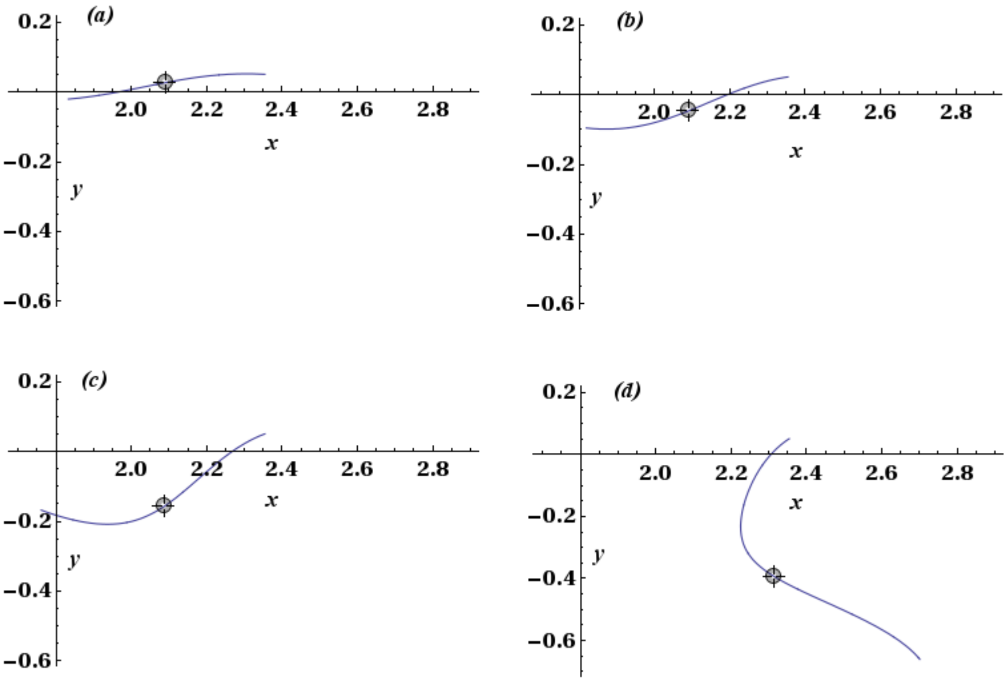

Figure 6.21: (a) to (d) represent projections onto the x-y plane of field configurations $\mathbf{B}$. All fields are generated at start points $(x = 2.35, y = 0.01\pi, z = 0)$. The respective α values are (a) $\alpha = 1$, (b) $\alpha = 2$, (c) $\alpha = 3$, (d) $\alpha = 4$. The positions of the curve's apex are marked on the diagrams by cross hairs. (d) appears at first sight to be significantly different from the other three. However, its shape is not so different. The degree of asymmetry has only slightly increased, but it has swapped from the downward moving section of curve to the upward moving section. Also as we shall see both start-end point and apex point orientations go through the same rotation (Figure 6.23).

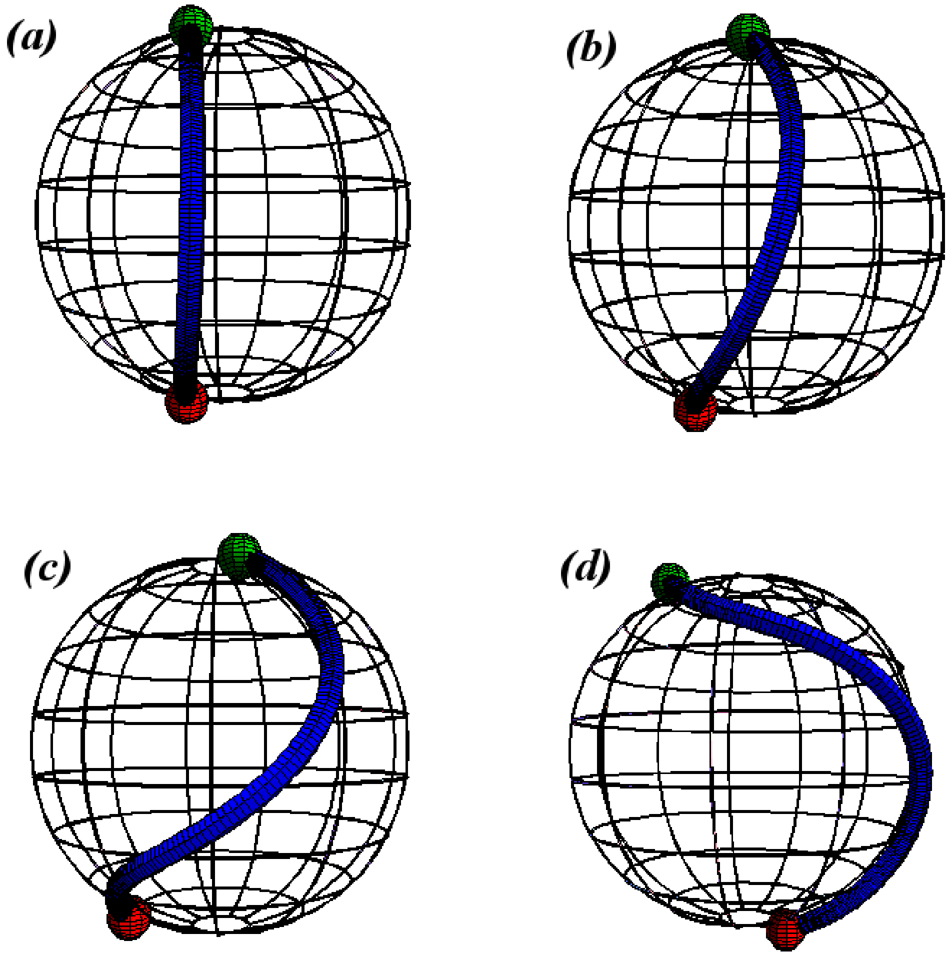

Figure 6.22: (a) to (d) represent the tantrix curves ($\widehat{\mathbf{T}}_{\mathbf{B}}$) of field configurations $\mathbf{B}$. All fields are generated at start points ($x = 2.35, y = 0.01\pi, z = 0$). The respective α values are (a) $\alpha = 1$, (b) $\alpha = 2$, (c) $\alpha = 3$, (d) $\alpha = 4$. As α is increased the degree of asymmetry in the tantrix curve increases. Specifically the section of $\widehat{\mathbf{T}}_{\mathbf{B}}$ in the southern hemisphere would occupy an increasingly large contributions towards $\mathcal{W}_{pl}$. Except in the case of (d) for which it is the northern hemispherical component which has the larger measure. Clearly as α is increased the shearing of the tantrix curve about the equator increases, leading to an increase in the total $\mathcal{W}_{pl}$ value.

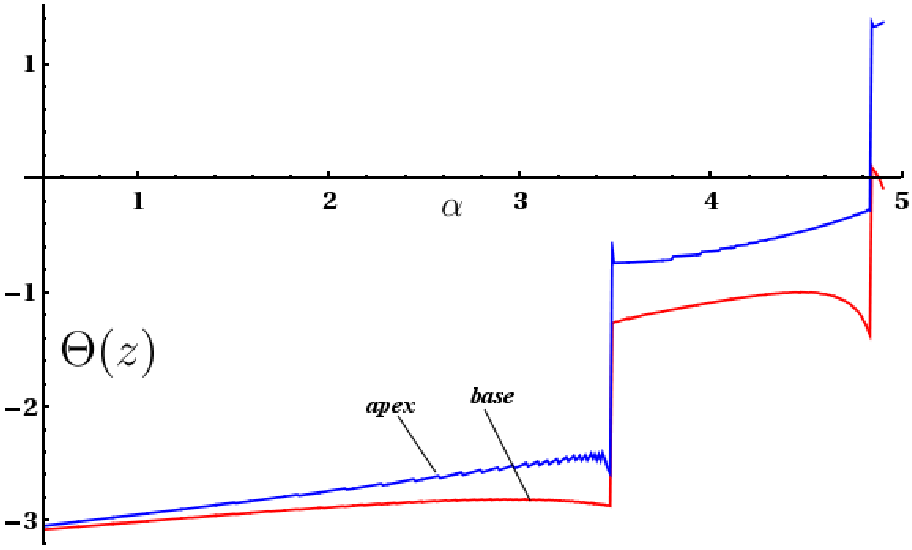

Figure 6.23: Plots of apex orientation $\Theta(z_{max})$ and footpoint orientation $\Theta(z=0)$ for $\alpha \in [0.5, 4.9]$, $(x=2.35, y=0.01\pi, z=0)$. We see that for α values, up to roughly 3.5, the apex orientation increases steadily. The base orientation does not change in the same manner, it increases at a slower rate at first and then decreases. As a result the magnitude of $\mathcal{W}_{pnl}$ increases with α over this period. The discontinuous jumps in orientation (due to the change in morphology detailed in Figures 6.21 and 6.22) occur for both apex and footpoint directions at the same time so the change in $\mathcal{W}_{pnl}$ is not particularly significant. This can be seen in Figure 6.16 this discontinuous jump in values only corresponds to a small peak in the $\mathcal{W}_{pnl}$ curve (at $\alpha \approx 3.5$). Further this discontinuous jump coincides with the field lines crossing a separatrix surface (see Figure 6.20).

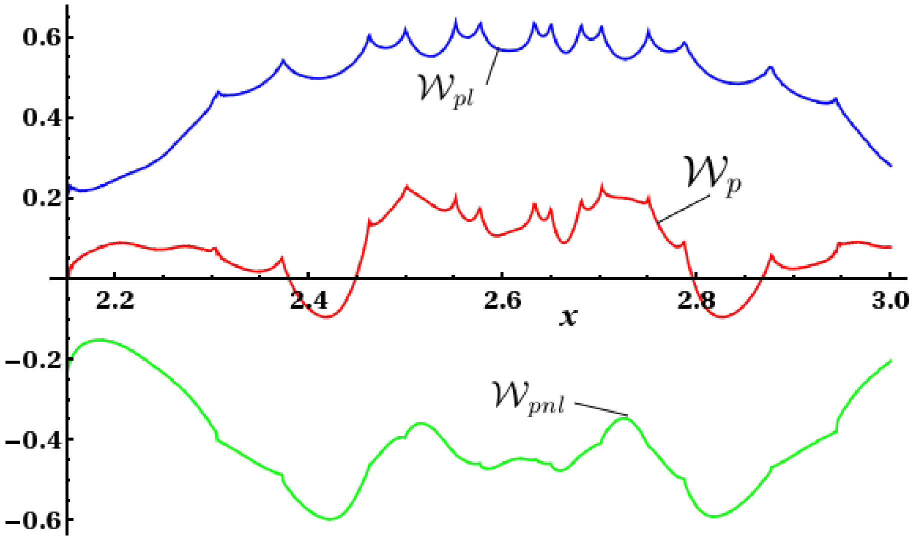

Figure 6.24: Plots of field line **B** $\mathcal{W}_p$, $\mathcal{W}_{pl}$ and $\mathcal{W}_{pnl}$ values for $y = 0.01\pi$, $\alpha = 4.9$, and varying x over the set $x \in [2.1, 3]$. We see for the majority of x-values $\mathcal{W}_p$ is positive. There are two regions $x \approx [2.38, 2.45]$ and $x \approx [2.79, 2.86]$, for which $\mathcal{W}_p$ is negative. Further, there are many discontinuous (in terms of the derivative of the measures) jumps in both all three measures. These jumps correspond to the field lines crossing separatrix surfaces.

rotation of its end point from the other cases. This is turn coincides with a similar rotation of the apex orientation ensuring the change in $\mathcal{W}_{pnl}$ is not significantly large. This rotation is said to lie in a different *separatrix* surface. Separatrix surfaces are defined as regions at whose boundaries field lines diverge (Longcope [66]). Figures 6.21 and 6.22 represent the x-y plane projection and tantrix curves ($\widehat{\mathbf{T}}_{\mathbf{B}}$) of field configurations **B**, shown in Figure 6.20. Both figures demonstrate that, in increasing α the degree of asymmetry is increased. This asymmetry causes a change in both $\mathcal{W}_{pl}$ and $\mathcal{W}_{pnl}$ (Figures 6.22 and 6.23). However, these changes generally appear to occur at the same rate. So it would appear that an increase in asymmetry does **not necessarily** lead to a change in the sign of $\mathcal{W}_p$.

6.4.4 Extreme α values - tall field structures

Choosing a large α value leads to more extreme field configurations. Fixing $y = 0.01\pi$, $\alpha = 4.9$, and varying x over the set $x \in [2.1, 3]$ we obtained values for the $\mathcal{W}_p$, $\mathcal{W}_{pl}$ and $\mathcal{W}_{pnl}$ of the field line **B** produced (Figure 6.24). For the majority of x values we see $\mathcal{W}_p$ is positively signed as a result of $\mathcal{W}_{pl}$ being greater than $\mathcal{W}_{pnl}$. This

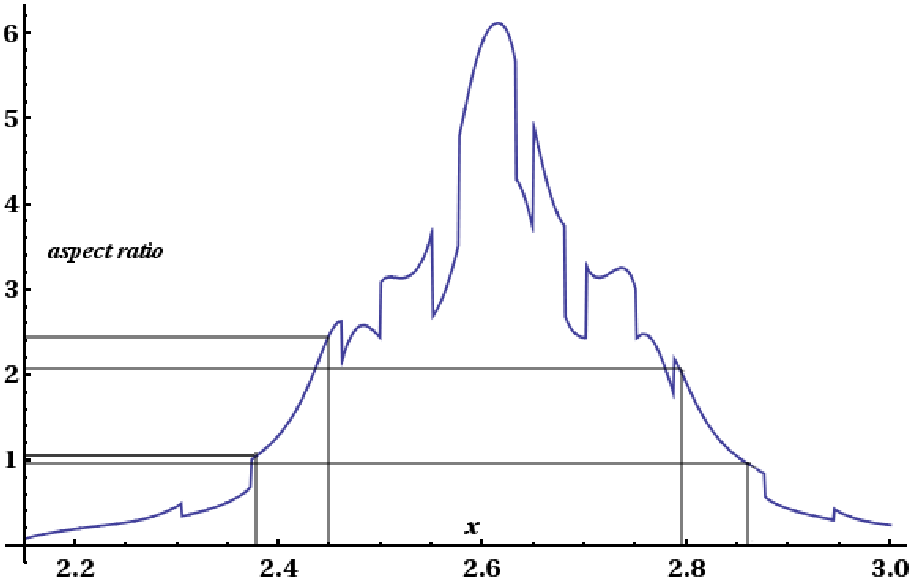

Figure 6.25: A plot of field line **B**'s aspect ratio for $y = 0.01\pi$, $\alpha = 4.9$, and varying x over the set $x \in [2.1, 3]$. Marked on the diagram are the points where $\mathcal{W}_p(\mathbf{B})$ changes sign; the sets of field lines with negative $\mathcal{W}_p$ values cover ranges of aspect ratio $\approx [1, 1.4]$. Though not all field configurations within this range have negative $\mathcal{W}_p$ values. Any field lines with aspect ratio above this range have positive $\mathcal{W}_p$ values.

would appear to be in opposition to the assumption made by Green *et al* [50] which aligns such forward S flux ropes with negative writhing (section 6.3.1). There are two significant start point subsets ($x \approx [2.38, 2.46]$ and $x \approx [2.79, 2.87]$) for which the $\mathcal{W}_p$ value is negative; we shall show that these structures are symmetric; though we shall see symmetry does not nescessarily imply negative $\mathcal{W}_p$ values.

Figure 6.25 depicts the aspect ratio of the field line $\mathbf{B}$ as evaluated over the same range. Marked on the figure are the values at which the sign changes (of $\mathcal{W}_p$) occur. It is clear the results tend to oppose the assumption of Green *et al* [50] of forward S sigmoids (we shall see that these configurations are S shaped) of significant height, having negative writhe values. In general they have positive $\mathcal{W}_p$ values, at least based on this study. Further, we see the possibility of $\mathcal{W}_p(\mathbf{B})$ changing sign at aspect ratios significantly greater than the symmetric field example. Indeed this range includes the start height (aspect ratio) detailed in the Török and Kliem MHD confined eruption simulation [110].

Figures 6.26, 6.27 and 6.28 depict field lines structures $\mathbf{B}$ in various forms. Figure 6.26 depicts the field line configurations for $\alpha = 4.9$, $y = 0.01\pi$ and x values of $x = 2.379$(a), $x = 2.41$(b), $x = 2.43$(c) and $x = 2.43$ (d). We see in Figure 6.24 these configurations all depict the field line morphologies over a range of x values for which the $\mathcal{W}_p$ measure changes sign from positive to negative and then back. As x is increased we see two geometrical changes in field line configuration. First of all the height of the field line increases and secondly the section of field line around the apex appears to rotate towards the viewer in an clockwise direction. In Figure 6.27 we see this rotation appears to coincide with a change from asymmetry with bias towards the upward pointing section of the field line, through symmetric configurations and then onto an asymmetric configuration, whose bias is towards the downward pointing section of the field line. This conclusion is matched by the tantrix sphere ($\widehat{\mathbf{T}}_{\mathbf{B}}$) diagrams, shown in Figure 6.28. In this case we see the decrease in asymmetry causes the change from positive to negative writhing, as x is increased further the asymmetry switches section of curve and as the symmetry increases $\mathcal{W}_p$ becomes positive again.

The analysis of the above paragraph would appear to suggest, for configurations whose morphologies are symmetric, the $\mathcal{W}_p$ value will be negative for field lines of significant scale. As previous simulations have tended to use symmetric flux ropes and field lines, this could at first sight validate the writhing assumptions of Green *et al* [50].

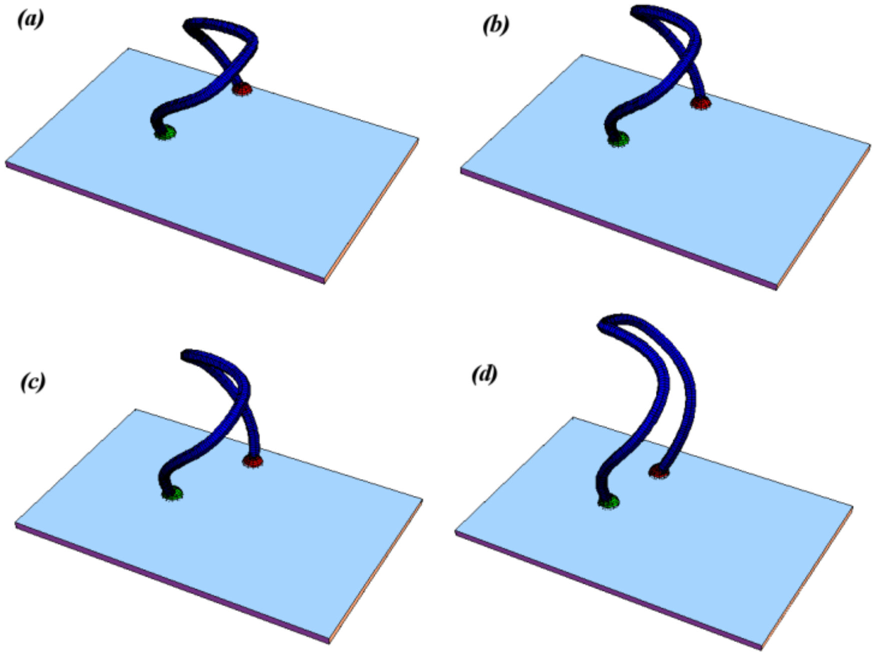

Figure 6.26: (a) to (d) represent the field line configurations $\mathbf{B}$, obtained for $\alpha = 4.9$, $y = 0.01\pi$ and x values of $x = 2.379$(a), $x = 2.4$(b), $x = 2.41$(c) and $x = 2.45$ (d). It can be seen that the apex orientation rotates in a clockwise direction. The polar writhe values are 0.00238213 (a),-0.0725992 (b),-0.0895121 (c) and 0.0181881 (d). During this rotation the sign of $\mathcal{W}_p$ changes from positive to negative and then back to positive (see Figure 6.24). We also note an increase in apex height across (a) to (d).

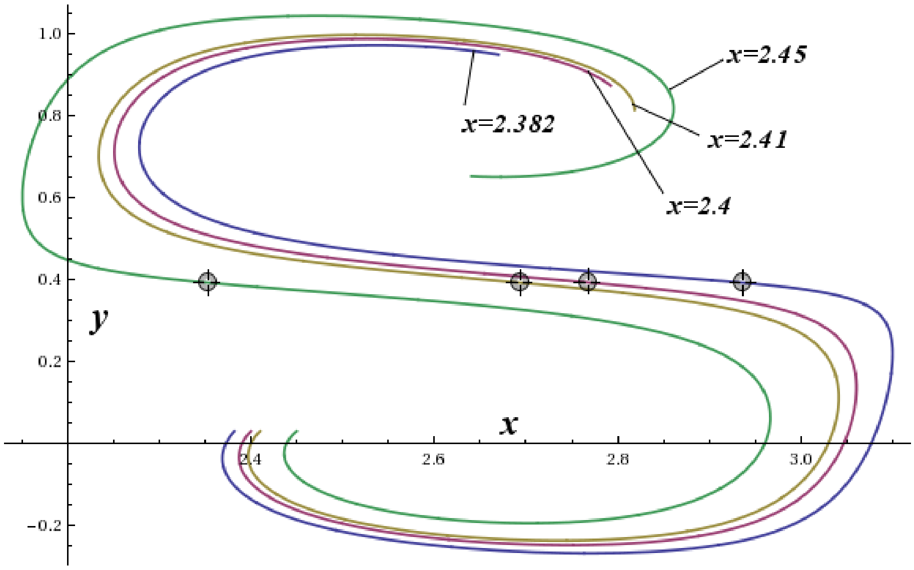

Figure 6.27: Depicted area the field line configurations **B**, projected onto the x-y plane, obtained for $\alpha = 4.9$, $y = 0.01\pi$ and x values of $x = 2.379$, $x = 2.40$, $x = 2.41$ and $x = 2.45$. The configuration at $x = 2.379$ is significantly asymmetric with a greater degree of total curvature in the section of curve joining the start point to the apex. As x is increased we see in the $x = 2.40$ and $x = 2.41$ a decrease in asymmetry. Finally the $x = 2.45$ sigmoid shape is again asymmetric with the greater degree of curvature in the endpoint-apex section of the field line configuration. To sum up there has been a transfer of asymmetry from the upward moving section of **B** to the downward moving section.

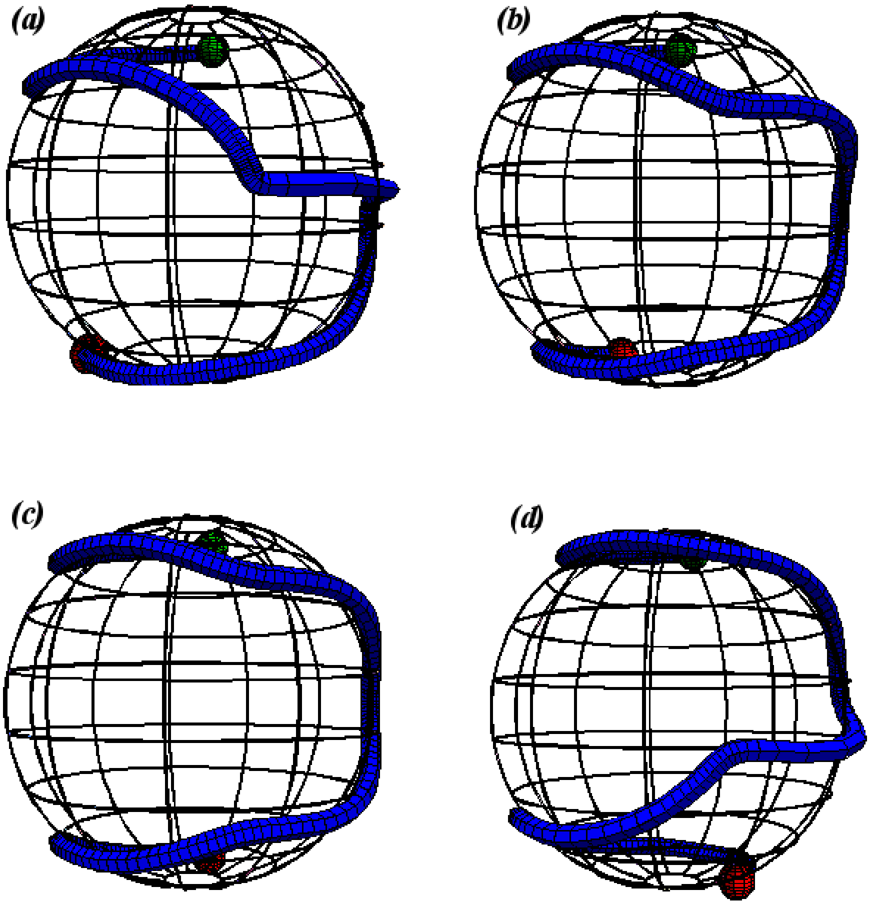

Figure 6.28: (a) to (d) represent the field line tantrix curves $\widehat{\mathbf{T}}_{\mathbf{B}}$, obtained for $\alpha = 4.9$, $y = 0.01\pi$ and x values of $x = 2.379$ (a), $x = 2.4$ (b), $x = 2.41$ (c) and $x = 2.45$ (d). For the tantrix curve in (a) the larger contribution to $\mathcal{W}_{pl}$ would come from the northern hemispherical components. In (b) and (c) the contributions from the northern and southern hemispherical components ($\frac{\mathrm{d}s}{\mathrm{d}z} > 0$ and $\frac{\mathrm{d}s}{\mathrm{d}z} < 0$ respectively) are closer to equality. In (d) the tantrix curve shows the magnitude of southern hemispherical contributions to $\mathcal{W}_{pl}$ would be greater than those from the northern hemisphere, the opposite scenario to that of (a). So as x has been increased there has been a change in asymmetry of the curves local writhing contributions from the upward moving field line section to the downward moving section.

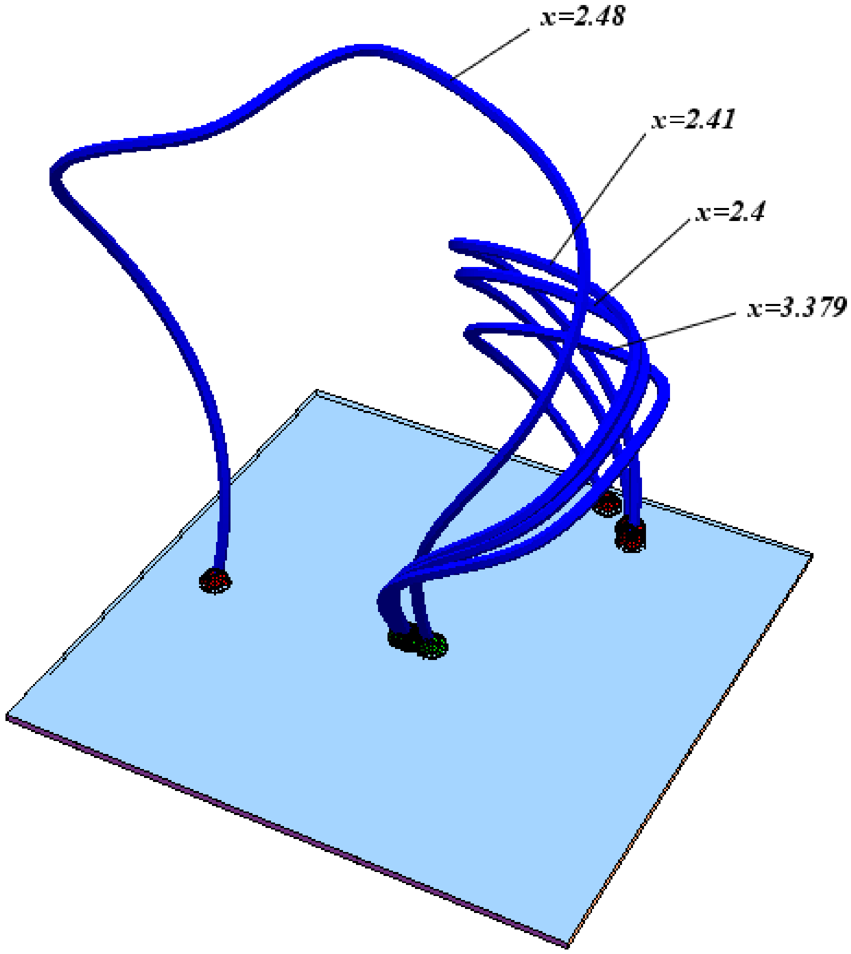

Figure 6.29: Illustrating field lines on either side of a separatrix surface. Depicted are the field line configurations **B** obtained for $\alpha = 4.9$, $y = 0.01\pi$ and x values of $x = 2.379$, $x = 2.40$, $x = 2.41$ and $x = 2.48$. The first three configurations ($x = 2.379$, $x = 2.40$, $x = 2.41$) have already been discussed. The final projection has occurred after the field has crossed a separatrix layer.

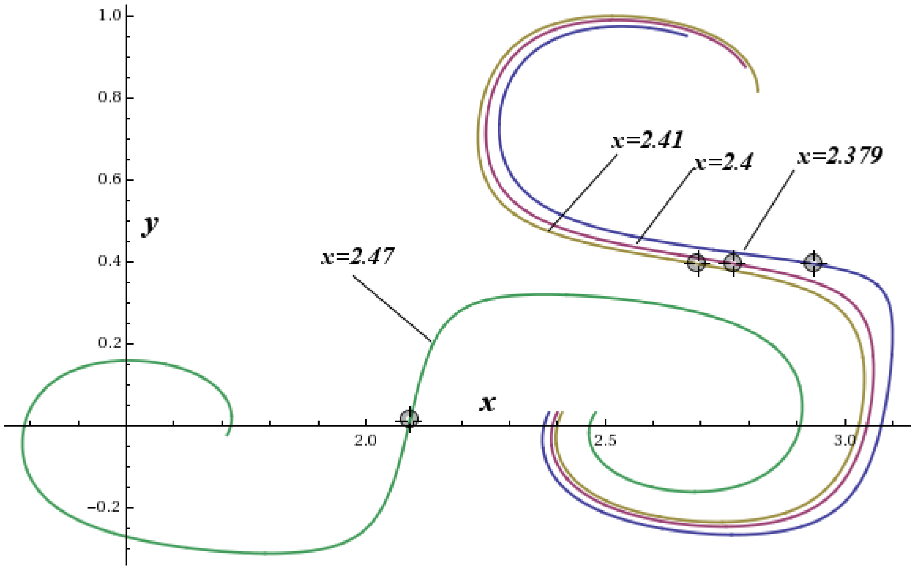

Figure 6.30: Illustrating field line projections on either side of a separatrix surface. Depicted are the field line configurations **B**, projected onto the x-y plane, obtained for $\alpha = 4.9$, $y = 0.01\pi$ and x values of $x = 2.379$, $x = 2.40$, $x = 2.41$ and $x = 2.48$. The first three configurations ($x = 2.379$, $x = 2.40$, $x = 2.41$) have already been discussed. The final projection has occurred after the field has crossed a separatrix layer. We note its structure appears to be close to symmetric.

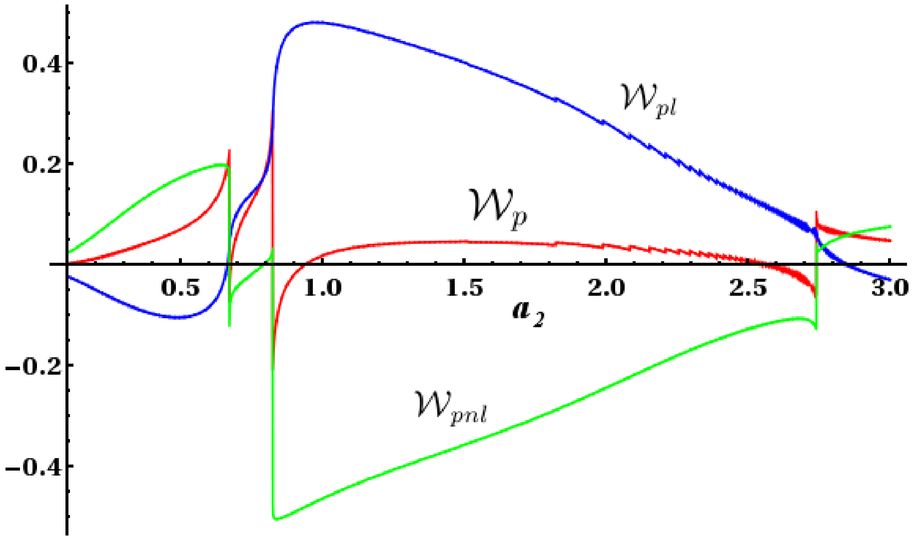

Figure 6.31: Plots of $\mathcal{W}_p(\mathbf{B})$, $\mathcal{W}_{pl}(\mathbf{B})$ and $\mathcal{W}_{pnl}(\mathbf{B})$, with start point ($x = 2.35$,$y = 0.01\pi$,$z = 0$) and $\alpha = 4.9$. a_2 is varied over a domain $a_2 \in [0, 3]$, with $a_1 = 1$ fixed. We see the $\mathcal{W}_p$ measure exhibits both positive and negative values. The change in sign of $\mathcal{W}_p(\mathbf{B})$ occurs in both continuous and discontinuous fashions. The discontinuous changes occur as a result of a large discontinuous change in $\mathcal{W}_{pnl}(\mathbf{B})$. The continuous changes occur due to the play off between the magnitudes of the $\mathcal{W}_{pl}$ and $\mathcal{W}_{pnl}$ contributions.

However, we now explore the consequences of crossing a separatrix layer. Figures 6.29 and 6.30 depict the filed line drawn out for $\alpha = 4.9$, $y = 0.01\pi$ and $x = 2.47$. We see in Figure 6.24 this configuration occurs to the right for a discontinuous jump in the various polar writhing values, specifically it occurs on the boundary layer of the separatrix surface containing the negative polar writhe configurations depicted in Figure 6.26. This field is close to symmetric, with positive value. The negative $\mathcal{W}_p$ values may be indicative of a particular separatrix surface rather than a function of the field line symmetry.

6.4.5 Changing the Fourier component weighting - increasing asymmetry

In the following section we induce a strong degree of asymmetry into the field by altering the weighting of the Fourier components contributing to our field model (equation 6.26). This is achieved by altering a_1 and a_2, in this section we fix $a_1 = 1$

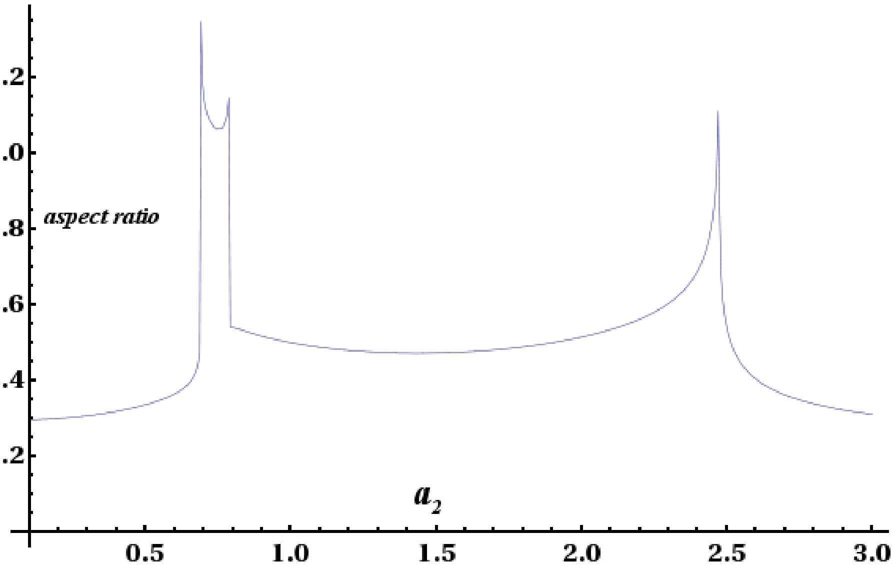

Figure 6.32: A plot of the aspect ratio of the field line (**B**) generated with a start point ($x = 2.35$,$y = 0.01\pi$,$z = 0$) and $\alpha = 4.9$. The Fourier component weighting a_2 is varied over a domain $a_2 \in [0, 3]$, with $a_1 = 1$ fixed. We note in general that the aspect ratio is below 0.6. There are two signifianct peaks (one actually has two peaks in close sucession) which correspond to the discontinuous changes in $\mathcal{W}_p$ depicted in Figure 6.31 and represent separatrix boundaries.

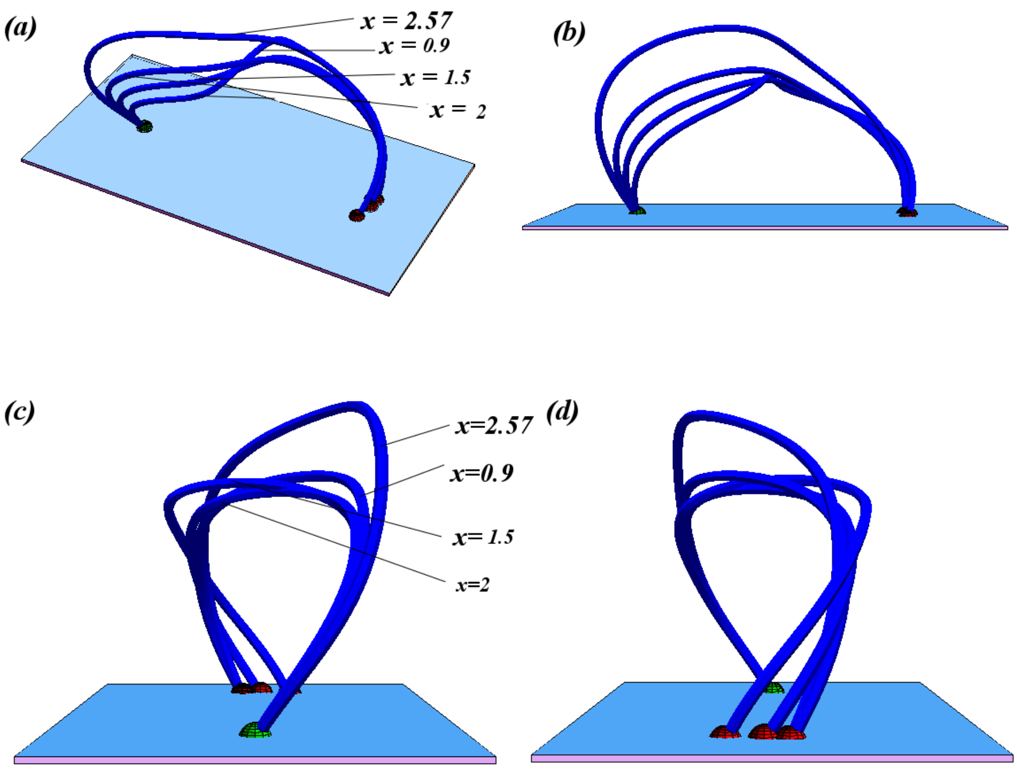

Figure 6.33: Field line configurations $\mathbf{B}$, obtained for $\alpha = 4.9$, $y = 0.01\pi$ and $x = 2.35$ and a components $a_2 = 0.9$, $a_2 = 1.5$, $a_2 = 2$ and $a_2 = 2.57$. In (a) we view from above (though not directly). Other viewpoints are (b) along the y direction, from the start point (c) and from the end point (d). It is maybe difficult to see from these figures but the increase in a causes an increase in the asymmetry of the configuration.

and vary a_2. Figure 6.31 details the $\mathcal{W}_p$, $\mathcal{W}_{pl}$ and $\mathcal{W}_{pnl}$ measures of field configurations $\mathbf{B}$, produced using a start point ($x = 2.35$,$y = 0.01\pi$,$z = 0$), $\alpha = 4.9$ (we use a large α value to generate as wide a range of morphological behavior as possible) and $a_2 \in [0, 3]$ (we note similar behavior to that defined in this section can be found by alternatively altering a_1). Figure 6.32 depicts the heights of such configurations. The $\mathcal{W}_p$, measure shows both positive and negative values, with the changes in sign occurring both continuously and discontinuously.

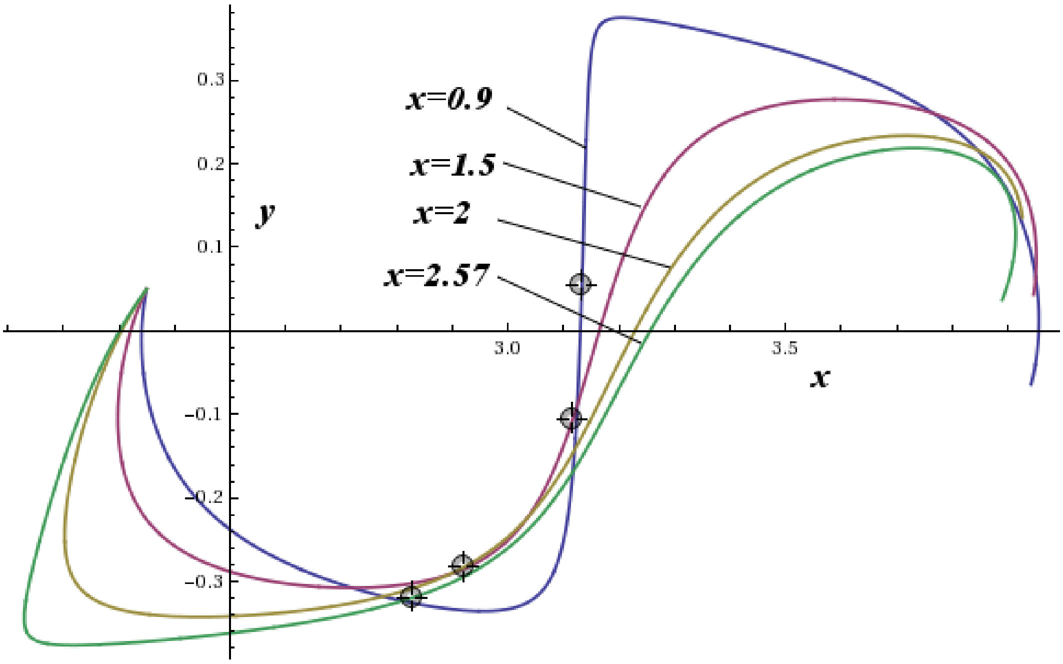

Figure 6.34: Field line configurations **B** are projected onto the x-y plane, obtained for $\alpha = 4.9$, ($x = 2.35$,$y = 0.01\pi$,$z = 0$) and a components $a_2 = 0.9$, $a_2 = 1.5$, $a_2 = 2$ and $a_2 = 2.57$. Plots $a_2 = 0.9$, $a_2 = 1.5$, appear to be fairly symmetric. Figures (c) and (d) however show a degree of asymmetry (the possibility of defining a measure of the asymmetry of these sigmoidal shapes will be discussed in this chapter's conclusions). This asymmetry manifests itself towards the section of the field joining the start point to the apex. The apex itself appears to rotate in a clockwise direction. It is not immediately clear from this diagram whether the local contribution to $\mathcal{W}_{pl}$ increases or decreases with this asymmetry.

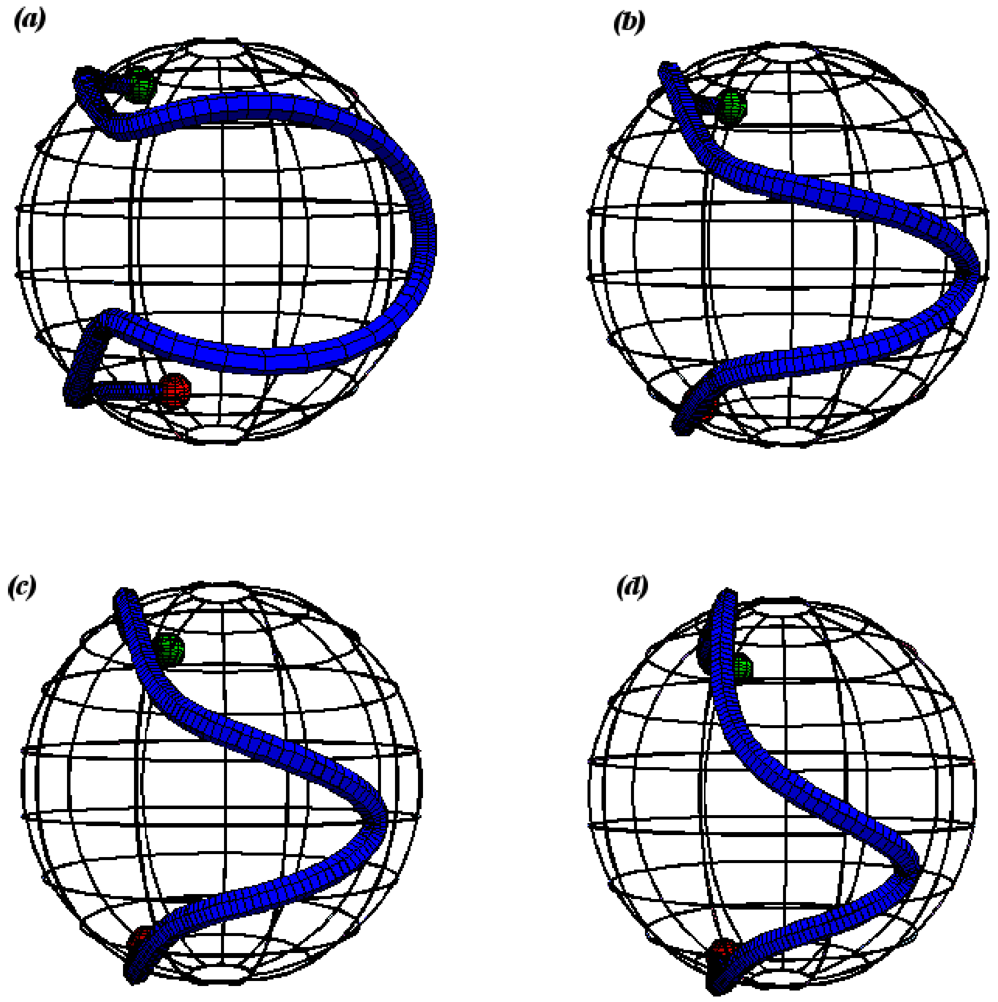

Figure 6.35: Depicted are the tantrix curves ($\widehat{\mathbf{T}}_{\mathbf{B}}$) of field line configurations $\mathbf{B}$, obtained for $\alpha = 4.9$, $y = 0.01\pi$ and $x = 2.35$ and a components $a_2 = 0.9$ (a), $a_2 = 1.5$ (b), $a_2 = 2$ (c) and $a_2 = 2.57$ (d). These figures allow us to assess the changing nature of the $\mathcal{W}_{pl}(\mathbf{B})$ contribution to $\mathcal{W}_p$. (a) is clearly close to symmetric with the areas bound by the northern and southern polar tantrix sections roughly equal. In (b) this still appears to be the case. However, if we compare (a) to (b) we see the section of tantrix curve in (a) which looks like a section of a circle has deformed into a more elliptic type shape, with the elliptic loop section traversing the sphere at polar angles (θ in spherical coordinates) much closer to the equator. As a result the $\mathcal{W}_{pl}$ contribution will increase. Comparing (b) to (c) and then (c) to (d) we see a further increase in asymmetry, also the range of azimuthal angles covered by the tantrix curve decreases leading to a decrease in the $\mathcal{W}_{pl}$ contributions. This effect is increased moving from (c) to (d).

Smoothly Changing $\mathcal{W}_p$ Sign

Concentrating on the domain $a_2 \in [0.85, 2.7]$, we see in Figure 6.31 $\mathcal{W}_p$ changes smoothly from negative to positive and then back to negative. Figure 6.33 depicts four field configurations spanning this region with both positive and negative values. Over this domain $\mathcal{W}_{pl}$ and $\mathcal{W}_{pnl}$ are oppositely signed (this is not always true of the domain $a_2 \in [0, 3]$), so the changing sign occurs as a result of the smoothly changing magnitude of both local and non-local contributions, as in our previous examples. Figure 6.33 depicts the view from above of the field line configurations depicted in 6.34, it is clear that the increase in a_2 induces an increasing degree of asymmetry in the field line configurations, which generally leads to positive $\mathcal{W}_p$ values, as with the last section, due to $\mathcal{W}_{pl}$ being of greater magnitude. The symmetric configuration ($a_2 = 0.9$) has a negative $\mathcal{W}_p$ value. However, a significantly asymmetric field line $a_2 = 2.45$ also has a negative $\mathcal{W}_p$ value. So for large α values the sign of $\mathcal{W}_p$ does not necessarily correlate to configurations which are either symmetric or asymmetric. It is interesting to note that both configurations with negative value ($a_2 = 0.9\ ,\ 2.45$) lie very close to a separatrix surface, again suggesting much of the interesting morphological behavior of the field lines occurs at these points.

Figure 6.35 gives us an insight into why this asymmetric configuration gains a negative $\mathcal{W}_p$ value. We take particular interest in configurations (b) through to (d). In (b) the field structure is still approximately symmetric. Also the elliptic loop section of the tantrix curve is close to the equator leading to a relatively large $\mathcal{W}_{pl}$ measure. In figure (c) we note two effects. First, the tantrix curve has become slightly asymmetric. Second the range of azimuthal angles which the tantrix curve traverses has become smaller in comparison to (b) leading to a decrease in the $\mathcal{W}_{pl}$ value. In (d) these two effects (asymmetry and decreasing azimuthal range), have become more pronounced. In fact the $\mathcal{W}_{pl}$ value has decreased so much relative to the $\mathcal{W}_{pnl}$ value that the total $\mathcal{W}_p$ is now negative. It would be extremely difficult to gauge the exact degree of changing value of the $\mathcal{W}_{pl}$ contribution using only a line of sight view of the field line.

6.4.6 Z Sigmoids with positive α

Among others Berger and Field [11] have previously shown that linear force free sigmoidal flux rope models models can produce Z shaped sigmoidal structures for positive α values. The caveat is that the structures require a dip in the field line

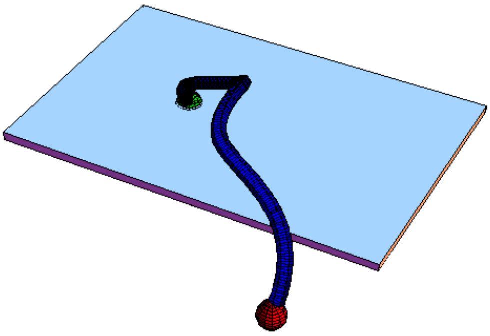

Figure 6.36: The field line **B**, generated from a start point ($x = 2.35, y = 0.01\pi, z = 0$), with $\alpha = 4.9$, $a_1 = 1$ and $a_2 = 0.6$. We note there are 4 local minima along the x-y direction. The middle section of the curve has a Z shaped sigmoidal structure. The curve appears to be fairly symmetric and there is no dip in the field line. The $\mathcal{W}_p$ value of this curve is $\mathcal{W}_p = 0.153581$

(see Figures 5 and 10 in [67]). In the following section we show that, for certain a_2 values, the sigmoidal structure generated by our model appears to form Z shaped sigmoidal structures, at least at their mid sections. Further, they do not dip (there is only one turning point along $\hat{z}$), at any point along their length. It should be noted that in general these configurations have low aspect ratios (< 0.4).

An example

Figure 6.36 depicts the field line **B**, generated from a start point ($x = 2.35, y = 0.01\pi, z = 0$), with $\alpha = 4.9$, $a_1 = 1$ and $a_2 = 0.6$. Figure 6.37 depicts this structure as seen from above. The structure is dominantly Z shaped at its centre and has no dip Its asymmetry is slight but still existant (see Figure 6.38). So the asymmetry of the field line structure offers an alternate possibility for Z shaped sigmoidal structures occurring without the need for a dip in the field structure. However, we must take care in labeling this structure Z shaped. An alternative viewpoint is that it is constructed of two S shapes linked at its centre. Seen from this point of view (double S shaped) the field line has the correct $\mathcal{W}_p$ sign and morphology. This result further reinforces the need for a full knowledge of the fields structure in order to accurately evaluate it writhe. Assumptions based on a two dimensional view of the field line

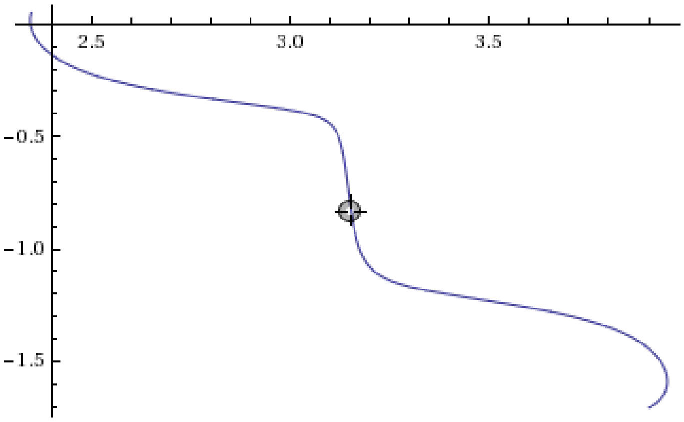

Figure 6.37: The field line **B** viewed from above, generated from a start point $(x = 2.35, y = 0.01\pi, z = 0)$, with $\alpha = 4.9$, $a_1 = 1$ and $a_2 = 0.6$. The central portion of the field line traces out a Z shape. The curve could alternatively be thought of as two S shaped sigmoids, joined at the apex, with the caveat that they are either entirely upward or downward moving.

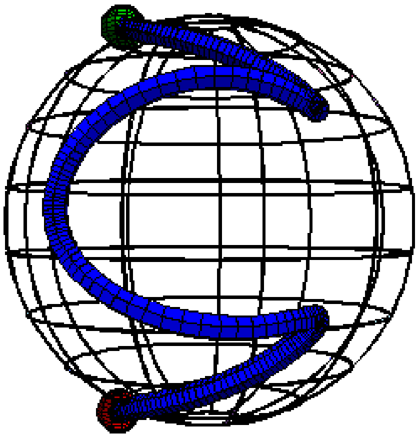

Figure 6.38: The tantrix curve $\widehat{\mathbf{T}}_{\mathbf{B}}$ a field line **B**, generated from a start point $(x = 2.35, y = 0.01\pi, z = 0)$, with $\alpha = 4.9$, $a_1 = 1$ and $a_2 = 0.6$. The diagram shows that the southern hemisphere component is slightly larger than its northern counterpart. Also we note the orientation $(\Theta(z = 0))$ between the startpoint-endpoint orientation and the apex orientation $\Theta(z_{max})$ (on the equator), is fairly small leading to the small $\mathcal{W}_{pnl}$ contribution.

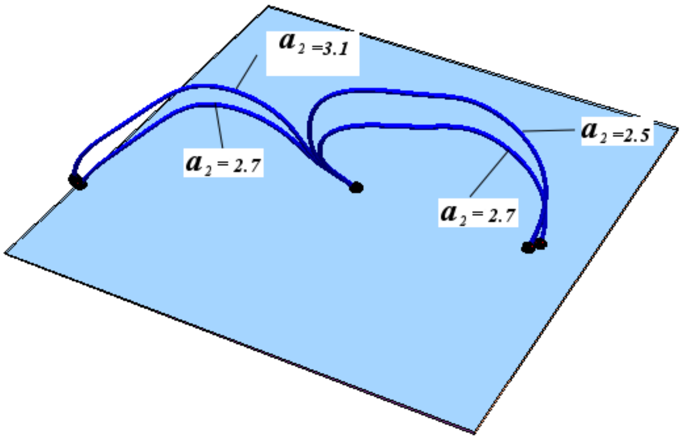

Figure 6.39: Field lines **B**, generated from a start point $(x = 2.35, y = 0.01\pi, z = 0)$, with $\alpha = 4.9$, with $a_2 = 2.5$, $a_2 = 2.7$, $a_2 = 2.9$, $a_2 = 3.1$. The $a_2 = 2.5$, $a_2 = 2.7$ lie on one side of a separatrix surface and $a_2 = 2.9$, $a_2 = 3.1$ another (see Figure 6.31). As x is increase the curves go from being S shaped to (centrally) Z shaped.

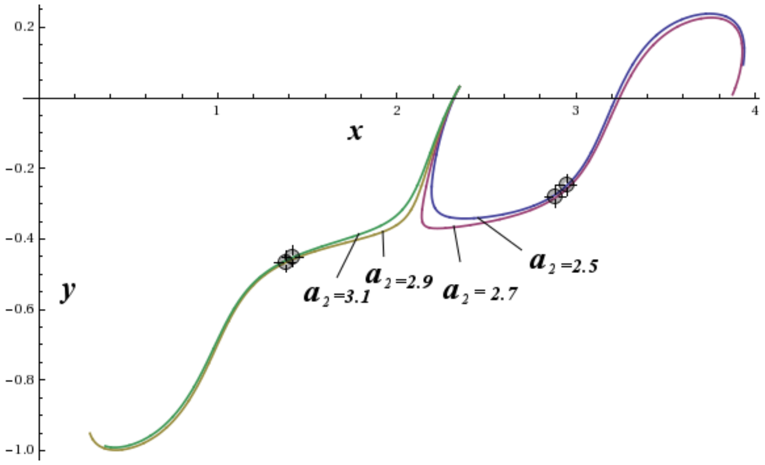

Figure 6.40: Projections, seen from above, of field lines **B**, generated from a start point $(x = 2.35, y = 0.01\pi, z = 0)$, with $\alpha = 4.9$, with $a_2 = 2.5$, $a_2 = 2.7$, $a_2 = 2.9$, $a_2 = 3.1$. The $a_2 = 2.5$, $a_2 = 2.7$ lie on one side of a separatrix surface and $a_2 = 2.9$, $a_2 = 3.1$ another (see Figure 6.31). As x is increase the curves go form being S shaped to (centrally) Z shaped.

or flux tube could lead to misleading assumptions regarding its morphology and $\mathcal{W}_p$ value. It is left to note that these structures occur for the range $a_2 \approx [0, 0.7]$ and $a_2 \approx [2.5, 3]$ (see Figures 6.39, 6.40), we note these field configuration can be seen in Figure 6.32 to have low aspect ratios (< 0.4).

6.5 Conclusions on open field line morphology

We have demonstrated, using a simple linear force free model, that the range of possible field line field configuration morphologies is significantly increased using the mechanism of asymmetric field line generation. The configurations generated were evaluated using the polar writhe formulation, which is the correct expression for coronal field structures. In particular we have demonstrated the existence of the following morphological phenomena:

- For taller or larger field line structures (aspect ratio > 1 and positive α) the majority of field line structures were asymmetric and had positive helicity (for S shaped structures), in opposition to the assumption in Green *et al* [50].
- Using positive α value we have shown that asymmetric field line configurations can change form positive $\mathcal{W}_p$ to negative (and vice versa), over a significant range of aspect ratios including ranges associated with active field regions.
- By allowing the field lines to develop asymmetric structures we can generate sigmoids which could be interpreted as being Z shaped (at least around their central region), for positive α values. These structures do not require a dip in the field line. Again the converse effect can be shown for negative α values, that is apparent forward S structures, with no dip. Further this effect seemed to occur in specific separatrix surfaces. It is to be noted these structures could be interpreted as being two inter-locked S shapes and could thus be seen to have the correct field line morphology.
- The differing separatrix surfaces, and in particular their boundaries, were shown to have a strong effect on the nature of the $\mathcal{W}_p$ measure.

In addition the results demonstrate that we require a full knowledge of the three dimensional field structure in order to accurately evaluate the polar writhe and helicity measures of a particular field line. In particular it was shown that we cannot accurately evaluate the local contribution to the field line morphology using two dimensional images.

6.5.1 Future study

The results contained within this chapter offer a glimpse of the wide range of possible morphological behavior available to field lines and possibly magnetic flux tubes. However, the model used was comparatively simple compared to the wide range of field modeling techniques in solar literature.

There exists a much wider range of linear and indeed potential field models, which consist of several field sources co-habiting in the same region (see Longcope [66] for an introduction), some of these configurations posses significantly asymmetric morphology. It would be interesting to apply the polar writhe based helicity expression to these models. For example would there be a dominant sign of field line helicities ? Further, numerical MHD simulations offer a more physically accurate evaluation of the sun's field line structure. Again the polar writhe formulation could be applied to assess the range of possible behavior available to the helicity of the field structures formed.

MHD simulations appear to offer a possible mechanism for the occurrence of the sigmoidal shapes viewed in Soft X ray imaging. This involves the development of current sheets (Fan and Gibson [41], Török and Kliem [110]). These simulations involve starting with a cylindrically symmetric flux rope which develops into symmetric sigmoidal flux rope configurations (in terms of the definition of symmetric discussed in section 6.3.3). It would be intriguing to see what the morphological consequences of developing non-symmetric flux tube configurations would be.

A final thought would be that some kind of asymmetry measure could prove very useful. For example we have seen that some apparently Z-shaped sigmoidal structures have α values usually associated with forward S shapes (see section 6.4.6). If we could define an asymmetry measure which could differentiate between these Z shapes and the Z shapes associated with negative α values, it would have implications for sigmoidal shape surveys (e.g. Pevstov, Canfield and Mclaymont [83], Burnette, Canfield, and Pevstov 2004 [19]).

Chapter 7

Conclusions

The central theme of this thesis concerns the quantification of a spacecurve's shape. The introduction covers the concepts of writhing and linking, as applied to a spacecurve and union of spacecurves respectively. The need for a new consistent, directionally specific measure of writhing, as applied to open spacecurves is established in section 1.6.

Chapter 2

The work in chapter 2 establishes a framework for evaluating writhing (as defined by equation 1.19) and linking (as defined by equation 1.16), in terms of a simple geometrical interpretation as areas bound on the surface of the unit sphere. It concerns closed spacecurves exclusively. This methodology is used extensively in the proceeding chapters in order to establish and explain the properties of various geometrical and topological quantities. The aim is to provide a framework which could also be applied to open spacecurves. The contents of this chapter expands upon previous work. The demonstrations contained within are not new results; however, two particular unit sphere demonstrations are of note.

- A geometrical demonstration of Fuller's Area theorem (see section 1.5.6) is performed. This demonstration is important as it is performed by simply considering the geometry of a single mapping (equation 2.2), as opposed to previous proofs which required the use of theorems of differential geometry which would not generally be applicable to open spacecurves.

- The properties of an expression for the writhing of open spacecurves, here termed $\mathcal{W}_z$ (used previously under differing names in Fain *et al* [40], Bouchiat and Mézard [17] and Rossetto and Maggs [92]), are established in terms of the unit sphere interpretation. In particular its is demonstrated that $\mathcal{W}(\mathbf{x}) = (\mathcal{W}_z - 1)\ mod\ 2$.

.

Chapter 3

Chapter 3 expands upon the work published in Berger and Prior [15], which developed a new directional measure of the writhing of an open spacecurve. This particular chapter details its derivation and establishes its properties for closed spacecurves. Particular results include:

- A directional measure of the linking of two spacecurves is defined, based on a methodology established for defining the Kontsevitch integral. This measure is shown, for closed spacecurves, to be equal to the $\mathcal{L}$ (equation 1.16). The advantage of this new linking expression is that it is a single integral (albeit with a sum).
- Using a directional twisting expression (equation 3.17) a measure of the directional writhing, termed *the polar writhe* is established. See section 3.2 for its derivation and equation (3.52) for its final definition in terms of an arbitrary direction of evaluation $\hat{a}$. This measure is consistently defined for all spacecurves, open or closed, and is shown to be framing independent (Theorem 85).
- For a closed spacecurve $\mathbf{x}$ the polar writhe defined to be equivalent to the $\mathcal{W}(\mathbf{x})$ measure defined by equation 1.19.
- Using its unit sphere interpretation, the polar writhe measure is shown to equate to the writhe expression in Fuller's first theorem when evaluated *mod* 2.

The above results are detailed in [15]. In addition the following is shown,

- For closed spaceurves it is demonstrated (in section 3.3.4), that the local component of the polar writhe, evaluated over a smoothly changing direction (see section 1.2.2 for the definition of smoothness implied), is equivalent to an evaluation of $\mathcal{W}$ using Fuller's second theorem (defined in section 1.5.6).

Chapter 4

Chapter 4 provides a comparison of the various measures of writhing, with regards to open spacecurves. It is demonstrated that there exists no general quantitative relationship between the expressions $\mathcal{W}$, $\mathcal{W}_z$ and $\mathcal{W}_p$. In particular the following is shown

- In comparison to $\mathcal{W}_z$, the $\mathcal{W}_p$ measure provides more information about the writhing of open spacecurves (see section 4.1). This is a result of its explicit evaluation of non-local winding, absent from the $\mathcal{W}_z$ measure.
- The $\mathcal{W}_z$ measure is shown generally to be a poor estimator of the writhing of open spacecurves
- In section 4.3 it is shown, for directionally specific spacecurves, the polar writhe measure is the most relevant measure of the morphological nature of the spacecurve under evaluation. In the case of non directionally specific space curves it is demonstrated that $\mathcal{W}$ is generally the most consistent measure of the curve's writhing.

Chapter 5

This chapter discusses the properties of $\mathcal{W}$ (section 5.1.2), and $\mathcal{W}_p$ (section 5.3), as applied to open spaceurves, in greater detail. Using the unit sphere interpretation properties of each expression are demonstrated. This discussion is of a level of detail that has not previously been performed for open spacecurves. In particular the following results are detailed:

- In section 5.2.1 a method of closing open spacecurves, such that the new closed measurement is that of the open spacecurve, is developed. This method has been used before (Rossetto and Maggs [92], Starostin [104], van der Heijden *et al* [114]). However, this new closure extends it to curves with arbitrarily oriented end tangents [1]. Using this closure gives two local expressions for the $\mathcal{W}$ of an open spacecurves, based on the Fuller writhing expressions (equations 5.7 and 5.15).

---

[1] Starostin detailed a closeure for a curve whose end tangents were in general position. His work differed in that he derived specific expressions for the $\mathcal{W}$ of the closure sections. In this we derived a closure which could be used to apply the Fuller expressions to all open spacecurves, assuming the non-oppostion condtion is obeyed.

- An expression for the non-local writhing $\mathcal{W}_{pnl}$ of open spacecurves is detailed in section 5.3.4. This expression could be used to construct an efficient algorithm for evaluating the non-local writhing of an arbitrary spacecurve which is of the order of the number of sections the curve is split into as opposed to the number of points comprising a numerical integration.
- A quantitative discussion regarding the choice of direction of evaluation, inherent to the polar writhe formulation, using example open curve studies. It is shown that the choice of direction can greatly affect the relevance of the $\mathcal{W}_p$ measure.

Chapter 6.

Chapter 6 details an application for the polar writhe measure in solar physics. The polar writhe framework is shown (in section 6.2.4) to be the correct measure of the helicity of coronal magnetic field lines and flux tubes. This measurement is used, in conjunction with a simple force-free field model, to evaluate the morphological properties of field line configurations. Particular attention is paid to the properties of asymmetric field lines.

- For taller or larger field line structures the majority were asymmetric and had a consistent $\mathcal{W}_p$ sign. However when the field lines developed symmetrical configurations the writhe changed sign. In general the sign of the fields $\mathcal{W}_p$ was in opposition to that assumed in previous work (Green *et al* [50]). See, in particular, sections 6.4.4 and 6.4.5.
- By allowing the field lines to develop asymmetric structures, configurations whose sigmoidal signature appeared to be the opposite of that expected were found (see section 6.4.6). These structures do not require a dip in the field line as previous examples have required.
- The more interesting changes in morphological behaviour of the field lines was shown to occur at separatrix surfaces.

7.0.2 Possible Future Study

The thesis has established a sound base for evaluating the writhing of open spacecurves. In addition Chapter 6 provides a demonstration of the applicability of the newly developed polar writhe measure. In section 1.6 of the introductory chapter a possible use of this new measure in the field of polymer modeling is briefly described, this could be one possible way of further applying the results detailed above.

Further suggested areas of study include:

- The Kontsevitch intergal can be applied to higher dimensions (for further details see Kontsevitch [60], Berger [14] and Chmutov and Duhzin [29]), thus an higher dimensional measure equivalent to the polar writhe may be constructed.
- DNA sections can be found fixed to cell wall boundaries. This is effectively a situation in which linked pair of curves are bound between two planes and would be correctly evaluated using the polar writhe measure.

Appendix A

Proofs of theorems

A.1 Proof of theorem 1 - page 80

Proof of Theorem 1 We will prove the theorem by counting crossings. Thus we employ (1.17) to relate the linking number to the signed number of crossings as seen with some projection angle. We will be particularly interested in projections perpendicular to $\hat{\mathbf{z}}$, i.e. with $\hat{\mathbf{n}}(\psi) = \cos\psi\hat{x} + \sin\psi\hat{y}$ for some azimuthal direction ψ. (See Berger [14] for a similar procedure). Let $C(\psi)$ be the number of crossings seen from direction ψ. The *average* signed number of crossings seen from these side directions is

$$\bar{f} = \frac{1}{2\pi}\oint_0^{2\pi} C(\psi)\,\mathrm{d}\psi. \tag{A-1}$$

Now consider piece i of curve $\mathbf{x}$ and piece j of curve $\mathbf{y}$. Suppose for the moment that both of these curve segments point upwards, $\mathrm{d}s/\mathrm{d}z > 0$. Suppose also that their extent in the z direction overlaps between $z = z_1$ and $z = z_2$. Then in this interval $\sigma_i = \sigma_j = 1$, and they wrap around each other through a net angle

$$\Delta\Theta_{ij} = \int_{z_1}^{z_2} \frac{\mathrm{d}\Theta_{ij}}{\mathrm{d}z}\mathrm{d}z. \tag{A-2}$$

In other words, the relative position vector $\mathbf{r}_{ij}$ rotates through a net angle $\Delta\Theta_{ij}$ between z_1 and z_2.

We assert that for pieces i and j, the perpendicular crossing number is

$$\bar{f}_{ij} = \sigma_i\sigma_j\frac{\Delta\Theta_{ij}}{\pi}. \tag{A-3}$$

To demonstrate this, consider an observer at azimuthal angle ϕ. This observer will see a crossing at heights z where the relative position vector $\mathbf{r}_{ij}$ points in the $\pm\phi$ direction. Now $\mathbf{r}_{ij}$ may rotate as it travels from z_1 to z_2. If $\mathbf{r}_{ij}$ swings all the way around n times between z_1 and z_2 ($\Delta\Theta_{ij} = 2\pi n$) then each observer will see $2n$ crossings (n times for when the vector points toward the observer, and n times for when the vector points away from the observer). Thus the quantity $\Delta\Theta_{ij}$ relates to how many times each observer sees a crossing.

If $|\Delta\Theta_{ij}| < \pi$ some observers will not see a crossing; in this case $|\Delta\Theta_{ij}|/\pi$ gives the fraction of observers seeing a crossing. Note that $\mathbf{r}_{ij}$ may wiggle back and forth, i.e. $\mathrm{d}\Theta_{ij}/\mathrm{d}z$ may not stay the same sign. But in this case observers will see crossings of both signs, which cancel out. Thus $\Delta\Theta_{ij}/\pi$ gives the *net* number of crossings, averaged over all projection angles, i.e. $\bar{f}_{ij}$.

So far we have assumed that $\sigma_i = \sigma_j = 1$. In general, the sign of the crossings will be positive if $\sigma_i = \sigma_j$ and $\Delta\Theta_{ij} > 0$. The sign becomes negative if one of the σs changes sign. Thus $\Delta\Theta_{ij}$ must be weighted by the product $\sigma_i\sigma_j$, leading to equation (A-3).

We now sum over all pairs of curve segments to give

$$\bar{f} = \frac{1}{\pi}\sum_{i=1}^{N}\sum_{j=1}^{M}\sigma_i\sigma_j\Delta\Theta_{ij}. \tag{A-4}$$

Finally, for a closed link, the signed number of crossings is the same for all projection angles and equals $2\mathcal{L}$. Thus the average $\bar{f}$ will also have this value,

$$\bar{f} = 2\mathcal{L}, \tag{A-5}$$

thus proving the theorem.

A.2 Proof of theorem 3 - page 85

Proof of Theorem 3 We surround the axis curve $\mathbf{x}$ with a tube. As in section 1.2.5, there is a family of secondary curves on the surface of the tube labelled by β; the $\beta = 0$ curve follows $\mathbf{x} + \epsilon\widehat{\mathbf{V}}$. We will calculate $\widetilde{\mathcal{L}}'$ and $\widetilde{\mathcal{T}}'$ for the secondary curves in the tube surface. The next step will be to average $\widetilde{\mathcal{L}}' - \widetilde{\mathcal{T}}'$ over all the secondary curves, and show that this average only depends on the geometry of the axis.

Let $\widehat{\mathbf{W}} = \widehat{\mathbf{T}} \times \widehat{\mathbf{V}}$ so that $\{\widehat{\mathbf{T}}, \widehat{\mathbf{V}}, \widehat{\mathbf{W}}\}$ is an orthonormal right-handed frame. We consider the neighborhood of some point on the curve which is not a maxima or minima, so that we can parameterize the curve by z. As twist and writhe do not change under a reversal of the direction of the curve, we can assume $\lambda = \mathrm{d}z/\mathrm{d}s > 0$, i.e. $\sigma > 0$.

The secondary curve labelled by β passes through the points $\mathbf{y}(z,\beta) = \mathbf{x}(z) + \epsilon\widehat{\mathbf{U}}(z,\beta)$ where

$$\widehat{\mathbf{U}}(z,\beta) = \cos\beta\ \widehat{\mathbf{V}}(z) + \sin\beta\ \widehat{\mathbf{W}}(z). \tag{A-6}$$

Note that $\mathrm{d}(\widehat{\mathbf{V}}\cdot\widehat{\mathbf{V}})/\mathrm{d}z = 0$, so $\widehat{\mathbf{V}}\cdot\widehat{\mathbf{V}}' = 0$ (we will no longer write the (z) dependence everywhere). Similarly, $\widehat{\mathbf{W}}\cdot\widehat{\mathbf{W}}' = 0$. Also, as $\widehat{\mathbf{V}}\cdot\widehat{\mathbf{W}} = 0$,

$$\omega \equiv \widehat{\mathbf{V}}'\cdot\widehat{\mathbf{W}} = -\widehat{\mathbf{V}}\cdot\widehat{\mathbf{W}}'. \tag{A-7}$$

These relations simplify the expression for the twist of the β curve, $\widetilde{\mathcal{T}}'(z,\beta)$. From equation 3.17 with $\sigma > 0$,

$$\begin{aligned}
2\pi\widetilde{\mathcal{T}}' &= \widehat{\mathbf{T}}\cdot\widehat{\mathbf{U}}\times\widehat{\mathbf{U}}' && \text{(A-8)}\\
&= \widehat{\mathbf{T}}\times(\cos\beta\widehat{\mathbf{V}} + \sin\beta\widehat{\mathbf{W}})\cdot(\cos\beta\ \widehat{\mathbf{V}}' + \sin\beta\ \widehat{\mathbf{W}}') && \text{(A-9)}\\
&= (\cos\beta\ \widehat{\mathbf{W}} - \sin\beta\ \widehat{\mathbf{V}})\cdot(\cos\beta\ \widehat{\mathbf{V}}' + \sin\beta\ \widehat{\mathbf{W}}') && \text{(A-10)}\\
&= \omega. && \text{(A-11)}
\end{aligned}$$

Note that the twist $\widetilde{\mathcal{T}}'$ is independent of β.

Next consider $\widetilde{\mathcal{L}}'$ using (3.1), as well as (3.11) applied to just the single pair $\mathbf{x}$ and $\mathbf{y}(\beta)$:

$$2\pi\widetilde{\mathcal{L}}' = \frac{\mathrm{d}\Theta(\mathbf{x},\mathbf{y})}{\mathrm{d}z} = \frac{\hat{\mathbf{z}}\cdot\mathbf{r}(z)\times\mathbf{r}'(z)}{|\mathbf{r}(z)|^2}\,. \tag{A-12}$$

Here $\mathbf{r}$ points from $\mathbf{x}(z)$ to the point on the secondary curve *at the same height* z (see Figure A.1). Let the arclength along the axis at the point $\mathbf{x}(z)$ be s. The tip of the $\mathbf{r}$ arrow is a point P on the secondary corresponding to a different axis arclength s_1:

$$\begin{aligned}
\mathbf{y}(s_1,\beta) &= \mathbf{x}(s_1) + \epsilon\widehat{\mathbf{U}}(s_1,\beta) && \text{(A-13)}\\
&\approx \mathbf{x}(s) + \epsilon\widehat{\mathbf{U}}(s,\beta) + \left(\widehat{\mathbf{T}}(s) + \epsilon\frac{\mathrm{d}\widehat{\mathbf{U}}(s,\beta)}{\mathrm{d}s}\right)(s_1 - s). && \text{(A-14)}
\end{aligned}$$

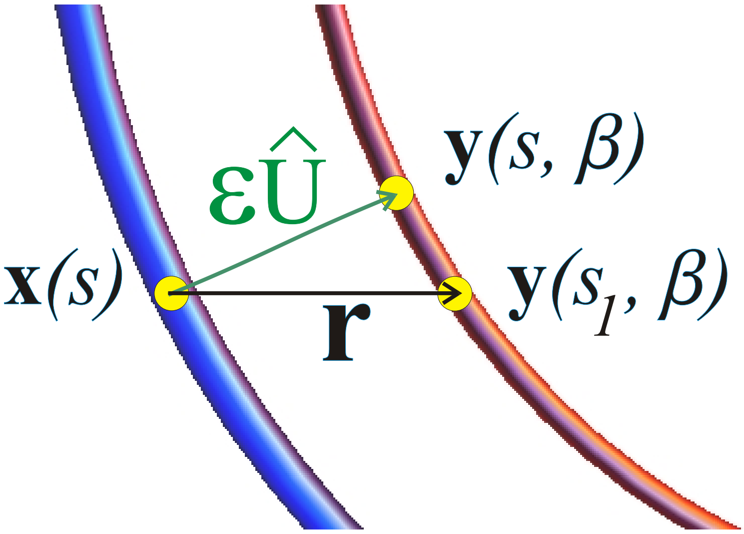

Figure A.1: The points $\mathbf{x}(z) = \mathbf{x}(s)$, $\mathbf{y}(s, \beta) = \mathbf{x}(s) + \epsilon\widehat{\mathbf{U}}$, and $\mathbf{y}(s_1, \beta) = \mathbf{x}(s) + \mathbf{r}$.

To first order in ϵ,

$$\begin{aligned} \mathbf{r} &= \mathbf{y}(s_1, \beta) - \mathbf{x}(s) && \text{(A-15)} \\ &\approx \epsilon\widehat{\mathbf{U}}(s, \beta) + \widehat{\mathbf{T}}(s)(s_1 - s). && \text{(A-16)} \end{aligned}$$

By definition $r_z = 0$, so

$$s_1 - s \approx -\epsilon U_z(s)/\hat{T}_z(s) = -\epsilon U_z(s)/\lambda(s). \tag{A-17}$$

Thus to first order in ϵ

$$\mathbf{r} = \epsilon(\widehat{\mathbf{U}} - \lambda^{-1} U_z \widehat{\mathbf{T}}). \tag{A-18}$$

We define $\mathbf{R} = \mathbf{r}/\epsilon$. Then (in the limit $\epsilon \to 0$)

$$2\pi\widetilde{\mathcal{L}}' = \frac{\hat{\mathbf{z}} \cdot \mathbf{R} \times \mathbf{R}'}{|\mathbf{R}|^2}, \qquad \mathbf{R} = \widehat{\mathbf{U}} - \lambda^{-1} U_z \widehat{\mathbf{T}}. \tag{A-19}$$

To go further, we will need two new orthonormal frames, and decompose $\mathbf{R}$ in these frames. Let $\mu = |\hat{\mathbf{z}} \times \widehat{\mathbf{T}}|$. The first new frame will be

$$\{\widehat{\mathbf{T}}, \widehat{\mathbf{f}}, \widehat{\mathbf{g}}\} = \{\widehat{\mathbf{T}}, \hat{\mathbf{z}} \times \widehat{\mathbf{T}}/\mu, \widehat{\mathbf{T}} \times (\hat{\mathbf{z}} \times \widehat{\mathbf{T}}/\mu)\}. \tag{A-20}$$

(The case where $\widehat{\mathbf{T}}$ is parallel to $\hat{\mathbf{z}}$ will be discussed at the end of the proof.) As $\widehat{\mathbf{V}}$ and $\widehat{\mathbf{W}}$ are perpendicular to $\widehat{\mathbf{T}}$, we can write

$$\begin{pmatrix} \widehat{\mathbf{V}} \\ \widehat{\mathbf{W}} \end{pmatrix} = \begin{pmatrix} \cos\psi(z) & \sin\psi(z) \\ -\sin\psi(z) & \cos\psi(z) \end{pmatrix} \begin{pmatrix} \widehat{\mathbf{f}} \\ \widehat{\mathbf{g}} \end{pmatrix} \tag{A-21}$$

for some angle $\psi(z)$. Then from (A-6),

$$\widehat{\mathbf{U}} = \cos(\beta+\psi)\ \widehat{\mathbf{f}} + \sin(\beta+\psi)\ \widehat{\mathbf{g}}. \tag{A-22}$$

Next let

$$\widehat{\mathbf{h}} = \hat{\mathbf{z}} \times \widehat{\mathbf{f}} = -\widehat{\mathbf{T}}_\perp/\mu, \tag{A-23}$$

and go to the frame $\{\hat{\mathbf{z}}, \widehat{\mathbf{f}}, \widehat{\mathbf{h}}\}$. In terms of these vectors

$$\begin{aligned} \widehat{\mathbf{g}} &= \mu^{-1}(\hat{\mathbf{z}} - T_z\widehat{\mathbf{T}}) && \text{(A-24)} \\ &= \mu^{-1}\left((1-\lambda^2)\hat{\mathbf{z}} - \lambda T_\perp\right) && \text{(A-25)} \\ &= \mu\hat{\mathbf{z}} + \lambda\widehat{\mathbf{h}}; && \text{(A-26)} \\ \widehat{\mathbf{T}} &= \lambda\hat{\mathbf{z}} - \mu\widehat{\mathbf{h}}. && \text{(A-27)} \end{aligned}$$

Substituting for $\widehat{\mathbf{g}}$ in (A-22) gives

$$\widehat{\mathbf{U}} = \mu\sin(\beta+\psi)\hat{\mathbf{z}} + \cos(\beta+\psi)\widehat{\mathbf{f}} + \lambda\sin(\beta+\psi)\widehat{\mathbf{h}}. \tag{A-28}$$

Finally, from (A-19)

$$\begin{aligned} \mathbf{R} &= \cos(\beta+\psi)\widehat{\mathbf{f}} + (\lambda + \lambda^{-1}\mu^2)\sin(\beta+\psi)\widehat{\mathbf{h}} && \text{(A-29)} \\ &= \cos(\beta+\psi)\widehat{\mathbf{f}} + \lambda^{-1}\sin(\beta+\psi)\widehat{\mathbf{h}}, && \text{(A-30)} \end{aligned}$$

and

$$\mathbf{R}^2 = \left(\cos^2(\beta+\psi) + \lambda^{-2}\sin^2(\beta+\psi)\right). \tag{A-31}$$

The z derivative is

$$\mathbf{R}' = \cos(\beta+\psi)\left(\lambda^{-1}\psi'\widehat{\mathbf{h}} + \widehat{\mathbf{f}}'\right) + \sin(\beta+\psi)\left(-\psi'\widehat{\mathbf{f}} + \lambda^{-1}\widehat{\mathbf{h}}' - \lambda'\lambda^{-2}\widehat{\mathbf{h}}\right). \tag{A-32}$$

We now proceed to calculate (A-19). Simple vector identities give

$$(\widehat{\mathbf{f}} \times \widehat{\mathbf{h}}' + \widehat{\mathbf{h}} \times \widehat{\mathbf{f}}') \cdot \hat{\mathbf{z}} = 0, \tag{A-33}$$

which helpfully removes a few terms. Also,

$$\begin{aligned} \widehat{\mathbf{f}} \times \widehat{\mathbf{f}}' &= \widehat{\mathbf{h}} \times \widehat{\mathbf{h}}' = \mu^{-2} \hat{\mathbf{z}} \cdot \widehat{\mathbf{T}} \times \widehat{\mathbf{T}}' && \text{(A-34)} \\ &= \mu^{-2} \lambda^{-1} \kappa B_z. && \text{(A-35)} \end{aligned}$$

Combining equations (A-29) to (A-35) gives

$$\frac{\hat{\mathbf{z}} \cdot \mathbf{R} \times \mathbf{R}'}{\mathbf{R}^2} = \frac{\lambda\psi' - \lambda' \cos(\beta+\psi)\sin(\beta+\psi)}{\big(\lambda^2 \cos^2(\beta+\psi) + \sin^2(\beta+\psi)\big)} + \frac{\kappa}{\lambda\mu^2} B_z. \tag{A-36}$$

Suppose we now average this expression over all secondary curves in the tube, i.e. over $0 \leq \beta < 2\pi$. The term involving λ' vanishes, and the last term is unaffected. The firsthttp://news.bbc.co.uk/sport1/hi/football/8389683.stm term gives

$$\frac{\lambda\psi'}{2\pi} \int_0^{2\pi} \frac{1}{\big(\lambda^2 \cos^2(\beta+\psi) + \sin^2(\beta+\psi)\big)} \, \mathrm{d}\beta = \psi'. \tag{A-37}$$

Thus (A-19) finally gives

$$2\pi \widetilde{\mathcal{L}}' = \psi' + \frac{1}{\lambda\mu^2} \kappa B_z. \tag{A-38}$$

Meanwhile, from (A-11),

$$\begin{aligned} 2\pi \widetilde{\mathcal{T}}' &= \omega = \widehat{\mathbf{V}}' \cdot \widehat{\mathbf{W}} && \text{(A-39)} \\ &= \psi' + (\cos\psi \widehat{\mathbf{f}}' + \sin\psi \widehat{\mathbf{g}}') \cdot (-\sin\psi \widehat{\mathbf{f}} + \cos\psi \widehat{\mathbf{g}}). && \text{(A-40)} \end{aligned}$$

Now the orthonormal vectors satisfy $\widehat{\mathbf{f}} \cdot \widehat{\mathbf{f}}' = \widehat{\mathbf{g}} \cdot \widehat{\mathbf{g}}' = 0$, while $\widehat{\mathbf{f}} \cdot \widehat{\mathbf{g}}' = -\widehat{\mathbf{f}}' \cdot \widehat{\mathbf{g}}$, so

$$\begin{aligned} 2\pi \widetilde{\mathcal{T}}' &= (\psi' + \widehat{\mathbf{f}}' \cdot \widehat{\mathbf{g}}) = (\psi' + \mu^{-2} \hat{\mathbf{z}} \times \widehat{\mathbf{T}}' \cdot (\widehat{\mathbf{T}} \times (\hat{\mathbf{z}} \times \widehat{\mathbf{T}}))) && \text{(A-41)} \\ &= \psi' + \frac{\lambda}{\mu^2} \hat{\mathbf{z}} \cdot \widehat{\mathbf{T}} \times \widehat{\mathbf{T}}' && \text{(A-42)} \\ &= \psi' + \frac{1}{\mu^2} \kappa B_z. && \text{(A-43)} \end{aligned}$$

Thus

$$2\pi\widetilde{\mathcal{W}}' = \frac{(1-\lambda)}{\mu^2}\frac{\kappa B_z}{\lambda}. \tag{A-44}$$

This proves the theorem for $0 < \lambda < 1$. For vertical points on the axis curve ($\lambda = 1$) the expression for $\widetilde{\mathcal{W}}'$ gives 0. This is expected, because for such points the rate of change of linking $\widetilde{\mathcal{L}}'$ should coincide with the rate of change of twisting $\widetilde{\mathcal{T}}'$ (the first measures winding about $\hat{\mathbf{z}}$, while the second measures winding about $\widehat{\mathbf{T}}$, and for vertical points $\hat{\mathbf{z}} = \widehat{\mathbf{T}}$). Thus the theorem extends to vertical points.

Finally, if the axis parameter s is reversed, then $\lambda \to -\lambda$ and $B_z \to -B_z$, but $\widetilde{\mathcal{W}}'$ should not change. In this case

$$2\pi\widetilde{\mathcal{W}}' = \frac{(1-|\lambda|)}{\mu^2}\frac{\kappa B_z}{\lambda} = \frac{1}{2\pi}\frac{1}{(1+|\lambda_i|)}\frac{\kappa B_z}{\lambda}. \tag{A-45}$$

Appendix B

A note on the algorithms used in this thesis

There were three basic algorithms used to define the quantities $\mathcal{W}$, $\mathcal{W}_z$ and $\mathcal{W}_p$.

B.1 Evaluating $\mathcal{W}$ as represented by equation (1.19)

In general there were no particularly time consuming evaluations performed in this thesis. As such each individual writhe calculation could be performed, in terms of a polygonal approximation, to a high degree of accuracy. The $\mathcal{W}$ of both open and closed spacecurves was evaluated using a polygonal approximation of equation (1.19). The following method, detailed in Klenin and Langowski [58] (Method 1a pages 311 − 312) was used, due to its simplicity. We consider a polygonal curve $\mathbf{x}$, which can be split into p connected linear segments. In general these connected segments will not have the same orientation. The contribution to the Gauss integral (1.19) due to segments $(\mathbf{x}_i, \mathbf{x}_j)$ is denoted $\frac{\omega_{ij}}{4\pi}$. The total integrand can be evaluated as

$$\mathcal{W} = 2\sum_{i=2}^{p}\sum_{j<i}^{p}\frac{\omega_{ij}}{4\pi}, \tag{B-1}$$

Following [58] we let points 1 and 2 be the end of a segment and denote that segment $\mathbf{x}_{12}$. Points 3 and 4 represent the ends of $\mathbf{x}_{34}$ (see Figure B.1). The absolute value of the Gauss integral, multiplied by 4π, is denoted as $\omega*$; the solid angle defined by all the observational directions in which $\mathbf{x}_{12}$ and $\mathbf{x}_{34}$ appear to cross with $\mathbf{x}$ nearest the viewpoint. Figure B.1 depicts this contribution. The area $\omega*$ can be quantified

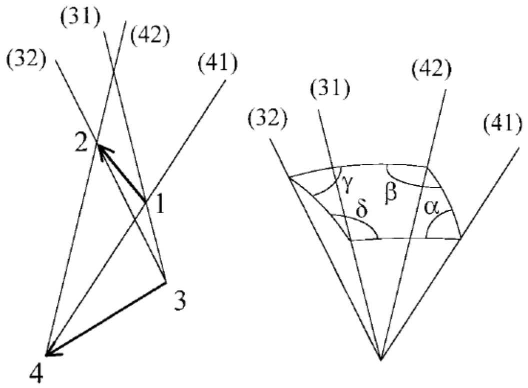

Figure B.1: Two segments of a discretised curve $\mathbf{x} = \mathbf{x}_1, \mathbf{x}_2, \mathbf{x}_3, ...\mathbf{x}_p$ are depicted in (a). These sections are those joining points 1 to 2 and 3 to 4 respectively. The four directions linking these points are labelled in (a). In (b) the various angles making the quadrangle area joining these directions are depicted.

as

$$\omega * = \alpha + \beta + \gamma + \delta - 2\pi. \tag{B-2}$$

where the angles α, β, γ and δ are those depicted in (b), Figure B.1. These angles can be evaluated in terms of the segment normals as

$$\mathbf{n}_1 = \frac{\mathbf{x}_{13} \times \mathbf{x}_{14}}{|\mathbf{x}_{13} \times \mathbf{x}_{14}|}, \tag{B-3}$$

$$\mathbf{n}_2 = \frac{\mathbf{x}_{14} \times \mathbf{x}_{24}}{|\mathbf{x}_{14} \times \mathbf{x}_{24}|}, \tag{B-4}$$

$$\mathbf{n}_3 = \frac{\mathbf{x}_{24} \times \mathbf{x}_{23}}{|\mathbf{x}_{24} \times \mathbf{x}_{23}|}, \tag{B-5}$$

$$\mathbf{n}_4 = \frac{\mathbf{x}_{23} \times \mathbf{x}_{13}}{|\mathbf{x}_{23} \times \mathbf{x}_{13}|}, \tag{B-6}$$

$$\tag{B-7}$$

and

$$\omega * = \arcsin(\mathbf{n}_1 \cdot \mathbf{n}_2) + \arcsin(\mathbf{n}_1 \cdot \mathbf{n}_2) + \arcsin(\mathbf{n}_1 \cdot \mathbf{n}_2) + \arcsin(\mathbf{n}_1 \cdot \mathbf{n}_2). \tag{B-8}$$

See [58] for more details on the derivation. Finally each contribution must be coupled with a sign (as in Figure 1.8), leaving

$$\frac{\omega}{4\pi} = \frac{\omega*}{4\pi} sign((\mathbf{x}_{34} \times \mathbf{x}_{12}) \cdot \mathbf{x}_{13}). \tag{B-9}$$

B.2 Evaluating $\mathcal{W}_z$

Calculations involving $\mathcal{W}_z(\mathbf{x})$ in this thesis were only performed on continuously parameterised smooth spacecurves. Evaluation of these curves, using (2.12), was performed using the Mathematica NIntegrate[] function (`http://reference.wolfram.com/mathematica/ref/NIntegrate` for notes on its implementation).

B.3 $\mathcal{W}_p$

In evaluating the polar writhe it is necessary to partition the curve by its critical points. Following Chapter 3 the discussion shall centre on a $\hat{z}$ parameterisation of the curve. In the general case the critical points are turning points along $\hat{z}$ (d$\mathbf{x}$/dz = 0), and points, $\mathbf{x}(z)$, which share a z value with either the start or end point (see section 5.3.4 for a discussion on critical points of open spacecurves). We shall first discuss the general open writhe algorithm and then specific closed curve and looped curve cases. In this thesis both smooth curve (Chapters 4 and 5) and polygonal curve calculations (Chapter 6) were used, the algorithm described below works for both cases.

Partitioning the curve

Consider an open spacecurve $\mathbf{x}$ parameterised by t, with m local maxima and n local minima. The curve is discretised into p connected linear segments $\mathbf{x}_i$; where $\mathbf{x} = \mathbf{x}_1, \mathbf{x}_2, \mathbf{x}_3, ...\mathbf{x}_p$. In this thesis the algorithms were performed using $p = 1000$. Turning points can be found by multiplying the difference in z value of neighbouring sections of curve. Consider neighbouring sections $\mathbf{x}_u(t)$ and $\mathbf{x}_v(t)$. The two sections are associated with 3 distinct parameter values t_1 , t_2 , t_3 , see (a) in Figure B.2. The product $(\mathbf{x}_u(t_1) - \mathbf{x}_u(t_2))_z.((\mathbf{x}_v(t_3) - \mathbf{x}_v(t_2))_z$ will be negative at a turning point pairing (see (b) in Figure B.2), and positive at all other pairings. The turning points are designated as the t_2 value for all neighbouring pairs for which $(\mathbf{x}_u(t_1) -$

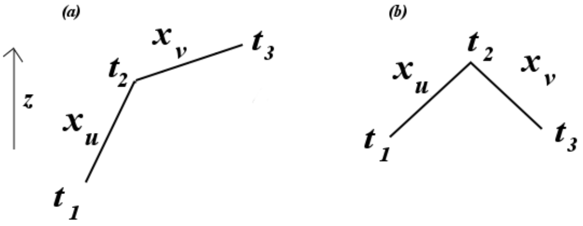

Figure B.2: The discretised construction used to identify turning points on a curve $\mathbf{x}(t)$, the direction of increasing z is indicated by an arrow to the left of the figure. In (a) we see two sections of the discretised curve $\mathbf{x}_u$ and $\mathbf{x}_v$. Section $\mathbf{x}_u$ joins points $\mathbf{x}(t_1)$ and $\mathbf{x}(t_2)$, and $\mathbf{x}_v$ joins $\mathbf{x}(t_1)$ and $\mathbf{x}(t_2)$. In (a) the product $(\mathbf{x}_u(t_1) - \mathbf{x}_u(t_2))_z.((\mathbf{x}_v(t_3) - \mathbf{x}_v(t_2))_z$ is positive. In the case of (b), a turning point along $\hat{z}$, the product is negative.

$\mathbf{x}_u(t_2))_z.((\mathbf{x}_v(t_3) - \mathbf{x}_v(t_2))_z < 0$. We then split the curve into $m + n + 1$ sections using these points. Using this data we can then evaluate the $\mathcal{W}_{pl}$ contribution.

$\mathcal{W}_{pl}$

We apply equation 3.53 over all sections, the integrations are performed using a variant of Simpson's Rule (see Press *et al* [87]).

$\mathcal{W}_{pnl}$

In order to evaluate the non-local contribution it is necessary to identify sections of the curve which overlap. This can be done by comparing the z ranges for each section say $[z_i^{min}, z_i^{max}]$ and $[z_j^{min}, z_j^{max}]$. If there is no overlap between these sections e.g. $z_i^{min} > z_j^{max}$, then there will be no contribution. If there is an overlap then there will necessarily be a contribution to $\mathcal{W}_{pnl}$. Once all overlapped section pairings have been obtained it is necessary to evaluate all full windings between each pair. To do this it is necessary to consider all $\mathbf{r}(z)$ orientations over each mutual z range. It is not however necessary to measure each orientation $\Theta(z)$. For example if we label each quadrant of possible $\Theta(z)$ values $1, 2, 3, 4$ and choose count every time the orientation passes from 2 to 3 as $+1$ and 3 to 2 as -1; we are counting the number of times the orientation is equal to π. If we choose to evaluate angles in sections 3 and 4 as being between $[0, \pi]$ not $[\pi, 2\pi]$, then this scheme will successfully count the number of full windings between each section having a $\mathcal{W}_{pnl}$ contribution.

In the general open curve case we can now evaluate $\mathcal{W}_{pnl}$ using (5.16) along with (5.17). However, we must note there are two cases which can be evaluated in a simpler manner.

B.3.1 Looped spacecurves

A characteristic of the field lines generated in Chapter 6 (see section 6.4) is that their start and end points lie on a mutual plane $z = 0$. Thus the start/end $\mathcal{W}_{pnl}$ contribution is restricted to a single evaluation of $\Theta(z = 0)$ (taking into account any additional full windings).

B.3.2 Closed spacecurves

As with the looped case the start/end contributions to $\mathcal{W}_{pnl}$ can be limited to a single contribution of the start-end tangent. We must be careful here to use the contribution for which the tangent is correctly oriented that is start-end or end-start.

Appendix C

Proof that B is a linear force free field. (see page 169)

It is required that our field (given by equation (6.25)), must satisfy the linear force free field equation 6.13. Taking the Laplacian of (6.25) gives

$$\nabla^2 \mathbf{B}(x,y,z) = \alpha^2 \left(\left(\frac{n\alpha - m\gamma}{k^2} \cos mx + ny, -\frac{m\alpha + n\gamma}{k^2} \cos mx + ny, \sin mx + ny \right) e^{-\gamma z} \right), \tag{C-1}$$

as required. Further it is clear that any linear superposition of (6.25) will also satisfy (6.13). It is also required that our field satisfy (6.3), (no magnetic monopoles). It can be checked that, when $\mathbf{B}$ is given by 6.25,

$$\nabla \cdot \mathbf{B} = 0 \tag{C-2}$$

Again this will be true of a linear superposition of (6.25). Thus we have satisfied the conditions required for a linear force free field.

Bibliography

[1] Abramenko V I, Wang T, Yurchishin V B, *Analysis of electric current helicity in active regions on the basis of vector magnetograms, Solar Phys.,* 168(1), 75-89, (1996).

[2] Altschuler M D, Newkirk G, *Magnetic fields and the structure of the solar corona, Solar phys.,* 9, 131- (1969).

[3] Amari T, Aly1 J J, Luciani J F, Boulmezaoud T Z, Mikic Z *Reconstructing the solar coronal magnetic field as a force-free magnetic field, Solar phys.,* 174(1-2), 129-149, (1997)

[4] Agarwal P, Edelsbrunner H, Wang Y, *Computing the writhing number of a polyagonal knot, Discrete. Comput. Geom.,* 32, 37-53, (2004).

[5] Aldinger J, Klapper I, Tabor M, *Formulae for the calculation and estimation of writhe, J. Knot. Theory. Ram,* 4(3), 343-372, 1995.

[6] Arnold V I, *The asymptotic Hopf invariant and its applications (In Russian): In Proc Summer School in Differential Equations, Ervevan, Armenian SSR Acad Sci,* 1974.

[7] Arnold V I, Khesin B, *Topological Methods in Hydrodynamics, New York: Springer,* (1992).

[8] Aschwanden M J, *Physics of the Solar Corona, Pub: Springer Verlag, New York,* (2004).

[9] Bates A.D, Maxwell A, *DNA topology, Oxford University Press*, (2005).

[10] Berger M A, *Rigorous new limits on magnetic helicity dissipation in the solar corona, Geophysical. and Astrophysical. Fluid Dynamics,* 30, 79-104, (1984)

[11] Berger M A, Field G B, *The topological properties of magnetic helicity, J Fluid Mech.,* 147, 133-148, (1984).

[12] Berger M A *Energy-crossing number relations for braided magnetic fields, Phys. Rev. Lett.,* 70, 705-708, (1993).

[13] Berger M A, *Magnetic helicity in space phyiscs,* Magentic helicity in space and laboratory plasmas, Amer Geophys Unions, Washington DC, 1-9, (1999).

[14] Berger M A, *Topological invariants in Braid theory, Lett. Math. Phys.,* 55, 181-192.(2001).

[15] Berger M A, Prior C B, *The writhe of open and closed curves J. Phys. A: Math. Gen.* 39, 8321-8348, (2006).

[16] Benham C J, *Onset of writhing in cicular elastic polymers, Phys. Rev. A,* 39(5), 2582-2585, (1989).

[17] Bouchiat C, Meźard M, *Elastic rod model of a supercoiled DNA molecule, Eur. Phys. J,* 2, 377-402, (2000).

[18] Bouchiat C, Mézard *A Reply to "Comment on Elasticity Model of a Supercoiled DNA molecule" Phys. Rev. Lett,* 88(8), 089802, (2002).

[19] Burnette A B, Canfield R C, Pevstov A A, *Photospheric and Coronal Currents in Solar Active Regions, Astrophys J.,* 606, 565-570, (2004).

[20] Bustamante C, Marko F D, Sigga E D, Smith S, *Entropic elasticity of lambda-phage DNA*, *Science,* 265, 1599-1600, (1994).

[21] Brereton M G, Shah S, *The configurational properties of topologoically entangled molecules, J. Phys. A: Math. Gen.,* 15, 985-999. (1982)

[22] Brereton M G, Vigilis T A, *The statistical mechanics of a melt of polymer rings J. Phys. A: Math. Gen.,* 28, 1149-1167, (1995).

[23] Canfield R C, Hudson H S, Mckenzie D E, *Sigmoidal Morphology and Eruptive Solar Activity, Geophys. Rev. Lett.,* 26(6), 627-630, (1999).

[24] Călugăreanu G, *Sur Les Classes D'Isotopie Des Noeuds Tridimensionnels et Leurs Invariants, Czechoslovak. Math. J,* 66, 588-625, (1959).

[25] Călugăreanu G, *Sur les enlacements tridimensionnels des courbes fermeés, Comm. Acad R.P. Romine,* 11, 829-832, (1961).

[26] Cantarella J, *On comparing the writhe of a smooth curve to the writhe of an inscribed polygon, SIAM. J. Numerical. Analysis,* 336(2), 191-207, (2005).

[27] Chae J, Moon Y D, Park Y D, *Determination of magnetic helicity content of solar active regions from SOHO.MDI magnetograms, Solar Phys.* 223, 39-55, (2004).

[28] Chiu Y T, Hilton H H, *Exact greens function method of solar force-free magnetic field computations with constant* $\boldsymbol{\alpha}$ *L theory and basic cases, Astrophysical J.,* 212, 873-885, (1977).

[29] Chmutov S V, Duzhin S V, *The Kontsevitch integral, Acta. Appl. Math.,* 66,155-190, (2001).

[30] Cimasoni D, *Computing the writhe of a knot, J Knot Theory. Ram.,* 10, 387-395, (2001).

[31] Crick F H C, *Linking numbers and nucleosomes, Proc. Natl. Acad. Sci. USA.,* 78(8), 2639-2643, (1976).

[32] Démoulin P, Mandrini C H, van Driel-Geszteyli L, Lopez Fuentes M C, Aulanier G, *The magnetic helicity injected by shearing motions, Solar Phys.,* 207, 87-110, (2002).

[33] Cromwell P, *Knots and links, Cambridge university press,* (2004).

[34] Démoulin P, van Driel-Gestztelyi L, Mandriani C H, Thompson B, Plunkett S, Kövári Z, Aulanier G, Young A, *What is the source of the magnetic helicity shed by CMEs? The long term helicity budget of AR 7978, Solar Phys.,* Astronomy and Astrophysics, 382, 650-665, (2002).

[35] Démoulin P, Berger M A, *Magnetic energy and helicity fluxes at the photospheric level,* Solar Phys., 213-228 (2003).

[36] Démoulin P, Pariat E, *Modelling and observations of photospheric magnetic helicity, Advances in space Research, in press.*

[37] Dennis M R, Hannay J H, *Geometry of Călugăreanu's theorem, Proc. R. Soc. London.,* , 461, 3245-3254, (2005).

[38] Eggar M H, *On Whites thorem, J. Knot. Th. Ram.* , 9, 611-615, (2000).

[39] Epple M *Orbits of asteroids, a braid, and the first link invariant, Math. Intelligencer,* 3, 20-27, (1998).

[40] Fain B, Rudnick J, Östlund S *Conformations of linear DNA, Phys. Rev. E,* 55(6), 7364-7368, (1997).

[41] Fan Y, Gibson S E, *Numerical simulations of three dimensional coronal magnetic fields resulting from the emergence of twisted magnetic flux tubes, Astrophys. J.,* 609, 1123-1133, (2004).

[42] Fixman M, Kovac J, *Polymer conformational statistics,III, Gaussian models of stiff chains, J. Chem. Phys,* 58, 1564- , (1973).

[43] Frank-Kamenetskii M D, Vologodskii A V, *Topological aspects of the physics of polymers: The theory and its biophysical applications, Soviet physics - Uzpekhi,* 24(8), 679-696, (1981).

[44] Fuller F B, *The writhing number of a space curve, Proc. Nat. Acad. Sci USA,* 69(4), 815-819, (1971).

[45] Fuller F B, *Decomposition of the linking number of a closed ribbon, a problem from molecular biology Proc. Natl. Acad. Sci. USA,* 75, 3557-3561, (1978).

[46] Gary G A, *Linear force-free magnetic fields for solar extrapolation and interpretation, Astrophys J,* 69 323-348 (1989)

[47] Gauss C F, *Werke, 12 Vols:Leipzig B G Teubner,* 1863-1933.

[48] Gibson S.E, Fan Y, Török T, Kliem B, *The evolving sigmoid: evidence for magnetic flux ropes in the corona before, during and after CMEs, Space Science Rev.,* 124, 131-144, (2006).

[49] Goulub L, Bookbinder J, DeLuca E, Karovska M, Warren H, Schrijvner C J, Shine R, Tarbell T, Title, Wolfson J, Handy B, Kankelborg C, *A new view of the solar corona from the transition region and coronal explorer (TRACE), Phys. Plasmas,* 6, 2205-, (1999).

[50] Green L M, Kliem B, Török, van Driel-Gezstelyi, Attrillm G.D.R, *Transient coronal sigmoids and rotating erupting flux ropes, Solar Phys.,* 365-391, (2007).

[51] Hannay J H, *Cyclic rotations, contractibility and Gauss-Bonnet, J.Phys.A: Math Gen,* 31, 321-324, (1998).

[52] Hagyard M J *Observed non-potential magnetic fields and the inferred flow of electric currents at a location of repeated flaring, Solar Phys.,* 117, 107-124, (1988).

[53] Hirsch M W, *Differential Topolgy, Pub: Springer Verlag, New York,* (1976).

[54] Kaiser M L, *The STEREO mission: and overview, Adv. Space Resaecrh,* 36(8), 1483-1488, (2005).

[55] Kamien R D, *The geometry of soft materials: a primer, Rev. Mod. Phys,* 74, 953-971, (2002).

[56] Kauffman L H. *Knots and Physics, World Scientific,* (1991).

[57] Kelvin W T, Tait P G, *Treatise on Natural Philosophy, 2 Vols, Cambridge University Press*, (1867).

[58] Klenin K, Langowski J, *Computation of writhe in modeling of supercoiled DNA, Biopolymers,* 54, 307-317, (2000).

[59] Kliem B, Titov V S, Török T, *Confined and ejective eruptions of kink-unstable flux ropes, Astron. and Astrophys.,* 413, 23-26, (2004).

[60] Kontsevitch M, *Vassiliev's Knot Invariants, Adv. Sov. Math.,* 16, 137-150, (1993).

[61] Kosugi, T, Matsuzaki K, Sakao T, Shimizu T, Sone Y, Tachikawa S, Hashimoto T, Minesugi K, Ohnishi A, Yamada T, Tsuneta S, Hara H, Ichimoto K, Suematsu Y, Shimojo M, Watanbe T, Shimada S, Davis J M, Hill L D, Owens J k, Title A M, Culhane J L, Harra L K, Doscheck G A, Golub L, *The Hinode (Solar-B) mission: an overview, Solar Phys.,* 243(1), 3-17, (2007).

[62] Kress R, *Linear Integral Equations Pub: Springer Verlag, New York,* (1999).

[63] Kusano K, Maseshiro T, T Yokoyama, Sakurai T, *Measurement of magnetic helicity injection and free energy loading into the solor corona,* 577, 501-512, (2002).

[64] Langevin R, *Differential geometry of curves and surfaces; from "An introduction to the geometry and topology of fluid flows", Kluwer Academic Pub: Dordrecht, Holland,* 13-33, (2001).

[65] Liu R , Gilbert H R, Alexander D, Su Y, *The effect of magnetic reconnection and writhing in a partial filament eruption, Astophys. J.,* 1508-1515, (2008).

[66] Longcope D, *Topological methods for the analysis of solar magnetic fields,* 2, 7-69, (2005).

[67] Low B.C, Berger M A, *A morphological study of helical coronal magnetic structures, Astrophys J,* 589(1), 644-657, (2003).

[68] Mackay D H, Gaizauskas V, Rickard G J, Priest E R, *Force-free and potential models of a filament channel in which a filament forms, Astophys J,* 486. 534-549. (1997).

[69] Maggs A C, *Writhing geometry at finite temperature: Random walks and geometric phases for stiff polymers, J. Chem. Phys.,* 114, 5888-5896, (2001).

[70] Maxwell J C, *Treatise on Electricity and Magnetism 2 Vols: Oxford: Clarendon press,* (1873).

[71] Magara T, Longcope D, *Sigmoid structure of an emerging flux tube, Astrophys. J.,* 559, 55-59, (2001).

[72] Magara T, Longcope D, *Injection of magnetic energy and magnetic helicity into the solar atmosphere by an emerging magnetic flux tube, Astrophys. J.,* 586, 630-649, (2003).

[73] Mermin N.D, Ho T L, *Circulation and Angular Momentum in a phase of superfliud Helium-3, Phys. Rev. Lett,* , 46, 1216-, (1976).

[74] Moffatt H K *The Degree of Knottedness of Tangled Vortex Lines J Fluid Mech* 35 117 (1969).

[75] Moffatt H K, Ricca R L, *Helicity and the Călugăreanu invariant, Royl. Soc. Lond. A.,* 439, 411-429, (1992).

[76] Moore R L, Sterling A.C, Hudson H.S, Lemen J R, *Onset of the magnetic explosion in solar flares and coronal mass ejections, Astrophys J.,* 552, 833- (2001).

[77] Moroz J, Nelson P, *Entropic elasticity of twist storing polymers, Macromolecules,* 31, 6333, (1998).

[78] Morse P M, Fesbach, *Methods of theoretical physics, New York: Mcgaw Hill,* (1953).

[79] Nakagawa Y, Raadu M A, Billings D E, McNamara D, *On the topology of filaments and chromospheric fibrils near sun spots,* Solar Phys., 19, 72-85, (1971).

[80] Nakagawa Y, Raadu M A, *On practical representation of magnetic field, Solar Phys.,* 25, 127-135, (1972).

[81] Orlandini E, Tesi M C, Whittington S G, Sumners D W, Janse van Rensburg E J, *The writhe of a self avoiding walk, J. Phys. A: Math Gen,* 27 333-338, (1994).

[82] Parker E N *The origin of solar activity, Ann Rev Atsron Astrophys,* 15, 45-68, (1977).

[83] Pevstov A A, Canfield R C, McClaymont A N, *On the subphotospheric origin of coronal electric currents, Astrophys J.,* 487, 973-977, (1997).

[84] Pevstov A A, Latushko S M, *Current helicity of the large scale photoshperic magnetic field,* 528, 999-1003, (2000)

[85] Pevstov A A, Balasubramaniam K S, Rogers J W, *Chirality of chromospheric filaments, Astrophys. J.*, 549, 109-124, (2003).

[86] Pevstov A A, *What helicity can tell us about solar magnetic fields,* J. Atsophs. Ast., 29, 49-56, (2008)

[87] Press W H, Teukolsky S, Vetterling W T, Flannery B P, *Numerical recipes: The art of scientific computing, Cambridge university press,* (2007).

[88] Pohl W F, *The self-linking number of a closed spacecurve, J. Math. and Mech.,* 17, 975-985 (1968).

[89] Pohl W L, *DNA and differential geometry, Math. Intelligencier,* 3, 20-27 (1981).

[90] Priest E R *Solar Magneto-hydrodynamics, Kluwer Academic Pub: Dordrecht, Holland,* (1981).

[91] Rossetto V, Maggs A C *Comment on "Elasticity model of a supercoild DNA molecule", Phys. Rev. Lett,* 88(8). 089801, (2002).

[92] Rosetto V, Maggs A C, *Writhing geometry of open DNA, J. Chem. Phys.,* 118 2864- (2003)

[93] Rust D M, Kumar A, *Evidence of helically kinked magnetic flux ropes in solar eruptions.* 464, 199-202, (1996).

[94] Rust D M, *The helical flux rope structure of solar filaments, Adv. Space. Res.* 32(10), 1895-1903, (2003).

[95] Samuel J, Sinha S, *Molecular elasticity and the geometric phase, Phys. Rev. Lett.,* 90(9), (2003).

[96] Samuel J, Sinha S, Ghosh A, *DNA elasticity, the topology of self avoidance, J Phys: cond. Matt.,* 18, 253-268, (2006).

[97] Scherrer P H, Bogart R S, Bush R I, Hoeksema J T, Kosovichev A G, Schou J, Rosenberg W, Springer L, Tarbell T D, Title A, Wolfson C J, Zayer I *The Solar Oscillations Investigation - Michaelson Doppler Imager, Solar Phys,* 162(1-2), 129-188, (2004).

[98] Schmidt H U, *On the observable effects of magnetic energy storage and release connected with solar flares, In: Symposium on physics of Solar flares, ed W N Ness: pub NASA sp-50,* 107-, (1964).

[99] Semel M, *Extrapolation functions for constant-alpha force-free fields - Green's method for the oblique boundary value, Solar Phys.,* 293, 293-299 (1988).

[100] Sternberg S, *Lectures in differential geometry, New York: Chelsea,* (1983).

[101] Solomon B, *Tantrices of spherical curves, Amer. Math. Monthly,* 103, 30-39, (1996).

[102] Sossinsky A, *Knots, mathematics with a twist. Harvard University Press,* (2002).

[103] Starostin E L, *Comment on "Cyclic rotations, contractibility and Gauss-Bonnet", J.phys. A:Math Gen,* 35 6183-6190 (2002)

[104] Starostin E L, *On the writhe of non-closed curves,* Chapter 26 in *Physical and numerical models in knot theory including applications to the life sciences,* 525-545, (2005).

[105] Smith S B, Finzi L, Bustamante C, *Direct mechanical measurements of the elasticity of single DNA molecules by using magnetic beads, Science,* 258 1122-1126, (1992)

[106] Taylor J B, *Relaxation of toroidal plasma and generation of reverse magnetic fields, Phys. Rev. Lett.,* 33, 1139-1141, (1974).

[107] Taylor J B, *Relaxation and magnetic reconnection in plasmas, Rev. Mod. Phys,* 58, 741-763, (1986).

[108] Titov V S, Demoulin P, *Basic topology of twisted magnetic configurations in solar flares,* 351, 720-720, (1999).

[109] Török T, Kleim B *The Kink instability in solar eruptions, Proccedings of the SOHO 15 Workshop - Coronal Heating, St Andrews, Scotland,* (2004).

[110] Török T, Kleim B *Confined and Ejective Eruptions of Kink-Unstable Flux Ropes, Astrophys J,* 630, 97-100, (2005).

[111] Travers A, Muskhelishvili G, *DNA supercoiling - a global transcriptional regulator for enterobacterial growth? Nature Rev. Microbiology,* 3, 157-169, (2005).

[112] Tsuneta A, Acton L, Bruner M, Lemen J, Brown W, Caravalho R, Catura R, Freeland S, Jurcevich B, Morrison M, Ogawara Y, Hirayama T, Owens J, *The soft X-ray telescope for the Solar-A mission, Solar Phys.,* 136, 37-67 (1991).

[113] van der Heijden G H M, Neukirch S, Goss V G A, Thompson J M T, *Instability and self-contact phenomena in the writhing of clamped rods, J Mech Sciences,* 45(1), 161-196, (2003).

[114] van der Heijden G H M, Peletier M A, Planque R, *On end rotation for open rods undergoing large Deformations, Quarterly of Applied Mathematics,* 65, 385-402, (2007).

[115] Vologodskii A V, Marko J F, *Extension of torsionally stressed DNA by external force, Biophys. J.,* 73, 123-132, (1997).

[116] Wang J C, *DNA Topoisomerases, Ann. Rev. Biochem.,* 65, 635-692, (1996).

[117] White J H, *Self linking and the Gauss intergal in higher dimensions, Am. J. Math.,* 91(3), 693-728, (1969).

[118] Woltjer L, *A Theorem on force free magnetic fields, Proc. Natl. Acad. Sci. USA,* 44, 489, (1958).